Parameter identification approaches with application to different classes of materials

von der Fakultät Maschinenbau
der Technischen Universität Dortmund
zur Erlangung des akademischen Grades

Doktor-Ingenieur (Dr.-Ing.)

genehmigte Dissertation

von

Robin Schulte

aus Wickede (Ruhr)

Vorsitz:	apl. Prof. PD Dr.-Ing.
	Dipl.-Inform. A. Zabel
Hauptreferent:	Prof. Dr.-Ing. habil. A. Menzel
Korreferenten:	Prof. B. Kiefer, Ph.D.
	Prof. Dr. M.G.R. Faes
Tag der Einreichung:	18.04.2023
Tag der mündlichen Prüfung:	27.10.2023

Bibliografische Information Der Deutschen Bibliothek
Die Deutsche Bibliothek verzeichnet diese Publikation in der Deutschen Nationalbibliografie; detaillierte bibliografische Daten sind im Internet über **http://dnb.ddb.de** abrufbar.

Bibliographic information published by Die Deutsche Bibliothek
Die Deutsche Bibliothek lists this publication in the Deutsche Nationalbibliografie; detailed bibliographic data is available in the Internet at **http://dnb.ddb.de**.

Schriftenreihe des Instituts für Mechanik

Herausgeber: Institut für Mechanik
Fakultät Maschinenbau
Technische Universität Dortmund
Leonhard-Euler-Str. 5
D-44227 Dortmund

Druck: Koffler DruckManagement GmbH

Als Manuskript gedruckt. Printed in Germany.

ISSN 2191-0022
ISBN 978-3-947323-45-6

To my family

Acknowledgements

This work is related to the research I conducted during my time as a research assistant at the Institute of Mechanics at TU Dortmund University and afterwards between 2017 and 2023. By this point, I would like to thank all the people who supported me during this time in so many different ways.

At first, I want to thank in particular my doctoral advisor Prof. Andreas Menzel for the opportunity of graduating in such an outstanding research team. It was a pleasure to deal with all the different research challenges under his guidance and to benefit from his inspiring scientific knowledge. He always had time for fruitful discussions in all the years of our great collaboration.

In addition, I would like to thank Prof. Björn Kiefer for his support, enthusiasm in the field of mechanics and for accepting to act as the co-referee of this thesis. Furthermore, many thanks go to Prof. Matthias Faes and Prof. Andreas Zabel for serving as third referee and chairman of the examination committee, respectively.

I will always remember the incredible time at the institute since it was so enjoyable to be part of such a group with a remarkable and excellent working atmosphere. Therefore, I thank Prof. Jörn Mosler for some great discussions and in particular Kerstin Walter and Christina McDonagh for their incredible support in all organisational aspects and the planning of our social events. Moreover, I am very grateful for the hardware and software support provided by Matthias Weiss. Special thanks also go to Dr. Thorsten Bartel and Prof. Richard Ostwald for their supervision and support in various projects.

In particular, I would like to deeply thank my office partners Dr. Karsten Buckmann and Isabelle Noll for the incredible working atmosphere and fruitful discussions—not only of scientific nature but also privately. Furthermore, I would like to thank Dr. Serhat Aygün, Dr. Alexander Bartels, Dr. Rolf Berthelsen, Dr. Till Clausmeyer, Dr. Dinesh Dusthakar, Volker Fohrmeister, Tim Furlan, Jan Gerlach, Gian-Luca Geuken, Dilek Güzel, Fabian Guhr, Marius Harnisch, Dr. Tim Heitbreder, Dr. Raphael Holtermann, Dr. Tobias Kaiser, Dr. Patrick Kurzeja, Henning Lammen, Alexander Niehüser, Felix Rörentrop, Dr. Lars Rose, Markus Schewe, Dr. Alexander Schowtjak, Dr. Christian Sievers, Leon Sprave, Dr. Tobias Waffenschmidt, Tillmann Wiegold, Hendrik Wilbuer and Carina Witt. Thank you very much for the great time and moments at work and afterwards.

Furthermore, my thanks go to all members of the research groups FOR 1509 and TRR 188 for the fruitful work and interdisciplinary discussions. In particular, I would like to thank my S01 project-partners Dr. Alexander Schowtjak, Jan Gerlach, Dr. Richard Ostwald and Dr. Till Clausmeyer.

Finally, I would like to sincerely thank my friends and especially my family—most of all my parents—for their outstanding support over all the years, especially during the phases of high workload. They are always there when I need them and make so many moments in my life special and unforgettable.

Dortmund, October 2023 Robin Schulte

Zusammenfassung

Die vorliegende Arbeit befasst sich mit verschiedenen Strategien der Parameteridentifikation bezüglich der multi-objektiven Optimierung unter Berücksichtigung von integralen Größen und Feldgrößen, um effizient Parameter von komplexen Materialmodellen zu identifizieren, wie beispielsweise Gradienten-erweiterte Schädigungsmodelle. Außerdem wird eine hybride Strategie entwickelt, um die Problematik der Bestimmung von adequaten Startwerten zu überwinden. Zu diesem Zweck wird ein künstliches neuronales Netz mit den simulierten Materialverhalten von diversen Parameterkombinationen trainiert. Anschließend wird die experimentell gemessene Materialantwort in das Netz eingegeben um eine Vorhersage der Parameter zu erhalten, die im Anschluss als qualitativ hochwertiger Startwert für eine multi-objektive Parameteridentifikation verwendet wird. In dieser Arbeit werden die hybride und die weiteren Strategien untersucht unter der Verwendung von verschiedener komplexer Materialmodelle und diverser Gruppen von Materialien. Zusätzlich wird ein Gradienten-erweitertes, mit Viskoelastizität unter finiter Dehnung gekoppeltes Schädigungsmodel entwickelt um effizient Schädigungseffekte in ratenabhängigen Materialien abzudecken. Des Weiteren wird im Kontext eines Laminat-basierenden Modells für ferroelektrische Materialien eine numerische Untersuchung bezüglich numerisch effizienter Fischer-Burmeister Ansätze durchgeführt, um die häufig auftretenden Karush-Kuhn-Tucker Konditionen zu lösen.

Abstract

This thesis deals with different parameter identification strategies regarding multi-objective optimisations including integral and field data in order to efficiently identify parameters of complex material models, e.g. gradient-enhanced damage models. In addition, to overcome the difficulty of finding appropriate starting values, a hybrid strategy is developed. For this purpose, an artificial neural network is trained with simulated material behaviours of various parameter combinations. Subsequently, the experimentally measured response is fed into the network to obtain a parameter prediction which is afterwards employed as qualitative starting value for a subsequent multi-objective parameter identification. In this work, the hybrid and the other strategies are investigated by employing different complex material models and various material groups. Moreover, a gradient-enhanced damage model coupled to finite strain viscoelasticity is developed to efficiently cover damage effects in rate-dependent material responses. Furthermore, in the context of a laminate-based model for ferroelectric materials, a numerical inves-

tigation is performed regarding numerically efficient Fischer-Burmeister approaches, to solve the frequently occurring Karush-Kuhn-Tucker conditions.

Publications

Key parts of this thesis are based on peer-reviewed journal articles, which were either published or submitted during the progress of this thesis.

1. T. Bartel, R. Schulte, A. Menzel, B. Kiefer, B. Svendsen: *Investigations on enhanced Fischer-Burmeister NCP functions: application to a rate-dependent model for ferroelectrics*, Archive of Applied Mechanics, 89:995-1010, 2019 [6].

2. R. Schulte, R. Ostwald, A. Menzel: *Gradient-Enhanced Modelling of Damage for Rate-Dependent Material Behaviour—A Parameter Identification Framework*, Materials, 13(14),3156, 2020 [110].

3. A. Schowtjak, R. Schulte, T. Clausmeyer, R. Ostwald, A.E. Tekkaya, A. Menzel: *ADAPT — A Diversely Applicable Parameter Identification Tool: Overview and full-field application examples*, International Journal of Mechanical Sciences, 213:106840, 2022 [104].

4. R. Schulte, C. Karca, R. Ostwald, A. Menzel: *Machine learning-assisted parameter identification for constitutive models based on concatenated loading path sequences*, European Journal of Mechanics - A/Solids, 98:104854, 2023 [113].

For all of the listed articles, the author of this thesis contributed essential parts considering the underlying theories, the algorithmic formulations and the preparation of the articles. Considering the peer-reviewed article [104], the author of this thesis together with the co-author Alexander Schowtjak mainly elaborated the theory and the implementation of the parameter identification tool ADAPT, which was published open-source, as well as the preparation of the paper. Specifically, the author of this thesis contributed to general sections of the article, e.g. introduction, methods or conclusion, and was responsible for the application of ADAPT to a gradient-enhanced damage formulation coupled to finite plasticity (Section 3.4 of the paper) and to visco-elastic damage (Section 4.1 of the paper). For the peer-reviewed journal articles [6, 110, 113], the author of this thesis contributed essential aspects with regard to the outline of the theory, carried out all of the numerical implementations and simulations, and prepared the articles.

During and alongside the preparation of this work, the following publications were completed

1. D.J. Hartl, B. Kiefer, R. Schulte, A. Menzel: *Computationally-efficient modeling of inelastic single crystal responses via anisotropic yield surfaces: Applications to shape memory alloys*, International Journal of Solids and Structures, 136-137:38-59, 2018 [30].

2. R. Schulte, A. Menzel, B. Svendsen: *A Laminate-Based Material Model Applied to Ferroelectrics*, Proceedings of the 3rd Seminar on The Mechanics of Multifunctional Materials, 18:105-108, 2018 [109].

3. R. Schulte, T. Bartel, A. Menzel, B. Kiefer, B. Svendsen: *Investigations on different Fischer-Burmeister functions applied to the modelling of ferroelectrics*, Proceedings in Applied Mathematics and Mechanics, 18:e201800331, 2018 [108].

4. R. Schulte, R. Ostwald, A. Menzel: *A computational framework for gradient-enhanced damage – implementation and applications*, Proceedings in Applied Mathematics and Mechanics, 20:e202000215, 2021 [111].

5. A. Schowtjak, S. Wang, O. Hering, T. Clausmeyer, J. Lohmar, R. Schulte, R. Ostwald, G. Hirt, A.E. Tekkaya: *Prediction and analysis of damage evolution during caliber rolling and subsequent cold forward extrusion*, Production Engineering: Research and Development, 14:33-41, 2020 [103].

6. K. Langenfeld, A. Schowtjak, R. Schulte, O. Hering, K. Möhring, T. Clausmeyer, R. Ostwald, F. Walther, A.E. Tekkaya, J. Mosler: *Influence of anisotropic damage evolution on cold forging*, Production Engineering: Research and Development, 14:115-121, 2020 [59].

The contributions in the proceedings [108, 109, 111] are related to conference participations of the author of this thesis. Regarding the content of this thesis, the proceedings [108, 109] are preliminary work which is included in the peer-reviewed article [6] and the proceeding [111] is included in the peer-reviewed article [110]. The author of the thesis contributed basic aspects regarding the outline of the theory, preparation of the slides, carried out the talk, executed the corresponding numerical implementations as well as the simulations and generated the contributions. With regard to the contribution [103], the author of this thesis only contributed to the preparation of the article and considering the contribution [59], the author only assisted in the preparation and thus, both works are not included in this thesis. Regarding the article [30], the author contributed to the numerical implementations and preparation of the article, mainly to the Sections 4.3, 4.4, Appendix B and Appendix C. However, this article is not included in this thesis.

Contents

Notation

Within this work, a consistent notation is employed which is explained by the context. Nevertheless, some of the basic relations are summarised in the following for reasons of clarity and comprehensibility.

Tensors The tensors of first, second and fourth order can be expressed in terms of their coefficients by employing a representation of the Cartesian basis vectors $\{\boldsymbol{e}_i\}$, with $i = 1, 2, 3$ spanning the three-dimensional Euclidean space $\mathbb{R}^3$, namely

$$\begin{aligned} \boldsymbol{v} &= v_i \, \boldsymbol{e}_i \ , \\ \boldsymbol{T} &= T_{ij} \, \boldsymbol{e}_i \otimes \boldsymbol{e}_j \ , \\ \mathsf{S} &= \mathsf{S}_{ijkl} \, \boldsymbol{e}_i \otimes \boldsymbol{e}_j \otimes \boldsymbol{e}_k \otimes \boldsymbol{e}_l \ . \end{aligned}$$

In this work, Einstein's summation convention is applied to obtain a clear notation and typically non-bold letters are employed for scalars, bold-face lower-case italic letters for first-order tensors (i.e. vectors), bold-face upper-case italic letters for second-order tensors and bold-face upper-case sans-serif letters for fourth-order tensors.

Inner tensor products The contractions of inner tensor products are depicted by dots and the number of dots specifies the number of contractions, namely

$$\begin{aligned} \boldsymbol{v} \cdot \boldsymbol{u} &= v_i \, u_i \ , \\ \boldsymbol{T} \cdot \boldsymbol{v} &= T_{ij} \, v_j \, \boldsymbol{e}_i \ , \\ \boldsymbol{T} \cdot \boldsymbol{K} &= T_{ij} \, K_{jk} \, \boldsymbol{e}_i \otimes \boldsymbol{e}_k \ , \\ \boldsymbol{T} : \boldsymbol{K} &= T_{ij} \, K_{ij} \ , \\ \mathsf{S} : \boldsymbol{T} &= \mathsf{S}_{ijkl} \, T_{kl} \, \boldsymbol{e}_i \otimes \boldsymbol{e}_j \ . \end{aligned}$$

If the number of contractions between two tensors is of the same level as the order of these tensors, a scalar is always obtained as result.

Outer tensor products Within this work, not only the standard outer tensor or dyadic products, respectively, indicated with the symbol $\otimes$ are employed, but also the non-standard outer tensor products $\overline{\otimes}$ and $\underline{\otimes}$, specifically

$$\begin{aligned}
\boldsymbol{v} \otimes \boldsymbol{u} &= v_i\, u_j\, \boldsymbol{e}_i \otimes \boldsymbol{e}_j \,, \\
\boldsymbol{T} \otimes \boldsymbol{K} &= T_{ij}\, K_{kl}\, \boldsymbol{e}_i \otimes \boldsymbol{e}_j \otimes \boldsymbol{e}_k \otimes \boldsymbol{e}_l \,, \\
\boldsymbol{T} \,\overline{\otimes}\, \boldsymbol{K} &= T_{ik}\, K_{jl}\, \boldsymbol{e}_i \otimes \boldsymbol{e}_j \otimes \boldsymbol{e}_k \otimes \boldsymbol{e}_l \,, \\
\boldsymbol{T} \,\underline{\otimes}\, \boldsymbol{K} &= T_{il}\, K_{jk}\, \boldsymbol{e}_i \otimes \boldsymbol{e}_j \otimes \boldsymbol{e}_k \otimes \boldsymbol{e}_l \,.
\end{aligned}$$

In summary, while the result of the dyadic product of two first-order tensors is a second-order tensor, a forth-order tensor is obtained by the dyadic products of two second-order tensors. Furthermore, the non-standard outer tensor products can be depicted in an alternative formulation as

$$\begin{aligned}
[\,\boldsymbol{T} \,\underline{\otimes}\, \boldsymbol{K}\,] : \boldsymbol{L} &= \boldsymbol{T} \cdot \boldsymbol{L}^{\mathrm{t}} \cdot \boldsymbol{K}^{\mathrm{t}} \,, \\
[\,\boldsymbol{T} \,\overline{\otimes}\, \boldsymbol{K}\,] : \boldsymbol{L} &= \boldsymbol{T} \cdot \boldsymbol{L} \cdot \boldsymbol{K}^{\mathrm{t}} \,, \\
[\,\boldsymbol{T} \,\overline{\otimes}\, \boldsymbol{v}\,] \cdot \boldsymbol{u} &= \boldsymbol{T} \cdot \boldsymbol{u} \otimes \boldsymbol{v} \,,
\end{aligned}$$

with $\boldsymbol{T}^{\mathrm{t}}$ denoting the transpose of $\boldsymbol{T}$. Moreover, the symmetric and skew-symmetric part of a second order tensor $\boldsymbol{T}$ are defined as

$$\begin{aligned}
\boldsymbol{T}^{\mathrm{sym}} &= \frac{1}{2}\,[\,\boldsymbol{T} + \boldsymbol{T}^{\mathrm{t}}\,] = \frac{1}{2}\,[\,T_{ij} + T_{ji}\,]\,\boldsymbol{e}_i \otimes \boldsymbol{e}_j \,, \\
\boldsymbol{T}^{\mathrm{skw}} &= \frac{1}{2}\,[\,\boldsymbol{T} - \boldsymbol{T}^{\mathrm{t}}\,] = \frac{1}{2}\,[\,T_{ij} - T_{ji}\,]\,\boldsymbol{e}_i \otimes \boldsymbol{e}_j \,.
\end{aligned}$$

Identity tensors The second-order identity tensor $\boldsymbol{I}$ is defined in terms of the Kronecker delta δ_{ij} as

$$\boldsymbol{I} = \delta_{ij}\, \boldsymbol{e}_i \otimes \boldsymbol{e}_j \,, \quad \text{with} \quad \delta_{ij} = \begin{cases} 1, & \text{if} \quad i = j \\ 0, & \text{if} \quad i \neq j \end{cases} .$$

The fourth-order identity tensor I and the symmetric part of the fourth-order identity tensor $\mathsf{I}^{\mathrm{sym}}$ are denoted as

$$\begin{aligned}
\mathsf{I} &= \boldsymbol{I} \overline{\otimes} \boldsymbol{I} \,, \\
\mathsf{I}^{\mathrm{sym}} &= \frac{1}{2}\,[\,\boldsymbol{I} \,\overline{\otimes}\, \boldsymbol{I} + \boldsymbol{I} \,\underline{\otimes}\, \boldsymbol{I}\,] \,.
\end{aligned}$$

Operators The employed gradient and divergence operations are denoted in index notation following the right-gradient and right-divergence definition—here exemplarily given for second-order tensors—as

$$\nabla_{\boldsymbol{X}} \boldsymbol{T} = \frac{\partial}{\partial X_k} \left[T_{ij}\, \boldsymbol{e}_i \otimes \boldsymbol{e}_j \right] \otimes \boldsymbol{e}_k = \frac{\partial T_{ij}}{\partial X_k}\, \boldsymbol{e}_i \otimes \boldsymbol{e}_j \otimes \boldsymbol{e}_k \,,$$
$$\nabla_{\boldsymbol{X}} \cdot \boldsymbol{T} = \nabla_{\boldsymbol{X}} \boldsymbol{T} : \boldsymbol{I} = \left[\frac{\partial T_{ij}}{\partial X_k}\, \boldsymbol{e}_i \otimes \boldsymbol{e}_j \otimes \boldsymbol{e}_k \right] : \left[\boldsymbol{e}_l \otimes \boldsymbol{e}_l \right] = \frac{\partial T_{il}}{\partial X_l} \boldsymbol{e}_i \,,$$

where the subscript of the Nabla operator $\nabla_\bullet$ typically relates to placements referred to the corresponding configuration.

1 Introduction

The thesis at hand is based on the research which was conducted at the *Institute of Mechanics* during the work in two research projects. One part of the research was carried out within project P6 *Microstructural Interactions and Switching in Ferroelectrics* of the research group FOR 1509 *Ferroic Functional Materials: Multi-scale Modeling and Experimental Characterization*. The second part was performed within project S01 *Scientific Service Project - Model integration* of the transregional research group CRC/Transregio 188 *Damage Controlled Forming Processes*. In both projects, a collaboration between the scientific research areas of process technologies, characterisation and modelling was essential. The first project dealt with the microstructural evolution of the domain switching in ferroelectrics, the second project covered the damage evolution during metal forming processes. The research in this work was initiated within the projects and further extended to this final thesis.

1.1 Motivation and state of the art

While the computational capabilities have increased massively over the recent decades, the requirements of the manufactured products have simultaneously equally increased, especially with respect to energy efficiency in all directions, e.g. in the manufacturing process as well as regarding the whole life cycle. Thus, the need for different materials and more complex material models covering more material mechanisms rises which results in a larger amount of material parameters. Furthermore, the simulations have to predict the material behaviour realistically in order to optimise the products in the preferred directions. To this purpose, it is important that the model parameters are accurately calibrated. Even though parameter identification (PI) has been known for decades, and as a common tool, there is still ongoing improvement—especially with regard to machine learning.

1.1.1 Ferroelectric materials and non-linear complementarity problems

During the last decades smart materials have gained a high relevance in many engineering applications, especially in the area of sensing and actuating. These materials pos-

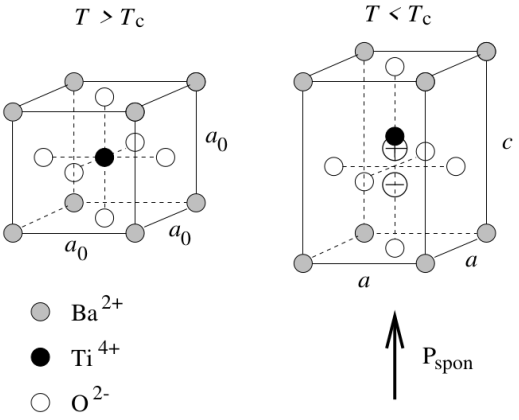

(a) The unit cell of ($BaTiO_3$) in the paraelectric phase—due to the symmetry—on the left and in the ferroelectric phase on the right. The orientation of P_{spon}, the spontaneous polarisation vector, is defined by the displaced titanium ion. Reprinted from M. Kamlah, Continuum Mech. Thermodyn. 13 (2001), 219-268,[46], with permission from Springer Nature.

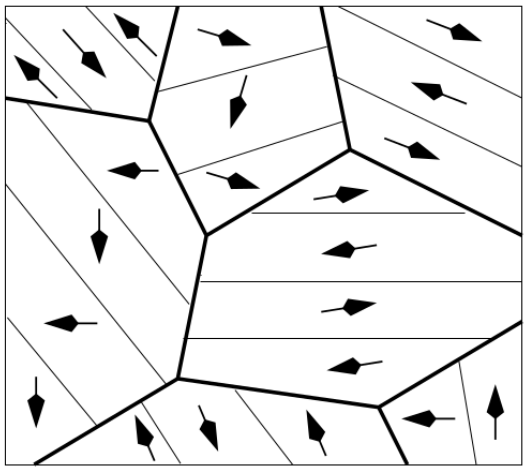

(b) Two-dimensional view of a crystallographic aggregate which was cooled below the Curie temperature. Domains as subregions of equal spontaneous polarisation are visible, such that macroscopically an isotropic state without any polarisation occurs. Reprinted from M. Kamlah, Continuum Mech. Thermodyn. 13 (2001), 219-268, [46], with permission from Springer Nature.

Figure 1.1: The piezoelectric property of the materials is based on the crystallographic microstructure. The crystallographic effects are briefly indicated in both two figures. For further details, please be referred to Kamlah [46], Lines and Glass [68], Tagantsev et al. [125].

sess the special property that a mechanical loading is transferred into a non-mechanical material response and vice versa. Piezoelectric materials are a subgroup of this class of material and are applied if a fast electro-mechanical material response is required, e.g. in sonar, acoustics and ultrasound and precision actuators, see e.g. [37, 68]. Their material behaviour is based on the polarisation of the crystal structure. In addition, ferroelectric materials lose their piezoelectric properties above a certain temperature, the Curie-temperature. Below this temperature, a spontaneous polarisation takes place based on the unit cell structure where the centres of the positive and negative charges no longer coincide, see Figure 1.1a. Among the most frequently used piezoelectric materials are barium titanate ($BaTiO_3$) and lead zirconate titanate (PZT), which mostly occur as polycrystals consisting of different grains with differently oriented crystals. Within these microstructures different domains with uniform spontaneous polarisation directions exist. Considering a tetragonal crystal structure below the Curie-temperature, six different spontaneous polarisation directions are possible. The composition or, say, the mixture of these different phases of the material governs the averaged polarisation and, as a consequence, the macroscopic material behaviour, see Figure 1.1b. For more information on this topic, the reader is referred to, e.g., [40, 46, 68, 125].

Such a material behaviour can be predicted by using mathematically sound material models that fulfil the thermodynamic equations. These models can be divided into three

different groups. On the one hand, phenomenological models with continuous evolution equations can be formulated to characterise the macroscopic material response, see, e.g. [46, 71, 80], while, on the other hand, micromechanically motivated models can be applied which are based on unit cell switching, see, e.g. [36, 39, 65, 67, 115]. Furthermore, phase field or level set approaches can be applied if the microstructure needs to be resolved in space and time, see, e.g. [45, 82, 105].
Laminate-based material models are dedicated to the micromechanical formulations, see, e.g., the review provided in [66]. Single-crystalline ferroelectric materials offer high magnitudes of actuation strains, the predictions of which can be achieved via this kind of approach. In [65], energy minimising multi-rank laminates for ferroelectric single crystals were introduced. Several different laminate approaches can be found in [129, 130, 136]. In [16, 17] a laminate-based model was developed, which is capable of simulating rate- and external stress-dependent domain evolution via suitable Gibbs energy and dissipation functions. Due to the fact that the underlying phase fractions are subjected to physically motivated constraints, the overall framework includes several Karush-Kuhn-Tucker (KKT) conditions. In this regard, nonlinear complementarity problem (NCP) functions were shown to provide sophisticated schemes to fulfil KKT conditions as an alternative to, e.g., active-set strategies. As one of the most frequently used NCP approaches, the Fischer-Burmeister functions introduced in [19] have been applied to problems in solid mechanics in [102] in the context of rate-independent crystal plasticity. Later, this approach was used in, e.g., [4, 5] in the context of material models for shape memory alloys based on energy relaxation concepts which involves both KKT conditions due to rate-independent evolution equations and due to mass constraints. In general, this approach is also applicable to different problems including inequality constraints in the context of contact mechanics.
However, it is well known that the original Fischer-Burmeister approach is prone to numerical instabilities, in particular due to the fact that the related function is not continuously differentiable everywhere. Therefore, several authors have suggested improvements of the original ansatz, e.g. in [12, 18, 47].

1.1.2 Gradient-enhanced continuum damage formulations

The adequate numerical prediction of material behaviour under complex loads and boundary conditions is of high significance in the product development context, particularly in view of today's trends towards more efficient and cost-effective production, but also in view of component safety requirements and appropriate component lifetime predictions. To this end, not only the material model formulation itself needs to be physically sound and able to capture all relevant material phenomena, but the corresponding model parameters also need to be identified properly. This process of model calibration is typically carried out with the help of optimisation-based parameter identification schemes which is described in the next section. Since the accurate prediction of many material mechanisms became more and more important in many engineering

applications, effects like damage have to be simulated properly especially with respect to metal forming processes. However, it is not only necessary to identify the point of failure but more importantly to characterise the evolution of damage prior to failure in order to e.g. control the damage evolution—and thus the material properties—during metal forming processes.

The first development regarding damage mechanics was accomplished by Kachanov [41]. In his work and in many following contributions in the field of classic damage mechanics, damage was considered as a local effect which was described by a single scalar damage variable reducing the effective area which induces material degradation. Further information regarding the classic damage mechanics can be found in [42, 55, 56, 64]. Nevertheless, the local character of these models does not consider the complex nature of damage evolution, e.g. its anisotropic property. To overcome this difficulty, subsequent works incorporated the anisotropic effect by using a tensorial damage variable, see e.g. [48, 61] and the references cited therein. Since the characterisation of damage is important in metal forming processes, ductile damage models have a broad application range. These models are either phenomenological damage models, e.g. the Lemaitre-type damage models—initially developed by Lemaitre [62, 63] and since then extended in several directions by many researchers—or damage models based on micromechanics, e.g. the well known Gurson model [29] which was extended to the popular GTN-model by Tvergaard and Needleman [131] and many further variants in the literature.

In addition, the local damage formulations have mesh dependency in common which is a massive disadvantage, since the finer the mesh, the more the damage region shrinks and even might vanish in the end. Alternatively, non-local damage formulations were introduced which can be categorised based on the extension type of the formulation, i.e. whether they have an integral or gradient shape. However, following Lasry and Belytschko [60], Polizzotto et al. [90], gradient formulations offer various advantages such that gradient-enhanced damage frameworks are more common in the literature. In [133], Waffenschmidt et al. developed a gradient-enhanced damage model for fibre-reinforced materials and large deformations and presented an implementation in Abaqus. The scalar $[1-d]$-type damage formulation with the local damage variable d only affects the anisotropic elastic response and the local free energy is then enhanced by a gradient contribution—following the approach of Dimitrijevic and Hackl [15]—namely, the gradient of the additional independent non-local damage variable. A penalty term is additionally introduced to ensure the equivalence of the local and non-local damage variable. This damage framework was further developed in Polindara et al. [88, 89] and Kiefer et al. [51]. However, the underlying framework of these works is based on a user element subroutine for the finite element program Abaqus. A user element formulation in Abaqus has various disadvantages, i.e. a high effort in developing and testing, the visualisation is not straight forward and requires some workarounds, additional element features like contact require further difficult extensions and the need of different element types requires a completely new implementation. These disadvantages were overcome by Ostwald et al. [86] with a damage regularisation framework which employs the heat-

equation solution capabilities of Abaqus for the damage regularisation. Thus, the model can be implemented as a user material subroutine avoiding the drawbacks of the previously mentioned approaches. This framework is in line with the works of Forest [20] and Miehe [83]. Sprave and Menzel [119] further extended this framework and computed complex boundary value problems based on a finite plasticity model coupled to a gradient-enhanced damage formulation. For further, advanced concepts in the context of gradient damage, see, e.g., the work by Liu and Jeffers [69] and the references cited therein.

The modelling of damage effects is still an ongoing challenge not only with respect to metals and its corresponding forming processes, but also with regard to many different material groups. It is for example highly relevant in biological applications and Polindara et al. [88, 89], Waffenschmidt et al. [134] developed gradient-enhanced damage formulations—on the basis of the already mentioned framework by Waffenschmidt et al. [133]—in order to simulate damage effects and its evolution in biological applications, e.g. blood vessels. Not only biological applications have recently become more important, but also alternative materials in many engineering applications have gained popularity, e.g. in the automotive industry due to the need of lightweight components. In this regard polymers are employed in many engineering applications. For example, thermoplastic polymers are requested due to their good thermomechanical properties and simple manufacturing processes, cf. [7]. Another interesting and promising material is an elastomer with self-diagnostic capabilities. Self-diagnostic poly(dimethylsiloxane) (PDMS) elastomers are produced by the addition of so-called mechanophore units which generate a chemical response towards mechanical loads, as discussed by, e.g., Brighenti and Artoni [11]. The specific PDMS elastomer containing a supramolecular detection probe was presented and developed by Früh et al. [22]. In this case, the elastomer reacts with strain-dependent levels of fluorescence when illuminated with UV light, thus enabling an in situ quantification of the material's strain and, potentially, damage state. Thus accurate constitutive models capturing various material mechanisms are required.

Different material models allow for the description of the mechanical behaviour of rate-dependent—or rather viscoelastic—materials such as the previously mentioned elastomer, mostly using either a convolution integral approach or a differential operator form of the constitutive relation. To name a few, Reese and Govindjee [92], for example, discussed a non-linear viscoelastic model that applies a non-linear evolution law that is valid for arbitrary deviations from thermodynamic equilibrium. Bergström and Boyce [8] proposed a constitutive model for the time-dependent behaviour of elastomers, motivated micromechanically by the relaxation of a single entangled chain in a polymer gel. Simo and Hughes [117] extended the well-established finite hyperelasticity framework with uncoupled volumetric-isochoric response towards viscous effects. In addition, Simo [116] already developed a finite strain viscoelastic damage model which incorpoartes a simple isotropic damage mechanism. Mergheim et al. [78] developed a constitutive model containing the curing in thermosetting materials combined with an isotropic gradient-enhanced damage model covering the process-induced damage evolution.

1.1.3 Parameter identification

The manufacturing of modern engineering components requires the accurate prediction of material properties, such as accumulation of damage and plasticity resulting from, e.g., metal forming processes applied to a workpiece. A full exploitation of the lightweight potential of modern materials and components requires not only appropriate material models, but also a precise calibration of such models. To this end, optimisation-based parameter identification schemes have been established in the literature, with important works on the subject including the contributions by, e.g., Kublik [58], Furukawa [23], Gelin [25], Mahnken [72–74, 76], Hartmann [31–33], and Kleuter [52, 53]. The classic, optimisation-based approaches include schemes for model calibration based on homogeneous and on inhomogeneous deformations, where the latter incorporate digital image correlation (DIC) methods.

The work of Mahnken and Stein [73] was a pioneering contribution in this field of research providing the theoretical and numerical aspects regarding the model calibration of metals. Further application examples were given by Mahnken in [74]. In Mahnken and Kuhl [75], a parameter identification framework for a gradient-enhanced damage model was introduced. However, since at the beginning only integral data, such as forces, was available for the consideration in the objective function, full field data, e.g. displacement fields, could not be considered to capture anisotropic effects or inhomogeneous deformation states. This became a common approach a few years later after the concept of DIC was well known, e.g. by Scheday and Miehe [100] or Kajberg and Lindkvist [43]. The incorporation of field data required a special treatment, e.g. regarding the interpolation, which was investigated in detail in the works of Kleuter et al. [53], Rieger [93], Scheday [101]. In [53], Kleuter et al. introduced a parameter identification scheme for finite viscoelastic material models where an error square functional—comparing experimentally-obtained inhomogeneous displacement fields with related finite element-based simulations—is minimised by using a gradient scheme. This gradient-based calibration process for finite viscoelasticity was studied in more detail and applied to different materials in [52]. The identification of material parameters for inelastic materials, using experimental data representing non-uniform stress and displacement distributions from the surface of the three-dimensional specimen, was established in the work of Mahnken and Stein [76]. An application of a parameter identification scheme for different constitutive models was presented in [72] where different identification methods, instabilities in least squares problems, and identification for small and non-uniform finite deformations were discussed. Hartmann [31] estimated the constitutive constants of hyperelasticity relations of the generalised polynomial-type and discussed the aspects related to the gradient and convexity behaviour in certain deformations. The particular optimisation methods that are generally applicable were illustrated in, e.g., [2, 70, 85, 91, 123]. More recent contributions on the subject of parameter identification include works that deal with full-field DIC including, e.g., sensitivity analyses [34] and temperature phenomena [95, 97].

Parameter identification methods based on full-field measurements can be categorised into different classes. The most commonly used is the *Finite Element Model Updating* (FEMU) method where a finite element simulation is performed within each iteration, and where the difference between the simulated and experimentally measured data is calculated in order to find the optimal solution, see e.g. [49, 72, 73]. Another method is the *Virtual Fields Method* (VFM) based on appropriate virtual field sets and the principle of virtual work, see e.g. [27, 98], though it is often difficult to gather the deformation data over the whole volume. For further information, the reader is referred to the overviews provided in, e.g., [3, 99] and references cited therein.

In order to improve the overall calibration procedure, the concept of artificial neural networks (ANN), which recently became very popular in all kinds of research fields, was integrated into the optimisation process. One of the first works in machine learning-assisted parameter identification for constitutive models has been established by Huber et al. [38]. Among the more recent works dealing with machine learning methods in the context of parameter identification, Ktari et al. [57] carry out parameter identification for anisotropic thin walled-tubes based on finite element analyses and supported by a neural network scheme. The work of Yao et al. [135] deals with a rate-dependent phenomenological model including coupled plasticity and damage. The authors investigate the effect of different rates of deformation as well as temperature levels and then establish a hybrid approach for parameter identification, combining a neural network with a subsequent genetic algorithm, where a single mode of deformation—namely a tensile experiment—is considered.

Zhang et al. [141] do not invoke a neural network, but instead a hybrid strategy involving a two-stage process in the context of parameter identification for thin-walled aluminium tube models. They approximate a starting value for the optimisation algorithm based on theoretical considerations, then carry out the optimisation-based solution of the inverse problem. The work highlights that proper starting values for the optimisation procedure are essential, but in some cases challenging to obtain.

The recent work of Guo et al. [28] presented a deep learning model, named CPINet, which combines a convolutional neural network for denoising processing and strain feature extraction and a long short-term memory neural network for identifying path-dependent constitutive model parameters based on strain field sequences, loads and geometry dimensions. As an example, the developed model is applied to an elastic-plastic constitutive model with isotropic hardening.

1.2 Objective of this work

The main objective of this work is the investigation of different parameter identification strategies which are modified, i.e. optimised, for the underlying material model in order to obtain the optimal parameter set and to introduce a framework which overcomes the general difficulty of finding appropriate starting values for the identification process

in general. For this purpose, as application examples, three different complex material models are chosen based on the variety of different captured material mechanisms as well as on the broad distribution over various material groups. The first application example is the gradient-enhanced damage model coupled to finite plasticity developed by Sprave and Menzel [119] which provides many advantages regarding the simulation of e.g. metal forming processes and which is based on the efficient gradient-enhanced damage framework by Ostwald et al. [86]. Since the underlying damage framework by Ostwald et al. provides numerous advantages over many other damage formulations, and since damage effects are of high interest in different material groups, the framework in this work was coupled to a finite strain viscoelasticity model. The basis of the constitutive viscoelasticity model used in this work is a convolution integral approach. The model is based on the well-established finite hyperelasticity framework with uncoupled volumetric-isochoric response that was extended towards viscous effects by Simo and Hughes [117]. The final example is completely different to the previous material models and covers the group of ferroelectric materials. The laminate-based model was developed by Dusthakar et al. [16, 17] and couples mechanical and electrical effects.
Besides the investigations regarding parameter identification and developing a finite-strain viscoelasticity model coupled to gradient-enhanced damage, the work covers a numerical study with respect to the treatment of KKT conditions by employing different Fischer-Burmeister approaches for the NCP functions. This was done since KKT conditions need to be solved for many material models, and Fischer-Burmeister functions provide an efficient solution scheme. Thus, different approaches are compared in terms of their effectiveness and efficiency.

Consequently, the work is structured as follows:

In **Chapter 2**, the classic parameter identification approaches based on homogeneous states of deformation are performed and investigated. Therefore, three different material models are introduced. The gradient-enhanced damage model coupled to finite plasticity, developed by Sprave and Menzel [119], is briefly summarised in Section 2.1 accompanied by investigations regarding the different parameter influences. In the following section, the finite strain viscoelasticity model coupled to gradient-enhanced damage is developed based on the damage framework by Ostwald et al. [86] and the viscoelasticity framework by Simo and Hughes [117]. In Section 2.3, the laminate-model for ferroelectrics, developed by Dusthakar et al. [16, 17], is briefly summarised and investigated towards the numerical efficiency of solving the NCP functions by employing different Fischer-Burmeister approaches. The presentation of the different underlying models is followed by a brief summary of classic non-linear optimisation approaches from the literature. Afterwards, in Section 2.5, all three material models are calibrated with respect to experimental data based on homogeneous deformation states. Three different strategies are therefore investigated. At first, a Nelder-Mead simplex algorithm is applied in order to identify all of the material parameters—except for those which are related to non-local contributions—at once, i.e. elasticity-, plasticity- and damage-related parameters.
Secondly, an optimisation-based framework is presented that enables the identification

of parameters for rate-dependent materials under large strains and subject to gradient-enhanced damage by using an efficient two-step approach. In the first step, basic constitutive parameters, in particular elastic parameters, are calibrated based on experiments reflecting homogeneous states of deformation and are later fixed in the second step, presented in Section 4.2. The particular material considered in this case is the self-diagnostic poly(dimethylsiloxane) (PDMS) elastomer. However, we restrict our elaborations to the purely mechanical properties of the elastomer, where later solely the inhomogeneous displacement field and the load-deflection curve are considered within the second step of the calibration process. A possible future extension of the framework proposed in this work could include an additional consideration of the fluorescence field emitted by the self-diagnostic specimen within the optimisation-based parameter identification procedure.
Thirdly, a very efficient strategy is chosen—which is however often not applicable. Since most of the material parameters of ferroelectric material models are characteristic for this class of material, they can be directly taken from the literature, in this case for $BaTiO_3$. Thus, only the two remaining model parameters had to be calibrated with respect to the characteristic butterfly and dielectric hysteresis curves. The parameter identification in this section was performed by Dusthakar et al. [17] and is only briefly summarised.

Nevertheless, a particular challenge that all these different strategies have in common is the identification of a proper starting value for the optimisation scheme. Profound knowledge is required of the interplay between constitutive parameters, evolution equations, and the final constitutive response reflected by a given material model in order to pre-determine a set of suitable starting values for the constitutive parameters involved. This is a challenge that becomes all the more relevant with modern, sophisticated and complex material models that might include dozens of parameters relating to effects such as damage, plasticity, temperature-dependence, microstructural information, etc.—which is applicable for all three application examples. Thus, in **Chapter 3**, we aim to overcome this challenge by a machine learning-scheme which automatically generates a set of high-quality starting values for the subsequent classic optimisation scheme. The main contribution of this work is the overall hybrid framework where the starting point for a full-field data based parameter identification is generated by an ANN which is trained with concatenated loading path sequences and not by the identification of the material parameters of a particular material. While the general structure of the approach is presented at the beginning of the chapter, the detailed description and investigation is given by directly employing the finite plasticity model coupled to gradient-enhanced damage as an example. Some comments on the selected neural network including the data sampling strategy and the network structure are presented in Section 3.1.2. The training, testing, statistical error quantification and hyper parameter optimisation of the neural network is then presented in Section 3.1.3, before the parameter identification results for two types of metals—a DP800 sheet metal and a 16MnCrS5 case hardening steel—are presented in Section 3.1.4 based on experiments with homogeneous deforma-

tions. The final prediction of the parameter set is used in Section 4.3.5 as the starting value for a classic parameter identification based on inhomogeneous states of deformation to obtain an accurate optimal parameter set. Additionally, the hybrid strategy is adapted to the laminate model for ferroelectrics in order to demonstrate that the framework can be easily applied to different material models, finite-element solvers and material groups with small adjustments. Even though most parameters were directly obtained from the literature and only two model parameters remained for the parameter identification, the identification of appropriate starting values was not straight forward. Thus, the hybrid strategy can be advantageous even for seemingly simple problems.

In the beginning of **Chapter 4**, the multi-objective optimisation tool *ADAPT—A Diversely Applicable Parameter Identification Tool* is briefly summarised. The optimisation tool was published open-source and can deal with all different kinds of finite element solvers and various kinds of experimental data—even incorporating different experiments in the objective function at once while maintaining an efficient calibration due to a parallelisation of the procedures. Thus, the tool is not only able to deal with integral data, such as forces, but also to incorporate field data, such as displacement or strain fields, and even microstructural data like pore evolution, e.g. regarding the characterisation of damage. The presentation of the optimisation process is followed by a description of the postprocessing and interpolation techniques, the multi-objective ansatz, as well as the incorporation of boundary conditions and a short description of characteristic implementation aspects.
Afterwards, the multi-objective optimisation technique is applied to the self-diagnostic elastomer. While the elastic parameters were already identified previously in a first step with respect to experimental data based on homogeneous deformation states, the damage-related parameters are identified considering integral and field data regarding inhomogeneous deformation states. For this purpose, the already identified elastic parameters are then kept fixed in view of the second step of model calibration. The inhomogeneous states of deformation activate gradient terms within the gradient-enhanced damage formulation considered in this work, so that mesh-objective damage effects can be captured within finite element-based simulations. With damage gradient terms activated due to inhomogeneous states of deformation, we proceed to the identification of damage-related model parameters in the second step of the model calibration procedure.
Subsequently, ADAPT is applied to calibrate material models for the sheet metal DP800. At first, a brief summary of the parameter identification for a simple plasticity model, performed by Schowtjak et al. [104], is presented in combination with an investigation towards the influence of different optimisation strategies. Afterwards, ADAPT is used to directly identify all material parameters of the finite plasticity model coupled to gradient-enhanced damage at once, including the non-local contributions since a multi-objective optimisation with respect to inhomogeneous deformation states is performed.
Finally, the prediction of the material parameters by the ANN in Section 3.1.4 is used as a starting value for a subsequent multi-objective parameter identification based on inhomogeneous states of deformation. This procedure reduces the computational cost

of a finite-element based multi-objective optimisation to a minimum since the starting value already lies quite close to the optimal solution. This is especially advantageous if the user is not familiar with the underlying material model and is unaware of any parameter range. The solution is compared to the result with an additional intermediate optimisation step which is employed in order to improve the starting value with regard to the data based on homogeneous deformation states.

2 Classic parameter identification based on homogeneous states of deformation

In this chapter, classic parameter identification strategies regarding one objective for the error functional, e.g. forces taken from load-displacement curves, are applied to different classes of material models. As already mentioned in the introduction, calibration processes are important in order to apply developed material models to specific materials, although they can be quite challenging. In general, the better the optimisation is performed and the closer the found local minimum is to the global minimum, the more reasonable and realistic the material behaviour can be simulated. Even the best and most complex material model that captures all different kinds of material effects is not capable of predicting the material behaviour sufficiently if the model is not calibrated properly to the specific material. Thus, it is important to invest sufficient effort into the parameter identification process. To this end, classic calibration strategies are presented in the following considering at first only homogeneous states of deformation. This type of information can be provided by standard experiments which are easily available and already sufficient to identify many material parameters.

At first, three different classes of material models are presented. In Section 2.1, a gradient-enhanced damage model coupled to finite plasticity developed by Sprave and Menzel [119, 120] is briefly summarised and some of the model parameters are fitted in Section 2.5.1. The material model was developed for different kinds of steel and the focus in this work lies on the sheet metal DP800 and the case-hardened steel 16MnCrS5. The formulation of this model is based on the gradient-enhanced damage framework derived by Ostwald et al. in [86]. In Section 2.2, the damage framework was applied to a different material class—polymers. Thus a finite strain viscoelasticity coupled with gradient-enhanced continuum damage model was developed in Schulte et al. [110] and the model formulation is given in Section 2.2. The corresponding parameter identification regarding homogeneous deformation states is given in Section 2.5.2. The identification of the damage-related model parameters is given in Chapter 4 where inhomogeneous states of deformation are taken into account. While both previous material models cover differ-

ent material classes, they are some way related with respect to their damage framework. Thus, as another application case, a completely different material model is given in Section 2.3. Here, a laminate-based electro-mechanically coupled material model for ferroelectric materials developed by Dushtakar et al. in [16, 17] is summarised. Since the underlying phase fractions are subjected to physically motivated strains, the consideration of these constraints is quite important for the material model. To this purpose, Fischer-Burmeister functions are incorporated into the model. In addition, considering the impact of these functions on the numerical efficiency of the model, different approaches of the FB functions are analysed in the section. The corresponding parameter identification following the classic parameter identification scheme was performed by Dushtakar et al. in [17] and is summarised in Section 2.5.3.

In Chapter 3, an alternative approach to the classic optimisation strategy, employing machine learning as already described in the introduction, is presented in order to improve the standard procedure in several directions.

Before the parameter identification is performed in Section 2.5, a brief overview of the different classic optimisation algorithms is given in Section 2.4.

2.1 Gradient-enhanced damage model coupled to plasticity

As we aim to apply different parameter identification procedures in the first application example to different types of metal alloys, a sufficiently generalised constitutive model needs to be employed. To this end, in this work we employ a constitutive model that is able to capture large deformations, a full coupling between damage and plasticity, and where a gradient-based damage regularisation scheme is included, thereby facilitating the simulation of mesh-objective damage evolution in the context of the finite element-based solution of inhomogeneous boundary value problems. The particular large-strain gradient-enhanced ductile damage model utilised in this work is in line with the formulation presented in [119] and is briefly reviewed in the following.

2.1.1 Large strain gradient-enhanced ductile damage formulation

In view of kinematics, let $\boldsymbol{X} \in \mathcal{B}_0$ denote material placements in a domain $\mathcal{B}_0$ reflecting the reference configuration of a body under consideration and let $\boldsymbol{x} = \boldsymbol{\varphi}(\boldsymbol{X}, t) \in \mathcal{B}_t$ denote spatial placements in the spatial domain $\mathcal{B}_t$ associated with the current configuration at time t. Moreover, $\boldsymbol{F} = \nabla_{\boldsymbol{X}} \boldsymbol{\varphi}$ represents the deformation gradient, mapping infinitesimal referential line elements $\mathrm{d}\boldsymbol{X}$ onto their spatial counterparts $\mathrm{d}\boldsymbol{x}$. Assuming a multiplicative decomposition of the deformation gradient into elastic and plastic contributions, $\boldsymbol{F} = \boldsymbol{F}^{\mathrm{e}} \cdot \boldsymbol{F}^{\mathrm{p}}$, the elastic Finger tensor $\boldsymbol{b}^{\mathrm{e}}$ is expressible as $\boldsymbol{b}^{\mathrm{e}} = \boldsymbol{F}^{\mathrm{e}} \cdot [\boldsymbol{F}^{\mathrm{e}}]^{\mathrm{t}}$, so that spatial logarithmic elastic strains $\boldsymbol{\varepsilon}^{\mathrm{e}}$ follow as $\boldsymbol{\varepsilon}^{\mathrm{e}} = \ln(\boldsymbol{b}^{\mathrm{e}})$.

The constitutive relations are modeled based on an overall Helmholtz energy potential Ψ being additively composed of local and non-local contributions, Ψ^{loc} and Ψ^{nl}, respectively, so that

$$\Psi(\boldsymbol{F}, \phi, \nabla_{\boldsymbol{X}}\phi, d_\phi, \boldsymbol{\mathcal{I}}^{\mathrm{p}}) = \Psi^{\mathrm{loc}}(\boldsymbol{F}, d_\phi, \boldsymbol{\mathcal{I}}^{\mathrm{p}}) + \Psi^{\mathrm{nl}}(\phi, \nabla_{\boldsymbol{X}}\phi, d_\phi)\,, \tag{2.1}$$

where d_ϕ and ϕ denote the local damage variable and the global damage field, respectively, and where $\boldsymbol{\mathcal{I}}^{\mathrm{p}}$ reflects plasticity-related internal variables, particularly $\boldsymbol{F}^p$ and the isotropic hardening variable, denoted as α in the following.

The local part of the Helmholtz energy takes into account an isochoric-volumetric split, where the specific form is chosen as

$$\begin{aligned}\Psi^{\mathrm{loc}}(\boldsymbol{F}, d_\phi, \boldsymbol{\mathcal{I}}^{\mathrm{p}}) &= \Psi^{\mathrm{vol}}(\boldsymbol{\varepsilon}^{\mathrm{e}}, d_\phi) + \Psi^{\mathrm{iso}}(\boldsymbol{\varepsilon}^{\mathrm{e}}, d_\phi) + \Psi^{\mathrm{p}}(\alpha) \\ &= \frac{K}{2}\, f^{\mathrm{vol}}(d_\phi)\, \left[\mathrm{tr}(\boldsymbol{\varepsilon}^{\mathrm{e}})\right]^2 + G\, f^{\mathrm{iso}}(d_\phi)\, \boldsymbol{\varepsilon}^{\mathrm{e,iso}} : \boldsymbol{\varepsilon}^{\mathrm{e,iso}} \\ &\quad + \frac{h}{n_{\mathrm{p}}+1}\, \alpha^{n_{\mathrm{p}}+1}\,,\end{aligned} \tag{2.2}$$

with volumetric, isochoric and plasticity-related—or rather hardening-related—energy contributions, Ψ^{vol}, Ψ^{iso}, and Ψ^{p}, respectively, which are further specified in terms of bulk modulus K, shear modulus G, and hardening-parameters h and n_{p}. For details on the derivation of the isochoric parts of the logarithmic strains, $\boldsymbol{\varepsilon}^{\mathrm{e,iso}}$, based on a spectral representation of $\boldsymbol{\varepsilon}^{\mathrm{e}}$, the reader is referred to, e.g., [119]. The non-local Helmholtz energy contribution is specified as

$$\Psi^{\mathrm{nl}}(\phi, \nabla_{\boldsymbol{X}}\phi, d_\phi) = \frac{c_{\mathrm{d}}}{2}\, \nabla_{\boldsymbol{X}}\phi \cdot \nabla_{\boldsymbol{X}}\phi + \frac{\beta_{\mathrm{d}}}{2}\, [\phi - d_\phi]^2\,, \tag{2.3}$$

with c_{d} being a regularisation parameter and β_{d} a penalty-type parameter, see related works, such as [51, 86, 133]. This gradient-extended format is in line with the micromorphic approach discussed by Forest [20] and with the multi-field incremental variational framework for gradient-extended standard dissipative solids established by Miehe [83].

As driving forces, we consider the Mandel stress tensor frequently employed in finite plasticity applications, which, in the special case of isotropic elasticity, is symmetric and can conveniently be represented in terms of $\boldsymbol{m} \coloneqq 2\, \partial_{\boldsymbol{b}^e}\Psi \cdot \boldsymbol{b}^e$. Moreover, we obtain an isotropic hardening stress $\beta \coloneqq -\,\partial_\alpha \Psi$ and a damage driving force $q \coloneqq -\,\partial_{d_\phi}\Psi$.

To complete the constitutive framework, we specify the plastic potential Φ^{p} as

$$\Phi^{\mathrm{p}}(\boldsymbol{m}_{\mathrm{eff}}, \alpha) = \| \,\mathrm{dev}(\boldsymbol{m}_{\mathrm{eff}})\, \| - \sqrt{\frac{2}{3}}\, h\, [\alpha_0 + \alpha]^{n_{\mathrm{p}}}\,, \tag{2.4}$$

with $\mathrm{dev}(\bullet) = [\bullet] - \frac{1}{3}[[\bullet] : \boldsymbol{I}]\boldsymbol{I}$ being the deviator operator in spatial representation. The damage potential Φ^{d} is specified as

$$\Phi^{\mathrm{d}}(q, d_\phi) = q_{\mathrm{eff}} - q_{\mathrm{min}} - q_{\mathrm{var}}\,[1 - f^q(d_\phi)]^{n_{\mathrm{d}}}\,, \tag{2.5}$$

where effective driving forces $\boldsymbol{m}_{\mathrm{eff}} \coloneqq \boldsymbol{m}/f_{\boldsymbol{m}}(d_\phi)$ and $q_{\mathrm{eff}} \coloneqq q/f_\alpha(\alpha)$ are introduced and where q_{min} and q_{var} represent damage threshold parameters. The damage functions $f_\bullet : \mathbb{R}_0^+ \to]0, 1]$ are chosen as $f_\bullet(d_\phi) = \exp(-\eta\,\xi_\bullet\,d_\phi)$ with η denoting a damage rate factor, and with $\xi_\bullet$ reflecting further damage-related constitutive coefficients. Suitable parameter ranges and choices for this particular constitutive formulation are provided in Section 2.1.2. Moreover, Equations (2.4) and (2.5) are combined with classic Karush-Kuhn-Tucker conditions, together with associative flow directions, in order to model plasticity and damage evolution, cf. [119].

2.1.2 Parameter ranges

In terms of classic PI approaches several different initial guesses for the parameter sets need to be chosen. Thus, it is important to identify the possible ranges of each parameter. In addition, regarding the machine learning approach in Chapter 3, besides the method of the sampling of the training data for the neural network shown in Section 3.1.3, the admissible interval of the parameters is also of importance. For some parameters the specific range is quite obvious, e.g. for Poisson's ratio or Young's modulus. However, some model parameters do not possess an obvious physical interpretation and thus the influence of those parameters on the model response needs to be analysed. In Section 2.1.1, the applied material model is summarised and this influence of the corresponding parameters is shown in Figures 2.1 and 2.2 in Section 2.1.3 with respect to a reference set of material parameters given in Table 2.1. In order to demonstrate the characteristic behaviour, a simple uni-axial tension test with a homogeneous deformation state, consisting of a loading, unloading and another loading phase, is simulated. Therefore, a total axial strain of 13.5 % is applied in loading direction in the first phase and subsequently the force is reduced to zero. Thereafter, the strain is increased to 32 %. It has to be mentioned that the shown influence of the parameters in general depends on the fixed values of the other parameters. Nevertheless, the basic influence can be demonstrated. With regard to the hybrid strategy of Chapter 3, in particular in view of the sampling methods of the training data, a vast amount of the various parameter combinations is taken into account for the neural network. Thus, the network is able to provide a good prediction for the chosen class of material avoiding over-fitting.

2.1.3 Parameter influences

As already mentioned in the previous section, in order to choose initial values for the parameter sets or later to define a training set for the neural network, it is important to

Table 2.1: Values of the material parameters of the reference set which are fixed while one of the parameters is analysed. For further details on the model formulation see Section 2.1.1. Reprinted from Schulte et al., European Journal of Mechanics - A/Solids 98:104854 (2023), [113], with permission under creative commons licence 4.0.

Symbol	Description	Reference set	Unit
E	Young's modulus	200.0	GPa
ν	Poisson's ratio	0.3	–
σ_{y_0}	initial yield stress	250.0	MPa
h	hardening parameter	1300.0	MPa
n_p	hardening exponent	0.25	–
q_var	variable damage threshold	20.0	MPa
n_d	damage exponent	0.667	–
η	damage rate factor	1.0	–
ξ_vol	volumetric damage factor	1.0	–
ξ_iso	isochoric damage factor	1.0	–
ξ_q	threshold factor	10.0	–
ξ_m	effective stress factor	1.0	–
η_α	coupling factor	2.5	–
c_d	regularisation parameter	0.54	N
β_d	penalty parameter	0.0	MPa
q_min	initial damage threshold	10.0	MPa

define the parameter ranges, as described in Section 2.1.2. The influence of the different parameters on the material response therefore has to be analysed. The influence of the parameters to be identified can be seen in Figures 2.1 and 2.2. Within the figures, each parameter is varied with respect to a reference parameter combination shown in Table 2.1.

2.2 Finite-strain viscoelasticity coupled with gradient-enhanced continuum damage

Viscoelastic material models can describe a large class of history- and rate-dependent materials. These materials differ from ideally elastic materials by time-dependent effects such as creep or relaxation. Polymeric rubber materials such as the elastomer considered in this work are typical representatives of this class of materials. Constitutive models for viscoelasticity either use a differential operator or convolution integral representation, where the constitutive model considered in this work is based on the latter approach. The convolution integral approach was described in detail in the works by Kaliske and

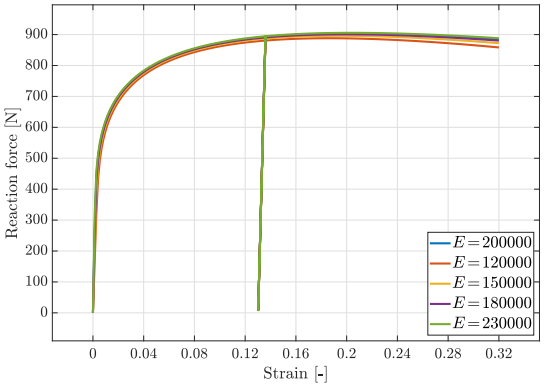

(a) Influence of Young's modulus E in MPa.

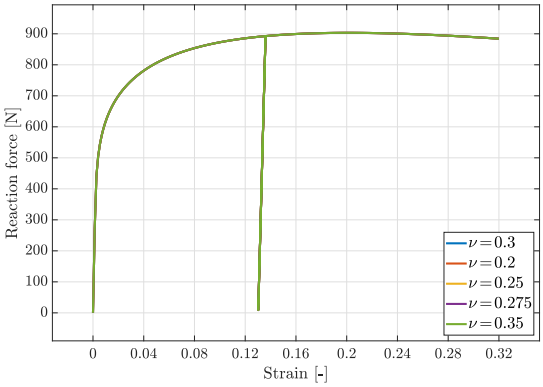

(b) Influence of Poisson's ratio ν.

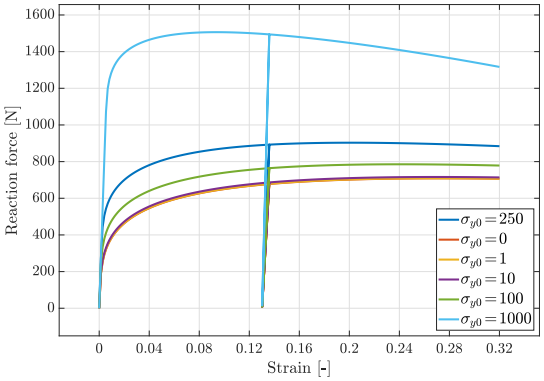

(c) Influence of the initial yield stress σ_{y0} in MPa.

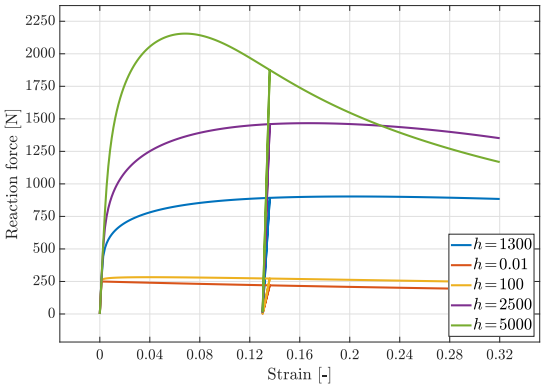

(d) Influence of the hardening parameter h in MPa.

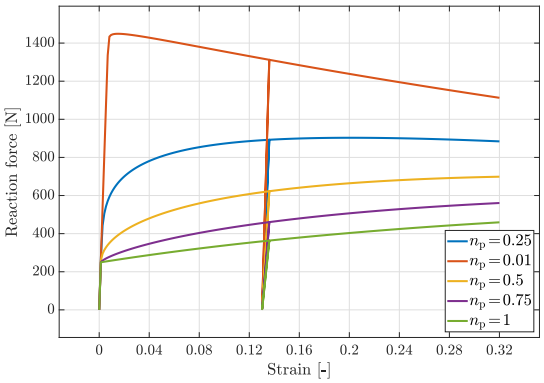

(e) Influence of the hardening exponent n_p.

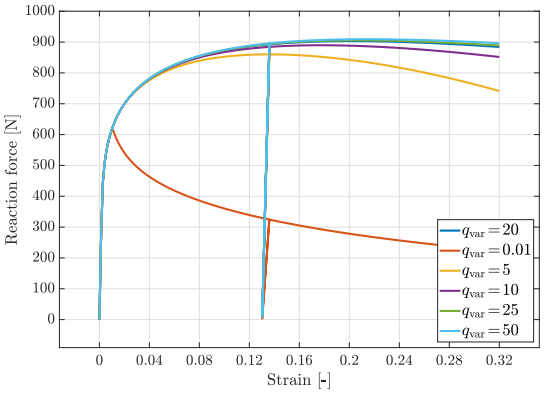

(f) Influence of the variable damage threshold q_var in MPa.

Figure 2.1: Impact of the different material parameters on the simulated load-displacement response for an exemplary tension test—Part 1. Reprinted from Schulte et al., European Journal of Mechanics - A/Solids 98:104854 (2023), [113], with permission under creative commons licence 4.0.

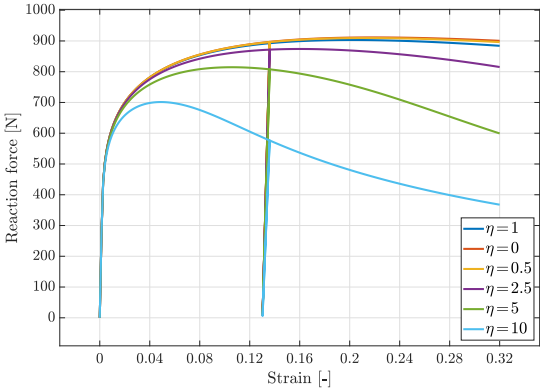

(a) Influence of the damage rate factor η.

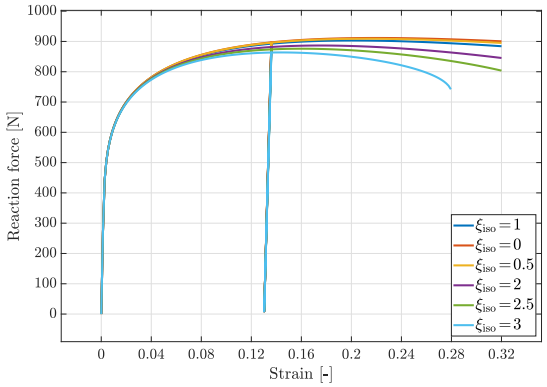

(b) Influence of the isochoric damage factor ξ_{iso}.

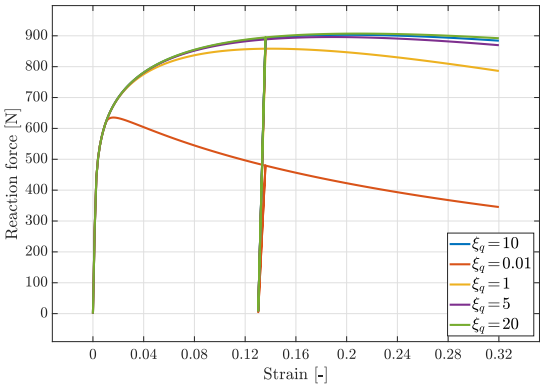

(c) Influence of the threshold factor ξ_q.

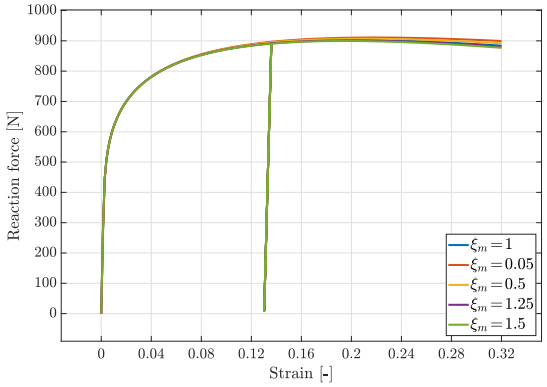

(d) Influence of the effective stress factor ξ_m.

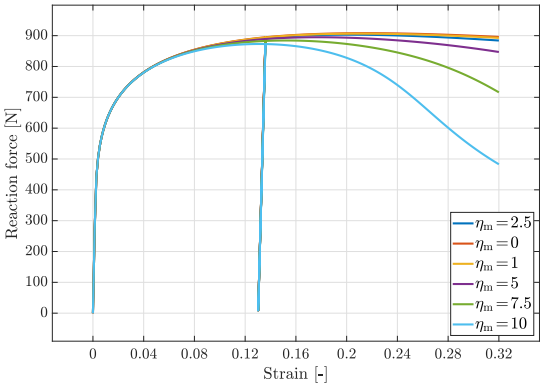

(e) Influence of the coupling factor η_α.

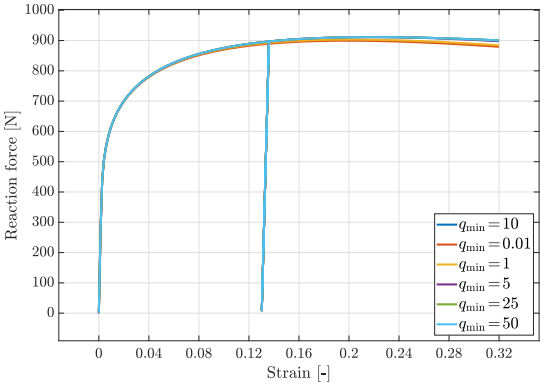

(f) Influence of the constant damage threshold q_{min} in MPa.

Figure 2.2: Impact of the different material parameters on the simulated load-displacement response for an exemplary tension test—Part 2. Reprinted from Schulte et al., European Journal of Mechanics - A/Solids 98:104854 (2023), [113], with permission under creative commons licence 4.0.

Rothert [44], Simo and Hughes [117], amongst others. The model formulation considered in this work is introduced as follows: Section 2.2.1 briefly summarises the classic finite strain hyperelastic constitutive relations with volumetric-isochoric decomposition. Section 2.2.2 proceeds with the generalisation of these relations to a finite strain viscoelastic model. An extension towards gradient-enhanced continuum damage is then briefly covered in Section 2.2.3.

2.2.1 Finite hyperelasticity with volumetric-isochoric decomposition

This section briefly outlines the hyperelastic local constitutive setting considered in the work at hand, which will then be extended towards finite viscoelasticity. The constitutive framework at hand facilitates the accommodation of any arbitrary hyperelastic response based on a local Helmholtz free energy function ψ_{loc}, enabling the use of higher order constitutive relations such as the Yeoh model.

The isochoric, i.e., volume-preserving, part $\bar{\boldsymbol{F}}$ of the deformation gradient $\boldsymbol{F}$ is defined as

$$\bar{\boldsymbol{F}} \coloneqq J^{-\frac{1}{3}} \boldsymbol{F}\,, \quad \text{with} \quad J = \det(\boldsymbol{F}) \quad \text{and} \quad \det(\bar{\boldsymbol{F}}) = 1\,. \tag{2.6}$$

In this context, $J^{\frac{1}{3}}\,\boldsymbol{I}$ is referred to as the volumetric part of the deformation gradient, with $\boldsymbol{I}$ denoting the second-order identity tensor. The standard and isochoric right Cauchy–Green deformation tensors are introduced via

$$\boldsymbol{C} \coloneqq \boldsymbol{F}^{\mathrm{t}} \cdot \boldsymbol{F} \quad \text{and} \quad \bar{\boldsymbol{C}} \coloneqq \bar{\boldsymbol{F}}^{\mathrm{t}} \cdot \bar{\boldsymbol{F}} = J^{-\frac{2}{3}}\,\boldsymbol{C}, \tag{2.7}$$

respectively.

In view of the hyperelastic contribution to the constitutive response, a local Helmholtz free energy function ψ_{hyp} of the form

$$\psi_{\text{hyp}}(\boldsymbol{C}) = \psi_{\text{vol}}(J) + \psi_{\text{ich}}(\bar{\boldsymbol{C}}) \tag{2.8}$$

is considered, where an additive decomposition into volumetric and isochoric energy contributions, ψ_{vol} and ψ_{ich}, respectively, is taken into account.

Within this modelling framework, the hyperelastic part of the Piola–Kirchhoff stress tensor follows as

$$\boldsymbol{S}_{\text{hyp}} \coloneqq 2\,\partial_{\boldsymbol{C}}\psi_{\text{hyp}}(\boldsymbol{C}) = J\,\partial_J\psi_{\text{vol}}(J)\,\boldsymbol{C}^{-1} + \bar{\boldsymbol{S}}_{\text{hyp}}\,, \tag{2.9}$$

where the isochoric contribution to the hyperelastic part of the Piola–Kirchhoff stress tensor is abbreviated as

$$\bar{\boldsymbol{S}}_{\text{hyp}} \coloneqq J^{-\frac{2}{3}} \left[2\,\partial_{\bar{\boldsymbol{C}}}\psi_{\text{ich}}(\bar{\boldsymbol{C}}) - \frac{1}{3}\,[2\,\partial_{\bar{\boldsymbol{C}}}\psi_{\text{ich}}(\bar{\boldsymbol{C}}) : \boldsymbol{C}]\boldsymbol{C}^{-1} \right] \tag{2.10}$$

for notational simplicity. It is noted that the well-established relations $\partial_{\boldsymbol{C}} J = \frac{1}{2}\, J\, \boldsymbol{C}^{-1}$ and $\partial_{\boldsymbol{C}} \bar{\boldsymbol{C}} = J^{-\frac{2}{3}} [\mathbf{I}^{\mathrm{sym}} - \frac{1}{3}\, \boldsymbol{C} \otimes \boldsymbol{C}^{-1}]$ were employed here.

The corresponding hyperelastic part of the spatial Kirchhoff stresses, $\boldsymbol{\tau}_{\mathrm{hyp}} = \boldsymbol{F} \cdot \boldsymbol{S}_{\mathrm{hyp}} \cdot \boldsymbol{F}^{\mathrm{t}}$, then follows as

$$\boldsymbol{\tau}_{\mathrm{hyp}} = J\, \partial_J \psi_{\mathrm{vol}}(J)\, \boldsymbol{I} + \mathrm{dev}\big(2\, \bar{\boldsymbol{F}} \cdot \partial_{\bar{\boldsymbol{C}}} \psi_{\mathrm{ich}}(\bar{\boldsymbol{C}}) \cdot \bar{\boldsymbol{F}}^{\mathrm{t}}\big)\ . \tag{2.11}$$

2.2.2 Extension of finite hyperelasticity to finite viscoelasticity

In view of a generalisation of the volumetrically-isochorically decoupled finite strain hyperelastic modelling framework outlined in Section 2.2.1 to finite viscoelasticity, $\boldsymbol{C}(t)$ is now assumed to be a function of time t. As a relation for the viscoelastic stress response in terms of Piola–Kirchhoff stresses $\boldsymbol{S}$ at time t, the form

$$\boldsymbol{S}(t) = \boldsymbol{S}_{\mathrm{hyp}}(t) - J^{-\frac{2}{3}} \sum_{i=1}^{N} \mathrm{DEV}(\boldsymbol{Q}_i(t)) \tag{2.12}$$

is considered and is in line with classic works such as [116, 117], where $\mathrm{DEV}(\bullet) := [\bullet] - \frac{1}{3}[[\bullet] : \boldsymbol{C}]\boldsymbol{C}^{-1}$. Here, $\boldsymbol{S}_{\mathrm{hyp}}(t)$ denotes the hyperelastic stress contribution defined in (2.9) and $\boldsymbol{Q}_i(t)$, with $i = 1, 2, \ldots, N$, represent stress-type tensor-valued internal variables. This form of the stress extension leaves the volumetric part of the constitutive response unaffected by viscous effects. Relation (2.12) reflects a finite strain generalisation of a classic generalised relaxation model with N being the number of Maxwell elements, each consisting of a (linear) spring and a (linear) dashpot. Conceptually speaking, in a simplified and linear setting, each Maxwell element would be characterised by a given spring stiffness, say E_i, and corresponding dashpot viscosity, say η_i; cf., e.g., [117].

For the evolution of the stress-type internal variables, rate equations of the type

$$\dot{\boldsymbol{Q}}_i(t) + \frac{1}{\tau_i}\, \boldsymbol{Q}_i(t) = \frac{\gamma_i}{\tau_i}\, \mathrm{DEV}\big(2\, \partial_{\bar{\boldsymbol{C}}} \psi_{\mathrm{ich}}(\bar{\boldsymbol{C}}(t))\big) \quad \text{with} \quad \lim_{t \to -\infty} \boldsymbol{Q}_i(t) = \boldsymbol{0}\,, \tag{2.13}$$

are considered, cf. [116, 117], with $\dot{\bullet}$ denoting the material time derivative and where τ_i are referred to as relaxation times. Parameters γ_i represent relative moduli subject to the restriction

$$\sum_{i=1}^{N} \gamma_i = 1 - \gamma_\infty\,, \tag{2.14}$$

with $\gamma_\infty \in [0, 1)$ determining the quasi-static (hyperelastic) limiting case of the material response. In a simplified and linear setting, as thoroughly introduced in [117], $\tau_i := \eta_i / E_i > 0$ and $\gamma_i = E_i / E_0 \in [0, 1]$ would be the parameters defining the properties of each Maxwell branch in the viscoelastic model. Here, $E_0 = E_\infty + \sum_i E_i$ is the stiffness

obtained in the (hyperelastic) limiting case reflected by infinitely high strain rates. In the context of the three-dimensional non-linear formulation at hand, this contribution is represented by the general Helmholtz free energy potential ψ_{hyp} that facilitates the incorporation of higher-order and even anisotropic constitutive relations.

The linearity of evolution equations (2.13) facilitates the standard closed-form convolution representation

$$\boldsymbol{Q}_i(t) = \frac{\gamma_i}{\tau_i} \int_{-\infty}^{t} \exp(-(t-s)/\tau_i)\, \mathrm{DEV}\big(2\, \partial_{\bar{\boldsymbol{C}}} \psi_{\mathrm{ich}}(\bar{\boldsymbol{C}}(s))\big)\, \mathrm{d}s\,. \tag{2.15}$$

Combining (2.15) with (2.12) and integration by parts yields an explicit expression for the stress response in terms of the Piola–Kirchhoff stress tensor of the form

$$\boldsymbol{S}(t) = J\, \partial_J \psi_{\mathrm{vol}}(J)\, \boldsymbol{C}^{-1}(t) + J^{-\frac{2}{3}}(t) \int_{-\infty}^{t} g(t-s)\, \frac{\mathrm{d}}{\mathrm{d}s}\big(\mathrm{DEV}\big(2\, \partial_{\bar{\boldsymbol{C}}} \psi_{\mathrm{ich}}(\bar{\boldsymbol{C}}(s))\big)\big)\, \mathrm{d}s\,, \tag{2.16}$$

where the relaxation function

$$g(t) = \gamma_\infty + \sum_{i=1}^{N} \gamma_i \exp(-t/\tau_i) \tag{2.17}$$

is incorporated.

The spatial counterpart of (2.16) is obtained by using $J^{-\frac{2}{3}}\, \boldsymbol{F} \cdot [\mathrm{DEV}(\bullet)] = \mathrm{dev}(\bar{\boldsymbol{F}} \cdot (\bullet) \cdot \bar{\boldsymbol{F}}^{\mathrm{t}})$, so that the convolution representation of the Kirchhoff stresses reads

$$\boldsymbol{\tau}(t) = J\, \partial_J \psi_{\mathrm{vol}}(J)\, \boldsymbol{I} + \int_{-\infty}^{t} g(t-s)\, \frac{\mathrm{d}}{\mathrm{d}s}\big(\mathrm{dev}\big(2\, \bar{\boldsymbol{F}} \cdot \partial_{\bar{\boldsymbol{C}}} \psi_{\mathrm{ich}}(\bar{\boldsymbol{C}}(s)) \cdot \bar{\boldsymbol{F}}^{\mathrm{t}}\big)\big)\, \mathrm{d}s\,. \tag{2.18}$$

For more detailed information on the derivation of well-established relations in the context of (undamaged) finite strain viscoelasticity based on a volumetric-isochoric split of the underlying Helmholtz free energy function, the reader is referred to classic monographs such as [10, 117], amongst other works.

The numerical solution of the convolution integrals introduced above is based on a transformation towards a recurrence formula, enabling the computation of the constitutive response based on the standard internal variable procedure, thereby bypassing the need to store the entire strain history that is individual to each material point in view of the later finite element application; see Appendix A for details on the numerical update procedure.

2.2.3 Incorporation of damage

We considered a gradient-regularised damage formulation in view of a mesh-objective solution of boundary value problems by using the finite element method, where the

constitutive response can include damage-induced softening. To this end, an overall Helmholtz free energy potential ψ is introduced, composed of local and non-local energy contributions, ψ_{loc} and ψ_{nloc}, in terms of $\psi = \psi_{\text{loc}} + \psi_{\text{nloc}}$.

The local Helmholtz free energy contribution, in extension of (2.8), takes the form

$$\psi_{\text{loc}}(\boldsymbol{C}, \kappa) = f_{\text{d}}(\kappa)\, \psi_{\text{vol}}(J) + f_{\text{d}}^{n_{\text{iso}}}(\kappa)\, \psi_{\text{ich}}(\bar{\boldsymbol{C}})\,, \tag{2.19}$$

where the volumetric and isochoric damage functions, $f_{\text{d}} \in (0, 1]$ and $f_{\text{d}}^{n_{\text{iso}}} \in (0, 1]$, are evaluated based on a common internal damage variable κ, but allow for an adjustment of the volumetric-isochoric damage distribution via the exponent $n_{\text{iso}} \in R$. The exponent n_{iso} is a material parameter that facilitates the modelling of a damage process that affects volumetric and isochoric contributions with different intensities.

The non-local energy contribution ψ_{nloc} enables the damage regularisation and consists of two contributions, namely a non-local gradient term $\psi_{\text{nloc}}^{\text{grad}}(\nabla_{\boldsymbol{X}}\phi; \boldsymbol{F})$ and a non-local penalty term $\psi_{\text{nloc}}^{\text{plty}}(\phi, \kappa)$, so that $\psi_{\text{nloc}}(\boldsymbol{F}, \phi, \nabla_{\boldsymbol{X}}\phi, \kappa) = \psi_{\text{nloc}}^{\text{grad}}(\nabla_{\boldsymbol{X}}\phi; \boldsymbol{F}) + \psi_{\text{nloc}}^{\text{plty}}(\phi, \kappa)$, with

$$\psi_{\text{nloc}}^{\text{grad}}(\nabla_{\boldsymbol{X}}\phi; \boldsymbol{F}) = \frac{c_{\text{d}}}{2}\, \nabla_{\boldsymbol{X}}\phi \cdot \boldsymbol{C}^{-1} \cdot \nabla_{\boldsymbol{X}}\phi = \frac{c_{\text{d}}}{2}\, \nabla_{\boldsymbol{x}}\phi \cdot \nabla_{\boldsymbol{x}}\phi\ , \tag{2.20}$$

$$\psi_{\text{nloc}}^{\text{plty}}(\phi, \kappa) = \frac{\beta_{\text{d}}}{2}\, [\phi - \kappa]^2\ . \tag{2.21}$$

Here, ϕ is the non-local damage variable that is coupled to the local damage variable κ via the penalty parameter β_{d}. Moreover, c_{d} represents a length scale-type regularisation parameter. With this particular choice of the non-local energy contributions, the Euler–Lagrange equations for the non-local damage field variable in spatial format take the form

$$c_{\text{d}}\, \nabla_{\boldsymbol{x}} \cdot [\nabla_{\boldsymbol{x}}\phi] - \beta_{\text{d}}\, [\phi - \kappa] = 0 \quad \text{in } \mathcal{B}_t\ , \tag{2.22}$$

$$\nabla_{\boldsymbol{x}}\phi \cdot \boldsymbol{n} = 0 \quad \text{on } \partial\mathcal{B}_t^y = \partial\mathcal{B}_t\,, \tag{2.23}$$

with $\boldsymbol{n}$ denoting the surface normal unit vector; see, e.g., [86] for more details on the associated relations, as well as on the numerical treatment within appropriately coupled finite element formulations.

The incorporation of the damage functions in the local free energy potential (2.19) induces Piola–Kirchhoff stresses of the form

$$\boldsymbol{S}_{\text{hyp}} \coloneqq 2\, \partial_{\boldsymbol{C}}\psi_{\text{loc}}(\boldsymbol{C}, \kappa) = J\, f_{\text{d}}(\kappa)\, \partial_J\psi_{\text{vol}}(J)\, \boldsymbol{C}^{-1} + f_{\text{d}}^{n_{\text{iso}}}(\kappa)\, \bar{\boldsymbol{S}}_{\text{hyp}}\,, \tag{2.24}$$

corresponding to spatial Kirchhoff stresses given by

$$\boldsymbol{\tau}_{\text{hyp}} = J\, f_{\text{d}}(\kappa)\, \partial_J\psi_{\text{vol}}(J)\, \boldsymbol{I} + \text{dev}\big(2\, f_{\text{d}}^{n_{\text{iso}}}\, \bar{\boldsymbol{F}} \cdot \partial_{\bar{\boldsymbol{C}}}\psi_{\text{ich}}(\bar{\boldsymbol{C}}) \cdot \bar{\boldsymbol{F}}^{\text{t}}\big)\ , \tag{2.25}$$

both of which are direct extensions of their purely hyperelastic counterparts introduced in (2.9) and (2.11).

The damage function affecting the isochoric part of the free energy function furthermore affects the evolution of viscous stress-type internal variables via

$$\dot{\boldsymbol{Q}}_i(t) + \frac{1}{\tau_i}\,\boldsymbol{Q}_i(t) = \frac{\gamma_i}{\tau_i}\, f_{\mathrm{d}}^{n_{\mathrm{iso}}}\,\mathrm{DEV}\big(2\,\partial_{\bar{\boldsymbol{C}}}\psi_{\mathrm{ich}}(\bar{\boldsymbol{C}}(t))\big)\ , \tag{2.26}$$

which basically reflects the damage-extended version of (2.13). This induces a convolution representation in terms of

$$\boldsymbol{Q}_i(t) = \frac{\gamma_i}{\tau_i}\int_{-\infty}^{t} \exp(-(t-s)/\tau_i)\, f_{\mathrm{d}}^{n_{\mathrm{iso}}}\,\mathrm{DEV}\big(2\,\partial_{\bar{\boldsymbol{C}}}\psi_{\mathrm{ich}}(\bar{\boldsymbol{C}}(s))\big)\,\mathrm{d}s\,, \tag{2.27}$$

see (2.15) for the corresponding expression that is associated with an undamaged setting.

Finally, the Piola–Kirchhoff stresses that fully incorporate viscous and damage effects take the form

$$\boldsymbol{S}(t) = J f_{\mathrm{d}}\,\partial_J\psi_{\mathrm{vol}}(J)\,\boldsymbol{C}^{-1}(t) + J^{-\frac{2}{3}}(t)\int_{-\infty}^{t} g(t-s)\,\frac{\mathrm{d}}{\mathrm{d}s}\big(f_{\mathrm{d}}^{n_{\mathrm{iso}}}\,\mathrm{DEV}\big(2\,\partial_{\bar{\boldsymbol{C}}}\psi_{\mathrm{ich}}(\bar{\boldsymbol{C}}(s))\big)\big)\,\mathrm{d}s\,, \tag{2.28}$$

which allows for the accommodation of arbitrary free energy functions, in particular energy functions of higher order such as the Yeoh model that appropriately captures the Treloar-type behaviour of materials such as the particular elastomer considered in this work.

The numerical solution of the above-introduced convolution integrals is based on a transformation towards a recurrence formula, enabling the computation of the constitutive response based on the standard internal variable procedure, thereby bypassing the need to store the entire strain history that is individual to each material point in view of the later finite element application; see Appendix A for details on the numerical update procedure.

Since the general framework can be applied to all kinds of energy functions and considering the type of material and its behaviour, the chosen hyperelastic material model is briefly presented in Section 2.2.4. The applied damage function f_{d} is specified in Section 2.2.5.

2.2.4 Hyperelastic material model

Considering the nearly incompressible, non-linear elastic material behaviour (see for example the stress-strain-response in Figure 2.24b), the Yeoh hyperelastic material model was chosen [137, 138]. In [139], Yeoh and Flemming argued that Rivlin's theory [94],

where the strain energy function depends on the first two invariants of the right Cauchy–Green tensor $\boldsymbol{C}$, to be specific

$$\psi_{\mathrm{Riv}} = \sum_{i,j=1}^{\infty} C_{ij}[I_1 - 3]^i[I_2 - 3]^j \,, \tag{2.29}$$

runs into difficulties with respect to the identification of the material parameters since the contributions cannot be perfectly determined separately in the experiments. Here, C_{ij} are the corresponding material parameters, and I_1 and I_2 are the first and second principal invariants related to the isochoric right Cauchy–Green tensor, respectively. Yeoh neglected the contribution of the second invariant assuming that no serious error would arise since the contribution would be sufficiently small with respect to the impact of the first invariant. In this work, however, the Yeoh energy potential

$$\psi_{\mathrm{ich}} = \sum_{i=1}^{3} C_i[\mathrm{tr}(\bar{\boldsymbol{C}}) - 3]^i \,, \tag{2.30}$$

serves as the isochoric contribution to overall energy potential, where C_i denote the underlying material parameters. This phenomenological material model was developed for rubber elasticity and is applied in this work as a first choice with respect to the mentioned material behaviour. The volumetric energy contribution ψ_{vol} is chosen in a standard manner as

$$\psi_{\mathrm{vol}} = \frac{1}{2} K \left[\frac{1}{2} \left[J^2 - 1 \right] - \ln(J) \right] \,, \tag{2.31}$$

where K denotes the bulk modulus of the material. The related energy contributions ψ_{ich} and ψ_{vol} can, however, be straightforwardly replaced within the general constitutive framework elaborated in this work in order to account for different particular material characteristics.

2.2.5 Damage function

The damage function mentioned in Section 2.2.3 was chosen to be of an exponential type, following [86, 133]. Thus, a damage initiation threshold, as well as a damage saturation rate can be used in the function

$$f_{\mathrm{d}}(\kappa) = 1 - d = \exp(-\eta_{\mathrm{d}} \langle \kappa - \kappa_{\mathrm{d}} \rangle) \,, \tag{2.32}$$

fulfilling the requirements for the damage function to be restricted to $f_{\mathrm{d}} : \mathbb{R}^+ \to (0, 1]$. Here, d denotes the classic damage variable with $d=0$ indicating zero damage and $d=1$ for 100% damage. The variable κ represents a related internal damage variable, while $\kappa_{\mathrm{d}} > 0$ is the damage threshold parameter, and η_{d} introduces the damage saturation

parameter. In addition, $\langle \bullet \rangle := \max\{0, \bullet\}$ represents the Macaulay brackets. Consequently, damage is obtained in the material if the local damage variable exceeds the damage threshold. The damage function for the isochoric energy contribution matches this chosen function except for the exponent n_{iso}. Thus, a relation between both functions is still given and only adjusted via this material parameter. The evolution of the internal damage variable κ is based on the associated form

$$\dot{\kappa} = \lambda \, \frac{\partial \Phi_{\text{d}}(\boldsymbol{F}, \phi, \nabla_{\boldsymbol{X}} \phi, \kappa)}{\partial q} \,, \tag{2.33}$$

where λ denotes a proper Lagrange multiplier, $\Phi_{\text{d}}(\boldsymbol{F}, \phi, \nabla_{\boldsymbol{X}} \phi, \kappa) = q(\boldsymbol{F}, \phi, \nabla_{\boldsymbol{X}} \phi, \kappa) - \kappa \leq 0$ represents the damage condition, and $q = -\partial[\psi_{\text{loc}} + \psi_{\text{nloc}}]/\partial\kappa$ is the energy release rate. Hence, apart from the balance of linear momentum, the Euler–Lagrange equation governing the non-local damage variable needs to be solved simultaneously. For further information regarding this regularised damage model and its implementation, see Ostwald et al. [86]. The implementation was performed in a user material subroutine (UMAT) in Abaqus following [86].

2.3 Laminate-model for ferroelectric materials

In this section, the laminate-model for ferroelectric materials is presented, starting with a brief outline of the underlying material model in Section 2.3.1. Subsequently, the different Fischer-Burmeister-type functions discussed in this section are introduced in Section 2.3.2. Section 2.3.3 provides numerical results and a detailed discussion with respect to the performances of the analysed schemes. This section is concluded with a summary regarding the investigations of the different FB functions in Section 2.3.4.

2.3.1 Constitutive model

The constitutive model to simulate switching behaviour of ferroelectrics, in particular $BaTiO_3$, shall be described in this section. The model considers small strain kinematics and is adopted from [17], to which the reader is referred to in view of a detailed discussion of the constitutive model.

We consider tetragonal unit cells, as representative for e.g. $BaTiO_3$ below the Curie temperature, and shall denote the polarisation direction of the respective variants by $\boldsymbol{p}_\alpha$, with $\alpha = 1, \ldots, n_v = 6$. The orthonormal base system $\{\boldsymbol{e}_{1,2,3}\}$ is assumed to be aligned with the crystallographic axes so that

$$\boldsymbol{p}_1 = -\,\boldsymbol{p}_2 = p^{\text{s}}\, \boldsymbol{e}_1 \,, \tag{2.34}$$

$$\boldsymbol{p}_3 = -\,\boldsymbol{p}_4 = p^{\text{s}}\, \boldsymbol{e}_2 \,, \tag{2.35}$$

$$\boldsymbol{p}_5 = -\,\boldsymbol{p}_6 = p^{\text{s}}\, \boldsymbol{e}_3 \,, \tag{2.36}$$

wherein p^{s} denotes the polarisation magnitude. Similarly, the states of spontaneous strains related to the respective variants are introduced as

$$\boldsymbol{\varepsilon}_1 = \boldsymbol{\varepsilon}_2 = [\,\varepsilon_1^{\mathrm{s}} - \varepsilon_2^{\mathrm{s}}\,]\,\boldsymbol{e}_1 \otimes \boldsymbol{e}_1 + \varepsilon_2^{\mathrm{s}}\,\boldsymbol{I}\,, \tag{2.37}$$

$$\boldsymbol{\varepsilon}_3 = \boldsymbol{\varepsilon}_4 = [\,\varepsilon_1^{\mathrm{s}} - \varepsilon_2^{\mathrm{s}}\,]\,\boldsymbol{e}_2 \otimes \boldsymbol{e}_2 + \varepsilon_2^{\mathrm{s}}\,\boldsymbol{I}\,, \tag{2.38}$$

$$\boldsymbol{\varepsilon}_5 = \boldsymbol{\varepsilon}_6 = [\,\varepsilon_1^{\mathrm{s}} - \varepsilon_2^{\mathrm{s}}\,]\,\boldsymbol{e}_3 \otimes \boldsymbol{e}_3 + \varepsilon_2^{\mathrm{s}}\,\boldsymbol{I}\,, \tag{2.39}$$

wherein $\varepsilon_1^{\mathrm{s}}$ and $\varepsilon_2^{\mathrm{s}}$ define the axial spontaneous strain magnitudes.

Moreover, let the directions of the polarisation vectors be represented by the unit vectors $\boldsymbol{a}_\alpha = \boldsymbol{p}_\alpha / \|\boldsymbol{p}_\alpha\|$, with $\|\boldsymbol{p}_\alpha\| = \sqrt{\boldsymbol{p}_\alpha \cdot \boldsymbol{p}_\alpha}$, which define the structural tensors $\boldsymbol{m}_\alpha = \boldsymbol{a}_\alpha \otimes \boldsymbol{a}_\alpha$. Based on this, the representation of the constitutive tensors – i.e. the fourth-order elasticity tensors, the third-order piezoelectric tensors and the second-order dielectric tensors – results in

$$\begin{aligned}\mathbf{E}_\alpha(\boldsymbol{a}_\alpha) = {}& \lambda^{\mathsf{E}}\,\boldsymbol{I} \otimes \boldsymbol{I} + 2\,\mu^{\mathsf{E}}\,\mathbf{I}^{\mathrm{sym}} + \alpha_1^{\mathsf{E}}\,[\,\boldsymbol{m}_\alpha \underline{\otimes}\, \boldsymbol{I} + \boldsymbol{I} \underline{\otimes}\, \boldsymbol{m}_\alpha\,] \\ & + 2\,\alpha_2^{\mathsf{E}}\,\boldsymbol{m}_\alpha \otimes \boldsymbol{m}_\alpha + \alpha_3^{\mathsf{E}}\,[\,\boldsymbol{m}_\alpha \otimes \boldsymbol{I} + \boldsymbol{I} \otimes \boldsymbol{m}_\alpha\,]\,, \end{aligned} \tag{2.40}$$

$$\mathbf{e}_\alpha(\boldsymbol{a}_\alpha) = -\,\beta_1^{\mathrm{e}}\,\boldsymbol{a}_\alpha \otimes \boldsymbol{I} - \beta_2^{\mathrm{e}}\,\boldsymbol{m}_\alpha \otimes \boldsymbol{a}_\alpha - \tfrac{1}{2}\,\beta_3^{\mathrm{e}}\,[\,\boldsymbol{I} \otimes \boldsymbol{a}_\alpha + \boldsymbol{I} \overline{\otimes}\, \boldsymbol{a}_\alpha\,]\,, \tag{2.41}$$

$$\boldsymbol{\epsilon}_\alpha(\boldsymbol{a}_\alpha) = -\,2\,\gamma_1^{\epsilon}\,\boldsymbol{I} - 2\,\gamma_2^{\epsilon}\,\boldsymbol{m}_\alpha\,. \tag{2.42}$$

The contribution of each variant at the level of a material point within the continuum considered is captured by adopting the concept of volume fractions embedded into the theory of mixtures. To be specific, let these volume fractions be related to the respective variants and be denoted by λ_α together with the constraints

$$\lambda_\alpha \geq 0 \qquad \text{and} \qquad \sum_{\alpha=1}^{n_v} \lambda_\alpha = 1\,. \tag{2.43}$$

Based on this, volume averaged (at the level of a material point) quantities can be introduced, which shall be denoted by $[\bullet]^{\mathrm{M}}(\boldsymbol{\lambda}) = \sum_{\alpha=1}^{n_v} \lambda_\alpha\,[\bullet]_\alpha$ with $\boldsymbol{\lambda} = [\,\lambda_1, \ldots, \lambda_{n_v}\,]$. Alternatively, laminate related fractions can be introduced, which directly refer to the laminate microstructure of the material. The laminate fractions can be expressed in terms of the volume fractions,

$$\mu^j = \begin{cases} 0 & \text{for} \quad \sum_{\alpha=1}^{j-1} \lambda_\alpha = 1\,, \\ \dfrac{\lambda_j}{1 - \sum_{\alpha=1}^{j-1} \lambda_\alpha} & \text{otherwise}\,, \end{cases} \tag{2.44}$$

with $j = 1, \ldots, n_v - 1$, and vice versa, i.e.

$$\lambda_\alpha = \begin{cases} \mu^\alpha \prod_{j=1}^{\alpha-1} [\, 1 - \mu^j \,] & \text{for} \quad \alpha = 1, \ldots, n_v - 1 \,, \\ \prod_{j=1}^{\alpha-1} [\, 1 - \mu^j \,] & \text{for} \quad \alpha = n_v \,. \end{cases} \tag{2.45}$$

cf. [9, 65, 136] and Figure 2.3. The laminate fractions are constrained by

$$0 \leq \mu^j \leq 1 \,. \tag{2.46}$$

Furthermore, volume averaging at material point level can be reformulated in terms of laminate fractions, namely $[\bullet]^{\mathrm{M}}(\boldsymbol{\lambda}(\boldsymbol{\mu})) = \sum_{\alpha=1}^{n_v} \lambda_\alpha(\boldsymbol{\mu})\, [\bullet]_\alpha$ with $\boldsymbol{\mu} = [\, \mu^1, \ldots, \mu^{n_v - 1} \,]$.

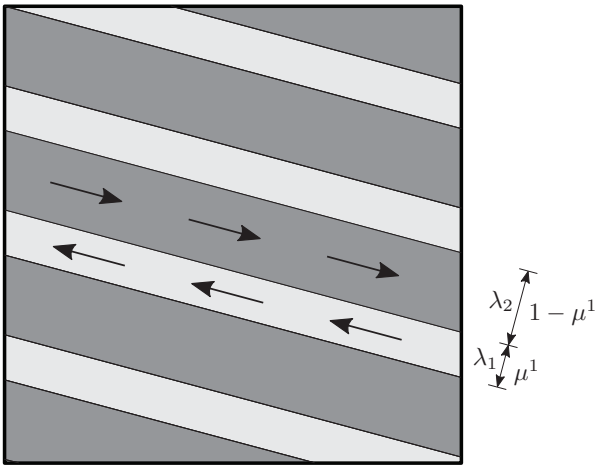

Figure 2.3: Illustration of the laminate microstructure with the definition of variant and laminate volume fractions λ_α and μ^j for two different variants, see also, e.g., [65] for further details. The arrows indicate the orientation of spontaneous polarisation vectors in the respective variant. Reprinted from Bartel et al., Arch. Appl. Mech. 89 (2019), 995-1010, [6], with permission from Springer Nature.

With theses definitions at hand, we next introduce the electric Gibbs energy H — denoted according to the definition provided in [118], for general discussions on the nomenclature of thermodynamic potentials in the electro-mechanically coupled case see also [81, 107] — based on which the stress tensor $\boldsymbol{\sigma} = \partial H / \partial \boldsymbol{\varepsilon}$, the dielectric displacements $\boldsymbol{d} = -\partial H / \partial \boldsymbol{e}$, as well as quantities $f^j = -\partial H / \partial \mu^j$ energetically conjugate to the laminate fractions can be derived. In this context, $\boldsymbol{\varepsilon}$ denotes the total strain tensor,

whereas $\boldsymbol{e}$ represents the electric field vector. We assume an additive decomposition of H into a piezoelectric contribution and an additional remanent term of the form

$$H(\boldsymbol{\varepsilon}^{\mathrm{e}}, \boldsymbol{e}, \boldsymbol{\mu}) = H^{\mathrm{piezo}}(\boldsymbol{\varepsilon}^{\mathrm{e}}, \boldsymbol{e}, \boldsymbol{\mu}) + H^{\mathrm{rem}}(\boldsymbol{\mu})\,, \tag{2.47}$$

$$H^{\mathrm{piezo}} = \tfrac{1}{2}\,\boldsymbol{\varepsilon}^{\mathrm{e}} : \mathbf{E}^{\mathrm{M}} : \boldsymbol{\varepsilon}^{\mathrm{e}} - \boldsymbol{e} \cdot \mathbf{e}^{\mathrm{M}} : \boldsymbol{\varepsilon}^{\mathrm{e}} - \tfrac{1}{2}\,\boldsymbol{e} \cdot \boldsymbol{\epsilon}^{\mathrm{M}} \cdot \boldsymbol{e} - \boldsymbol{p}^{\mathrm{M}} \cdot \boldsymbol{e}\,, \tag{2.48}$$

$$H^{\mathrm{rem}} = \frac{1}{c}\left[\frac{1}{2}\,p^{\mathrm{sat}}\,\ln\left(1 - [\,p^{N}(\boldsymbol{\mu})\,]^2\right) + \|\boldsymbol{p}^{\mathrm{M}}\|\,\mathrm{arctanh}\big(p^{N}(\boldsymbol{\mu})\big)\right], \tag{2.49}$$

with $\boldsymbol{\varepsilon}^{\mathrm{e}} = \boldsymbol{\varepsilon} - \boldsymbol{\varepsilon}^{\mathrm{M}}$, the additional material parameter c, and $p^{N}(\boldsymbol{\mu}) = \|\boldsymbol{p}^{\mathrm{M}}\|/p^{\mathrm{sat}}$.

The laminate fractions do not evolve for states within the admissible domain introduced via

$$\mathbb{E} := \left\{ f^j(\boldsymbol{\varepsilon}^{\mathrm{e}}, \boldsymbol{e}, \boldsymbol{\mu}) \,\middle|\, \Phi^j(f^j) := |f^j| - g^{\mathrm{c},j}(\boldsymbol{\mu}) \le 0\,;\;\; j = 1, \ldots, n_v - 1 \right\}, \tag{2.50}$$

wherein the coercive field ($e^{\mathrm{c}}_{90^\circ,180^\circ}$) related threshold quantities are defined as

$$g^{\mathrm{c},1}(\boldsymbol{\mu}) = 2\,e^{\mathrm{c}}_{180^\circ}\,p^{\mathrm{s}}\,\mu^2 + e^{\mathrm{c}}_{90^\circ}\,p^{\mathrm{s}}\,[\,1 - \mu^2\,]\,, \tag{2.51}$$

$$g^{\mathrm{c},2}(\boldsymbol{\mu}) = e^{\mathrm{c}}_{90^\circ}\,p^{\mathrm{s}}[\,1 - \mu^1\,]\,, \tag{2.52}$$

$$g^{\mathrm{c},3}(\boldsymbol{\mu}) = [\,2\,e^{\mathrm{c}}_{180^\circ}\,p^{\mathrm{s}}\,\mu^4 + e^{\mathrm{c}}_{90^\circ}\,p^{\mathrm{s}}\,[\,1 - \mu^4\,]\,]\,[\,1 - \mu^1\,]\,[\,1 - \mu^2\,]\,, \tag{2.53}$$

$$g^{\mathrm{c},4}(\boldsymbol{\mu}) = e^{\mathrm{c}}_{90^\circ}\,p^{\mathrm{s}}\,[\,1 - \mu^1\,]\,[\,1 - \mu^2\,]\,[\,1 - \mu^3\,]\,, \tag{2.54}$$

$$g^{\mathrm{c},5}(\boldsymbol{\mu}) = 2\,e^{\mathrm{c}}_{180^\circ}\,p^{\mathrm{s}}\,[\,1 - \mu^1\,]\,[\,1 - \mu^2\,]\,[\,1 - \mu^3\,]\,[\,1 - \mu^4\,]\,, \tag{2.55}$$

cf. [136]. Rate dependent evolution equations, activated for non-admissible states, are introduced as

$$\dot{\mu}^j = \frac{1}{\eta}\left\langle |f^j| - g^{\mathrm{c},j}(\boldsymbol{\mu}) \right\rangle^m \frac{f^j}{|f^j|} \qquad \text{for} \qquad j = 1, \ldots, n_v - 1\,, \tag{2.56}$$

wherein $\langle[\bullet]\rangle = \max\{0, [\bullet]\}$, which shows that the dissipation inequality $\sum_{j=1}^{n_v-1} f^j\,\dot{\mu}^j \ge 0$ is satisfied.

2.3.2 Fischer-Burmeister-based algorithms

In this chapter, the original Fischer-Burmeister NCP function according to [19] is introduced and some of its characteristics are discussed. In addition, some enhanced methods based on this original approach are presented.

2.3.2.1 Original Fischer-Burmeister approach

As pointed out in Section 2.3.1, the constitutive framework includes the consideration of the physically-motivated restrictions

$$r_I^j := \mu^j \geq 0 \tag{2.57}$$
$$r_{II}^j := 1 - \mu^j \geq 0 \,, \tag{2.58}$$

with $j = 1, \ldots, n_v - 1$. In view of the underlying energetic approach elaborated in Section 2.3.1, an enhanced form of the electromechanical stored energy density is defined as

$$H_{\mathrm{enh}}(\boldsymbol{\varepsilon}^{\mathrm{e}}, \boldsymbol{e}, \boldsymbol{\mu}, \boldsymbol{\Gamma}_I, \boldsymbol{\Gamma}_{II}) := H(\boldsymbol{\varepsilon}^{\mathrm{e}}, \boldsymbol{e}, \boldsymbol{\mu}) - \sum_{j=1}^{n_v-1} \Gamma_I^j \, r_I^j - \sum_{j=1}^{n_v-1} \Gamma_{II}^j \, r_{II}^j \,, \tag{2.59}$$

with $\boldsymbol{\Gamma}_I = [\, \Gamma_I^1, \ldots, \Gamma_I^{n_v-1} \,]$ and $\boldsymbol{\Gamma}_{II} = [\, \Gamma_{II}^1, \ldots, \Gamma_{II}^{n_v-1} \,]$ as Lagrange-type parameters. As a consequence, the evolution equations (2.56) are rewritten as

$$\dot{\mu}^j = \frac{1}{\eta} \big\langle |f_{\mathrm{enh}}^j| - g^{\mathrm{c},j}(\boldsymbol{\mu}) \big\rangle^m \, \frac{f_{\mathrm{enh}}^j}{|f_{\mathrm{enh}}^j|} \,, \tag{2.60}$$

with $f_{\mathrm{enh}}^j = -\,\partial H_{\mathrm{enh}} / \partial \mu^j$, which are subjected to the complementarity conditions

$$r_i^j \geq 0, \qquad \Gamma_i^j \geq 0, \qquad r_i^j \, \Gamma_i^j = 0, \qquad \text{with} \quad i = I, II \,. \tag{2.61}$$

However, it was shown for different kinds of constitutive models, e.g. crystal plasticity models, that the consideration of such complementarity conditions can be challenging and that it has significant influence on the efficiency of the underlying algorithms, see, e.g., [102]. Such complementarity conditions mainly occur in the context of rate-independent evolution equations and physically-motivated restrictions of the values of phase volume fractions or the like. A sophisticated way to circumvent the explicit consideration of these equality and inequality constraints stems from [19] and has been introduced to problems in continuum mechanics and material modelling by [102]. To be more precise, the Fischer-Burmeister non-linear complementarity problem functions (or short, Fischer-Burmeister NCP functions), namely

$$\xi_i^j(r_i^j, \Gamma_i^j) := \sqrt{[r_i^j]^2 + [\Gamma_i^j]^2} - [r_i^j + \Gamma_i^j] = 0, \tag{2.62}$$

may substitute all of the conditions in (2.61). Figures 2.4 and 2.5 reveal the main characteristics of this kind of function, where the original Fischer-Burmeister NCP function shall be labelled f_{FB}^0 here for later purposes. Roots of f_{FB}^0 only exist in the case of $r_i^j \geq 0$ and $\Gamma_i^j = 0$ or, vice versa, $r_i^j = 0$ and $\Gamma_i^j \geq 0$. The projections $f_{\mathrm{FB}}^0(0, \Gamma_i^j)$ and $f_{\mathrm{FB}}^0(r_i^j, 0)$ are not continuously differentiable at $\{r_i^j, \Gamma_i^j\} = \{0, 0\}$.

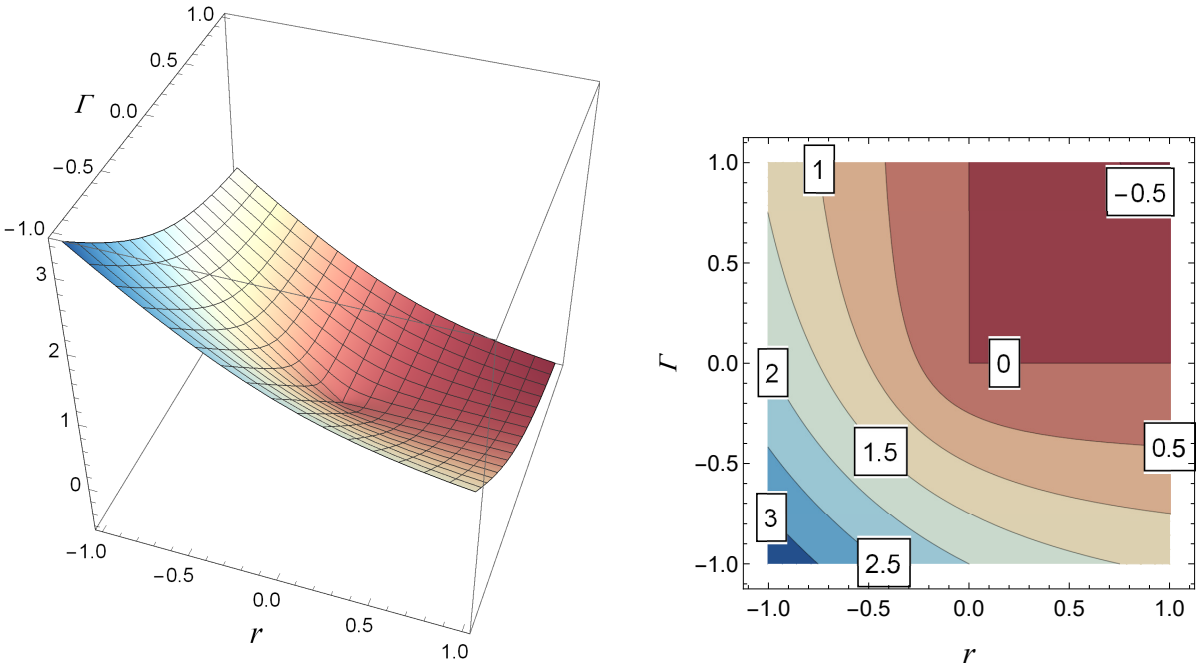

Figure 2.4: Illustration of the Fischer-Burmeister NCP function as three dimensional plot (left) and contour plot (right) depending on r and a generalised Lagrange-type parameter Γ. Reprinted from Bartel et al., Arch. Appl. Mech. 89 (2019), 995-1010, [6], with permission from Springer Nature.

As shown in, e.g., [4, 5, 50], the Fischer-Burmeister NCP functions allow a sophisticated implementation of complementarity conditions by solving the system of equations

$$\mathbf{R}(\mathbf{V}) = \left[\, \zeta_{\mu^1} \dots \zeta_{\mu^{n_v-1}} \quad \xi_I^1 \dots \xi_I^{n_v-1} \quad \xi_{II}^1 \dots \xi_{II}^{n_v-1} \,\right]^{\mathrm{t}} \doteq \mathbf{0} \tag{2.63}$$

without the need of, e.g., cumbersome active set search strategies. Here,

$$\mathbf{V} := \left[\, \mu^1 \dots \mu^{n_v-1} \quad \Gamma_I^1 \dots \Gamma_I^{n_v-1} \quad \Gamma_{II}^1 \dots \Gamma_{II}^{n_v-1} \,\right]^{\mathrm{t}} \tag{2.64}$$

denotes a generalised list of unknowns and the quantities

$$\zeta_{\mu^j} := \mu^j - {}^n\mu^j - F^j \,, \tag{2.65}$$

with

$$F^j := \Delta t\, \dot{\mu}^j = \frac{\Delta t}{\eta} \left\langle |f_{\mathrm{enh}}^j| - g^{\mathrm{c},j}(\boldsymbol{\mu}) \right\rangle^m \frac{f_{\mathrm{enh}}^j}{|f_{\mathrm{enh}}^j|} \,, \tag{2.66}$$

reflect the time-discretised form of the evolution equations with ${}^n\mu^j$ as the value of μ^j at the former time step t_n, whereas the index referring to the current time step t_{n+1} is

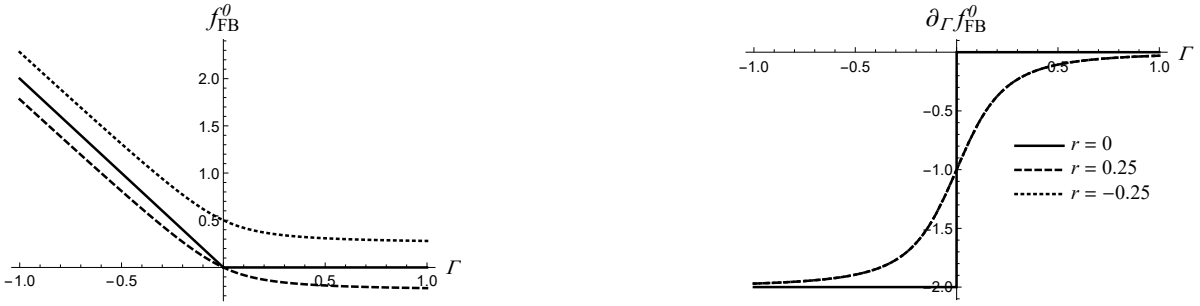

Figure 2.5: Projections of the Fischer-Burmeister NCP function (left) and the corresponding derivatives with respect to Γ (right) for different values of r. Reprinted from Bartel et al., Arch. Appl. Mech. 89 (2019), 995-1010, [6], with permission from Springer Nature.

skipped in order to simplify notation. A standard method to solve (2.63) is the Newton-Raphson scheme with iteration index l, where the solution is obtained via incremental updates of the form

$$ {}^{l+1}\mathbf{V} = {}^{l}\mathbf{V} - {}^{l}\left[\frac{\mathrm{d}\mathbf{R}}{\mathrm{d}\mathbf{V}}\right]^{-1} \cdot {}^{l}\mathbf{R} \,. \tag{2.67} $$

The Jacobian can in general be represented by using the following submatrices via

$$ \frac{\mathrm{d}\mathbf{R}}{\mathrm{d}\mathbf{V}} = \begin{bmatrix} \dfrac{\mathrm{d}\zeta_{\mu^j}}{\mathrm{d}\mu^k} & \dfrac{\mathrm{d}\zeta_{\mu^j}}{\mathrm{d}\Gamma^k_I} & \dfrac{\mathrm{d}\zeta_{\mu^j}}{\mathrm{d}\Gamma^k_{II}} \\ \dfrac{\mathrm{d}\xi^j_I}{\mathrm{d}\mu^k} & \dfrac{\mathrm{d}\xi^j_I}{\mathrm{d}\Gamma^k_I} & \dfrac{\mathrm{d}\xi^j_I}{\mathrm{d}\Gamma^k_{II}} \\ \dfrac{\mathrm{d}\xi^j_{II}}{\mathrm{d}\mu^k} & \dfrac{\mathrm{d}\xi^j_{II}}{\mathrm{d}\Gamma^k_I} & \dfrac{\mathrm{d}\xi^j_{II}}{\mathrm{d}\Gamma^k_{II}} \end{bmatrix} \,. \tag{2.68} $$

To be more specific, these submatrices—all of which exhibit the dimension $[n_v - 1] \times [n_v - 1]$—are given by

$$ \frac{\mathrm{d}\zeta_{\mu^j}}{\mathrm{d}\mu^k} = \delta^{jk} - \frac{\partial F^j}{\partial \mu^k} \,, \tag{2.69} $$

$$ \frac{\mathrm{d}\zeta_{\mu^j}}{\mathrm{d}\Gamma^k_I} = -\frac{\partial F^j}{\partial \Gamma^k_I} \,, \tag{2.70} $$

$$ \frac{\mathrm{d}\zeta_{\mu^j}}{\mathrm{d}\Gamma^k_{II}} = -\frac{\partial F^j}{\partial \Gamma^k_{II}} \,, \tag{2.71} $$

$$ \frac{\mathrm{d}\xi^j_I}{\mathrm{d}\mu^k} = \delta^{jk} \left[\frac{r^j_I}{\sqrt{[r^j_I]^2 + [\Gamma^j_I]^2}} - 1\right] \,, \tag{2.72} $$

$$\frac{\mathrm{d}\xi_I^j}{\mathrm{d}\Gamma_I^k} = \delta^{jk} \left[\frac{\Gamma_I^j}{\sqrt{[r_I^j]^2 + [\Gamma_I^j]^2}} - 1 \right] , \tag{2.73}$$

$$\frac{\mathrm{d}\xi_I^j}{\mathrm{d}\Gamma_{II}^k} = 0^{jk} , \tag{2.74}$$

$$\frac{\mathrm{d}\xi_{II}^j}{\mathrm{d}\mu^k} = -\delta^{jk} \left[\frac{r_{II}^j}{\sqrt{[r_{II}^j]^2 + [\Gamma_{II}^j]^2}} - 1 \right] , \tag{2.75}$$

$$\frac{\mathrm{d}\xi_{II}^j}{\mathrm{d}\Gamma_I^k} = 0^{jk} , \tag{2.76}$$

$$\frac{\mathrm{d}\xi_{II}^j}{\mathrm{d}\Gamma_{II}^k} = \delta^{jk} \left[\frac{\Gamma_{II}^j}{\sqrt{[r_{II}^j]^2 + [\Gamma_{II}^j]^2}} - 1 \right] . \tag{2.77}$$

The terms in (2.72), (2.73), (2.75), and (2.77) reveal two general drawbacks of the original Fischer-Burmeister approach in the context of its numerical implementation:

- Intuitive choices for the initial values of the underlying variables such as $\mu^j = 0$ or $\mu^j = 1$ for some $j = 1, \ldots, n_v - 1$ and, as a consequence, $r_I^j = 0$ or $r_{II}^j = 0$ together with $\Gamma_i^j = 0$ lead to a singularity of the Jacobian introduced in (2.68).
- In contrast to, e.g., (2.69), these terms are likely to take values such as 1 and -1 which are essentially independent from the chosen physical units. As a consequence, the eigenvalues and the condition number of the Jacobian (2.68) also depend on the chosen units. In other words, the robustness of the algorithm is highly affected by the specific numerical values of, e.g., the underlying Young's moduli.

In order to overcome these general drawbacks, we propose the following:

1. Even if it is intuitively clear that $r_i^j = 0$ is the correct solution for a specific time step of the overall calculation (for some i, j), the initial guess for the underlying variables should result in $r_i^j \neq 0$. In the context of the constitutive model used in this section, we do not set $\mu^j = 0$ or $\mu^j = 1$ as initial values, but rather $\mu^j = \delta_\mu$ or $\mu^j = 1 - \delta_\mu$, where δ_μ is a small number, e.g. $\delta_\mu = 10^{-4}$.
2. In some cases, the initial guess of $\Gamma_i^j = 0$ may be far off the actual solution. It turns out that an initial choice of $\Gamma_i^j = \Gamma^0 > 0$, e.g. $\Gamma_0 = 10^{-4}$, significantly increases the algorithm's robustness, even if $\Gamma_i^j = 0$ are the correct solutions. The values of Γ_i^j should be initialised in this manner in every load step.
3. Physical units should be used that lead to rather small values of the related quantities, for instance GPa for Young's moduli.

Remark 1 *In general, NCP functions of any kind, e.g. without further smoothing techniques, exhibit the property of being non-differentiable, at least at certain "points". Therefore, it is generally concluded that Newton-type solution schemes are not applicable for the underlying system of equations. In practice, however, such methods turn out to be applicable and even suitable if—in the specific case of the Fischer-Burmeister NCP functions—the recommendations 1.–3. made above are taken into account.*

Remark 2 *A significant drawback of the original Fischer-Burmeister approach is the limitation in dealing with monotone complementarity problems since the underlying function is too flat in the positive orthant, cf. [12].*

2.3.2.2 Extended Fischer-Burmeister-type NCP functions

As indicated above, the implementation of the original Fischer-Burmeister NCP function—despite its beneficial features—may suffer from specific shortcomings. Therefore, several approaches have been established in order to increase the efficiency of solution procedures for systems of equations such as (2.63). In this section, we investigate the applicability and performance of the following NCP functions based on the original Fischer-Burmeister approach in the context of the constitutive model presented in Section 2.3.1:

$$f_{\mathrm{FB}}^{I} := \sqrt{[r_i^j]^2 + [\Gamma_i^j]^2 + 2\,\delta^2} - [r_i^j + \Gamma_i^j] \tag{2.78}$$

$$f_{\mathrm{FB}}^{II} := \lambda \left[\sqrt{[r_i^j]^2 + [\Gamma_i^j]^2 + 2\,\delta^2} - [r_i^j + \Gamma_i^j]\right] + [1-\lambda]\sqrt{\left\langle r_i^j\right\rangle^2 \left\langle \Gamma_i^j\right\rangle^2 + 2\,\delta^2} \tag{2.79}$$

$$f_{\mathrm{FB}}^{III} := \lambda \left[\sqrt[4]{[r_i^j]^4 + [\Gamma_i^j]^4 + 2\,\delta^4} - [r_i^j + \Gamma_i^j]\right] + [1-\lambda]\sqrt[4]{\left\langle r_i^j\right\rangle^4 \left\langle \Gamma_i^j\right\rangle^4 + 2\,\delta^4} \tag{2.80}$$

$$f_{\mathrm{FB}}^{IV} := \sqrt{[r_i^j]^2 + [\Gamma_i^j]^2 + 2\,\delta^2} - [r_i^j + \Gamma_i^j] - \alpha\sqrt{\left\langle r_i^j\right\rangle^2 \left\langle \Gamma_i^j\right\rangle^2 + 2\,\delta^2} \tag{2.81}$$

$$f_{\mathrm{FB}}^{V} := \sqrt{\left[\sqrt{[r_i^j]^2 + [\Gamma_i^j]^2 + 2\,\delta^2} - [r_i^j + \Gamma_i^j]\right]^2 + \alpha\,\left[\left\langle r_i^j\right\rangle \left\langle \Gamma_i^j\right\rangle\right]^2} \tag{2.82}$$

In these relations δ reflects a perturbation parameter, $\lambda \in]0,1]$ and $\alpha \in [0,\infty[$ are scaling parameters.

The NCP function given in (2.78) stems from [47] and is referred to as smoothed Fischer-Burmeister NCP function. Figures 2.6 and 2.7 show the main characteristics of these enhanced NCP functions: In comparison to the original approach, the smoothed function is continuously differentiable everywhere. As shown in Appendix B, the roots of the original NCP function are only calculated in an approximative sense, where the accuracy depends on the specific choice for the perturbation parameter δ. More precisely speaking, the equality constraint to be solved by using this approach is $r_i^j\,\Gamma_i^j = \delta^2$.

Following [18], Equation (2.79) reflects a smoothed penalised Fischer-Burmeister NCP function on the basis of the NCP function introduced in [12], which is illustrated in

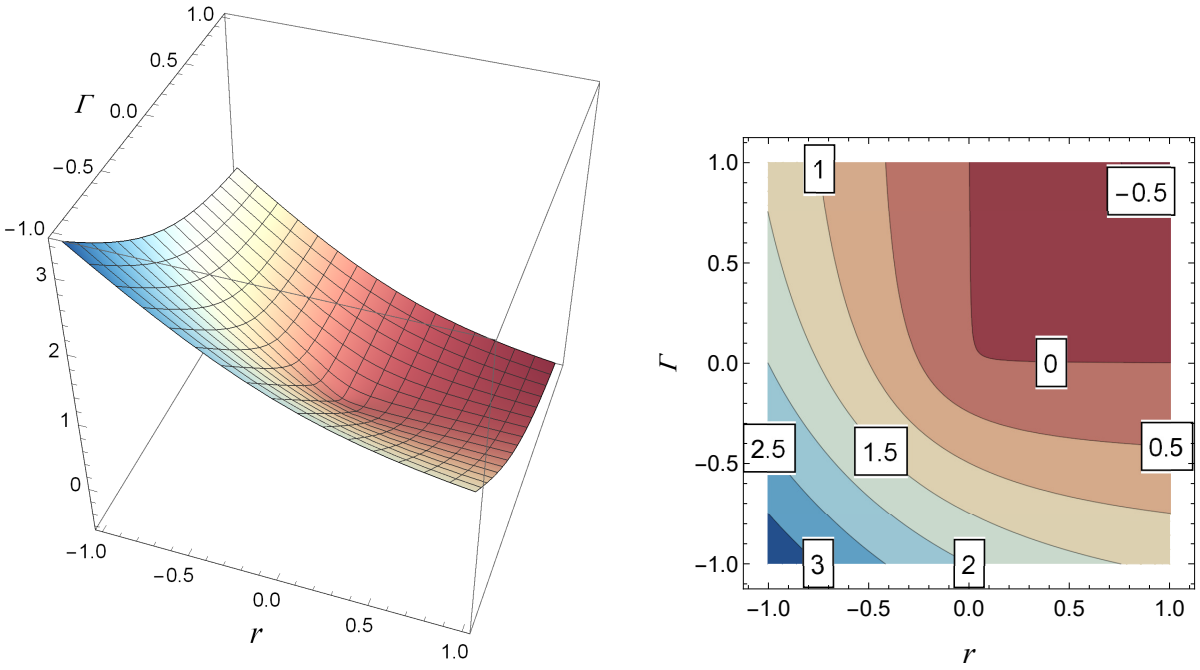

Figure 2.6: Illustration of the smoothed Fischer-Burmeister NCP function f_{FB}^{I} as three dimensional plot (left) and contour plot (right) depending on r and a generalised Lagrange-type parameter Γ. Here, the perturbation parameter $\delta = 0.05$ has been chosen for illustration purposes. Reprinted from Bartel et al., Arch. Appl. Mech. 89 (2019), 995-1010, [6], with permission from Springer Nature.

Figure 2.8 in terms of contour plots for different values of the scaling parameter λ. The NCP-function provided in (2.80) is based on f_{FB}^{II} with modifications inspired by [13, 14].

The fourth alternative investigated here is given by (2.81) which is a modification of the regularised FB function as presented in [122] which is also referred to as scaled penalised FB function therein. Exemplary visualisations of this function are given in Figure 2.9 for different values of the scaling parameter α. It is also shown in the aforementioned work that this specific FB-function may be regarded as a modified version of the NCP function established by [12]. Furthermore, the smoothing approach introduced in [47] has been applied, so that this function could be referred to as smoothed and scaled regularised FB function. Finally, the last NCP function investigated is given in (2.82) which is adopted from [121] with modifications according to [47].

2.3.3 Numerical examples

In this section the different NCP functions discussed in this contribution are applied in the context of the constitutive model presented in Section 2.3.1 and compared to each other in view of their convergence behaviour. Prior to the detailed discussion, the general material response is visualised in Figures 2.10 and 2.11, cf. [17].

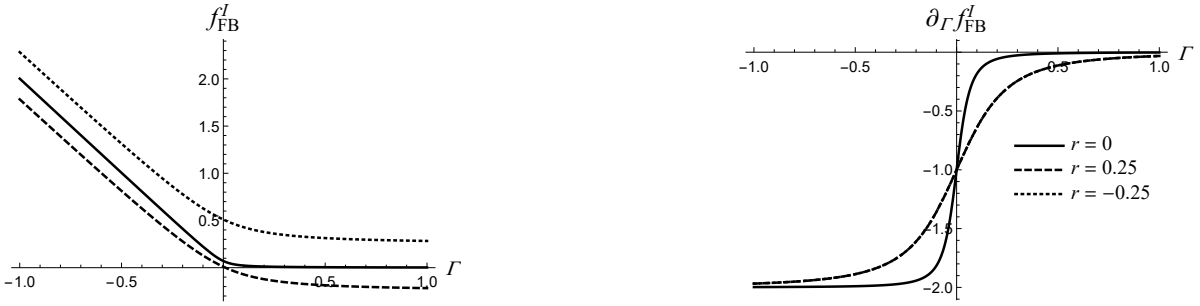

Figure 2.7: Projections of the smoothed Fischer-Burmeister NCP function f^I_{FB} (left) and the corresponding derivatives with respect to Γ (right) for different values of r. Here, the perturbation parameter $\delta = 0.05$ has been chosen for illustration purposes. Reprinted from Bartel et al., Arch. Appl. Mech. 89 (2019), 995-1010, [6], with permission from Springer Nature.

The results are obtained due to an electromechanical loading, implemented through a constant compressive stress $\boldsymbol{\sigma} = -2.7\ \boldsymbol{e}_3 \otimes \boldsymbol{e}_3$ MPa and a cyclically applied electric field $\boldsymbol{e} = e_3(t)\ \boldsymbol{e}_3$ with $e_3(0) = 0$, $e_3 \in [-1.25\,\mathrm{kV/mm}, 1.25\,\mathrm{kV/mm}]$, and the loading rate $\dot{e}_3 = \pm 1\,\mathrm{kV/[mm\,s]}$. In the following, the behaviour of the different NCP functions is analysed for two different time steps indicated in Figures 2.10 and 2.11, viz. $t_I = 0.8\,\mathrm{s}$ and $t_{II} = 1.1\,\mathrm{s}$. These time steps have been selected due to the fact that the related convergence studies turned out to be most meaningful. As can be seen in Figure 2.11(left), the first time step t_I marks a state shortly after λ_6 becomes zero, and t_{II} reflects a state shortly before λ_5 becomes one. In the unloaded state, all variants are energetically equally favourable so that $\lambda_i = 1/6$ with $i = 1, \ldots, 6$ are used as inititial values.

2.3.3.1 Comparison of different approaches at $t = t_I = 0.8\,\mathrm{s}$

In this section, the influence of the weighting factor δ and scaling parameter λ are discussed at $t = t_I = 0.8\,\mathrm{s}$. The prescribed time increment is chosen as $\Delta t = 0.02\,\mathrm{s}$ so that t_I is reached in load step 40. Figures 2.12 and 2.13 show the values of the residual depending on the number of iteration steps. Five methods are compared, namely the smoothed Fischer-Burmeister approach based on f^I_{FB}, the smoothed penalized Fischer-Burmeister NCP function using f^{II}_{FB} for $\lambda = 0.1$ and $\lambda = 0.9$, and the modified version of the latter using f^{III}_{FB} also with $\lambda = 0.1$ and $\lambda = 0.9$. The remaining NCP functions f^{IV}_{FB} and f^{V}_{FB} are discussed separately in Section 2.3.3.3.

Neglecting the results for $\delta = 10^{-2}$ at first, the algorithms based on f^{III}_{FB} show the same ($\delta = 10^{-12}$, $\delta = 10^{-8}$) or at least a very similar ($\delta = 10^{-6}$) behaviour as the algorithm based on f^I_{FB}. The convergence of the NCP function f^{II}_{FB} with $\lambda = 0.9$ is similar to the convergence of the previously mentioned NCP functions as well, for $\lambda = 0.1$, however, the algorithm based on f^{II}_{FB} shows an instability due to the occurring jump before fulfilling the chosen tolerance of 10^{-8}. It can be concluded that for rather small values of λ, where the stabilisation term within the function f^{II}_{FB} is dominating, the convergence behaviour worsens. The precise value of the perturbation parameter δ does not significantly affect

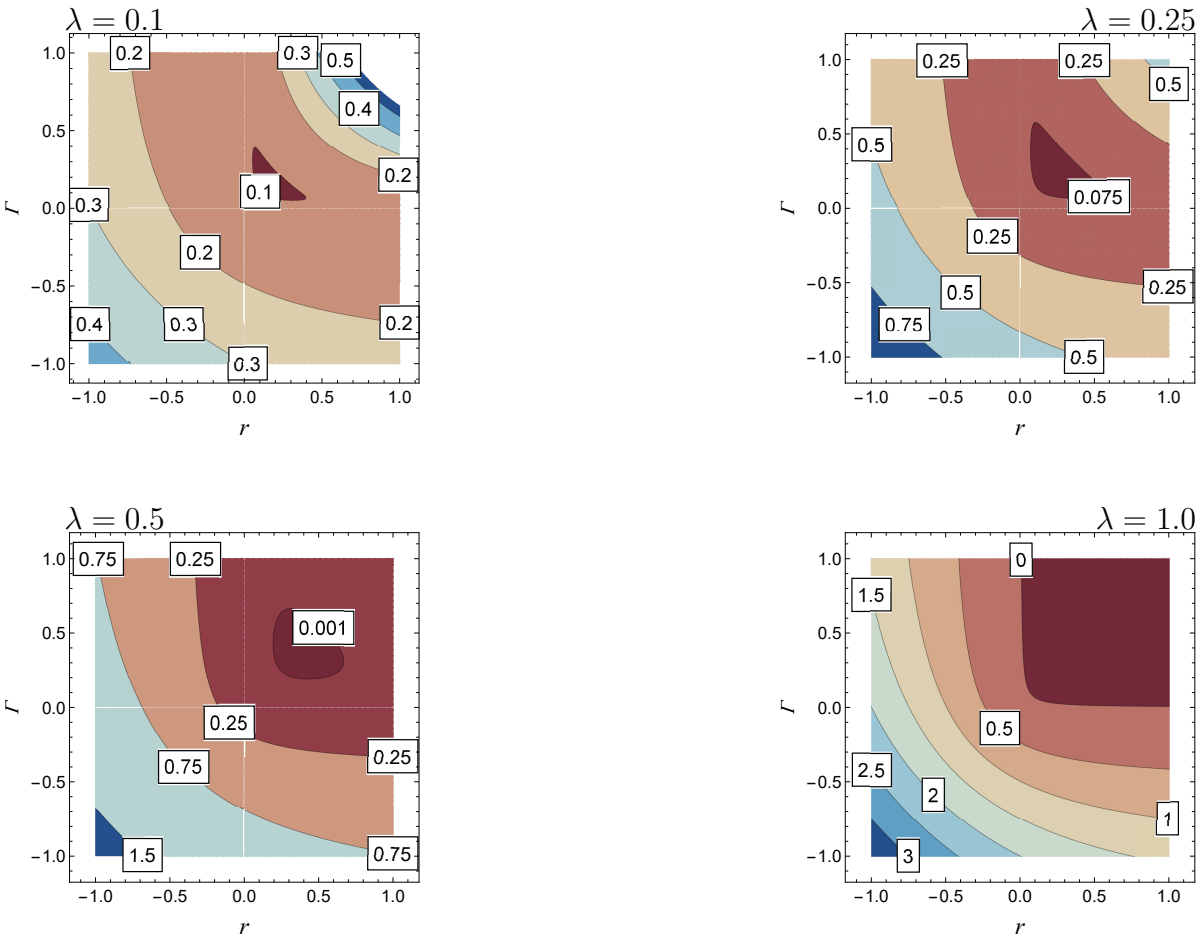

Figure 2.8: Illustration of the smoothed penalised Fischer-Burmeister NCP function f_{FB}^{II} as contour plots for different values of the scaling parameter λ. Here, the perturbation parameter $\delta = 0.01$ has been chosen for illustration purposes. Reprinted from Bartel et al., Arch. Appl. Mech. 89 (2019), 995-1010, [6], with permission from Springer Nature.

the convergence behaviour of the applied schemes. In general, all applied methods exhibit a linear convergence even though a Newton-Raphson scheme is properly applied which reflects a general drawback of algorithms based on Fischer-Burmeister functions, cf. Remark 2. As can be seen in Figure 2.13(right), all analysed schemes converge quadratically for $\delta = 10^{-2}$. However, such large values of δ may not be chosen due to the fact that the underlying constraints may significantly be violated which becomes obvious by the graphs in Figure 2.16, even though these refer to a different time step, as well as by the derivation provided in Appendix B.

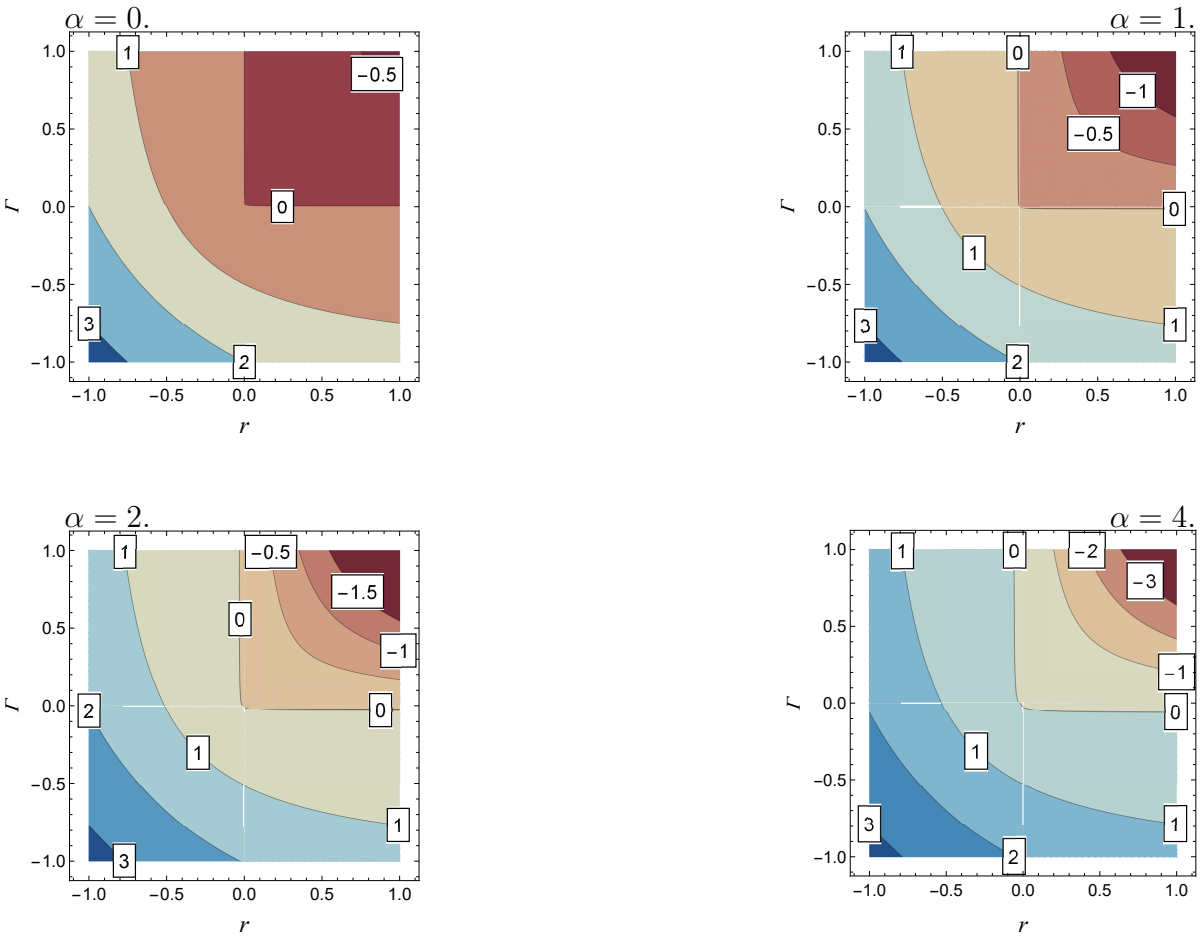

Figure 2.9: Illustration of the smoothed and scaled regularised Fischer-Burmeister NCP function f_{FB}^{IV} as contour plots for different values of the scaling parameter α. Here, the perturbation parameter $\delta = 0.01$ has been chosen for illustration purposes. Reprinted from Bartel et al., Arch. Appl. Mech. 89 (2019), 995-1010, [6], with permission from Springer Nature.

2.3.3.2 Comparison of different approaches at $t = t_{II} = 1.1\,\mathrm{s}$

The results shown in Figure 2.14 refer to the chosen value of $\delta = 10^{-6}$ for the perturbation parameter and the time step $t = t_{II} = 1.1\,\mathrm{s}$. The prescribed time increment is $\Delta t = 0.02\,\mathrm{s}$ and, as an alternative, $\Delta t = 0.002\,\mathrm{s}$ so that t_{II} is reached in load step 55 and load step 550, respectively. In this time step, the algorithms based on both f_{FB}^{II} and f_{FB}^{III} with a dominating stabilisation term, i.e. $\lambda = 0.1$, show significant numerical instabilities for $\Delta t = 0.02\,\mathrm{s}$. In contrast to the example above, the worst convergence behaviour is in the case obtained with the NCP function f_{FB}^{III}, where changes with respect to the active set occur due to the jumps in the value of the residual. For smaller time increments of $\Delta t = 0.002\,\mathrm{s}$, the convergence behaviour of the different approaches become more similar.

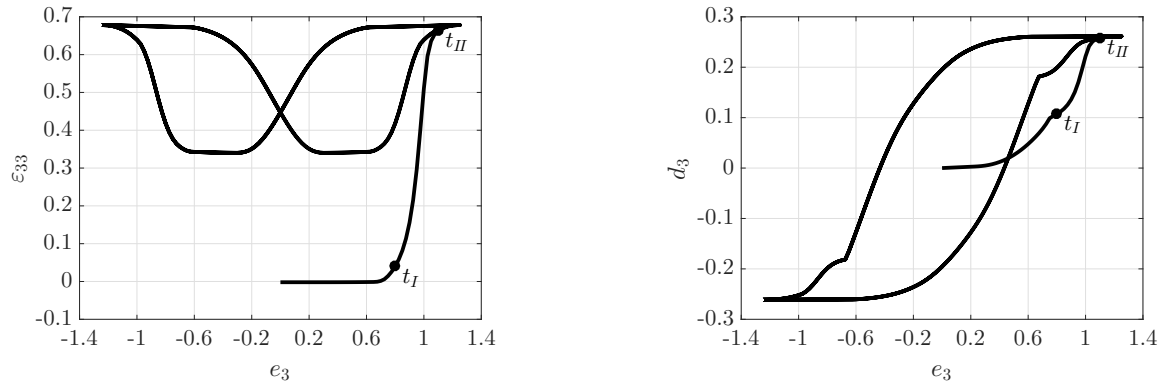

Figure 2.10: Material response predicted by the underlying constitutive framework according to [17] in terms of $\varepsilon_{33}(e_3)$ (left) and $d_3(e_3)$ (right). The labels t_I and t_{II} indicate two representative time steps used for the subsequent convergence studies. Reprinted from Bartel et al., Arch. Appl. Mech. 89 (2019), 995-1010, [6], with permission from Springer Nature.

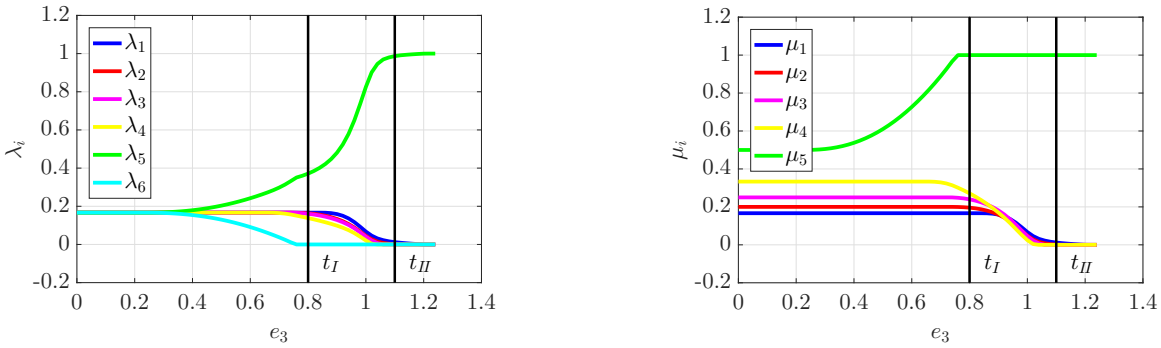

Figure 2.11: Material response predicted by the underlying constitutive framework according to [17] in terms of $\lambda_i(e_3)$ (left) and $\mu^j(e_3)$ (right) for monotonic loading. The labels t_I and t_{II} indicate two representative time steps used for the subsequent convergence studies. Reprinted from Bartel et al., Arch. Appl. Mech. 89 (2019), 995-1010, [6], with permission from Springer Nature.

Even more significant discrepancies between the different approaches can be obtained by setting the perturbation parameter to $\delta = 10^{-4}$. As illustrated in Figure 2.15, two algorithms even diverge and do not provide a proper solution for the specified time step $t = t_{II} = 1.1\,\mathrm{s}$ with $\Delta t = 0.02\,\mathrm{s}$. Interestingly, the two algorithms which exhibit the worst convergence behaviour in the above examples, namely f_{FB}^{II} and f_{FB}^{III} with dominant stabilisation terms, i.e. $\lambda = 0.1$, perform rather well in this example. In contrast, the smoothed Fischer-Burmeister approach f_{FB}^{I} as well as f_{FB}^{III} with $\lambda = 0.9$ oscillate and do not converge. This is rather unexpected due to the fact that these two algorithms performed best in the above examples. The algorithm based on the NCP function f_{FB}^{II} with $\lambda = 0.9$ also shows oscillations at the very beginning of the iteration process but then first slightly deviates from the, say, failing algorithms based on f_{FB}^{I} as well as f_{FB}^{III} and finally results in a proper solution. It is, however, noteworthy that all algorithms

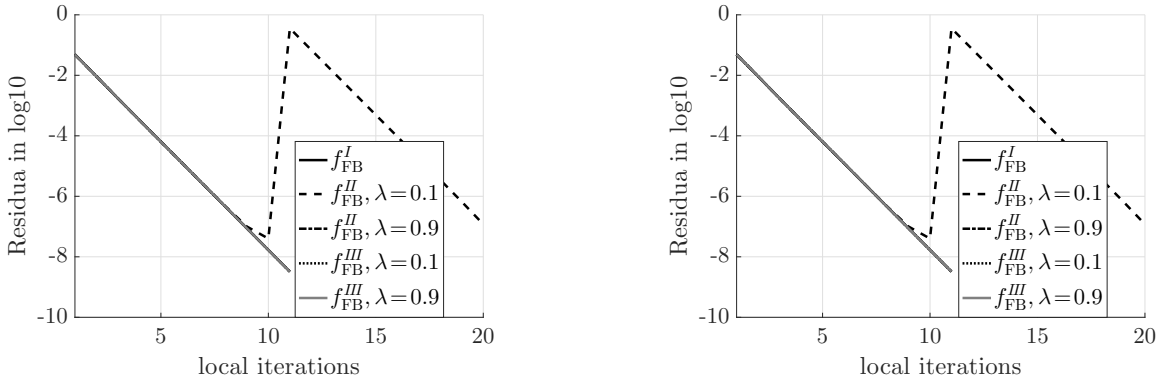

Figure 2.12: Evolution of the residua of the different FB functions plotted over the number of local iterations at $t = t_I = 0.8\,\mathrm{s}$ with $\Delta t = 0.02\,\mathrm{s}$ and $\delta = 10^{-12}$ (left) and $\delta = 10^{-8}$ (right). Reprinted from Bartel et al., Arch. Appl. Mech. 89 (2019), 995-1010, [6], with permission from Springer Nature.

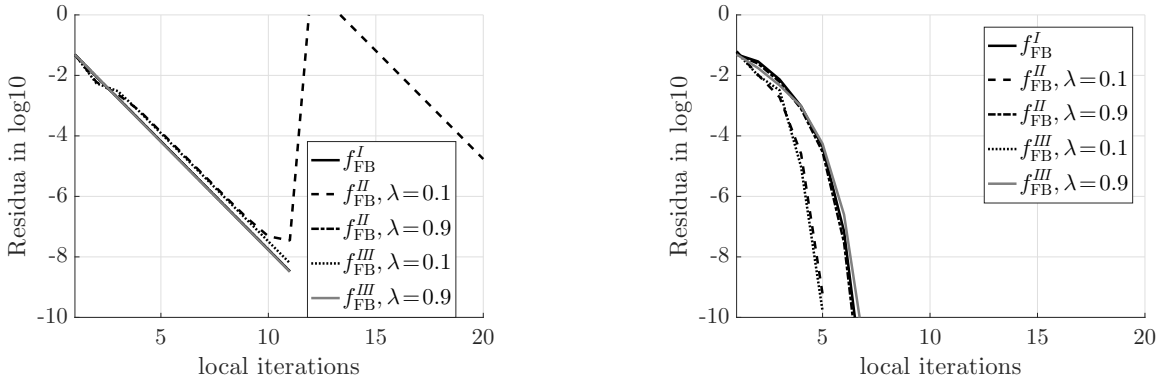

Figure 2.13: Evolution of the residua of the different FB functions plotted over the number of local iterations at $t = t_I = 0.8\,\mathrm{s}$ with $\Delta t = 0.02\,\mathrm{s}$ and $\delta = 10^{-6}$ (left) and $\delta = 10^{-2}$ (right). Reprinted from Bartel et al., Arch. Appl. Mech. 89 (2019), 995-1010, [6], with permission from Springer Nature.

except the one based on f_{FB}^{II} with $\lambda = 0.1$ will diverge in this or a subsequent time step so that the results shown in Figure 2.10 and 2.11 cannot be obtained. Smaller values of the time increment such as $\Delta t = 0.002\,\mathrm{s}$ provide similar results for all analysed schemes. The rather large value of $\delta = 10^{-4}$ results in, e.g., $\lambda_5 = 1.001$ which might be considered inaccurate. Even higher values of δ such as 10^{-2} further increase the stability of the respective algorithm but definitely violate the underlying constraints in an unacceptable manner, cf. Figure 2.16.

2.3.3.3 Analyses with respect to f_{FB}^{IV} and f_{FB}^{V}

In this section, the focus is placed on the performances of the algorithms based on the NCP functions f_{FB}^{IV} and f_{FB}^{V}. According to our investigations, those algorithms always behave similarly to the algorithm using f_{FB}^{I} in the context of the present constitutive

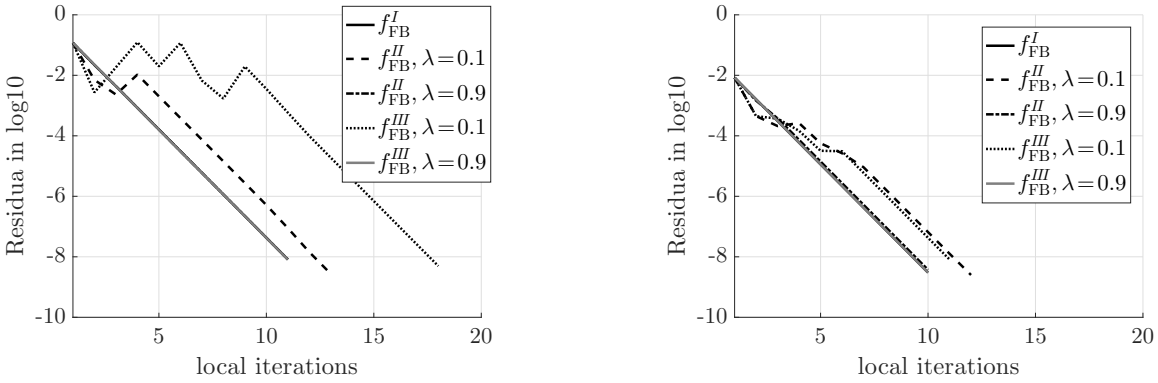

Figure 2.14: Evolution of the residua of the different FB functions plotted over the number of local iterations at $t = t_{II} = 1.1\,\mathrm{s}$ for $\delta = 10^{-6}$ with $\Delta t = 0.02\,\mathrm{s}$ (left) and $\Delta t = 0.002\,\mathrm{s}$ (right). Reprinted from Bartel et al., Arch. Appl. Mech. 89 (2019), 995-1010, [6], with permission from Springer Nature.

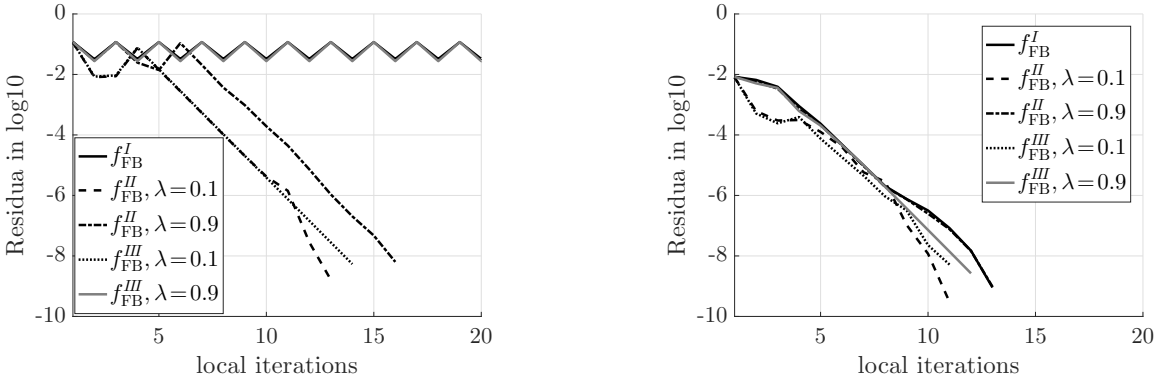

Figure 2.15: Evolution of the residua of the different FB functions plotted over the number of local iterations at $t = t_{II} = 1.1\,\mathrm{s}$ for $\delta = 10^{-4}$ with $\Delta t = 0.02\,\mathrm{s}$ (left) and $\Delta t = 0.002\,\mathrm{s}$ (right). Reprinted from Bartel et al., Arch. Appl. Mech. 89 (2019), 995-1010, [6], with permission from Springer Nature.

framework independent of the precise values of α, cf. Figure 2.17. This also holds for examples where f^I_{FB} turns out to yield inaccurate results or even diverging iterations.

2.3.4 Summary

In this section, the numerical stability and efficiency of five different modified Fischer-Burmeister NCP functions is investigated. For this purpose, these are applied to the laminate-based material model for ferroelectrics taken from [17] which is also summarised in Section 2.3.1.

The analysis of the convergence behaviour of the different approaches based on a Newton-Raphson scheme reveals that unambiguous comparative statements regarding the effectiveness and efficiency of the respective algorithms are hardly possible. For rather small time increments, all applied schemes perform similarly and lead to robust

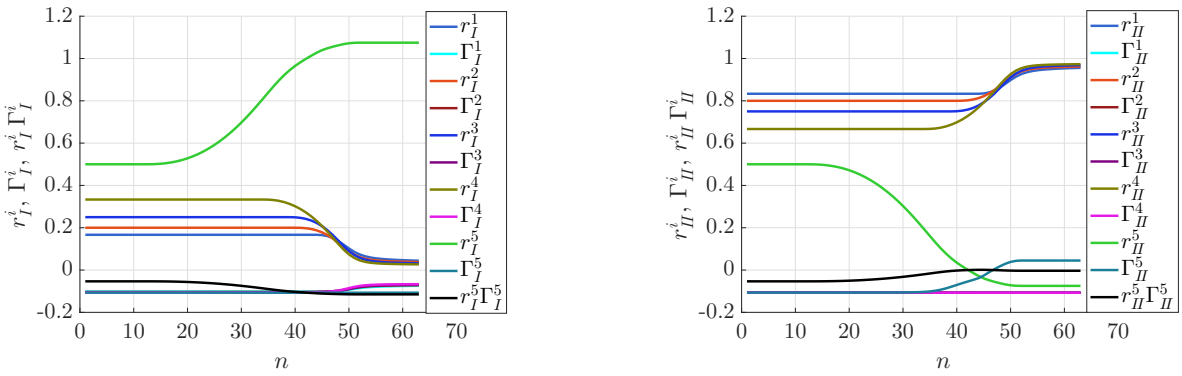

Figure 2.16: First (left) and second (right) set of constraints and corresponding Lagrange multipliers plotted over the number of global iterations at $t = t_{II} = 1.1\,\mathrm{s}$, while using the f_{FB}^{III} function with $\delta = 10^{-2}$, $\lambda = 0.1$ and $\Delta t = 0.02\,\mathrm{s}$. Reprinted from Bartel et al., Arch. Appl. Mech. 89 (2019), 995-1010, [6], with permission from Springer Nature.

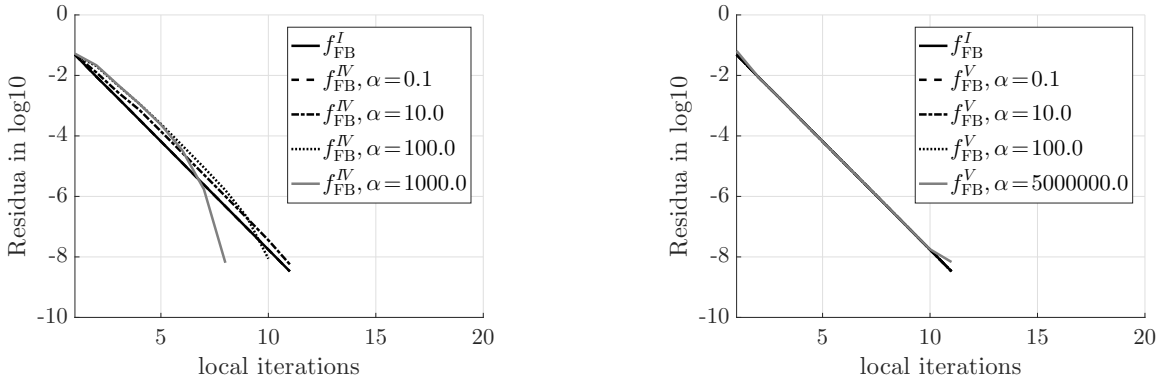

Figure 2.17: Convergence study of the impact of the scaling parameter α on the residua of the NCP functions f_{FB}^{IV} (left) and f_{FB}^{V} (right) at $t = t_I = 0.8\,\mathrm{s}$, with $\Delta t = 0.02\,\mathrm{s}$ and $\delta = 10^{-6}$. Reprinted from Bartel et al., Arch. Appl. Mech. 89 (2019), 995-1010, [6], with permission from Springer Nature.

algorithms which allow the simulation of cyclic loading paths. However, smaller time increments result in higher computational costs which necessitates approaches with improved efficiency. When using larger time increments one needs to carefully adjust the underlying parameters such as the weighting factor λ and the perturbation parameter δ. Concerning the latter, higher values for δ may result in stable Newton schemes, however, not necessarily. Moreover, higher values of δ result in more significant violations of the underlying constraints. In this regard, one should rather use small values for the perturbation parameter δ, even $\delta = 10^{-12}$ worked out well according to our investigations. In addition, the scaling parameter λ should be chosen to be large enough so that the stabilising term does not dominate the actual Fischer-Burmeister NCP function. It is noteworthy, though, that for sufficiently small values of δ and sufficiently large values of λ the penalised Fischer-Burmeister function f_{FB}^{II} and its modified version f_{FB}^{III} as well as

f_{FB}^{IV} and f_{FB}^{V} could not be shown to perform significantly better than the straight-forward smoothed Fischer-Burmeister function f_{FB}^{I}. In future work it could be of interest to further enhance the algorithms by introducing non-constant parameters δ, λ, and α similar to updated Lagrange multiplier approaches.

2.4 Classic non-linear optimisation algorithms

In this section, a brief introduction and summary to the huge field of optimisation problems is given following the works of Alt [2], Geiger and Kanzow [24], Luenberger and Ye [70], Mahnken [72], Nocedal and Wright [85]. More detailed information can be taken from these sources, the master thesis of [112], the PhD theses of Kleuter [52], Rose [96], Scheday [101] or the habilitation thesis of Mahnken [74].

Optimisation problems occur in various application fields. In the field of material modelling, parameter identification is generally known as the optimal fitting of the parameters of an underlying material model with regard to experimental data under consideration of necessary physical or mathematical constraints. In the perfect case, the material parameters can be directly identified based on specific experiments where the parameters impact the material behaviour uncoupled from each other, e.g. the Young's modulus E and the Poisson's ratio ν in a one-dimensional tension test within the elastic region. Unfortunately, this is generally not possible for many material models depicting a non-linear, inelastic, anisotropic or coupled—e.g. a thermo-mechanical model—material behaviour. Nevertheless, it is possible in many cases to identify a certain subset of the parameters based on some specific experiments which improves the overall efficiency and performance of the optimisation process.

Furthermore, it is very important to be aware of the following possible sources of non-conformances to be able to analyse the deviations between the measured and predicted material behaviour, even if the "optimal" parameter set is used:

- Modelling errors: The complex real material behaviour cannot be captured completely by developed material models and consequently the parameter identification is always restricted to the precision of the applied material model.

- Measuring errors: Since specimens are not completely identical and because even standardised experiments, e.g. following ISO-standard, cannot eliminate measuring errors, several experiments have to be performed under the same conditions and statistically evaluated to achieve reliable experimental data.

- Simulation errors: Numerical errors occur during the optimisation process as well as during the simulations with the developed material model and thus have to be taken into account.

In the end, simulations are performed in order to predict the real material behaviour based on a given material model, the corresponding parameters, loading history and

its initial conditions. This is denoted as the direct problem. However, to identify the optimal set of material parameters for a specific material, the inverse or indirect problem has to be solved. For this purpose, the simulated material response is compared to the experimentally measured response for a given material model, loading history and initial conditions. Since the amount of experimental material data is generally larger than the total set of model parameters, the inverse problem is over-determined and thus a unique solution is usually not achievable. Nevertheless, the optimal parameter set can be obtained by employing a least-square minimisation. The inverse problem can be formulated as

$$f(\boldsymbol{\kappa}) := \frac{1}{2}\left\|\boldsymbol{w} \cdot [\mathcal{M}\,\boldsymbol{f}(\boldsymbol{\kappa}) - \boldsymbol{f}^{\exp}]\right\|^2 \rightarrow \min_{\forall \boldsymbol{\kappa} \in \mathcal{K}}, \tag{2.83}$$

where $\boldsymbol{w}$ is a set of weighting factors which can be used to increase or decrease, respectively, the impact of specific data points on the optimisation, e.g. if the experimental data is not equally reliable over the whole range or if the simulated response has to be more accurate at certain points. Since usually the simulated and experimentally measured data points do not coincide, $\mathcal{M}$ symbolises an abstract projection operator which is in the simplest case a linear interpolation in order to compare both sets. Furthermore, $\boldsymbol{f}(\boldsymbol{\kappa})$ denotes the simulated force vector with the current parameter set $\boldsymbol{\kappa}$ which is compared to the experimentally measured force vector $\boldsymbol{f}^{\exp}$ if the displacements are prescribed. In the case of a homogeneous deformation where only scalar information is taken into account, the force vector contains the integral force at discrete time steps of the loading path. The whole set of admissible material parameters $\mathcal{K}$ is defined as

$$\mathcal{K} = \{\boldsymbol{\kappa} \,|\, \boldsymbol{h}(\boldsymbol{\kappa}) = \boldsymbol{0},\, \boldsymbol{g}(\boldsymbol{\kappa}) \leq \boldsymbol{0}\}\ , \tag{2.84}$$

with $\boldsymbol{h}(\boldsymbol{\kappa})$ and $\boldsymbol{g}(\boldsymbol{\kappa})$ being the sets of equality and inequality constraints, respectively. These constraints are necessary for many parameters, e.g. even for the two most known parameters of an isotropic, linear-elastic material model, the Young's modulus $E > 0$ and the Poisson's ratio $-1 \leq \nu \leq 1/2$.

In all scientific and engineering fields optimisation is one of the basic tasks. Following Nocedal and Wright [85], optimisation problems can be categorised based on the characteristic of the objective function and its corresponding constraints—e.g. linear, non-linear, convex—on the amount of variables or many other categories. One of the basic distinctions is between zero-order methods where only the objective function evaluations are taken into account and between first-order methods where, additionally to the function evaluations itself, their corresponding gradients are required. The different algorithms are otherwise also classified into being either deterministic or stochastic. The most known example of the latter group is the Monte-Carlo method. Algorithms of this group choose the parameter set of the next iteration step purely random-based without any consideration of the achieved information of previous steps. These algorithms are very simple to implement but computationally also very inefficient. The efficiency of

a purely stochastic method can be improved by employing an evolution-strategy based algorithm. In contrast, the deterministic algorithms are generally more efficient. Common examples are the gradient-based Gauss-Newton and the gradient-free Nelder-Mead simplex method. In the literature, the algorithms are mainly classified into constrained and unconstrained methods.

2.4.1 Unconstrained optimisation algorithms

In the case of *unconstrained optimisation algorithms*, even if some variables may possess a form of natural constraint, the constraints do not affect the solution at all. Nevertheless, unconstrained algorithms can consider bounds of the parameters if a penalty method is incorporated in the implementation.

Gradient-based optimisation algorithms are very efficient since the information of the gradient is considered in the objective function as well. In this group of algorithms, the parameter set of the next iteration $\boldsymbol{\kappa}_{i+1}$ is calculated based on the previous set $\boldsymbol{\kappa}_i$ and a specific search direction $\boldsymbol{s}_i$ which incorporates the information of the gradient, i.e.

$$\boldsymbol{\kappa}_{i+1} = \boldsymbol{\kappa}_i + \alpha_i \, \boldsymbol{s}_i \,, \tag{2.85}$$

where α_i is denoted as the step size parameter. While the step size parameter has to fulfil $\alpha_i > 0$, the following condition for the search direction has to be ensured

$$\nabla^{\mathrm{t}}_{\boldsymbol{\kappa}} f(\boldsymbol{\kappa}_i) \cdot \boldsymbol{s}_i(\boldsymbol{\kappa}_i) < 0 \,. \tag{2.86}$$

Furthermore, the following one-dimensional minimisation problem

$$f(\boldsymbol{\kappa}_{i+1}(\alpha_i)) = f(\boldsymbol{\kappa}_i + \alpha_i \, \boldsymbol{s}_i) \rightarrow \min \tag{2.87}$$

can be used to calculate the step size parameter α_i and the optimal step size can be determined by the roots of the necessary condition

$$\mathrm{d}_{\alpha_i} f(\alpha_i) = 0 \,, \tag{2.88}$$

which can be solved in closed form for some special cases or numerically by using regula falsi or the Newton-Raphsom scheme. Considering the definition of the search direction, many different approaches have been developed. A straightforward approach is the method of steepest decent, where the search direction is defined as $\boldsymbol{s}_i := -\nabla_{\boldsymbol{\kappa}} f(\boldsymbol{\kappa}_i)$ such that it is tangential to the corresponding isoline. Another possibility is the conjugate-gradient method which is very convenient for large non-linear optimisation problems since the Hessian matrix $\boldsymbol{H}(\boldsymbol{\kappa}_i) := \nabla^2_{\boldsymbol{\kappa}\boldsymbol{\kappa}} f(\boldsymbol{\kappa}_i)$ is not required, the step computation is not based on matrix operations and it does not require a large vector storage. In contrast, the Newton-Raphson method—with a search direction of $\boldsymbol{s}_i = -\boldsymbol{H}^{-1}(\boldsymbol{\kappa}_i) \cdot \nabla_{\boldsymbol{\kappa}} f(\boldsymbol{\kappa}_i)$—enables a quadratic convergence. However, a locally positive definite Hessian matrix

is required and its inversion is computationally rather expensive. The computational cost can be reduced by employing Quasi-Newton methods where the inverse Hession is replaced by different updating relations, e.g. Davidson, Fletcher and Powell (DFP) or the Broyden-Fletcher-Goldfarb-Shanno (BFGS) method.

Since the derivation of the gradient of the objective function is not always straightforward and can imply a high effort, it can be overall more efficient to employ simpler but numerically less efficient algorithms, or some libraries in e.g. *Python* provide the opportunity to determine the gradient numerically. While the latter option might be helpful, it can be even more efficient to use gradient-free strategies. Thus, a zero-order method, the Nelder-Mead simplex algorithm is employed in this work for many application cases since it is provided in several optimisation packages, e.g. the *scipy* optimisation package in Python, and is a simple, robust, reliable and quite efficient algorithm. The method was developed by Nelder and Mead [84] and is only briefly summarised here. If an objective function contains n different parameters, the method spans a simplex with $n+1$ corner points, denoted as $P_0, P_1, \ldots, P_n$. The final simplex, containing the final minimum, is obtained once the vertex with the highest function value $P_{\max}$ was replaced with a new point within each iteration until a specified tolerance is reached. For this purpose, the method comprises three main operations—reflection, expansion and contraction—to replace the vertex with the highest function value such that the simplex is shrunken to the final simplex where $\sqrt{\sum_i [y_i - y_c]^2/n}$ is below the user-defined tolerance. Here, y_i denotes the function value of the corner points P_i and y_c denotes the function value of the centroid of the simplex P_c. The operations of this method are schematically visualised in Figure 2.18. In each iteration, at first a reflection is performed for $P_{\max}$ such that the reflected point $P^\star$ is obtained via

$$P^\star = [1+\alpha]\, P_c - \alpha\, P_{\max}\,, \tag{2.89}$$

where α denotes the reflection coefficient, which is defined positive. Thus, the reflected point is on the line intersecting P_c and $P_{\max}$ and placed opposing to $P_{\max}$. Quantity $y^\star$ is the corresponding function value of $P^\star$. If $y^\star \in (y_{\min}, y_{\max})$, the vertex $P_{\max}$ is replaced by the reflected point $P^\star$ and the optimisation process continues with the new simplex. However, if $y^\star \leq y_{\min}$, a new minimum is found and the expansion operation is performed to expand the simplex further in the new minimum direction. The expanded point $P^{\star\star}$ is achieved by

$$P^{\star\star} = \gamma\, P^\star + [1-\gamma]\, P_c\,, \tag{2.90}$$

where $\gamma > 1$ is used as expansion coefficient. If the function value $y^{\star\star}$ of $P^{\star\star}$ is lower than the previous function minimum of the simplex, $P_{\max}$ is replaced with the expanded point $P^{\star\star}$. However, if $y^{\star\star} > y_{\min}$, $P_{\max}$ is only replaced by the reflected point $P^\star$ and the optimisation process continues with the new simplex. Nevertheless, if $y^\star$ is still higher than any other function value of the other vertices, the contraction operation has to be

performed. If in addition $y^\star < y_{\max}$, the reflected point $P^\star$ is set as $P_{\max}$. The contracted point is defined as

$$P^{\star\star} = \beta\, P_{\max} + [1-\beta]\, P_{\mathrm{c}}\,, \tag{2.91}$$

with $\beta \in (0,1)$ denoting the contraction coefficient, which controls the magnitude of the contraction, such as α and γ for the other operations. However, if $y^{\star\star}$ is still higher than $y_{\max}$ and $y^\star$, i.e. the contraction was not successful, each of the vertices P_i has to be reduced to $[P_i + P_{\min}]/2$ in order to shrink the overall simplex.

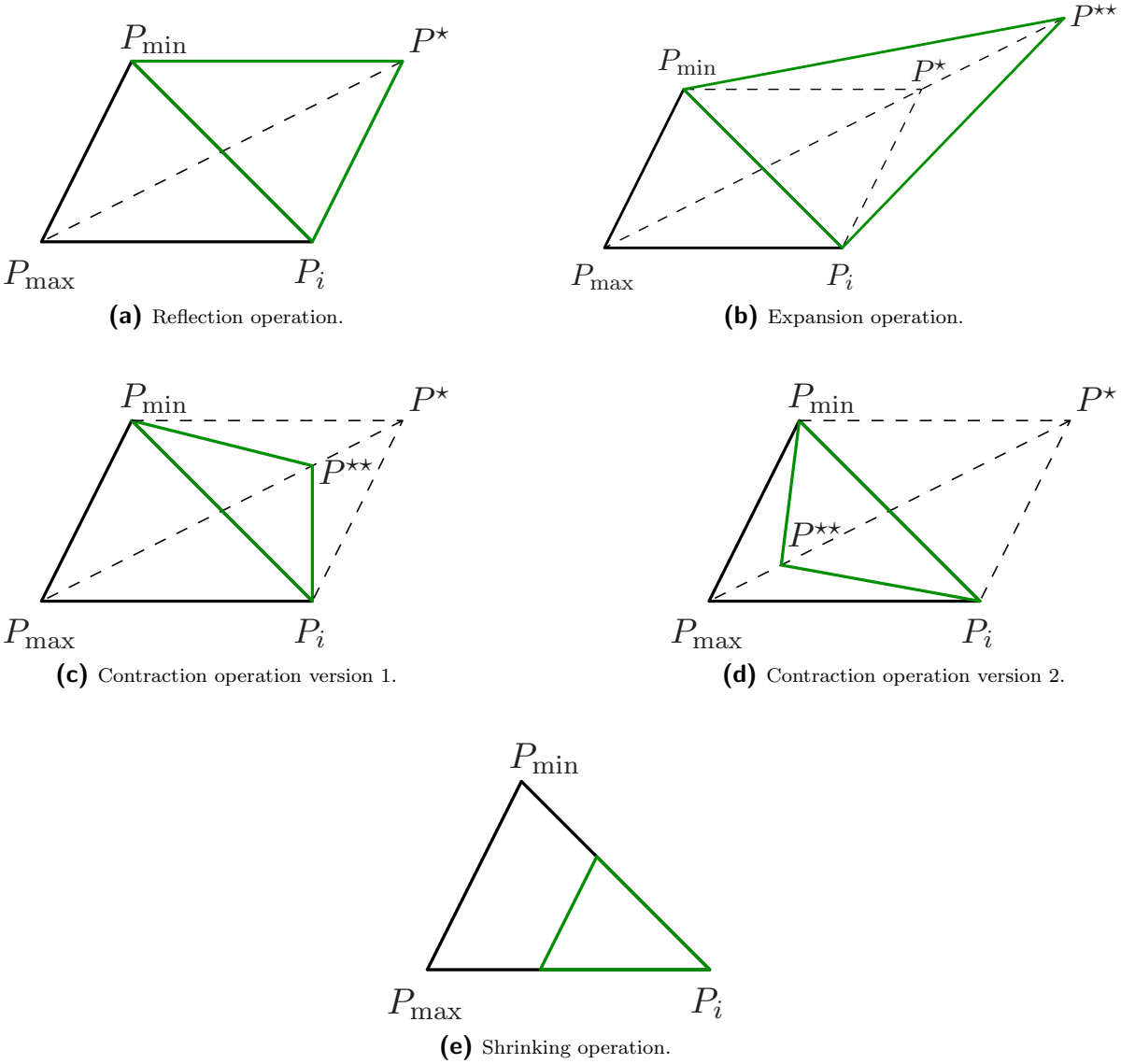

(a) Reflection operation.

(b) Expansion operation.

(c) Contraction operation version 1.

(d) Contraction operation version 2.

(e) Shrinking operation.

Figure 2.18: Schematic visualisation of the different Nelder-Mead simplex operations following [84].

A well laid out flowchart and more detailed information is given in [84].

Alternatively, even though a stochastic method causes a high computational effort, it can be employed for the inverse problem since it is a rather simple and robust strategy which can overcome local minima based on the random selection in each iteration. However, as already mentioned before, the efficiency can be improved by using evolution strategy-based algorithms which adopt the biological evolution process and which are driven by the principles of mutation and selection. At the beginning, a set of start vectors is selected, defined as parent generation, and subsequently, following a random number generation providing a Gaussian distribution around the parent generation, a corresponding number of offspring vectors is generated. This symbolises the principle of mutation in evolution processes. In the subsequent selection step, a set of different parameter combinations providing the lowest objective function values is selected as the parent generation of the next iteration step following the principle of survival of the fittest. Since the standard, single-branch algorithm, where only one parameter set is chosen for the parent generation, is not very efficient, a multi-branch evolution strategy-based algorithm can improve the overall efficiency where many different sets are selected simultaneously.

The two latter mentioned algorithms are implemented in the optimisation tool—developed in [104]—applied within this work and summarised in Section 4.1.

2.4.2 Constrained optimisation algorithms

In the case of *constrained optimisation algorithms*, constraints of the parameters are crucial with regard to the solution of the objective function. The corresponding constraints can be either simple bounds of the parameter, e.g. for the Poisson's ratio $-1 \leq \nu \leq 1/2$, a common linear constraint, for example if the sum of the parameters should be less equal 1, or even non-linear inequality constraints. Following this the optimisation problem takes the form

$$f(\boldsymbol{\kappa}) \rightarrow \min\,, \quad \text{s.t.} \quad \boldsymbol{h}(\boldsymbol{\kappa}) = \boldsymbol{0} \quad \text{and} \quad \boldsymbol{g}(\boldsymbol{\kappa}) \leq \boldsymbol{0}\,, \tag{2.92}$$

where $\boldsymbol{h}(\boldsymbol{\kappa})$ and $\boldsymbol{g}(\boldsymbol{\kappa})$ denote the sets of equality and inequality constraints, respectively. However, the solutions to this problem can be found by reformulating the optimisation problem into the Lagrange functional

$$\mathcal{L}(\boldsymbol{\kappa}, \boldsymbol{\mu}, \boldsymbol{\lambda}) := f(\boldsymbol{\kappa}) + \boldsymbol{\mu}^{\mathrm{t}}\, \boldsymbol{h}(\boldsymbol{\kappa}) + \boldsymbol{\lambda}^{\mathrm{t}}\, \boldsymbol{g}(\boldsymbol{\kappa}) \rightarrow \mathrm{stat}\,, \tag{2.93}$$

which is required to be stationary and where $\boldsymbol{\mu} := [\mu_1, \ldots, \mu_{n_h}]^t$ and $\boldsymbol{\lambda} := [\lambda_1, \ldots, \lambda_{n_g}]^{\mathrm{t}}$ are denoting the vectors of the corresponding Lagrange multipliers. Integers n_h and n_g are the numbers of equality and inequality constraints, respectively. If the following Karush-Kuhn-Tucker (KKT) conditions are satisfied, the necessary stationary require-

ment of the Lagrange functional is fulfilled and a local constrained minimum exists so that

$$\begin{aligned} \nabla_{\boldsymbol{\kappa}} \mathcal{L}(\boldsymbol{\kappa}^\star, \boldsymbol{\mu}^\star, \boldsymbol{\lambda}^\star) = \nabla_{\boldsymbol{\kappa}} f(\boldsymbol{\kappa}^\star) + \nabla_{\boldsymbol{\kappa}} \boldsymbol{h}(\boldsymbol{\kappa}^\star) \cdot \boldsymbol{\mu}^\star + \nabla_{\boldsymbol{\kappa}} \boldsymbol{g}(\boldsymbol{\kappa}^\star) \cdot \boldsymbol{\lambda}^\star &\stackrel{!}{=} \mathbf{0}\,, \\ \nabla_{\boldsymbol{\mu}} \mathcal{L}(\boldsymbol{\kappa}^\star) = \boldsymbol{h}(\boldsymbol{\kappa}^\star) &= \mathbf{0}\,, \\ \nabla_{\boldsymbol{\lambda}} \mathcal{L}(\boldsymbol{\kappa}^\star) = \boldsymbol{g}(\boldsymbol{\kappa}^\star) &\leq \mathbf{0}\,, \\ \boldsymbol{\lambda}^\star &\geq \mathbf{0}\,, \\ \boldsymbol{\lambda}^\star \cdot \boldsymbol{g}(\boldsymbol{\kappa}^\star) &= 0\,, \end{aligned} \tag{2.94}$$

where i and j are the running indices of the equality and inequality constraints. Furthermore, it is essential that the evaluation of the Hessian of the Lagrange function at the optimal point has to be positive definite. If this is applied to convex problems, it provides the advantage that these KKT conditions are already the sufficient conditions for a global minimum. The solution of the KKT conditions can be obtained by employing different kinds of algorithms, e.g. the active-set strategy, penalty method, complementarity function approaches by Fischer-Burmeister, see Section 2.3.2, or staggered solution schemes. Three of the algorithms are presented and applied in Kiefer et al. [51].

2.5 Parameter identification for homogeneous states of deformation using classic optimisation methods

In this section, several parameter identification procedures are performed considering homogeneous states of deformation. Thus, only specific loading path sequences of characteristic standard experimental tests, e.g. the forces during a loading phase of a tensile test, are taken into account for the error functional of the inverse identification. In the following, the three previously introduced material models are calibrated with respect to selected materials by using classic parameter identification methods. While for the first two application cases a Nelder-Mead simplex algorithm was chosen, a constrained Sequential Quadratic Programming (SQP) method was employed for the last application example.

2.5.1 Finite plasticity model coupled to damage

The first application example is the gradient-enhanced damage model coupled to finite plasticity presented in Section 2.1. However, since only homogeneous states of deformation are considered in this chapter, the parameters associated with the local parts of the model cannot be identified and are deactivated by setting and fixing the penalty parameter β_{d} at a value of 0.0, see Tables 2.2–2.4. Thus, the local damage variable d_ϕ

is no longer related to the global damage variable ϕ. The employed experiments are presented in Section 3.1.1.

Table 2.2: Finally identified parameter sets for the sheet metal DP800 and the case-hardened steel 16MnCrS5 based on the first initial parameter set 1. The fixed parameters are not calibrated within this section.

Symbol	Description	Initial guess 1	DP800	16MnCrS5	Unit
f	objective function value	100	44.81	7.62	%
E	Young's modulus	23	23	36.106	GPa
ν	Poisson's ratio	0.035	0.035	$1.81 \cdot 10^{-5}$	–
σ_{y0}	initial yield stress	99.99	102.49	174.46	MPa
h	hardening parameter	499.94	512.434	463.361	MPa
n_p	hardening exponent	0.1	0.1	0.1	–
q_var	variable damage threshold	5	5	8.213	MPa
n_d	damage exponent		fixed at 0.667		–
η	damage rate factor	1	1	1.101	–
ξ_vol	volumetric damage factor		fixed at 1.0		–
ξ_iso	isochoric damage factor	0.3	0.3	0.264	–
ξ_q	threshold factor	2	2	1.581	–
ξ_m	effective stress factor	0.15	0.15	0.184	–
η_α	coupling factor	1	1	0.15	–
c_d	regularisation parameter		fixed at 0.54		N
β_d	penalty parameter		fixed at 0.0		MPa
q_min	initial damage threshold	4.999	4.999	2.081	MPa

For this application, the Nelder-Mead simplex algorithm turned out to be a proper choice. Since the simplex algorithm tends to get stuck in local minima, several parameter identification procedures with different starting sets had to be performed to find the best local minimum. For this purpose, three different starting values for the parameters were chosen as shown in Tables 2.2–2.4. The different sets were selected based on the parameter ranges mentioned in Section 2.1.2 in order to have one set located at the lower bounds of the parameters, one located in the middle and another one located at the upper bounds. Nevertheless, not all of the parameters could be changed with regard to this scheme since the underlying material model is quite sensitive with respect to some material parameter combinations. This demonstrates the difficulty of finding manually appropriate starting values especially if the user is not familiar with the model and the parameter influences. To emphasise this issue some of the parameters are fixed for simplicity reasons since it would be too time consuming for the user while finding parameter sets related to successful simulations close to the chosen direction.

Table 2.3: Finally identified parameter sets for the sheet metal DP800 and the case-hardened steel 16MnCrS5 based on the first initial parameter set 2. The fixed parameters are not calibrated within this section.

Symbol	Description	Initial guess 2	DP800	16MnCrS5	Unit
f	objective function value	36.96	1.13	1.24	%
E	Young's modulus	114.998	182.348	131.317	GPa
ν	Poisson's ratio	0.175	0.162	0.217	–
σ_{y_0}	initial yield stress	99.99	106.159	11.39	MPa
h	hardening parameter	499.94	1243.474	760.481	MPa
n_p	hardening exponent	0.1	0.157	0.163	–
q_var	variable damage threshold	25	0.005	19.763	MPa
n_d	damage exponent		fixed at 0.667		–
η	damage rate factor	5	3.918	6.143	–
ξ_vol	volumetric damage factor		fixed at 1.0		–
ξ_iso	isochoric damage factor	1.5	1.342	1.968	–
ξ_q	threshold factor	10	15.194	12.022	–
ξ_m	effective stress factor	0.75	0.528	$2.97 \cdot 10^{-7}$	–
η_α	coupling factor	4.998	0.404	3.001	–
c_d	regularisation parameter		fixed at 0.54		N
β_d	penalty parameter		fixed at 0.0		MPa
q_min	initial damage threshold	24.996	40.783	30.694	MPa

Analysing the results with the first initial guess with regard to the sheet metal DP800 in Table 2.2 and the Figures 2.19 and 2.20a, it can be concluded that the Nelder-Mead simplex algorithm gets stuck in a local minima quite close to the initial guess. The algorithm could not find a proper direction to further reduce the objective function value. The final objective function value and especially the comparison of the corresponding simulated and experimentally measured tensile curve demonstrate that this local minima is far away from an appropriate solution. In comparison, the second initial guess already provides an error function value lower than the obtained local minimum of the first calibration procedure. Furthermore, the found local minimum of the second identification process fits the experimentally measured tensile behaviour quite well with a deviation of only 1.13%, cf. Table 2.3. If the stress-strain curves in Figures 2.19 and 2.20b are taken into account, the very accurate match of the experimental data is visible, even though the stress-strain behaviour of the second initial guess was also not close to the realistic material behaviour, see Figure 2.20b. Starting with the third initial guess a local minimum with an objective function value of 1.2% is obtained which is very close to the final function value of the second calibration procedure. However, comparing all of the final parameter values, a huge deviation in most of the parameters can be observed, cf. Tables

2.3 and 2.4. In contrast, both of finally obtained stress-strain curves fit the experimentally measured curve very accurately, see Figures 2.19 and 2.20. A difference is mainly visible at the beginning of plastification. Considering that the last two local minima differ vastly in the obtained parameters but that both accurately fit the experimental data, it indicates that the material model is very complex and that the combination of the different material properties allows multiple parameter combinations to show a nearly equal material behaviour—at least with respect to a rather simple tensile test if all material parameters are simultaneously identified.

Table 2.4: Finally identified parameter sets for the sheet metal DP800 and the case-hardened steel 16MnCrS5 based on the first initial parameter set 3. The fixed parameters are not calibrated within this section.

Symbol	Description	Initial guess 3	DP800	16MnCrS5	Unit
f	objective function value	100	1.2	0.87	%
E	Young's modulus	206.999	226.05	132.959	GPa
ν	Poisson's ratio	0.315	0.277	0.296	–
σ_{y0}	initial yield stress	99.99	158.54	56.36	MPa
h	hardening parameter	499.94	1174.807	774.599	MPa
n_p	hardening exponent	0.1	0.159	0.217	–
q_var	variable damage threshold	44.999	39.645	47.463	MPa
n_d	damage exponent		fixed at 0.667		–
η	damage rate factor	9	7.564	9.863	–
ξ_vol	volumetric damage factor		fixed at 1.0		–
ξ_iso	isochoric damage factor	2.7	0.222	0.53	–
ξ_q	threshold factor	18	15.194	16.183	–
ξ_m	effective stress factor	1.35	$6.19 \cdot 10^{-5}$	1.319	–
η_α	coupling factor	8.997	2.03	7.978	–
c_d	regularisation parameter		fixed at 0.54		N
β_d	penalty parameter		fixed at 0.0		MPa
q_min	initial damage threshold	44.993	19.923	39.97	MPa

The chosen three initial guesses were also used in the next step for the calibration of the model with regard to the cased-hardened steel 16MnCrS5. As it can be seen in Tables 2.2-2.4, in summary all of the obtained local minima have a quite low objective function value which is quite reasonable since all of the initial guesses are already relatively close to the experimentally measured stress-strain curve, cf. Figure 2.22. While the first obtained local minimum exhibits the highest function value and the identified material parameters are very different to the other results, the other two objective function values are relatively close to each other. Furthermore, some of their material parameters are only slightly different, e.g. Young's modulus or the hardening parameter,

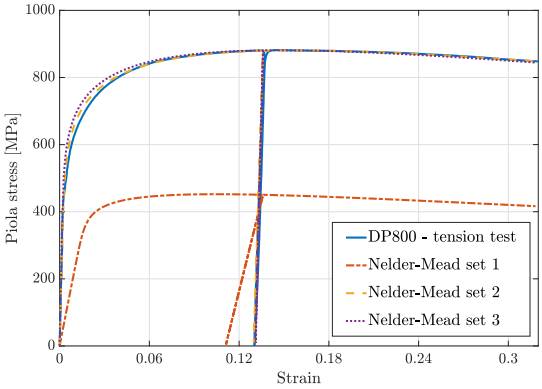

(a) Stress-strain curves of the tension test, with strain defined as $\varepsilon = \Delta l / l_0$.

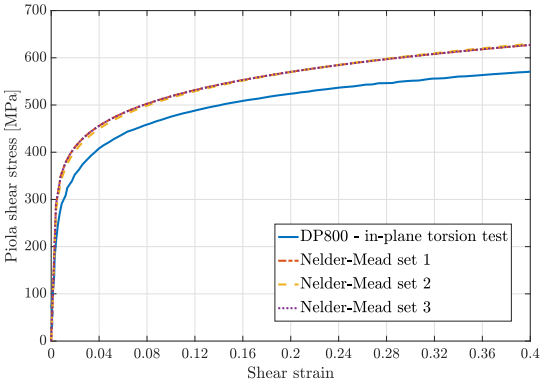

(b) Shear stress-shear strain curves of the in-plane torsion test, with the shear strain defined as the related shear component of the Green-Lagrange strain tensor $\boldsymbol{E} = \left[\boldsymbol{F}^{\mathrm{t}} \cdot \boldsymbol{F} - \boldsymbol{I}\right]/2$ with the factor two.

Figure 2.19: For the DP800 sheet metal, the simulation results with the optimal parameter sets, obtained from the parameter identification with the three different initial guesses, cf. Tables 2.2–2.4, are compared to the experimental curves. The calibration was based only on tensile data, i.e. only the displacements of the two loading phases and the forces of the unloading phase of the tensile test were considered within the objective function. The shear deformation was not included in the error functional and is used for validation purpose.

even though most of them still extremely differ. Comparing the stress-strain curves of the results, as expected, the first solution shows the least agreement with the experimental data while the other two solutions are quite accurate with regard to the tensile behaviour. However, the third solution suits the plastification and damage evolution more accurately, cf. Figures 2.21a and 2.22. The difference is clearly more recognisable in the validation with the compression test, see Figure 2.21b. While the simulation with the second local minimum is aborted, the simulation with the third identified parameter set finishes successfully. The visible decrease in the compressive stress of the last result is huge, and thus also the deviation from the experimentally measured curve. This is based on the tension-compression asymmetry which is not included in the underlying version of the material model. Finally, the third parameter identification provided the most accurate result regarding elasticity, plasticity and damage evolution, and the only deviations from the experimental data are due to the fact that the Lüders extension and the tension-compression asymmetry are not incorporated in the employed version of the material model.

In Section 3.1, an alternative approach to this parameter identification is presented in the form of a hybrid strategy. For this purpose, a neural network is trained with the material model in order to provide a good starting point for a subsequent multi-objective parameter identification, shown in Section 4.3.5. This strategy makes it possible to overcome the difficulty of finding appropriate initial guesses while additionally reducing

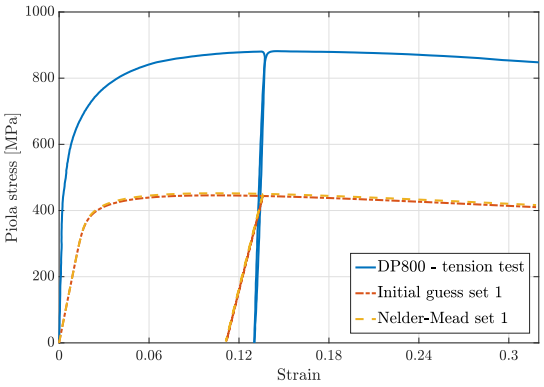

(a) Stress-strain curves of the tension test based on the first initial guess, with strain defined as $\varepsilon = \Delta l / l_0$.

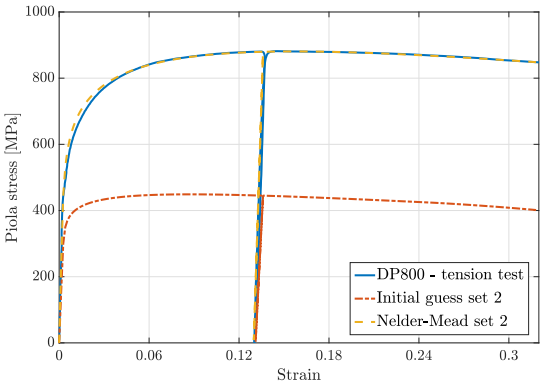

(b) Stress-strain curves of the tension test based on the second initial guess, with strain defined as $\varepsilon = \Delta l / l_0$.

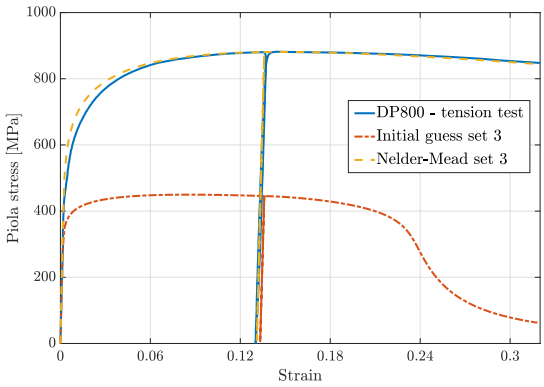

(c) Stress-strain curves of the tension test based on the third initial guess, with strain defined as $\varepsilon = \Delta l / l_0$.

Figure 2.20: For the DP800 sheet metal, the calibration performance based on the different initial parameter sets is visualised regarding the simulation results with the initial guess and the finally identified parameter sets. However, the initial guesses of set 1 and 3 result in incomplete simulations and only the 4th and 11th iteration, respectively, provided a parameter combination with a successful simulation. Thus, the simulation results of those sets are visualised in the figure instead of the corresponding initial guess.

the effort for the user. In addition, a classic multi-objective parameter identification using the optimisation tool *ADAPT*, see [104], is given in Section 4.3.4.

2.5.2 Finite-strain viscoelasticity model coupled to damage

For the next application example, the finite-strain viscoelasticity model coupled to damage, presented in Section 2.2, is calibrated to a special polymer—a self-diagnostic PDMS elastomer. In this case, once again the Nelder-Mead simplex algorithm is used for the identification of the material parameters. However, since the gradient-enhanced damage formulation is based on the same framework, in a first step, only the viscoelastic

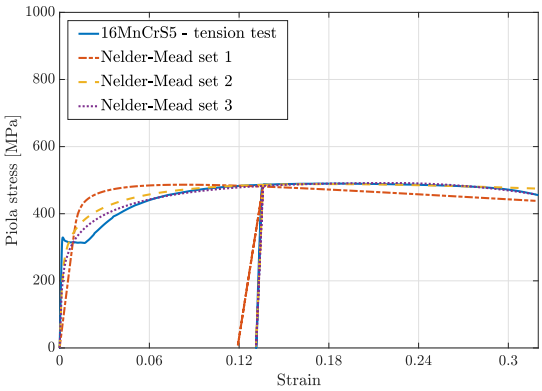

(a) Stress-strain curves of the tension test, with strain defined as $\varepsilon = \Delta l / l_0$.

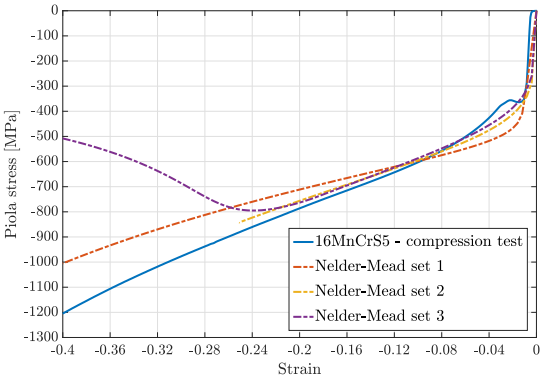

(b) Stress-strain curves of the compression test, with strain defined as $\varepsilon = \Delta l / l_0$.

Figure 2.21: For the 16MnCrS5 case-hardened steel, the simulation results with the optimal parameter sets, obtained from the parameter identification with the three different initial guesses, cf. Tables 2.2–2.4, are compared to the experimental curves. The calibration was based only on tensile data, i.e. only the displacements of the two loading phases and the forces of the unloading phase of the tensile test were considered within the objective function. The compression test was not included in the error functional and is used for validation purpose.

material parameters are identified with respect to three characteristic tests based on homogeneous deformation states. At first, the corresponding experiments are presented, followed by the description of the applied parameter identification strategy and the final results.

2.5.2.1 Homogeneous deformation tests

In the following, all accomplished types of experiments for the self-diagnostic PDMS elastomer are briefly presented in order to provide an overview of the experimental data required for the subsequent parameter identification of the implemented material model. For most of the experiments, a micro-testing machine by Kammrath & Weiss GmbH (Dortmund, Germany) was used; cf. Figure 2.23a. The machine can be combined with a CCD camera system from Chemnitzer Werkstoffmechanik GmbH (Chemnitz, Germany), which is of importance considering the need to track the displacement field for the inhomogeneous deformation tests in Section 4.2.1. The inhomogeneous deformation tests are required for the full parameter identification of the damage-related material parameters in Section 4.2.2. Figure 2.23b presents a screenshot of the software VEDDAC strain. The software was linked with the CCD camera and provided additional information on the displacement field during the experiment. The CCD camera additionally took a photo during each time step and delivered the changes in the displacement field directly to the DDS3 software of the testing machine. In the post-processing, the software VEDDAC could be used to extract all required displacement information from the photos taken during the experiment. Since the material was a transparent soft polymer, a stochastic

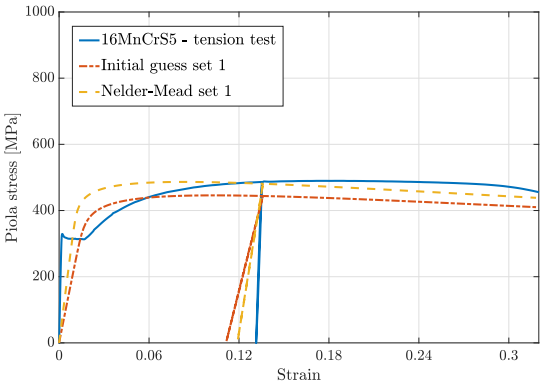

(a) Stress-strain curves of the tension test based on the first initial guess, with strain defined as $\varepsilon = \Delta l / l_0$.

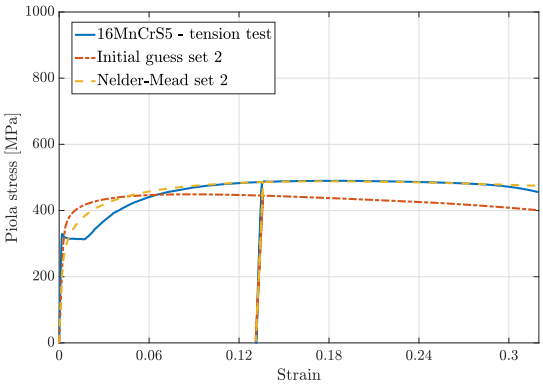

(b) Stress-strain curves of the tension test based on the second initial guess, with strain defined as $\varepsilon = \Delta l / l_0$.

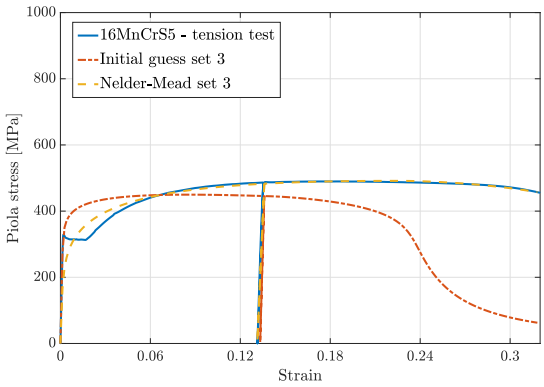

(c) Stress-strain curves of the tension test based on the third initial guess, with strain defined as $\varepsilon = \Delta l / l_0$.

Figure 2.22: For the 16MnCrS5 case-hardened steel, the calibration performance based on the different initial parameter sets is visualised regarding the simulation results with the initial guess and the finally identified parameter sets. However, the initial guesses of set 1 and 3 result in incomplete simulations and only the 4th and 11th iteration, respectively, provided a parameter combination with a successful simulation. Thus, the simulation results of those sets are visualised in the figure instead of the corresponding initial guess.

pattern was sprayed onto the specimens with graphite spray. Consequently, the software was able to track all specific positions of the specimen up to the end of the experiment. The following experiments were conducted with virgin material samples, thereby avoiding the influences of Mullin's effect or the strain history on the material response. The environmental conditions were room conditions, including room temperature. As a first step, experiments with homogeneous deformation states were conducted. In order to receive sufficient experimental data for the calibration of the viscoelastic material parameters, three different types of experiments were carried out. Apart from uni-axial tensile tests (cf. Figure 2.24), relaxation tests (see Figure 2.25), as well as creep tests (cf. Figure 2.26) provided the experimental data basis for the following parameter identifi-

cation; see Section 2.5.2.2. Tensile tests with different strain rates were not considered here, as we instead focused on capturing the viscosity-related parameters of the material via the explicit incorporation of creep and relaxation characteristics within the error square functional. In the case of all these experiments, a homogeneous rectangular specimen with an initial length of 25 mm, thickness of 2.2 mm, and width of 10 mm was used. An example of the specimen is shown in Figure 2.23b at the beginning of the corresponding loading path.

(a) Micro-testing machine by Kammrath & Weiss GmbH.

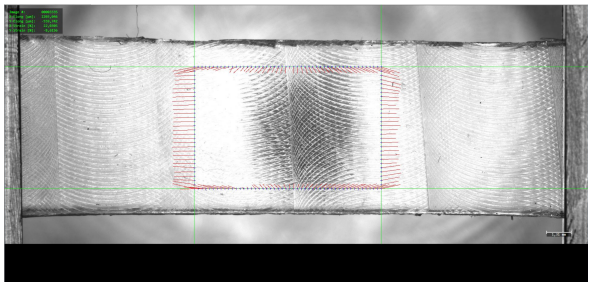

(b) Rectangular specimen in the micro-testing machine under tension visible via the VEDDAC strain software.

Figure 2.23: Experimental setting—the micro-testing machine by Kammrath & Weiss GmbH in combination with the CCD camera system by Chemnitzer Werkstoffmechanik GmbH providing load-displacement data, as well as the displacement field on the surface. Reprinted from Schulte et al., Materials 13(14):3156 (2021), [110], with permission under creative commons 4.0.

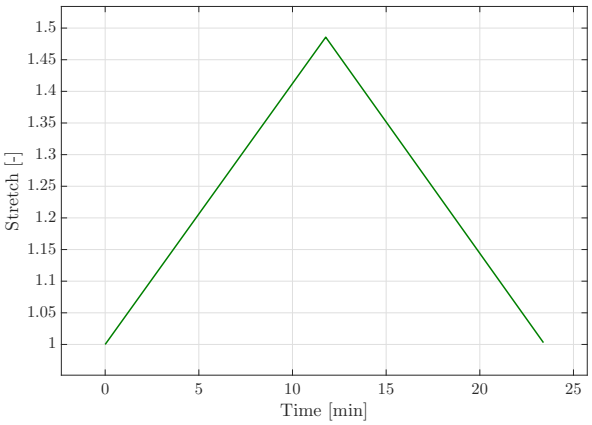

(a) Strain-time curve.

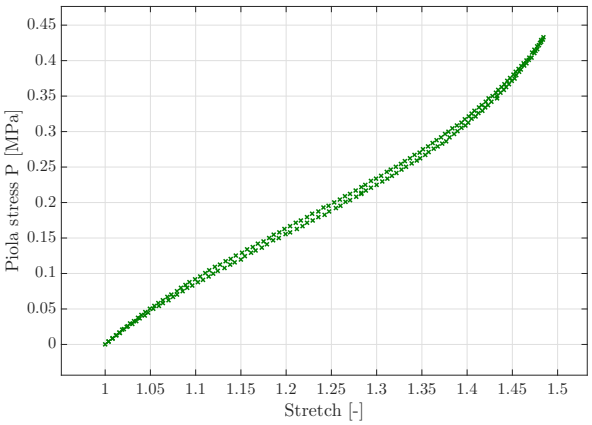

(b) Nominal stress (P_{11})-stretch (λ) curve.

Figure 2.24: Tensile test results of the micro-testing machine, where the strain path shown in **(a)** is applied which results in the nominal stress shown in **(b)**. Reprinted from Schulte et al., Materials 13(14):3156 (2021), [110], with permission under creative commons 4.0.

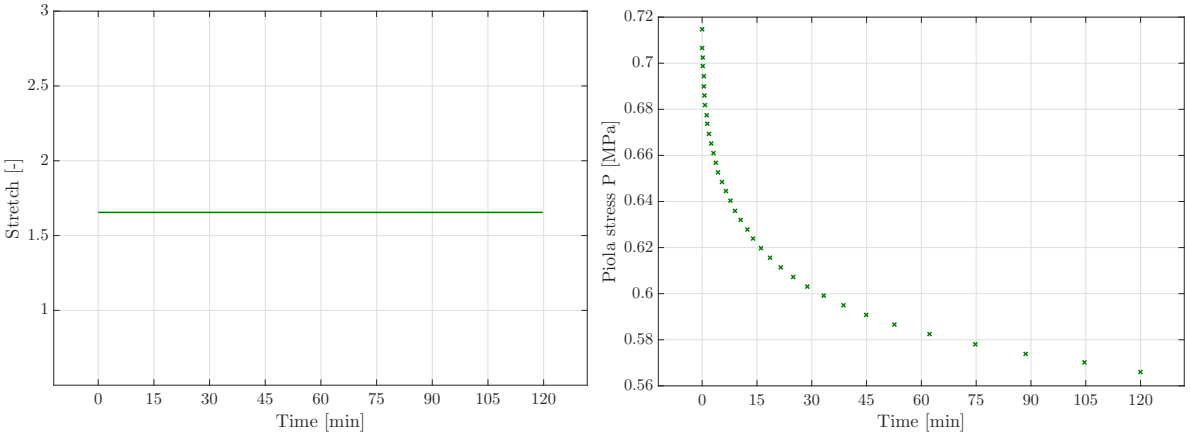

(a) Strain-time curve.

(b) Nominal stress (P_{11})-time curve.

Figure 2.25: Relaxation test results of the micro-testing machine, where the stretch level shown in **(a)** is fixed which results in the nominal stress decrease over time shown in **(b)**. Reprinted from Schulte et al., Materials 13(14):3156 (2021), [110], with permission under creative commons 4.0.

2.5.2.2 Parameter identification

In the context of parameter identification procedures, it is advantageous to compute the Piola stress tensor as a quantity, facilitating the comparison of experimental and simulated material response; cf. Section 2.5.2.1. The Piola stress tensor $\boldsymbol{P}$ is related to the Piola–Kirchhoff stress tensor $\boldsymbol{S}$ and the Kirchhoff stress tensor $\boldsymbol{\tau}$ via

$$\boldsymbol{P} = \boldsymbol{\tau} \cdot \boldsymbol{F}^{-\mathrm{t}} = \boldsymbol{F} \cdot \boldsymbol{S} \,, \tag{2.95}$$

where the sensitivity of the Piola stress with respect to the deformation gradient is denoted as $\mathbf{A}$, in particular,

$$\mathbf{A} = \frac{\partial \boldsymbol{P}}{\partial \boldsymbol{F}} = \frac{\partial^2 \psi_{\mathrm{loc}}}{\partial \boldsymbol{F} \otimes \partial \boldsymbol{F}} \,, \tag{2.96}$$

or, expressed in index notation,

$$\mathsf{A}_{aAbB} = \frac{\partial^2 \psi_{\mathrm{loc}}}{\partial F_{aA}\, \partial F_{bB}} \,. \tag{2.97}$$

Moreover, $\mathbf{A}$ relates to the spatial elasticity tensor $\mathbf{e}$ via

$$\mathsf{A}_{aBcD} = F^{-1}_{Bb}[\mathsf{e}_{abcd} + \tau_{ac}\delta_{bd}]F^{-1}_{Dd} \,. \tag{2.98}$$

It is noted that the tangent operator, as typically required within implicit finite element formulations, respectively so-called constitutive drivers, is based on $\mathbf{A} = \mathrm{d}\boldsymbol{P}/\mathrm{d}\boldsymbol{F}$.

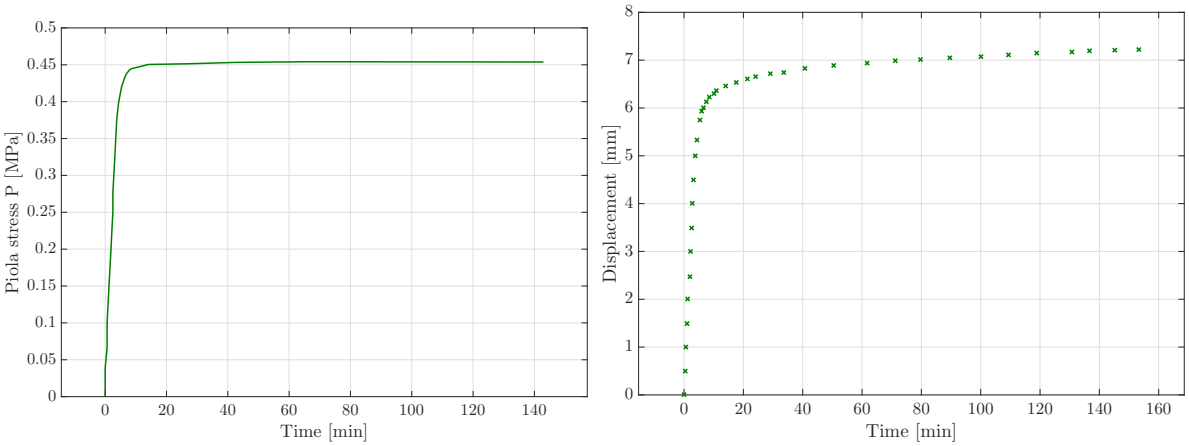

(a) Nominal stress (P_{11})-time curve.

(b) Displacement (u)-time curve.

Figure 2.26: Creep test results of the micro-testing machine, where the stress shown in **(a)** is fixed over time which results in the displacement change shown in **(b)**. Reprinted from Schulte et al., Materials 13(14):3156 (2021), [110], with permission under creative commons 4.0.

The Yeoh-type hyperelastic energy function was combined with the constitutive viscoelasticity model, presented in Section 2.2, including two Maxwell elements. Apart from the Yeoh material parameters C_1, C_2 and C_3, the viscoelastic parameters γ_1 and γ_2, denoting the relation of the stiffness of each Maxwell element with respect to the pure elastic Young's modulus, and τ_1, τ_2, representing the ratio of the viscosity to the stiffness in each Maxwell element, need to be identified. Regarding the parameters, it has to be mentioned that the material was assumed to be nearly incompressible, and thus, Poisson's ratio was fixed to $\nu = 0.49$. Thus, seven material parameters needed to be identified.

Since these seven material parameters could be identified via experiments of homogeneous deformation states, strain- and stress-driven constitutive drivers were implemented in MATLAB instead of full finite element (FE) simulations in order to reduce the computational cost within each iteration of the parameter identification. The pseudo-codes of both types of constitutive drivers are depicted in Algorithms 1 and 2 in the Appendix A.2. The fminsearch-algorithm in MATLAB was used for the parameter identification, minimising the goal function with respect to the difference in the simulated and experimental reaction force over all load steps, i.e.

$$f = w^{\mathrm{T}} \sum_t w_t^{\mathrm{T}} \left| P_t^{\mathrm{T,exp}} - P_t^{\mathrm{T,sim}}(\boldsymbol{\kappa}) \right|^2 + w^{\mathrm{R}} \sum_t w_t^{\mathrm{R}} \left| P_t^{\mathrm{R,exp}} - P_t^{\mathrm{R,sim}}(\boldsymbol{\kappa}) \right|^2 + w^{\mathrm{C}} \sum_t w_t^{\mathrm{C}} \left| u_t^{\mathrm{C,exp}} - u_t^{\mathrm{C,sim}}(\boldsymbol{\kappa}) \right|^2 , \tag{2.99}$$

where w^{T}, w^{R}, and w^{C} denote the weighting factors for the tensile, creep, and relaxation test, respectively. The additional weighting factors w_t^{T}, w_t^{R}, and w_t^{C} were introduced to emphasise specific time steps t of each experiment and to appropriately scale stress and displacement contributions.

In the following, the viscoelastic material parameters are identified via the three tests based on homogeneous deformation states, presented in Section 2.5.2.1.

If the parameters of the Yeoh-model were solely fitted with respect to the tensile test, the simulated material response of the identified parameters matched the experimental data perfectly. Next, the relaxation parameters were obtained with respect to the relaxation and creep test, though the material behaviour highly depended on the previously identified Yeoh parameters. Thus, the experimental relaxation and creep response could not be sufficiently matched via optimisation of the relaxation parameters only. Consequently, all of the material parameters were identified simultaneously for all three different experiments in order to obtain the best parameter set reflecting the complete material behaviour. The comparison of the simulated and experimental material behaviour is shown in Figure 2.27 for the optimised parameter set. The corresponding parameter set is presented in Table 2.5.

In the graphs shown in Figure 2.27, the experimental results of the relaxation and creep tests are nearly perfectly matched, and only slight differences in the diagrams can be seen at certain points. The simulated material response of the tensile test overestimated the experimental curve, but captured the general tendency. The tensile test could be captured better by increasing the associated weight within the objective function (2.99) at the cost of the accuracy with which creep and relaxation tests were captured. The focus here was set on the rate-dependent constitutive characteristics that were captured with high accuracy. Though beyond the scope of this work, a precise capturing of tensile, creep, and relaxation test at the same time could be achieved by introducing higher order energy functions and a larger number of independent Maxwell branches within the constitutive framework provided. The accompanying increase in parameter identification complexity due to a significantly increased number of constitutive parameters could then be dealt with by using parameter correlation matrices.

Considering the curve of the tensile test, especially the values and the signs of the Yeoh parameters are important, since the first parameter C_1 weights the linear behaviour of the stress strain-response, whereas C_2 scales the quadratic term of the isochoric energy contribution resulting in the decreasing slope. The third parameter C_3 corresponds to the third-order polynomial contribution of the energy function and thus yields the increasing slope at the end of the loading path. Thus, different values for the Yeoh parameters would probably fit the tensile response way better; the dependence on the relaxation parameters, however, would result in a worse fit of the relaxation and creep behaviour. Higher order contributions to the Helmholtz free energy, in particular the isochoric contribution, would therefore provide a potential in order to capture the tensile test response better.

The identified viscoelastic material parameters were used as fixed values for the subsequent optimisation of the damage-related parameters in Section 4.2.

Table 2.5: Optimised set of material parameters for the Yeoh material model, as well as the relaxation parameters for the two Maxwell elements. Reprinted from Schulte et al., Materials 13(14):3156 (2021), [110], with permission under creative commons 4.0.

Symbol	Description	Final set	Unit
C_1	Yeoh parameters	0.19550588	MPa
C_2		0.11198637	MPa
C_3		0.00685930	MPa
γ_1	Relative moduli	0.12862148	-
γ_2		0.36026686	-
τ_1	Relaxation times	1879.5892	s
τ_2		68.729741	s

2.5.3 Laminate-based model for ferroelectric materials

This section gives a short summary of the parameter identification process of the laminate-based model for ferroelectric materials performed in Dusthakar et al. [17]. Most of the required parameters have already been identified in experiments and taken directly from the literature. These parameters define the linear piezoelectric response behaviour and the coercive electric field constants. The remaining two model, respectively fitting, parameters need to be calibrated with respect to characteristic experimental data. In the case of piezoelectric materials, butterfly and dielectric hysteresis curves contain the required data. In the following, the calibration is performed with regard to single crystal $BaTiO_3$ samples. The Sequential Quadratic Programming (SQP) method was used for the parameter identification process minimising the least square error of the objective function.

As it can be seen in Table 2.6, the piezoelectric coupling coefficients as well as the permittivity parameters were taken from Zgonik et al. [140]. The computed values by Schröder and Keip [106] were selected for the transversely-isotropic elasticity components. From Yen et al. [136] the spontaneous polarisation and strain coefficients were taken in addition to the coercive electric field limits for 90° and 180° domain switching. All of the parameters were identified for single crystal tetragonal $BaTiO_3$. Furthermore, the magnitude of the saturation polarisation was assumed to be equal to the spontaneous polarisation value with regard to a perfect single crystal without any impurities.

Nevertheless, the developed model by Dusthakar et al. [17] contains further model parameters with an impact on the non-linear hysteric behaviour. These remaining two fitting parameters were calibrated in [17] with respect to the characteristic experimentally measured butterfly and dielectric hysteresis curves taken from Shieh et al. [114], see

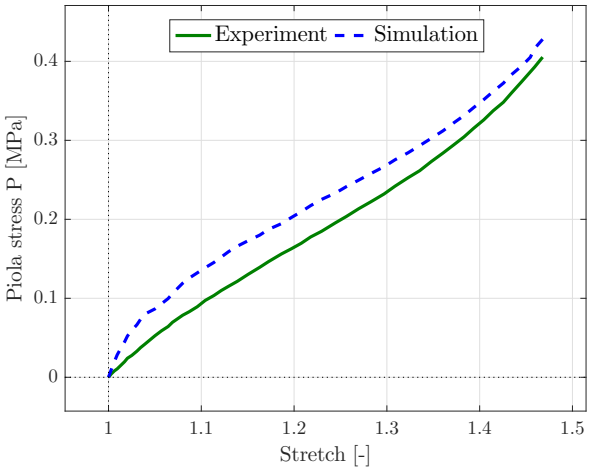

(a) Tensile test—comparison of experimental and simulated material response.

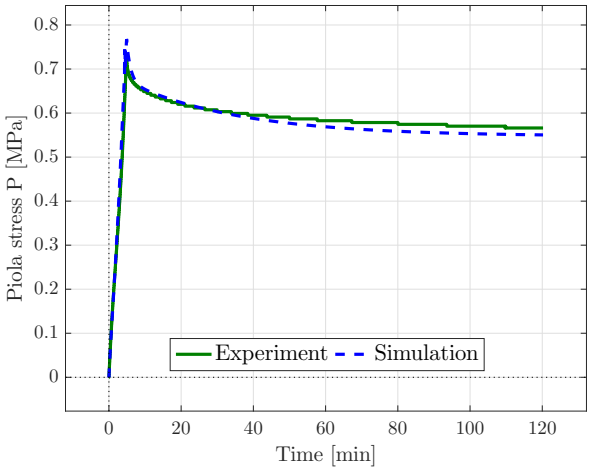

(b) Relaxation test—comparison of experimental and simulated material response.

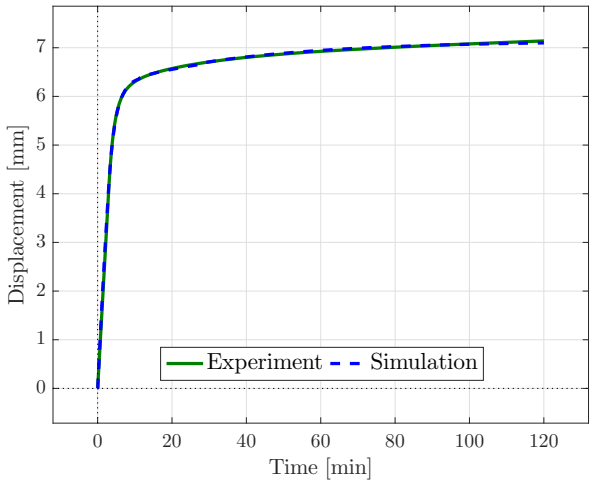

(c) Creep test—comparison of experimental and simulated material response.

Figure 2.27: Comparison of experimental and simulation results of the (**a**) tensile, (**b**) relaxation, and (**c**) creep tests for uni-axial stress states, using the optimised set of material parameters; cf. Table 2.5. Reprinted from Schulte et al., Materials 13(14):3156 (2021), [110], with permission under creative commons 4.0.

Figure 2.28. Shieh et al. based their studies on unpoled [001]-oriented $BaTiO_3$ tetragonal single crystal samples with a length of 5 mm, a width of 5 mm and a depth of 2 mm. A combined electromechanical loading path was applied to the samples consisting of a constant compressive stress of six different levels in the range of 0 MPa and 2.7 MPa and a cyclic electric field of $E_3^{\max} = \pm 1.25\,\mathrm{kV}$ at a frequency of 0.2 Hz. In the following numerical simulations, the strains ε_{33} and dielectric displacements D_3 were

Table 2.6: Material parameters of the laminate-based material model developed by Dusthakar et al. [17]. The values in the table of the parameters from [17] were taken from the literature [106, 136, 140]. Reprinted from Dusthakar et al., Mechanics of Materials 117:235-254 (2018), [17], with permission from Springer Nature.

Symbol	Description	Value	Unit	Reference
e_{311}	lateral piezoelectric coefficient	-0.7	$\mathrm{C/m^2}$	[140]
e_{333}	axial piezoelectric coefficient	6.7	$\mathrm{C/m^2}$	[140]
e_{131}	piezoelectric shearing coefficient	34.2	$\mathrm{C/m^2}$	[140]
ϵ_0	vacuum permittivity	8.854×10^{-12}	F/m	[140]
ϵ_{11}	dielectric permittivity	$2200\,\epsilon_0$	F/m	[140]
ϵ_{33}	dielectric permittivity	$56\,\epsilon_0$	F/m	[140]
E_{1111}	elastic stiffness	237.4×10^3	MPa	[106]
E_{1122}	elastic stiffness	92.6×10^3	MPa	[106]
E_{1133}	elastic stiffness	111×10^3	MPa	[106]
E_{3333}	elastic stiffness	151×10^3	MPa	[106]
E_{1313}	elastic stiffness	61×10^3	MPa	[106]
P^{s}	spontaneous polarisation	0.26	$\mathrm{C/m^2}$	[136]
η_1^{s}	spontaneous strain coefficient	0.67	%	[136]
η_2^{s}	spontaneous strain coefficient	-0.42	%	[136]
$E^{\mathrm{c}}_{90^\circ}$	coercive electric field for 90° switching	0.26	kV/mm	[136]
$E^{\mathrm{c}}_{180^\circ}$	coercive electric field for 180° switching	0.23	kV/mm	[136]
P^{sat}	saturation polarisation	0.26	$\mathrm{C/m^2}$	-
η^{p}	viscosity-type parameter	0.01	$\mathrm{m^2/Cs}$	-

calculated for the applied boundary conditions by using a constitutive driver routine, following. [50, 79, 80].

In [17], the viscosity-type parameter η^{p} was fixed at a constant value during the parameter identification process due to the fixed electrical loading frequency in the experiments. The parameter η^{p} was set to $\eta^{\mathrm{p}} = 0.01\,\mathrm{m^2/Cs}$. The remaining two fitting parameters were calibrated by minimising a least-square function $f(\boldsymbol{\kappa})$, where $\boldsymbol{\kappa}$ denotes the remaining parameter vector $\boldsymbol{\kappa} = \{m, c\}$. Scalar m is the viscous-like parameter which was introduced in the rate-dependent dissipation equation and c is the hysteresis shape exponent which influences the remnant energy contribution. Both parameters have to be greater than 0. Thus, Dusthakar et al. have chosen the following non-linear constrained optimisation problem

$$\boldsymbol{\kappa} = \arg\min_{\boldsymbol{\kappa}} \{f(\boldsymbol{\kappa})\} \qquad \text{such that} \qquad \boldsymbol{\kappa} = \{m > 0, c > 0\}\,, \tag{2.100}$$

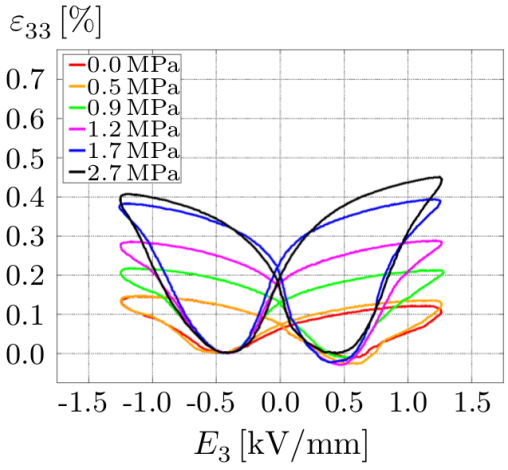

(a) Experimentally measured butterfly curves.

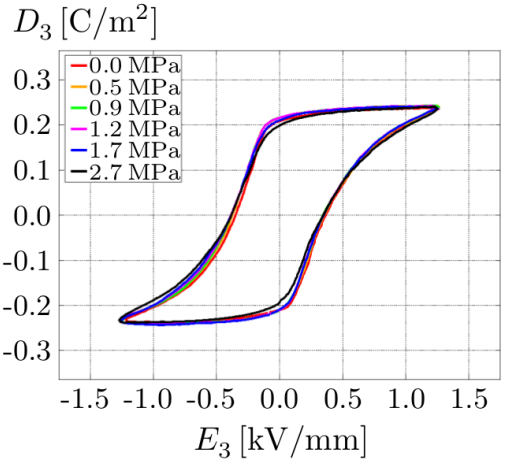

(b) Experimentally measured dielectric hysteresis loops.

Figure 2.28: The Figure of the experimentally measured butterfly curves and dielectric hysteresis loops for a [001]-oriented $BaTiO_3$ tetragonal single crystal is taken from Dusthakar et al. [17]. They extracted the data from Shieh et al. [114]. The single crystal was subjected to six different levels of a constant compressive stress while a cyclic electric field of $E_3^{\max} = \pm 1.25\,\mathrm{kV}$ at a frequency of 0.2 Hz. Reprinted from Dusthakar et al., Mechanics of Materials 117:235-254 (2018), [17], with permission from Springer Nature.

where the least-square functional is depicted as

$$f(\boldsymbol{\kappa}) = \frac{1}{2} \sum_{k=1}^{T} \left[\sum_{i=1}^{N_1^k} w_1^{ki} \left| \varepsilon_{33}^{ki,\mathrm{sim}}(\boldsymbol{\kappa}, E_3^{ki,\mathrm{exp}}) - \varepsilon_{33}^{ki,\mathrm{exp}}(E_3^{ki,\mathrm{exp}}) \right|^2 \right. \tag{2.101}$$

$$\left. + \sum_{j=1}^{N_2^k} w_2^{kj} \left| D_3^{kj,\mathrm{sim}}(\boldsymbol{\kappa}, E_3^{kj,\mathrm{exp}}) - D_3^{kj,\mathrm{exp}}(E_3^{kj,\mathrm{exp}}) \right|^2 \right] . \tag{2.102}$$

While index $T = 6$ denotes the amount of different curves for the six applied stress magnitudes, cf. Figure 2.28, the indices N_1^k and N_2^k depict the number of data points that were extracted from both characteristic curves with respect to each k^{th}-set of externally applied stress magnitude. In the objective function, for each stress level, the difference of the simulated strain $\varepsilon_{33}^{ki,\mathrm{sim}}(\boldsymbol{\kappa}, E_3^{ki,\mathrm{exp}})$ and the dielectric displacements $D_3^{kj,\mathrm{sim}}(\boldsymbol{\kappa}, E_3^{kj,\mathrm{exp}})$ to the experimentally measured ones, $\varepsilon_{33}^{ki,\mathrm{exp}}(E_3^{ki,\mathrm{exp}})$ and $D_3^{kj,\mathrm{exp}}(E_3^{kj,\mathrm{exp}})$, are taken into account. Therefore, an interpolation between the simulated results and the experimental data is performed. w_1^{ki} and w_2^{kj} represent the non-negative, scalar weighting factors which are defined as

$$w_1^{ki} := \Delta t^{ki,\mathrm{exp}} / \Delta t^{ki,\mathrm{sim}} \qquad \text{and} \qquad w_2^{kj} := \Delta t^{kj,\mathrm{exp}} / \Delta t^{kj,\mathrm{sim}} , \tag{2.103}$$

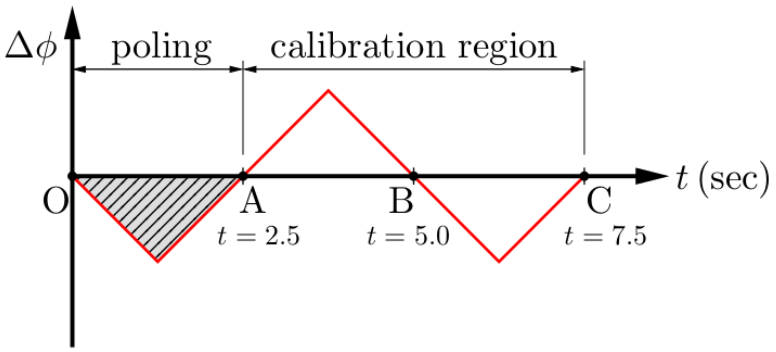

Figure 2.29: The corresponding loading curve for the simulations performed within each iteration of the calibration process. The applied potential difference is plotted over time. Reprinted from Dusthakar et al., Mechanics of Materials 117:235-254 (2018), [17], with permission from Springer Nature.

with Δt denoting the time step size between any two time steps of the underlying loading curve. In Shieh et al. [114], the experimental curves were presented for one complete triangular loading cycle, though no information on the loading path preceding the shown curves was provided. However, based on the obtained data from [114], Dusthakar et al. [17] started with the remnant configuration of the samples, cf. Figure 2.28. Therefore, the poled sample is loaded and unloaded once at a frequency of 0.2 Hz with respect to the simulations in order to reach the remnant state of the specimens, marked by the shaded region OA in Figure 2.29, as shown in the experiments. The part of the simulated material response which is considered for the comparison to the experimental data starts at point A, see Figure 2.29.

First, Dusthakar et al. [17] used the *ga solver* (generic algorithm) of the *Optimization Toolbox* in *MATLAB* in order to find proper initial values for both remaining model parameters. This initial process was performed independently for each of the different stress magnitudes. A suitable starting point was chosen for each parameter from the obtained list of parameter values. Secondly, the chosen initial values were used in a following parameter identification by using the *fmincon solver*, performing a constrained non-linear minimisation, in combination with the SQP-based algorithm in *MATLAB*. This time, all of the different curves are simultaneously taken into account. Finally, after considering all data of the applied six different stress magnitudes, the optimal viscous-type and hysteresis shape parameters are identified as

$$m = 1.494 \qquad \text{and} \qquad c = 3.648\,. \tag{2.104}$$

Considering the large effort which was necessary in [17] to identify these two remaining parameters, an alternative approach for the generation of qualitative starting points is presented in Section 3.2.

3 Machine-learning assisted parameter identification based on homogeneous states of deformation

In general, regarding the calibration of all different kinds of material models, three basic approaches are established in order to identify an initial guess for a parameter identification procedure:

- Guess of a random starting point.
- Definition of possible intervals for each parameter and selection of random parameter values within the respective intervals in order to generate starting values.
- Stepwise parameter identification, e.g. in case of elastoplasticity: Identification of elastic parameters in a first step. Thereafter, these elastic parameters are fixed and the calibration of plastic parameters is performed. This procedure can be continued for, respectively applied to, every parameter class. As a result, one starting point is generated.

The first strategy can be considered the most challenging, inefficient and costly approach. The second method reduces the search space, though it might not be possible to identify a proper interval for every parameter. The third strategy might lead to a very good starting point but requires special algorithmic treatment. Another application specific strategy was performed in Dusthakar et al. [17] and summarised in Section 2.5.3 which improved the quality of the starting point by investing a high effort. In conclusion, all approaches require knowledge of the corresponding material model or success in guessing a proper starting point.

The work in this chapter seeks to contribute to this discussion by proposing a machine learning-based two-stage hybrid optimisation approach. In the first stage a model-specific neural network predicts certain starting values, where the latter are then directly transferred to a classic optimisation algorithm in order to obtain a mathematically optimal solution in a second stage. In addition, an intermediate stage of a subsequent

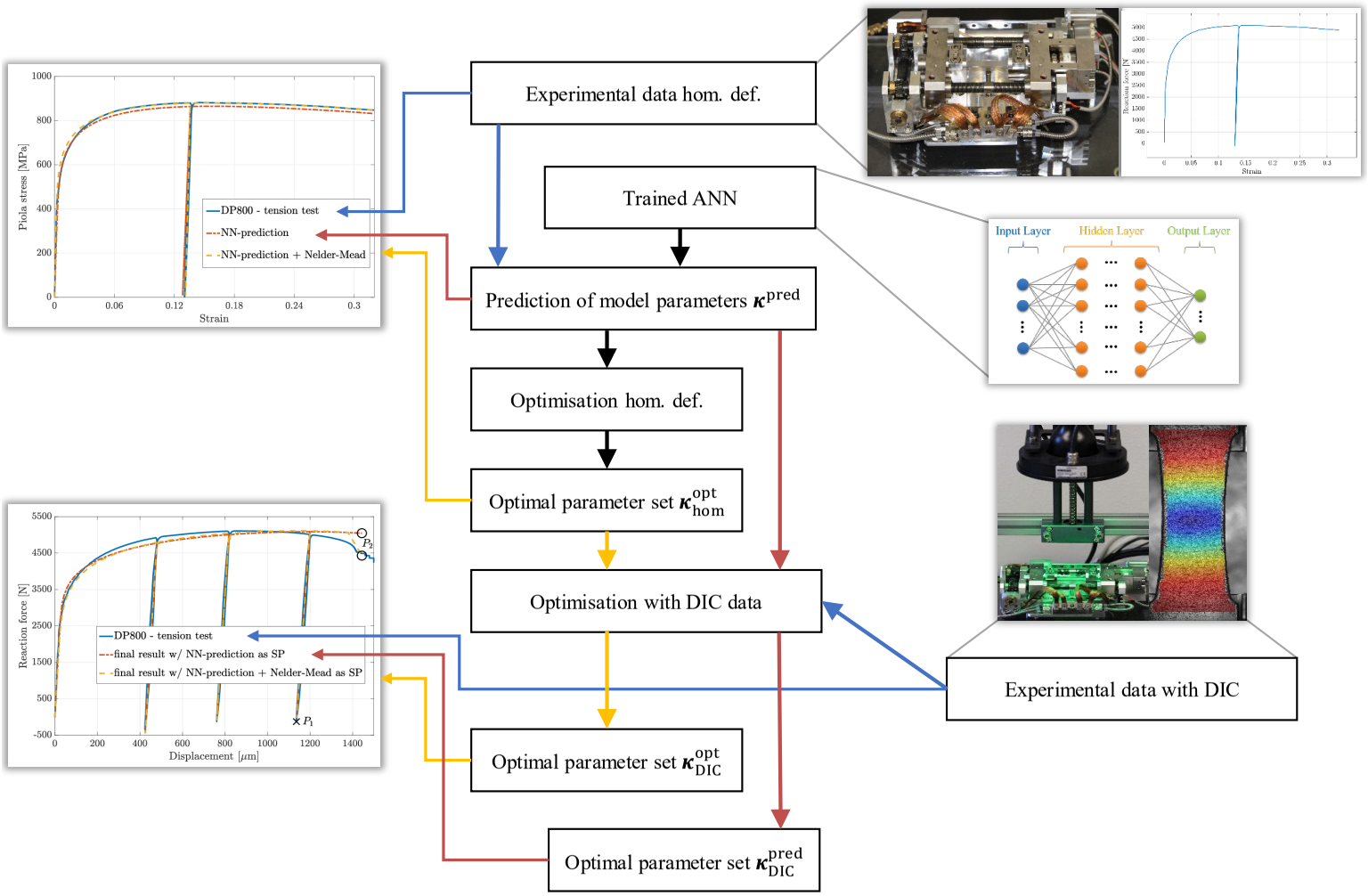

Figure 3.1: Overall machine learning-assisted parameter identification scheme proposed in this work. In the first step, experimental data based on homogeneous deformation states is fed into a neural network, cf. Figure 3.2, yielding a high-quality prediction of suitable parameters for the underlying constitutive model. The predicted parameters $\boldsymbol{\kappa}^{\text{pred}}$ are used as starting values for a classic optimisation scheme, yielding the optimal solution $\boldsymbol{\kappa}^{\text{opt}}_{\text{hom}}$ in a fully automated manner. The obtained solution might then again be considered as a starting value for the DIC-based calibration of non-local model parameters, which is necessary for the chosen material model. Alternatively, the predicted parameters $\boldsymbol{\kappa}^{\text{pred}}$ can be directly chosen as starting values for the DIC-based calibration. Reprinted from Schulte et al., European Journal of Mechanics - A/Solids 98:104854 (2023), [113], with permission under creative commons licence 4.0.

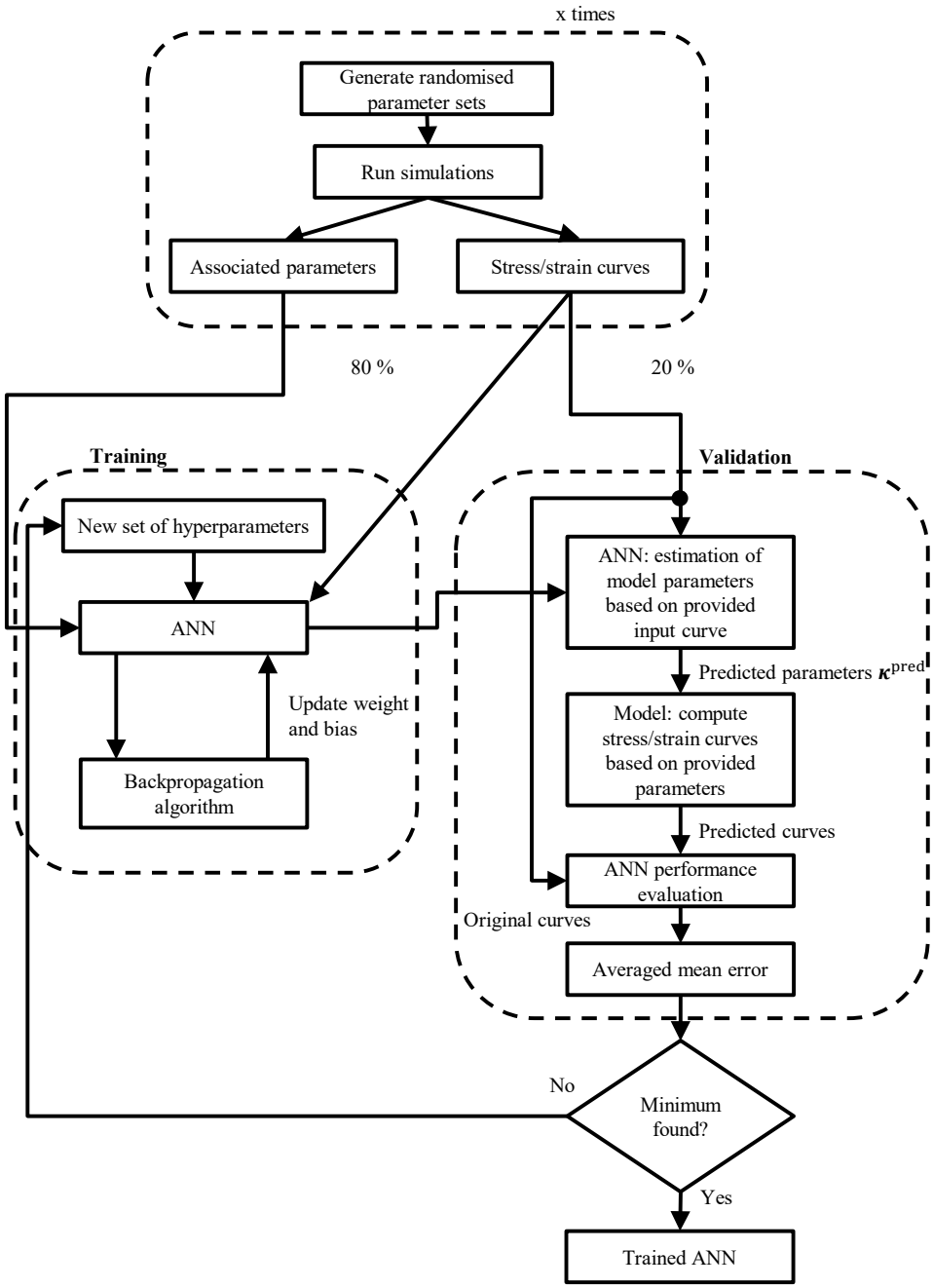

Figure 3.2: Visualisation of the training and validation procedure applied to the artificial neural network (ANN). A superordinate scheme for the optimisation of the network's hyperparameters is already incorporated here. The ANN is used to predict a set of parameters $\boldsymbol{\kappa}^{\mathrm{pred}}$, which is then fed into a subsequent classic optimisation procedure, cf. Figures 3.1 and 3.3. Reprinted from Schulte et al., European Journal of Mechanics - A/Solids 98:104854 (2023), [113], with permission under creative commons licence 4.0.

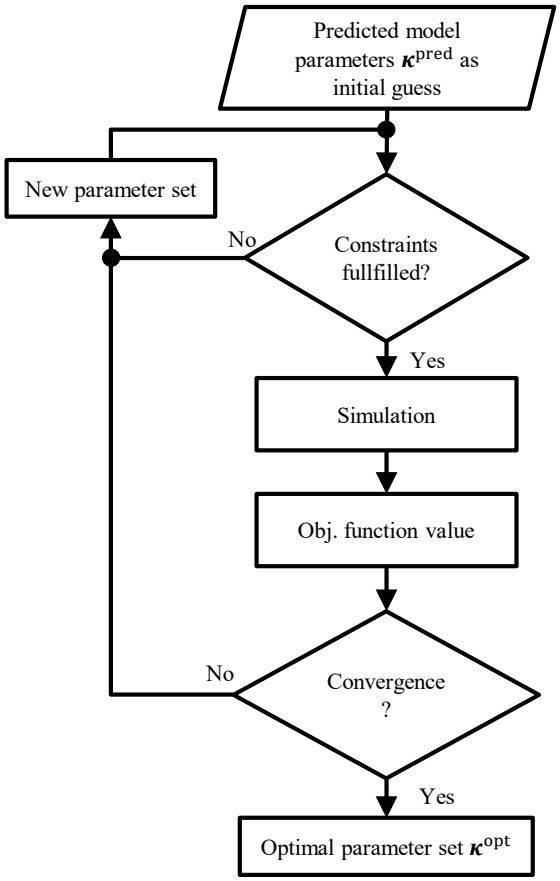

Figure 3.3: Flowchart depicting a classic deterministic optimisation algorithm, such as a basic Nelder-Mead simplex algorithm, which we feed with the parameter set $\boldsymbol{\kappa}^{\mathrm{pred}}$ identified by the neural network, cf. Figures 3.1 and 3.2. Reprinted from Schulte et al., European Journal of Mechanics - A/Solids 98:104854 (2023), [113], with permission under creative commons licence 4.0.

calibration with respect to the homogeneous states of deformation is included in order to evaluate as to whether the neural network already provides a sufficient solution. While the first and the intermediate stages perform the simulations by using a FE-model in terms of one-element with corresponding boundary conditions (by analogy with a constitutive driver) enabling us to compute uni-axial stress states, the second stage is based on simulations of an inhomogeneous boundary value problem in order to evaluate full-field data. This strategy provides the advantage that the network only has to be trained once per model and can subsequently be applied to different materials without further effort. Furthermore, the already trained network can be provided along the corresponding material model such that the user immediately obtains the optimal starting value for the classic parameter identification. The scheme we propose makes it easier to take into account any combination of experimental *loading path sequences* for the model calibration, where *loading path sequences* refer to both homogeneous modes of deformation—such

as tension, compression, shear—as well as to modes of loading, particularly loading-unloading sequences occurring in, e.g., experimental step tests. Furthermore, different types of loading path sequences such as temperature levels can be considered. In line with the loading path sequences occurring in the considered experimental tests, a model-specific neural network is trained by repeated evaluation of the model response for the pre-defined loading path sequences at random parameter sets.

The particular experimental data to which the model is to be fitted is then deliberately decomposed into the same loading path sequences, which are then normalised, concatenated, and used as input data for the neural network, enabling the algorithm to predict proper model-related constitutive parameters. These parameters are then transferred as starting values to a classic optimisation procedure, see Figure 3.1, which is an inverse parameter identification using full-field data in combination with finite element simulations. In this work, the FEMU method, cf. Section 1.1.3, is applied for an application example of the second stage in Section 4.3.5. Besides the hybrid strategy, the FEMU method is employed for all multi-objective optimisation schemes in Chapter 4.

In Section 3.1, the general procedure of the developed hybrid strategy is directly explained, presented and analysed by employing a specific application example. For this purpose, the finite plasticity model coupled to gradient-enhanced damage, cf. Section 2.1, is considered as the underlying material model since it takes many material characteristics into account and thus is a very complex material model. Hence, it is quite difficult to calibrate the model to specific materials, especially if the user is not profoundly familiar with the model and its parameters. Furthermore, a second application example is given in Section 3.2, where a neural network is trained for the laminate-based model for ferroelectrics, presented in Section 2.3, in order to improve the complex starting point generation of the model parameters, cf. Section 2.5.3, and to demonstrate the capability of the hybrid strategy to cope with all kinds of loading path sequences.

3.1 Machine-learning assisted parameter identification introduced for a gradient-enhanced damage formulation

In this section, the hybrid strategy is presented alongside a first application example of a finite plasticity model coupled to a (gradient-enhanced) damage framework, cf. Section 2.1. In order to demonstrate some advantages of the model, the model is calibrated to two different materials, a DP800 sheet metal and a case-hardened steel 16MnCrS5, and different loading path sequences are taken into account. First, the required experiments are shown in Section 3.1.1, followed by the presentation of the structure of the networks in Section 3.1.2 and the corresponding training process in Section 3.1.3. In Section 3.1.4, the quality of the predictions of the neural networks is compared to the results of a sub-

sequent classic parameter identification with respect to the experimental data presented in the next section. This parameter identification process based on the homogeneous states of deformation is closed with a short discussion of important aspects of the overall process. The final second step of the hybrid strategy, where the parameter prediction of the artificial neural network is employed as a starting set for a subsequent classic multi-objective parameter identification, is demonstrated in Section 4.3.5.

3.1.1 Experiments

The goal of this work is not only to train a neural network with a constitutive model, to be specific a large strain gradient-enhanced ductile damage model, but also to calibrate the model to experimentally measured material behaviour. Two exemplary materials for the application in metal forming processes are selected, i.e. a sheet metal DP800 and a case-hardened steel 16MnCrS5. Since both materials apply to different production process chains, distinct fundamental experiments were conducted for the materials. The experiments were conducted by Sprave and Menzel [119] and Hering [35]. All experiments were carried out under room conditions.

3.1.1.1 Tension test

For both materials, the common tension test at sufficiently low loading rates is the first characteristic fundamental test. Since the key goal of this work is to generate a neural network which autonomously predicts a high quality starting set of parameters for a subsequent classic parameter identification for efficiency reasons, the simulations are restricted to homogeneous states of deformation resulting in a prediction of sufficient accuracy. Thus, it would be ideal to have (quasi) homogeneous states of deformation in the experiments as well. In the case of the DP800, Sprave and Menzel [119] extracted the homogeneous states of deformation of the tensile test following the procedure described in the paper, namely by relating the total tensile force to changes in length of a certain segment of the test specimen. The tensile test was conducted on a micro-tensile machine by Kammrath & Weiß with a 10 kN load cell. The corresponding displacement response is measured by an optical extensometer with the digital image correlation (DIC) system Veddac 7. This leads to the DP800 tensile reaction force-strain curve in Figure 3.4. The initial cross-sectional area is $5.775\,\mathrm{mm}^2$. Since it is not straightforward to extract a comparable flat sample for the case-hardened steel 16MnCrS5 due to its availability as rod material, respectively specimen, a cylindrical tension sample following DIN 50125-B 8x40 with a cross section diameter of 8 mm and an initial length for the tactile macro-extensometer of 40 mm is employed. This tension test was conducted on the universal testing machine Zwick Roell Z250 and the tension test followed the DIN EN ISO 6892-1 (2017) norm. For more information please be referred to [35].

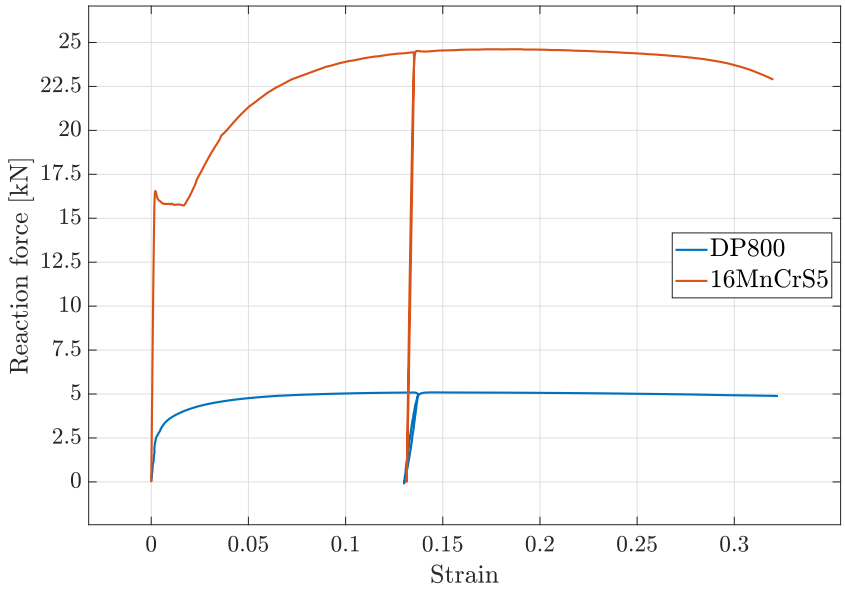

Figure 3.4: Tension test data for both considered materials, i.e. DP800 and 16MnCrS5, with strain defined as $\varepsilon = \Delta l / l_0$. Both experiments include an unloading phase at $\varepsilon \approx 0.135$, but refer to different sizes of test specimen, cf. [35, 119]. Reprinted from Schulte et al., European Journal of Mechanics - A/Solids 98:104854 (2023), [113], with permission under creative commons licence 4.0.

In the first step, a strain of $\varepsilon = 0.135$ is applied on the samples for both materials. Subsequently, an unloading phase is conducted where the force is reduced to zero followed by a reloading until a total strain of 0.32 is reached, cf. Figure 3.4.

3.1.1.2 Compression test

Since the case-hardened steel 16MnCrS5 is typically available as a rod material, a compression test is natural to identify characteristic behaviour of the material. The geometry of the sample is a cylinder with a diameter of 10.2 mm and a height of 15 mm. For the compression test, an initial load of 20 N, a rate of the compressive stress of 30 MPa/s and a data sampling rate of $0.0067\,\mathrm{s}^{-1}$ were chosen. The measured compressive reaction force-strain curve is shown in Figure 3.5.

3.1.1.3 In-plane torsion test

In the case of the sheet metal DP800, an in-plane torsion test, detecting simple shear-type loading, is more convenient to be carried out than a compression test. The results depicted in Figure 3.6 were obtained and published by Kolpak et al. [54]. Further information on the theory of in-plane torsion tests can be found in, e.g., Traphöner et al. [128]. For this test, a circular specimen with a diameter of 80 mm was used including circumferential grooves. In the groove root, the thickness of the specimen reduces to the

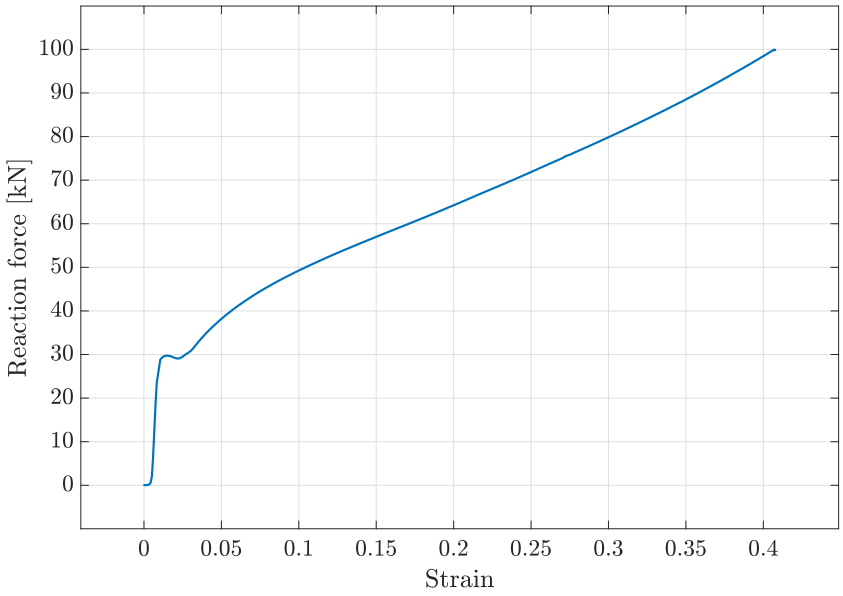

Figure 3.5: Compression test of the case-hardened steel 16MnCrS5 with strain defined as $\varepsilon = \Delta l / l_0$, cf. [35]. Reprinted from Schulte et al., European Journal of Mechanics - A/Solids 98:104854 (2023), [113], with permission under creative commons licence 4.0.

half of the initial thickness $t_0 = 1.5\,\mathrm{mm}$, and the groove radius is 4 mm while the radius distance is 12.4 mm. The Piola shear stress is calculated via

$$\tau(r) = \frac{M}{2\,\pi\,t(r)\,r^2}\,, \tag{3.1}$$

where M is the measured torque, t the local initial sheet thickness and r the radial position. The shear strain is measured via DIC. More detailed information regarding the experiment can be found in [54].

3.1.2 Neural network for parameter identification

In the following, the general structure of the employed artificial neural networks (ANN) is discussed, starting with the generation of the required training data and then discussing the influence of the various parameters to be identified. The structure of the networks, in particular the hyperparameters, is subsequently addressed.

3.1.2.1 Sampling of training data

In order to provide a feasible amount of training data for the neural network, randomised parameter combinations are simulated by the constitutive model to generate a dataset of "curves" enabling supervised learning approaches. Considering the goal of this work, i.e. to generate a parameter set as a starting point for a subsequent classic parameter

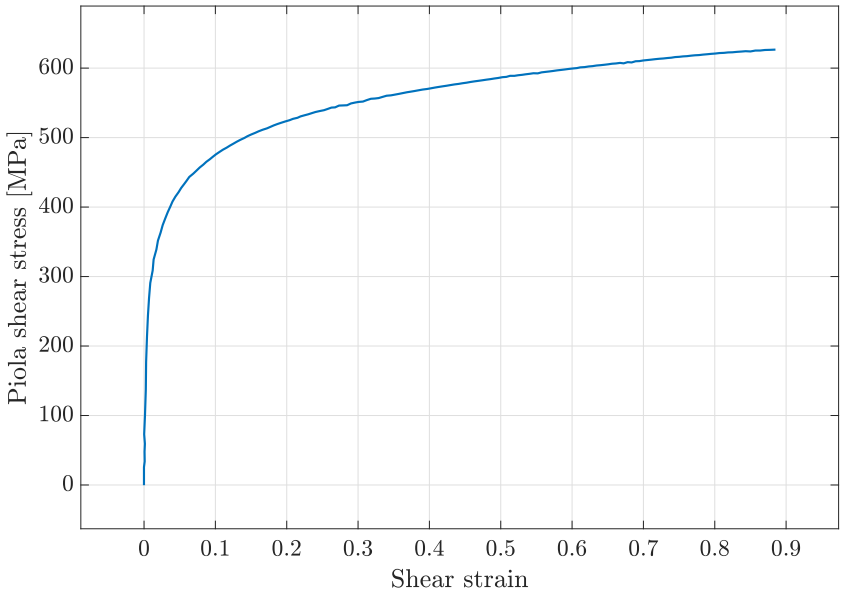

Figure 3.6: In-plane torsion test of the sheet metal DP800 with the shear strain, here scaled by factor two, defined as the related shear component of the Green-Lagrange strain tensor $\boldsymbol{E} = \left[\boldsymbol{F}^{\mathrm{t}} \cdot \boldsymbol{F} - \boldsymbol{I}\right]/2$, cf. [54]. Reprinted from Schulte et al., European Journal of Mechanics - A/Solids 98:104854 (2023), [113], with permission under creative commons licence 4.0.

identification, only a sufficient approximation is required and, thus, only homogeneous states of deformation are taken into account. This results in lower computational costs for each simulation with a different parameter set than compared to the simulation of more complex boundary value problems. Consequently, a larger amount of various parameter combinations can be simulated within reasonable computational time. To be specific, 6×10^4 simulations were conducted for each of the exemplary experiments. However, not all of the different variations result in a reasonable combination of the model parameters and in a successful simulation. For example only 22521 of the 6×10^4 combinations were completed successfully in the case of the tensile test simulation. This demonstrates the sensitivity of the model with respect to the possible parameter combinations.

Since not only the amount of data but also the distribution of the different parameter combinations is important for the generation of a qualitative training set, the sampling of the data has an impact on the prediction capabilities of the neural network. Hence, two basic sampling methods are compared in the following.

3.1.2.2 Random sampling

For the first method, the Random Sampling (RS), a classic randomising function is used to generate 6×10^4 values for each parameter within the admissible parameter range. Thus, the required amount of random values within the interval is given, although an even distribution of all 6×10^4 values in the interval is not guaranteed, albeit the

probability for a broad distribution being high. This random sampling method can be mathematically described as

$$\begin{aligned} &R_k \in [0,1]\,, \text{ with } \quad k = 1, \ldots, 6 \times 10^4\,, \\ &\kappa_i \in [\kappa_i^{\min}, \kappa_i^{\max}]\,, \\ &\kappa_i^k = \kappa_i^{\min} + R_k\,[\kappa_i^{\max} - \kappa_i^{\min}]\,, \end{aligned} \tag{3.2}$$

where R_k denotes the random number, κ_i^k the i-th material parameter in its interval of the corresponding minimum and maximum value.

3.1.2.3 Latin Hypercube Sampling

An alternative basic method to random sampling is Latin Hypercube Sampling (LHS). For this method, the interval is divided into subintervals and a random value is generated within each of these subintervals. This leads to an even distribution over the total parameter range. In addition, the position of the values for each subinterval is random within the generated array for each parameter. Thus, well mixed parameter combinations over the whole training data set are ensured.

An LHS function returns a Latin Hypercube sample matrix X of size $n \times p$. For each column of X, the n values are randomly arranged with one value from each subinterval $(0, 1/n)$, $(1/n, 2/n)$, ... , $(1 - 1/n, 1)$, and randomly permuted, where n is the specified amount of samples and where p is the amount of variables, i.e. material parameters. Basically, a random perturbation different for each column, respectively parameter, is applied to the midpoint in each interval, e.g. for the first interval $0.5/n$. Furthermore, the distribution of the intervals is random within each column.

An example for four parameters with ten sample points is

$$X = \begin{bmatrix} 0.1893 & 0.2569 & 0.0147 & 0.5583 \\ 0.8038 & 0.1089 & 0.9378 & 0.1950 \\ 0.5995 & 0.6818 & 0.3649 & 0.3097 \\ 0.3225 & 0.8736 & 0.4487 & 0.8055 \\ 0.9183 & 0.9854 & 0.1598 & 0.2509 \\ 0.0131 & 0.3864 & 0.5924 & 0.7511 \\ 0.7916 & 0.7131 & 0.2760 & 0.6662 \\ 0.6600 & 0.5420 & 0.6877 & 0.9100 \\ 0.2740 & 0.0450 & 0.7816 & 0.0631 \\ 0.4200 & 0.4855 & 0.8760 & 0.4889 \end{bmatrix}. \tag{3.3}$$

To be specific, each column of X contains one random number in each of the 10 intervals $(0, 0.1)$, $(0.1, 0.2)$, $(0.2, 0.3)$, $(0.3, 0.4)$, $(0.4, 0.5)$, $(0.5, 0.6)$, $(0.6, 0.7)$, $(0.7, 0.8)$, $(0.8, 0.9)$, and $(0.9, 1)$. In summary, the LHS provides a more even distribution of the parameter ranges and consequently a better training data set. Nevertheless, a large

amount of samples in combination with a small parameter range and a low sensitivity of the material response with respect to parameter changes reduces the advantage of LHS over the simple random sampling.

3.1.2.4 Structure of the neural network

Considering the application in this work, a feedforward neural network is selected. To be specific, a multilayer perceptron regressor (MLPregressor) is used here. The activation function is set to the rectified linear unit function $f(x) = \max\{0, x\}$. As a solver, we employ a stochastic gradient-based optimiser suggested by Kingma, Diederik, Ba, see [87]. The learning rate is initially set to 0.0001, while the shuffling of samples within each iteration is turned off. Furthermore, the random number generation for weights and bias initialisation is fixed to 1. The definition of the hidden layers is discussed in the following paragraph. All other settings maintain the default values as described in the documentation of the scikit-learn 1.0.2 package.

In order to find the optimal depth of the neural network, six different integer parameters are introduced to generate a variety of networks while maintaining a reduced amount of parameters. Therefore, three of the parameters a, b, and c are used to generate a polynomial p of the form

$$p(x) = a\,x^2 + b\,x + c\,. \tag{3.4}$$

The polynomial is evaluated at six positions, i.e. $x = 0, 1, 2, 3, 4, 5$, to obtain the corresponding amount of neurons for the different layers. The amount of layers is defined by the last three parameters. They describe the frequency of the layers with a specified amount of neurons.

To give an example, the parameter set $p_{\mathrm{NN}} = [1, 9, 2, 6, 60, 170]$ generates the polynomial $p(x) = 6\,x^2 + 60\,x + 6$ and the corresponding network with the fully connected hidden layers $[170, 236, 314, 314, 314, 314, 314, 314, 314, 314, 314, 404, 404, 404, 404, 404, 404, 404, 404, 404, 506, 506, 620, 620]$. The first two numbers of neurons each occur only in one layer. The next two numbers each appear in 9 layers and the last two numbers each in two layers. Even though the use of only six integers with this method restricts the solution space for the possible hyperparameters, it enables a sufficiently large subset of different combinations and an efficient structure to find a sufficient set of hyperparameters.

3.1.3 Training of the neural network

This section presents the training and validation process of the neural networks based on different sampling techniques. Subsequently, the influence of a hyperparameter optimisation is demonstrated.

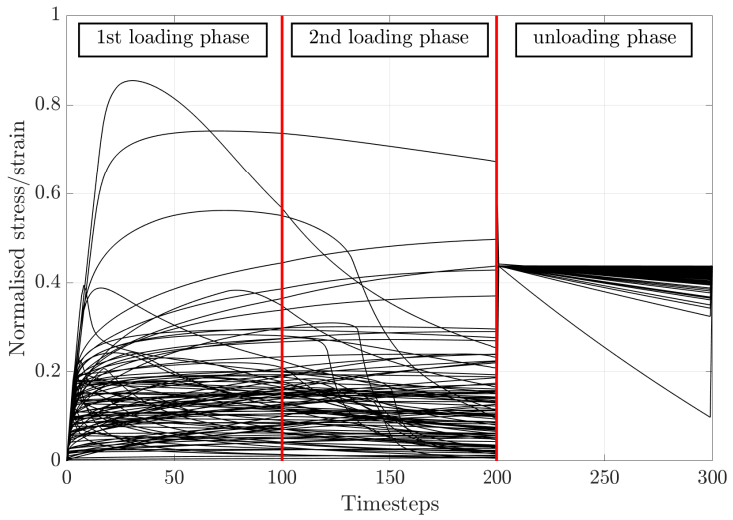

Figure 3.7: Random selection of 100 curves of the training data set already arranged in the input format for the neural network. The input data consists of three concatenated normalised modes, where the modes correspond to the structure of the desired experimental data shown in Figure 3.4. Reprinted from Schulte et al., European Journal of Mechanics - A/Solids 98:104854 (2023), [113], with permission under creative commons licence 4.0.

3.1.3.1 Training and testing of the neural network

As input data for the neural network, the load-displacement curves are not directly used. Since the displacement is prescribed in the loading phases and the force is reduced to zero during the unloading phases, the relevant information for the network are the forces, respectively stresses, for the loading phases and displacements, respectively strains, for the unloading phases. Since the stresses and strains have different units, the values are normalised based on the maximum occurring value over all simulations for each component. For reasons of simple implementation, the input data is arranged as follows: normalised stresses of the first loading phase, normalised stresses of the second loading phase followed by the normalised strain of the unloading phase. A random selection of 100 curves of the input data for the tensile test is shown in Figure 3.7. In order to demonstrate the distribution of the training data, the frequency is shown in a heatmap for both loading phases in Figure 3.8. Some exemplary curve shapes are shown in Figure 3.9.

In Section 3.1.2, the neural network was introduced, mentioning the structure of the network as well as the different sampling techniques and the parameter ranges. In the following, the mentioned structure with the initial hyperparameters is used in order to compare the performance of the network based on the different sampling methods. For this purpose, three distinct criteria are chosen:

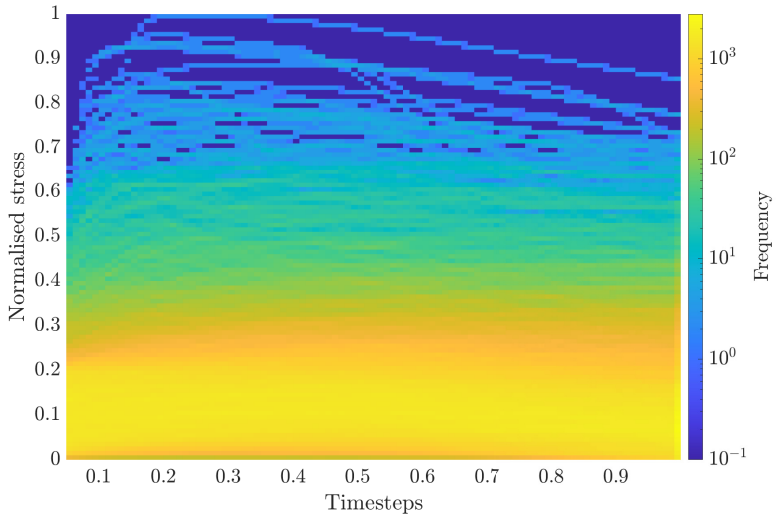

Figure 3.8: Heatmap of all curves of the training data set already arranged in the input format for the neural network demonstrating the frequency distribution and thus the modeling range. The input data consists of three concatenated normalised modes, where the modes correspond to the structure of the desired experimental data shown in Figure 3.4. Reprinted from Schulte et al., European Journal of Mechanics - A/Solids 98:104854 (2023), [113], with permission under creative commons licence 4.0.

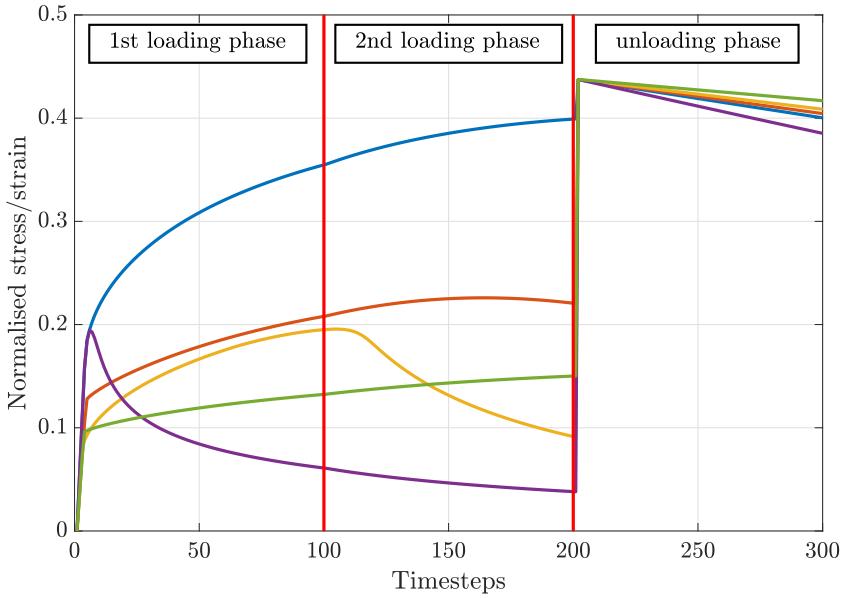

Figure 3.9: Random selection of 5 curves of the training data set already arranged in the input format for the neural network showing a view of the various curve shapes. The input data consists of three concatenated normalised modes, where the modes correspond to the structure of the desired experimental data shown in Figure 3.4. Reprinted from Schulte et al., European Journal of Mechanics - A/Solids 98:104854 (2023), [113], with permission under creative commons licence 4.0.

- The first criterion is the mean absolute error

$$\delta_{\mathrm{MAE}} = \sum_{j=1}^{n_{\mathrm{td}}} \frac{\delta_{\mathrm{AE}}^{j}}{n_{\mathrm{td}}}\,, \tag{3.5}$$

  with n_{td} being the number of test data sets. Moreover, δ_{AE}^{j} denotes the absolute error

$$\delta_{\mathrm{AE}}^{j} = \sum_{i=1}^{n_s} \frac{\left| \int \bullet_i^{\mathrm{inp}} \mathrm{d}t - \int \bullet_i^{\mathrm{pred}} \mathrm{d}t \right|}{\max\left\{ \left| \int \bullet_i^{\mathrm{inp}} \mathrm{d}t \right|, \left| \int \bullet_i^{\mathrm{pred}} \mathrm{d}t \right| \right\}} \Bigg|^{j}\,, \tag{3.6}$$

  with j denoting the number of the corresponding test data set, n_s being the number of input sections, respectively modes, e.g. $n_s = 3$, considering the deviation between the original curve of the test data set, used as input for the network, and the simulated curve based on the corresponding predicted parameter set. The deviation is summarised for all three curve sections and subsequently averaged over the whole test data set to determine the mean absolute error.

- The percentage of test data sets which have a curve deviation of less than 10 %. The 10 %-criterion was chosen in order to obtain the amount of test data sets with a sufficient accuracy for the application in this work.

- The average deviation of the original and predicted material parameters of the test data set.

The network performance based on the random sampling method results in a mean absolute error of $\delta_{\mathrm{MAE}} = 10.68\,\%$. In addition, 65.85 % of the test data expose an absolute error of less than 10 %.

In contrast, the performance based on the Latin Hypercube Sampling technique leads to a mean absolute error of $\delta_{\mathrm{MAE}} = 7.90\,\%$. Furthermore, 76.2 % of the test data feature an absolute error of less than 10 %.

The performance of both networks is visualised in Figures 3.10 and 3.11, respectively. While the deviation of each curve of the test data set from the median curve is plotted in horizontal direction, the absolute error, calculated via equation (3.6), is assigned in vertical direction. The heatmap shows the frequency of test data sets regarding both properties. Hence, a high frequency at the bottom of the figure reflects a high performance of the neural network. As it can be seen in Figure 3.10, the heatmap shows a clustering of the data sets over the whole bottom region. Thus, most of the curves are predicted quite accurately and independent of the deviation to the median curve. Nevertheless, the figure presents some data sets with a less accurate prediction and the sets have a larger frequency with a higher deviation to the median curve. Comparing

these results with those of Figure 3.11 which are based on the LHS, the average error of the prediction decreases even further, and especially those curves lying closer to the median curve have a nearly perfect match between the original curve and its prediction. Furthermore, the amount of data sets with a higher deviation also decreases.

When only taking the third criteria into account, i.e. the parameter deviation shown in Table 3.1, a summarising statement is not directly obvious since in some parameters the RS method performs better than the LHS. Interestingly, the performance of the elastic (E, ν) and plastic parameters (σ_{y_0}, h, n_p) is slightly better with the RS and slightly worse for the damage related parameters.

In conclusion, the performance of the network based on the Latin Hypercube Sampling is clearly better than the random sampling. Consequently, the LHS trained network is used in the following.

While the curve deviation shows the prediction capabilities of the neural network, the deviation of each parameter of the original and predicted values is not necessarily based on the network performance. Since the network identifies the features of the inputs—the curves—and since the network predicts a set of parameters producing a low curve deviation, the ANN provides a good result. The possible larger parameter deviation is probably based on modelling effects, e.g. several parameter combinations can lead to comparable results, i.e. different local minima exist. Considering the results in Table 3.1, the prediction of the first five parameters—elastic and plastic—is quite good, whereas the damage related material parameters show a larger deviation. Hence, either these parameters depend on each other leading to local minima or the experimental setting is not sufficient to identify these parameters. Probably both aspects apply since one unloading phase between two loading phases might be not enough in order to identify the relevant local minima.

3.1.3.2 Optimisation of the hyperparameters

As already mentioned in Section 3.1.2.4, the hyperparameters need to be optimised to find the network with the best performance. Thus, a random search algorithm was chosen to find the best possible parameter set. Since the result of the previous section was that the LHS method is superior over the RS approach, the hyperparameters were only optimised for the LHS technique.

While the initially chosen set of hyperparameters already showed quite good results, the overall net performance could be further improved with this set of hyperparameters, i.e. $p_\mathrm{NN}^\mathrm{opt} = [3, 1, 3, 27, 40, 260]$. This leads to the network structure $[260, 260, 260, 327, 327, 327, 448, 623, 852, 852, 852, 1135, 1135, 1135]$ following the scheme described in Section 3.1.2.4. The overall runtime of the complete training process increased by approximately 60 % on a standard computer. Nevertheless, considering that the training of a specific model only has to be performed once and subsequently can be applied to different experimental inputs, an increase in the network performance is worth a possible increase in computational time.

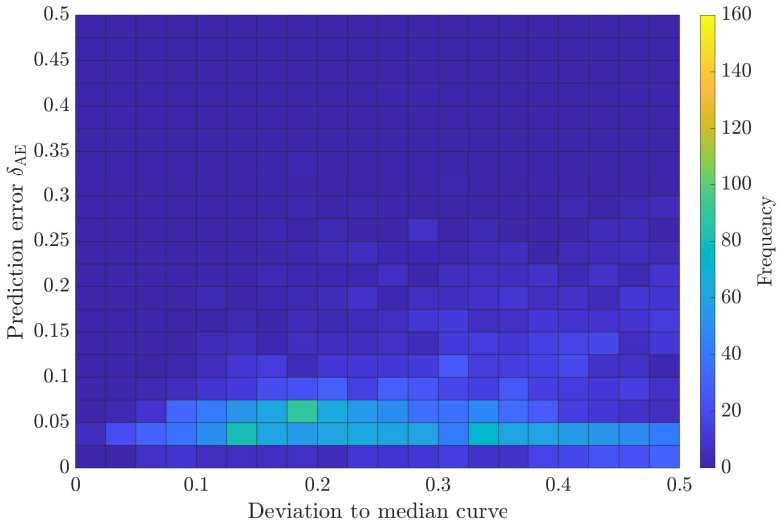

Figure 3.10: Heatmap of the network performance for the initial hyperparameters based on the RS showing the frequency of the 2k test data sets with respect to their curve deviation from the median curve and curve deviation of predicted and original curve. A clustering in the bottom of the figure reflects a high network performance. Reprinted from Schulte et al., European Journal of Mechanics - A/Solids 98:104854 (2023), [113], with permission under creative commons licence 4.0.

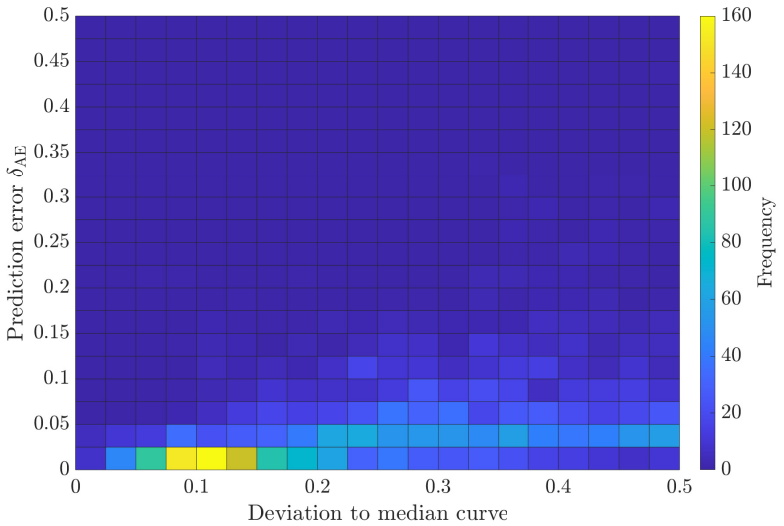

Figure 3.11: Heatmap of the network performance for the initial hyperparameters based on the LHS showing the frequency of the 2k test data sets with respect to their curve deviation from the median curve and curve deviation of predicted and original curve. A clustering in the bottom of the figure reflects a high network performance. Reprinted from Schulte et al., European Journal of Mechanics - A/Solids 98:104854 (2023), [113], with permission under creative commons licence 4.0.

Table 3.1: Average deviation of the original and predicted parameters of the complete test data set for the initial hyperparameter set based on the RS and LHS. The fixed parameters are not calibrated within this work. Reprinted from Schulte et al., European Journal of Mechanics - A/Solids 98:104854 (2023), [113], with permission under creative commons licence 4.0.

Symbol	Description	Deviation w/ RS	Deviation w/ LHS
E	Young's modulus	11.70 %	11.72 %
ν	Poisson's ratio	10.52 %	10.92 %
σ_{y_0}	initial yield stress	9.18 %	9.51 %
h	hardening parameter	8.77 %	9.19 %
n_p	hardening exponent	12.53 %	12.86 %
q_var	variable damage threshold	21.19 %	21.58 %
n_d	damage exponent	fixed	fixed
η	damage rate factor	20.19 %	19.97 %
ξ_vol	volumetric damage factor	fixed	fixed
ξ_iso	isochoric damage factor	20.06 %	19.31 %
ξ_q	threshold factor	24.89 %	24.89 %
ξ_m	effective stress factor	21.11 %	20.67 %
η_α	coupling factor	22.28 %	21.74 %
c_d	regularisation parameter	fixed	fixed
β_d	penalty parameter	fixed	fixed
q_min	initial damage threshold	21.69 %	21.57 %

The mean absolute error of the curve deviation, calculated for each test data set via equation (3.5), decreased to $\delta_\mathrm{MAE} = 6.5\,\%$. Furthermore, the amount of test data sets with a curve deviation of less than 10 % increased to 88.65 %. Hence, the network performance improved noticeably with respect to the initial guess. The performance is visualised in Figure 3.12 and can be compared to Figure 3.11 showing that the overall prediction accuracy of the network for nearly all data sets increases considerably. The dispersion of the absolute error decreases over the whole region of the test data. Thus, the heatmap reflects the good performance of the network with optimised hyperparameters. In Figure 3.13, the corresponding loss curve shows the evolution of the squared error over the training epochs.

Comparing the values of the parameter deviations in Table 3.2 and 3.1, it can be seen that the prediction accuracy increases for all of the different material parameters, except for the first three parameters which increase negligibly.

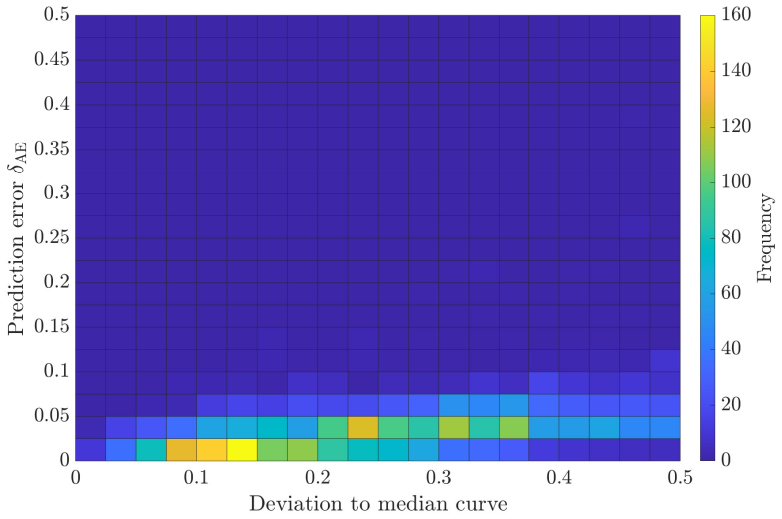

Figure 3.12: Heatmap of the network performance for the optimal hyperparameters showing the frequency of the 2k test data sets with respect to their curve deviation from the median curve and curve deviation of predicted and original curve. A clustering in the bottom of the figure reflects a high network performance. Reprinted from Schulte et al., European Journal of Mechanics - A/Solids 98:104854 (2023), [113], with permission under creative commons licence 4.0.

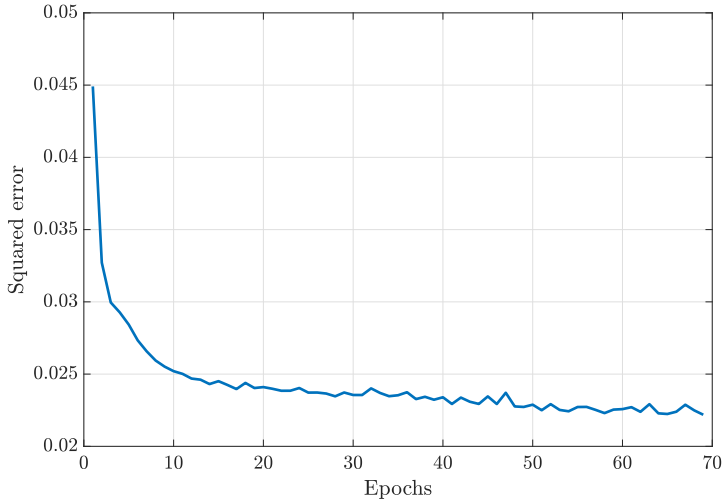

Figure 3.13: Loss curve of the network performance for the optimal hyperparameters demonstrating the evolution of the squared error over the training epochs. Reprinted from Schulte et al., European Journal of Mechanics - A/Solids 98:104854 (2023), [113], with permission under creative commons licence 4.0.

Table 3.2: Average deviation of the orignal and predicted parameters of the complete test data set for the optimal hyperparameter set. The fixed parameters are not calibrated within this work. Reprinted from Schulte et al., European Journal of Mechanics - A/Solids 98:104854 (2023), [113], with permission under creative commons licence 4.0.

Symbol	Description	Parameter deviation
E	Young's modulus	11.82 %
ν	Poisson's ratio	10.96 %
σ_{y_0}	initial yield stress	9.28 %
h	hardening parameter	7.02 %
n_p	hardening exponent	9.64 %
q_var	variable damage threshold	21.32 %
n_d	damage exponent	fixed
η	damage rate factor	19.38 %
ξ_vol	volumetric damage factor	fixed
ξ_iso	isochoric damage factor	18.97 %
ξ_q	threshold factor	24.64 %
ξ_m	effective stress factor	20.46 %
η_α	coupling factor	21.07 %
c_d	regularisation parameter	fixed
β_d	penalty parameter	fixed
q_min	initial damage threshold	21.05 %

3.1.4 Parameter identification for homogeneous states of deformation

After the testing of the neural network, experimental data is used to find a prediction of the material parameter set for a specific material. Therefore, the ANN predicts the model parameters of the experimental curve based on the knowledge obtained from the training process. This can be mathematically expressed via

$$\delta_\mathrm{EP} = \sum_{i=1}^{n_s} \frac{\int \bullet_i^\mathrm{exp} \mathrm{d}t - \int \bullet_i^\mathrm{pred} \mathrm{d}t}{\max\left\{\int \bullet_i^\mathrm{exp} \mathrm{d}t, \int \bullet_i^\mathrm{pred} \mathrm{d}t\right\}}, \tag{3.7}$$

where the $\bullet$ can be either referred to stresses or to strains depending on the segment of the curve, i.e. loading or unloading phase. Depending on the prediction capabilities of the trained networks, the deviation of the experimental and predicted curve can already be sufficiently small enough. Since the main objective of the approach developed in this work is to find an optimal starting value for a subsequent optimisation-based parameter

identification, it is advantageous, though not necessary, that the prediction is already sufficiently accurate. Thus, in the final step, the optimisation tool minimises the error functional $f(\boldsymbol{\kappa})$ in order to obtain the optimal parameter set $\boldsymbol{\kappa}^{\mathrm{opt}}$, i.e.

$$\min \left\{ f(\boldsymbol{\kappa}) = \sum_{i=1}^{n_s} \frac{\int \bullet_i^{\mathrm{exp}} \mathrm{d}t - \int \bullet_i^{\mathrm{sim}}(\boldsymbol{\kappa}) \mathrm{d}t}{\max \left\{ \int \bullet_i^{\mathrm{exp}} \mathrm{d}t, \int \bullet_i^{\mathrm{sim}}(\boldsymbol{\kappa}) \mathrm{d}t \right\}} \right\} \rightarrow \boldsymbol{\kappa}^{\mathrm{opt}} . \tag{3.8}$$

By doing so, the deviation of the experimental and simulated curves based on the current material parameter set $\boldsymbol{\kappa}$ is minimised until the optimal solution $\boldsymbol{\kappa}^{\mathrm{opt}}$ is found. In this case, the classic Nelder-Mead simplex algorithm [84] was a proper approach for the calibration of the material parameters. A more detailed description of the method and the underlying tool can be found in [104].

The optimal material parameters for two different materials shall be identified. The first material is a sheet metal DP800 and the second one is a case-hardened steel 16MnCrS5. Both are commonly used in metal forming processes and, consequently, possible damage effects within the material need to be taken into account in order to achieve an accurate prediction of the material properties occurring after the corresponding process routes. The accurate prediction of damage evolution during, e.g., forming processes allows the full utilisation of the lightweight potential of modern engineering components, cf. [126, 127]. As mentioned before, different types of experiments are available for both materials. Hence, if only one network is trained to obtain a prediction for the parameters of both materials, only the tension test can be used for the input of the neural network. Otherwise, two networks have to be trained based on a tension and an in-plane torsion test for the first metal and on a tension and compression test for the second material. Both methods shall be compared with respect to their prediction capabilities.

3.1.4.1 Network based on tensile data

In a first step, one network only based on tensile data was trained. The corresponding network performance was shown in Section 3.1.3.2. The following results are obtained on the basis of LHS and the optimal hyperparameters.

3.1.4.1.1 Steel DP800

To begin with the experimental tensile data of the DP800 from Figure 3.4 was transformed into the proper input format for the network. The network immediately presented a predicted parameter set for the material, see Table 3.3. The comparison of the corresponding simulated curve based on the predicted parameters with the experimental curve are shown in Figure 3.14. The predicted curve already matches the experimentally measured curve quite well, except that the curve lies slightly below the experimental curve over all three load phases. The deviation between the curves is only $\delta_{\mathrm{EP}} = 3.47\,\%$ which

is already a very good prediction by the network. To demonstrate the influence of the hyperparameters, the deviation of the prediction increases to $\delta_{\mathrm{EP}} = 19.28\,\%$ if the initial values for the hyperparameters, shown in Section 3.1.2.4, are used.

Table 3.3: Predicted material parameters of the DP800 based on LHS and using the optimal set of hyperparameters. The predicted parameters are compared to the optimised parameter set of the subsequent Nelder-Mead-simplex algorithm. The fixed parameters are not calibrated within this work. Reprinted from Schulte et al., European Journal of Mechanics - A/Solids 98:104854 (2023), [113], with permission under creative commons licence 4.0.

Symbol	Description	NN-prediction	Nelder-Mead	Unit
f	objective function value	3.47	1.02	%
E	Young's modulus	141.77	228.415	GPa
ν	Poisson's ratio	0.274	0.346	–
σ_{y_0}	initial yield stress	100.043	150.398	MPa
h	hardening parameter	1226.002	1205.834	MPa
n_{p}	hardening exponent	0.166	0.168	–
q_{var}	variable damage threshold	26.187	30.312	MPa
n_{d}	damage exponent	fixed at 0.667		–
η	damage rate factor	2.478	1.359	–
ξ_{vol}	volumetric damage factor	fixed at 1.0		–
ξ_{iso}	isochoric damage factor	0.973	0.747	–
ξ_q	threshold factor	10.307	7.352	–
ξ_m	effective stress factor	0.802	0.001	–
η_α	coupling factor	3.673	2.701	–
c_{d}	regularisation parameter	fixed at 0.54		N
β_{d}	penalty parameter	fixed at 0.0		MPa
q_{min}	initial damage threshold	25.623	28.392	MPa

Even if the prediction of the neural network is already very good, a subsequent Nelder-Mead simplex algorithm can increase the match of the experimental results even further. Figure 3.14d shows that nearly a perfect match of the experimental material response can be achieved by the material model with the optimised parameter set $\boldsymbol{\kappa}^{\mathrm{opt}}$, though, the stress response is slightly overestimated at the beginning of plastification. The difference based on equation (3.8) decreases to $f(\boldsymbol{\kappa}^{\mathrm{opt}}) = 1.02\,\%$. The comparison of the corresponding stress-strain curves, see Figure 3.14d, reflects the mentioned behaviour. Even though the improvement of the curve deviation is marginal, the difference in some of the material parameters is quite distinct, e.g. for the Young's modulus, see Table 3.3. This demonstrates that a different combination of the parameters can lead to a comparable material response shown in the stress-strain curves. Hence, it is still very important to pre-identify as many material parameters as possible in order to find the

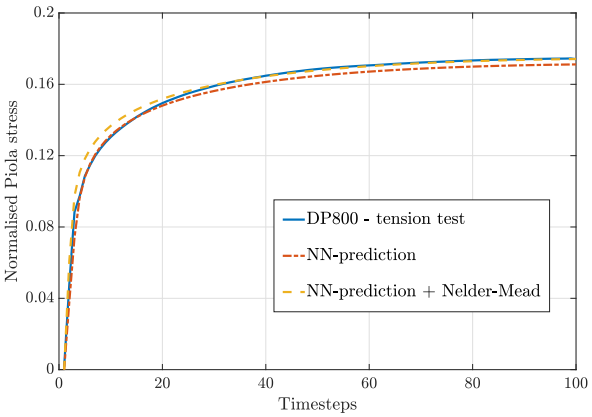

(a) Stress curves of the first loading phase of the tension test.

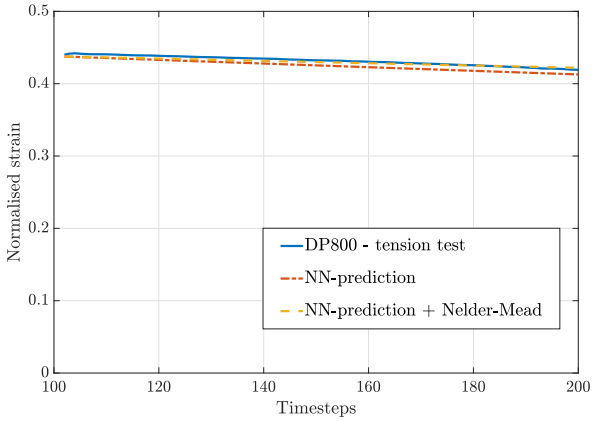

(b) Strain curves of the unloading phase of the tension test, with strain defined as $\varepsilon = \Delta l / l_0$.

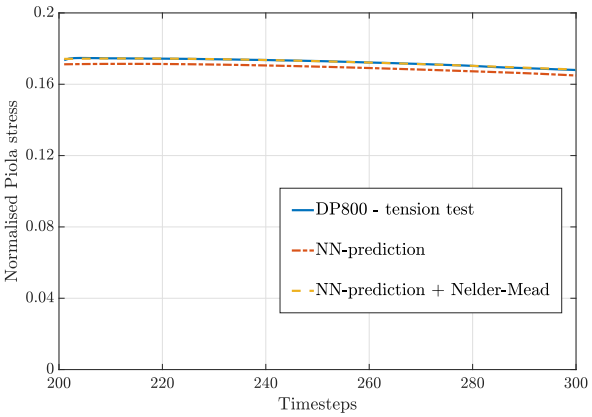

(c) Stress curves of the second loading phase of the tension test.

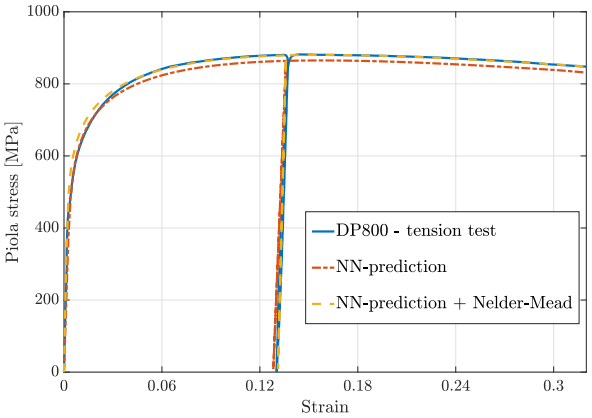

(d) Stress-strain curves of the tension test, with strain defined as $\varepsilon = \Delta l / l_0$.

Figure 3.14: For the DP800 sheet metal, the simulation results with the predicted parameter set of the neural networks, based on the training data of the tension test, are compared to the curves simulated with the optimised parameter set of the Nelder-Mead simplex algorithm and the experimental curves. Here the LHS generated the corresponding data basis. See Section 3.1.3 with regard to the separation and normalisation of the phases. Reprinted from Schulte et al., European Journal of Mechanics - A/Solids 98:104854 (2023), [113], with permission under creative commons licence 4.0.

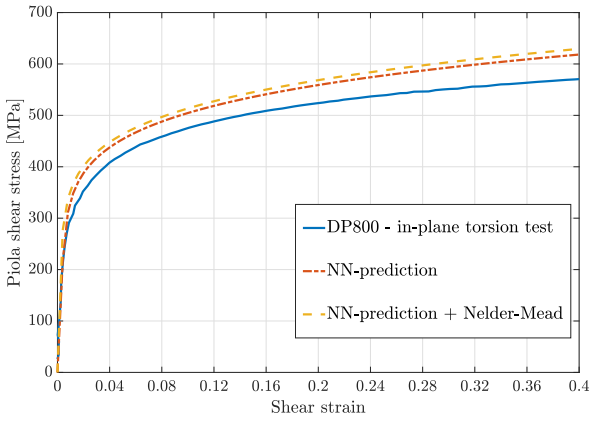

Figure 3.15: For the in-plane torsion test of the DP800 sheet metal, the curve of the Piola shear stress over the shear strain, with the shear strain defined as the related shear component of the Green-Lagrange strain tensor $\boldsymbol{E} = \left[\boldsymbol{F}^{\mathrm{t}} \cdot \boldsymbol{F} - \boldsymbol{I}\right]/2$ with the factor two, is compared to the shear stress-shear strain curve simulated with the optimised parameter set of the Nelder-Mead simplex algorithm. Here the LHS generated the corresponding data basis. Reprinted from Schulte et al., European Journal of Mechanics - A/Solids 98:104854 (2023), [113], with permission under creative commons licence 4.0.

most suitable parameter set. Nevertheless, by using the ANN for the generation of a good starting point there is at least the possibility of using such a large amount of parameters.

Since the constitutive model was so far only calibrated with respect to tensile data in the case of the artificial neural network as well as the classic optimisation approach, the final optimised set of parameters almost perfectly matches the tensile material behaviour. However, it will be important to find out how the model is capable of predicting the other characteristic behaviour patterns of the material with the optimised set of parameters. Therefore, the in-plane torsion test is simulated, once again assuming a homogeneous state under simple shear, cf. [54, 128], and compared to the experimentally measured material response, cf. Section 3.1.1. The results are shown in Figure 3.15. With a curve deviation of $\delta_{\mathrm{EP}} = 5.62\,\%$ the prediction of the shear loading case is quite accurate, though the stress level is overestimated. Since the Piola stress level was slightly higher for the simulated tension test with the optimised parameter set, the deviation from the experimental curve increases to $f(\boldsymbol{\kappa}^{\mathrm{opt}}) = 7.21\,\%$. Nevertheless, with both curves a sufficient match of the material behaviour is achieved. In Section 3.1.4.2, these results are compared to the solution if the simple shear behaviour is included in the training data of the neural network.

3.1.4.1.2 Steel 16MnCrS5

Next, the experimental data of the tensile test of the case-hardened steel 16MnCrS5, cf. Figure 3.4, is entered into the network. Considering the results in Figure 3.16, the predicted curve of the ANN matches the experimental curve quite well. The stress level is only slightly underestimated in the middle of the first loading phase and slightly overes-

timated in the second loading phase. The overall deviation of the curves is $\delta_{\mathrm{EP}} = 6.10\,\%$. The corresponding predicted material parameters are shown in Table 3.4. Nevertheless, the simulated material behaviour can never match this experimental curve perfectly since the experimentally observed Lüders extension is not included in the model.

Table 3.4: Predicted material parameters of the 16MnCrS5 based on LHS and using the optimal set of hyperparameters. The predicted parameters are compared to the optimised parameter set of the subsequent Nelder-Mead-simplex algorithm. The fixed parameters are not calibrated within this work. Reprinted from Schulte et al., European Journal of Mechanics - A/Solids 98:104854 (2023), [113], with permission under creative commons licence 4.0.

Symbol	Description	NN-prediction	Nelder-Mead	Unit
f	objective function value	6.1	2.65	%
E	Young's modulus	173.751	134.759	GPa
ν	Poisson's ratio	0.277	0.311	–
σ_{y_0}	initial yield stress	107.568	104.813	MPa
h	hardening parameter	868.199	789.801	MPa
n_{p}	hardening exponent	0.321	0.271	–
q_{var}	variable damage threshold	29.463	49.998	MPa
n_{d}	damage exponent	fixed at 0.667		–
η	damage rate factor	5.4	5.14	–
ξ_{vol}	volumetric damage factor	fixed at 1.0		–
ξ_{iso}	isochoric damage factor	1.138	1.439	–
ξ_q	threshold factor	9.327	6.166	–
ξ_m	effective stress factor	1.029	0.833	–
η_α	coupling factor	4.899	4.916	–
c_{d}	regularisation parameter	fixed at 0.54		N
β_{d}	penalty parameter	fixed at 0.0		MPa
q_{min}	initial damage threshold	13.769	12.364	MPa

After the classic optimisation, the simulated material response almost perfectly matches the experimental curve of the 16MnCrS5, except for the Lüders extension which is not included in the model, cf. 3.16. The deviation following equation (3.8) is $f(\boldsymbol{\kappa}^{\mathrm{opt}}) = 2.65\,\%$.

After the final optimised parameter set was found, the prediction accuracy with respect to the compressive material behaviour is informative. Though, in contrast to the DP800 where the shear behaviour was well predicted, the prediction of the compression test shows only a nearly perfect result until a certain strain level is reached, cf. Figure 3.17. Afterwards, the stress decreases significantly. This is due to the fact that a tension-compression asymmetry is not included in this version of the material model and that this material behaviour is not included in the training data of the neural network.

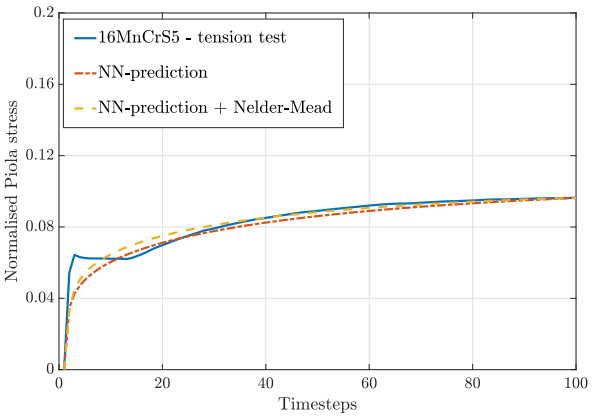

(a) Stress curves of the first loading phase of the tension test.

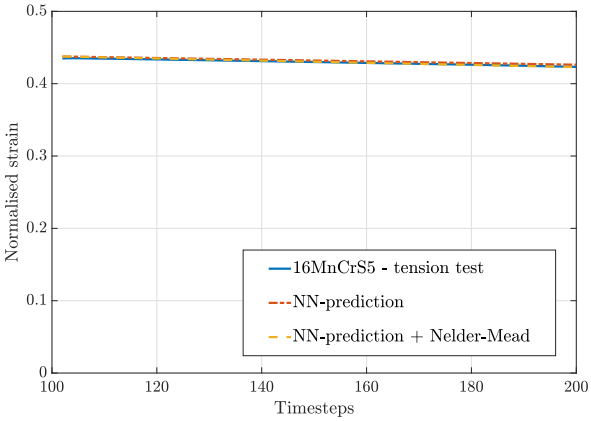

(b) Strain curves of the unloading phase of the tension test, with strain defined as $\varepsilon = \Delta l / l_0$.

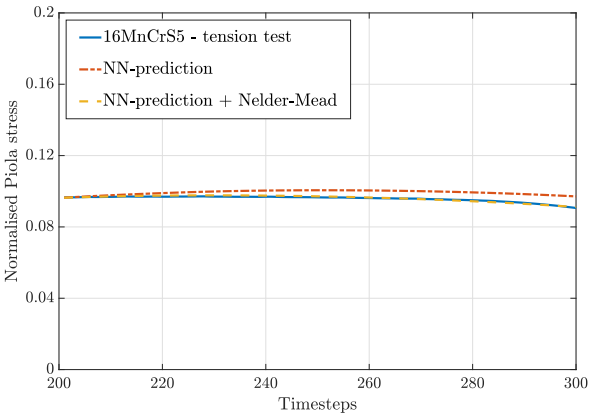

(c) Stress curves of the second loading phase of the tension test.

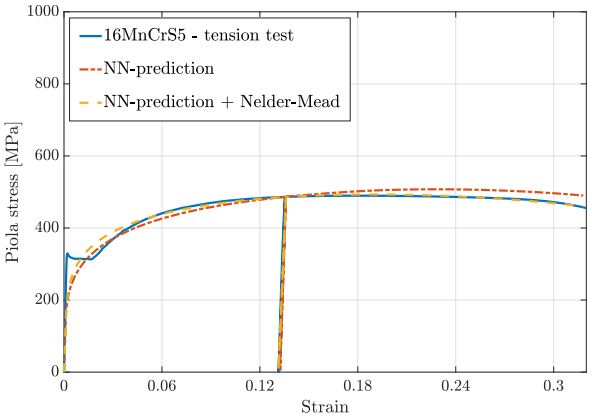

(d) Stress-strain curves of the tension test, with strain defined as $\varepsilon = \Delta l / l_0$.

Figure 3.16: For the 16MnCrS5 case-hardened steel, the simulation results with the predicted parameter set of the neural networks, based on the training data of the tension test, are compared to the curves simulated with the optimised parameter set of the Nelder-Mead simplex algorithm and the experimental curves. Here the LHS generated the corresponding data basis. See Section 3.1.3 with regard to the separation and normalisation of the phases. Reprinted from Schulte et al., European Journal of Mechanics - A/Solids 98:104854 (2023), [113], with permission under creative commons licence 4.0.

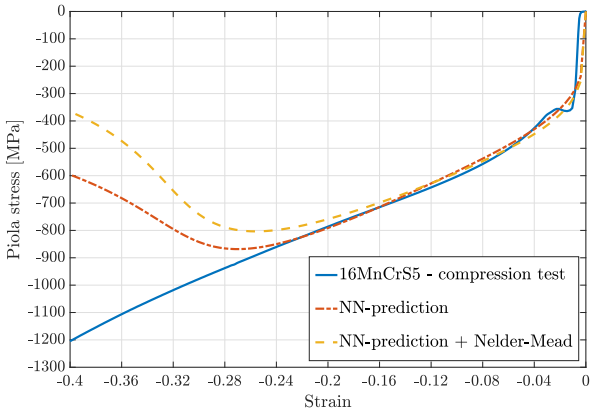

Figure 3.17: For the compression test of the 16MnCrS5 case-hardened steel, the curve of the compression Piola stress over the strain, with strain defined as $\varepsilon = \Delta l / l_0$, is compared to the compression stress-strain curve simulated with the optimised parameter set of the Nelder-Mead simplex algorithm. Here the LHS generated the corresponding data basis. Reprinted from Schulte et al., European Journal of Mechanics - A/Solids 98:104854 (2023), [113], with permission under creative commons licence 4.0.

The curve deviation reaches $f(\boldsymbol{\kappa}^{\mathrm{opt}}) = 9.69\,\%$ which is quite high compared to the very good fit of the tensile test.

3.1.4.2 Two networks each based on two experiments

In order to evaluate whether the prediction accuracy can be further improved for both loading paths, the training data contains simulations of both types of experiments in the following. However, as mentioned before, only different types of experiments are available for both materials. Hence, two different networks have to be trained based on the combination of tensile data with in-plane torsion data and tensile data with compression data, respectively. It is important to mention that, for the previous networks based only on tensile data, 22521 simulations were completed successfully. In comparison, the total data set for the following networks is clearly lower since only the intersection of material parameter combinations which were successfully finished for both types can be considered. In the case of tensile and compression data 7168 different parameter combinations and in the case of tensile and in-plane torsion data 9155 parameter sets can be used.

3.1.4.2.1 Steel DP800

In a first step, the training of the neural network based on tensile and in-plane torsion data was conducted with the optimised hyperparameter set of Section 3.1.3.2, denoted in the following as network A. Since the hyperparameter set was not fitted to the new network, it was only to be expected that the prediction would probably be less accurate than when using only one type of training data. This expected less accuracy is visible in Figure 3.18, though the difference is quite marginal. The corresponding mean absolute

error is $\delta_{\mathrm{MAE}} = 12.49\,\%$ and only 64.0 % of the test data expose an absolute error of less than 10 %. Afterwards, the hyperparameters were calibrated for the network by using both types of data for the training process, denoted as network B, and the network performance could be improved to a mean absolute error of $\delta_{\mathrm{MAE}} = 11.86\,\%$. Furthermore, 65.6 % of the test data feature an absolute error of less than 10 %. Not only the network performance seemed to improve marginally, but the prediction accuracy also only slightly improved, cf. Figure 3.18. While the stress-strain behaviour is overestimated with network A, it is marginally underestimated with network B. The curve deviation can be further improved with the subsequent Nelder-Mead simplex algorithm. Nevertheless, even after the optimisation, the accuracy of the in-plane torsion data is still overestimated while the tensile curve matches nearly perfectly, showing almost the same result as the network which was only trained with tensile data. However, the stress-strain curve of the tensile test fits more accurately since the stress level is no longer overestimated at the beginning of plastification.

3.1.4.2.2 Steel 16MnCrS5

Analogously to the sheet metal, the first network, where the training process is based on the combination of tensile and compression data, was trained with the set of hyperparameters from Section 3.1.3.2. For this setting, denoted as network A, the prediction accuracy improved markedly for both types of loading data compared to the prediction of the network based only on tensile data, see Figure 3.20. Especially the damage evolution under compression is avoided, i.e. $\dot{q} = 0$ for $\mathrm{tr}(\boldsymbol{\varepsilon}^{\mathrm{e}}) < 0$, so that a very good fit of the compressive material response is achieved. Though, since the impact of damage evolution under tensile loading is minor, damage does not occur at all. Consequently, a tension-compression asymmetry needs to be included into the material model in order to accurately simulate the correct material behaviour. Even though the prediction accuracy of network A is quite good, the corresponding network performance shows a mean absolute error of $\delta_{\mathrm{MAE}} = 12.59\,\%$. In addition, 60.3 % of the test data expose an absolute error of less than 10 %. Next, the hyperparameters were optimised for the network based on both types of simulation data, denoted as network B. The network performance could be improved markedly to a mean absolute error of $\delta_{\mathrm{MAE}} = 9.84\,\%$. Furthermore, 70.8 % of the test data feature an absolute error of less than 10 %, the prediction accuracy of the experimental curve decreased massively, not lying close to the experimental curve at all, cf. Figure 3.20. Even with the subsequent Nelder-Mead simplex algorithm it was not possible to find a minimum lying close enough to the experimental curve. However, by using the predicted parameter set of network A with the inferior performance, the Nelder-Mead simplex algorithm was capable of finding a nearly perfect solution, where not only the loading and unloading states of the tensile test but also the loading phase of the compression test nearly perfectly matched.

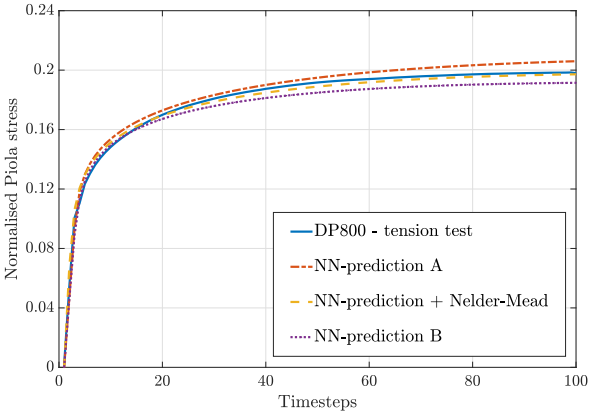

(a) Stress curves of the first loading phase of the tension test.

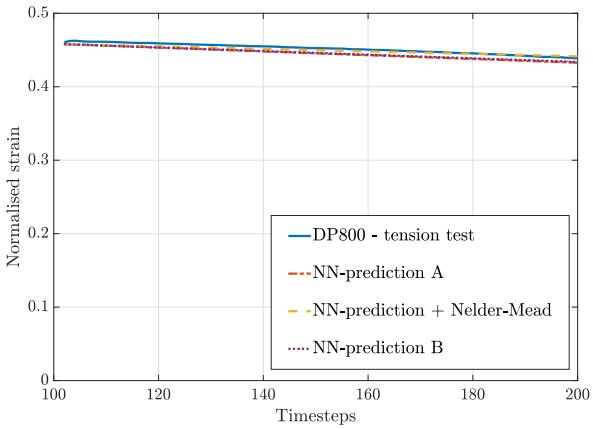

(b) Strain curves of the unloading phase of the tension test, with strain defined as $\varepsilon = \Delta l / l_0$.

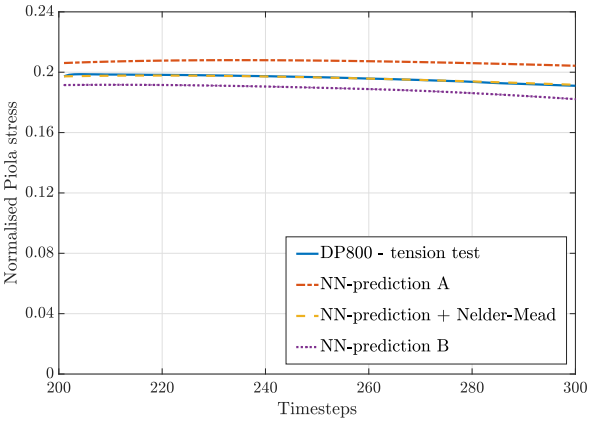

(c) Stress curves of the second loading phase of the tension test.

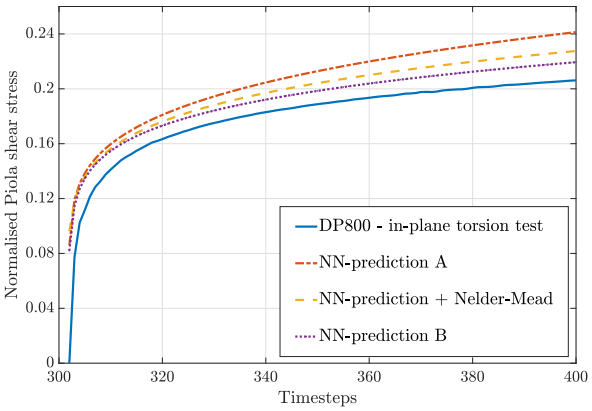

(d) Shear stress curves of the in-plane torsion test.

Figure 3.18: For the DP800 sheet metal, the simulation results with the predicted parameter sets of the neural networks A and B, based on the combined training data of the tension and in-plane torsion test, are compared to the curves simulated with the optimised parameter set of the Nelder-Mead simplex algorithm and the experimental curves. Here the LHS generated the corresponding data basis. See Section 3.1.3 with regard to the separation and normalisation of the phases. Reprinted from Schulte et al., European Journal of Mechanics - A/Solids 98:104854 (2023), [113], with permission under creative commons licence 4.0.

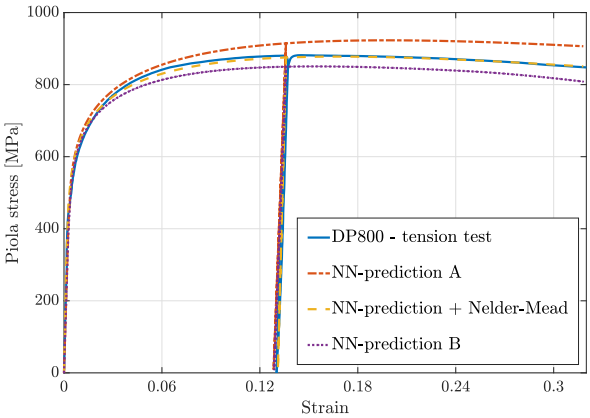

(a) Stress-strain curves of the tension test, with strain defined as $\varepsilon = \Delta l / l_0$.

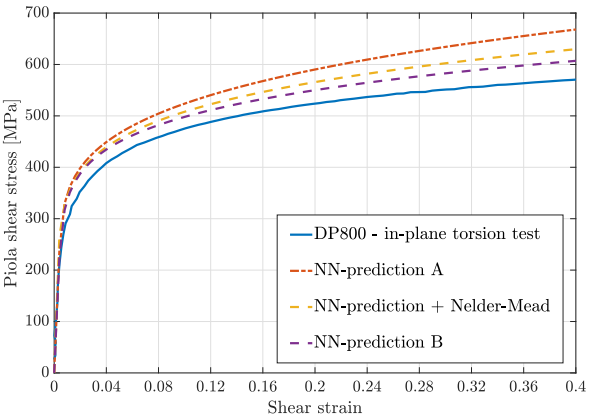

(b) Shear stress-shear strain curves of the in-plane torsion test, with the shear strain defined as the related shear component of the Green-Lagrange strain tensor $\boldsymbol{E} = \left[\boldsymbol{F}^{\mathrm{t}} \cdot \boldsymbol{F} - \boldsymbol{I}\right]/2$ with the factor two.

Figure 3.19: For the DP800 sheet metal, the simulation results with the predicted parameter sets of the neural networks A and B, based on the combined training data of the tension and in-plane torsion test, are compared to the curves simulated with the optimised parameter set of the Nelder-Mead simplex algorithm and the experimental curves. Here the LHS generated the corresponding data basis. Reprinted from Schulte et al., European Journal of Mechanics - A/Solids 98:104854 (2023), [113], with permission under creative commons licence 4.0.

3.1.4.3 Discussion

The previously presented results highlight the challenges and the benefits of using artificial neural networks for the prediction of a starting point for a subsequent parameter identification for constitutive material models. First of all, the distinct smaller set of training data—less than the half amount of the tensile data—might be one reason for the overall, sometimes worse network performance of the previous two sections. In addition, the robustness is not quantifiable yet since a larger data set would be required, especially experimental data. Furthermore, the experimental curve can be an outlier of the training data of network B where the network is not capable of giving an accurate prediction. Nevertheless, it could be advantageous to set up a preceding feature extraction, e.g. an autoencoder, in order to identify the influence of each parameter in more detail. This becomes even more important for more complex material models since it was already shown in Ktari et al. [57] that the so-called hybrid strategy works perfectly for simple types of material models with a low amount of corresponding parameters to be identified. Furthermore, a preceding feature extraction can reduce the network complexity and thus reduce the computational costs of the training process.

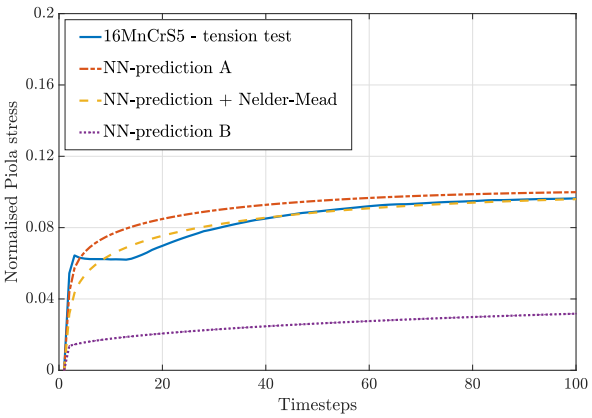

(a) Stress curves of the first loading phase of the tension test.

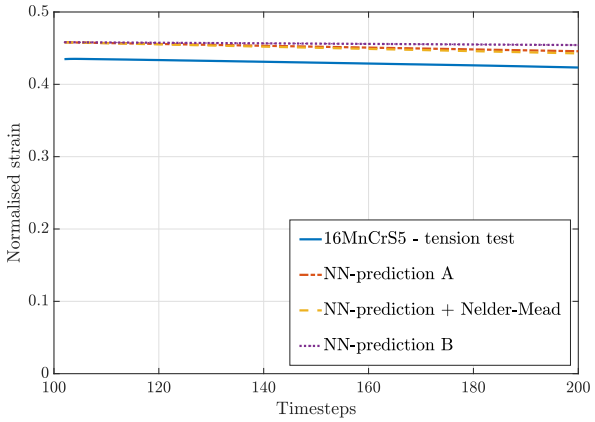

(b) Strain curves of the unloading phase of the tension test, with strain defined as $\varepsilon = \Delta l / l_0$.

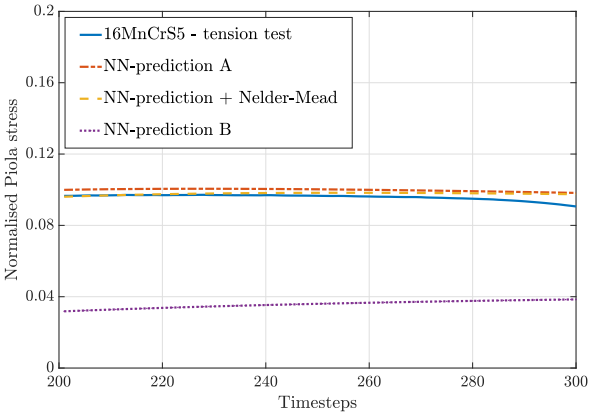

(c) Stress curves of the second loading phase of the tension test.

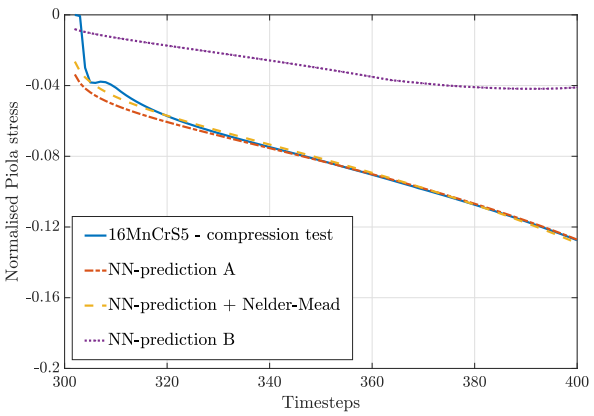

(d) Stress curves of the compression test.

Figure 3.20: For the 16MnCrS5 case-hardened steel, the simulation results with the predicted parameter sets of the neural networks A and B, based on the combined training data of the tension and compression test, are compared to the curves simulated with the optimised parameter set of the Nelder-Mead simplex algorithm and the experimental curves. Here the LHS generated the corresponding data basis. See Section 3.1.3 with regard to the separation and normalisation of the phases. Reprinted from Schulte et al., European Journal of Mechanics - A/Solids 98:104854 (2023), [113], with permission under creative commons licence 4.0.

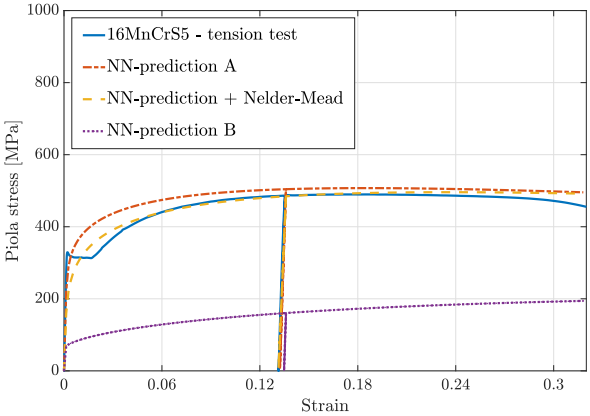

(a) Stress-strain curves of the tension test, with strain defined as $\varepsilon = \Delta l / l_0$.

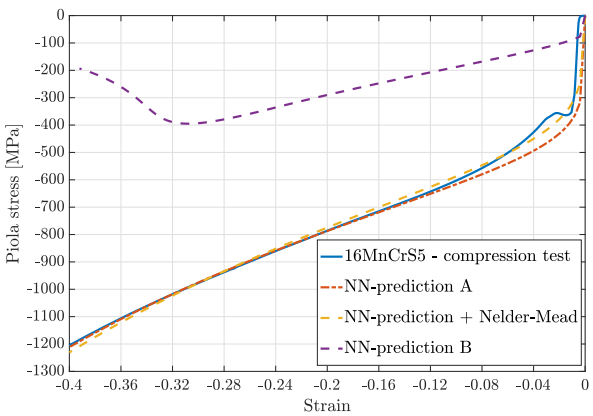

(b) Stress-strain curves of the compression test, with strain defined as $\varepsilon = \Delta l / l_0$.

Figure 3.21: For the 16MnCrS5 case-hardened steel, the simulation results with the predicted parameter sets of the neural networks A and B, based on the combined training data of the tension and compression test, are compared to the curves simulated with the optimised parameter set of the Nelder-Mead simplex algorithm and the experimental curves. Here the LHS generated the corresponding data basis. Reprinted from Schulte et al., European Journal of Mechanics - A/Solids 98:104854 (2023), [113], with permission under creative commons licence 4.0.

3.2 Machine-learning assisted parameter identification applied to a laminate-based material model for ferroelectrics

After the general structure of the hybrid approach was explained and demonstrated previously with regard to a finite plasticity model coupled to (gradient-enhanced) damage, another application example is presented in this section. For this purpose, a different material model is chosen—an electro-mechanically coupled laminate-based model for ferroelectric materials, see Section 2.3. This example provides several advantages emphasising the benefits and capabilities of the hybrid approach. The chosen model is completely different to the previous example and describes another class of materials exhibiting an electro-mechanical coupling and, thus, the characteristic loading path sequences which have to be considered for the parameter identification are totally different. Furthermore, in Dusthakar et al. [17], the authors had to develop a sophisticated strategy to obtain proper starting values for a subsequent PI of the two remaining model parameters, cf. Section 2.5.3. The general experimental setting is depicted in that section. The authors employed a generic algorithm in order to find initial guesses for the material parameters. To this end, they performed the calibration procedures independently for each of the different applied stress magnitudes to receive a list of parameter values, and a suitable starting point was subsequently chosen for each parameter. This starting set was used for the calibration of the parameters where the experimental data of all stress

magnitudes was considered simultaneously. The overall effort of the calibration process of the parameters can be reduced by employing the presented new hybrid strategy. The implemented tool is able to deal with different kinds of simulation solvers and various kinds of concatenated loading path sequences by incorporating only small adjustments in the code. To give another example of a machine learning framework, the Keras API of TensorFlow is chosen to generate the ANN for this material model.

For the generation of the training data, the range has to be defined of both fitting parameters $\boldsymbol{\kappa} = \{m, c\}$, with m denoting the viscous-like parameter and c the hysteresis shape exponent, influencing the remnant energy contribution, cf. Section 2.3 and 2.5.3. While the first parameter is restricted to a range of $m \in [1, 5]$, for the second parameter $c \in [1, 10]$ turned out to be an admissible range. In total a set of 10000 parameter combinations was generated by using the previously mentioned Latin Hypercube Sampling. However, not all of these parameter combinations lead to successful simulations of the defined loading path, cf. Section 2.5.3, such that only approximately half of the combinations where successful and thus usable for the training data set.

The characteristic information of this material class is shown by the butterfly and dielectric hysteresis curves depicted in Section 2.5.3. Thus, two characteristic curves are generated for each loading setting. In Shieh et al. [114], a total of six different compressive stress levels were applied between 0 MPa and 2.7 MPa, such that 12 different curves have to be considered in the parameter identification process. For further details please be referred to Section 2.5.3. Since the cyclic electric field E_3 is prescribed, the strains ε_{33} and dielectric displacements D_3 for the different stress magnitudes are normalised and concatenated in order to generate the input of the ANN. Since in [17] most of the parameters for $BaTiO_3$ were already taken from the literature, only the two remaining parameters m and c constitute the corresponding output of the ANN.

As in the previous example, 20% of the overall simulated data set was separated as test data and not part of the network training. After the ANN was trained, the test data set is employed to analyse the deviation of the predicted to the original parameters of the test data set. As it can be seen in Table 3.5, the average deviation of the parameters is less than 1% for both parameters in the case of the optimal set of hyperparameters. Even the occurring maximum deviation of the first parameter for one specific set is only 1.14% and for the second parameter only 6.8%. Thus, the trained ANN is capable of predicting the laminate-based material model very accurately.

Table 3.5: Average deviation of the original and predicted parameters of the complete test data set for the initial hyperparameter set based on the LHS.

Symbol	Description	Parameter deviation
m	viscous-like parameter	0.23%
c	hysteresis shape exponent	0.91%

However, the prediction of the parameters by the network for the experimental data of $BaTiO_3$ varies from the optimal parameter set identified with the SQP algorithm in

[17]. While the viscous-like parameter is at least near the optimal solution, the hysteresis shape exponent is higher than the identified result, cf. Table 3.6. Nevertheless, comparing the butterfly and hysteresis curves on the left sides of Figures 3.22-3.25, it can be seen that the deviation of both simulated responses—with the predicted and the calibrated parameter set—deviate markedly from the experimentally measured curves. While the deviation of the hysteresis curves is on a comparable level for the six different applied constant compressive stress magnitudes and the calibrated solution is always slightly better than the predicted solution, the deviation of the butterfly curves increases distinctly with a decreasing applied compressive stress level. While the butterfly curves generally fit better with the calibrated solution, the predicted solution is capable of reflecting some sections of the curves better, e.g. the connection point of the butterfly wings for some stress levels. Considering the predicted and calibrated solution, the predicted parameters can already be used as proper starting values for a subsequent classic parameter identification leading to the same minimum. Nevertheless, taking the parameter deviations of the test data set and the curves in the figures into account, it is clear that the simulated material response of the model is not capable of perfectly matching the experimental data. Two important notable differences are e.g. the asymmetry and the variation of the butterfly curves under different applied compressive stress levels. Thus, the experimental data of the butterfly curves was symmetrised with respect to the y-axis—at $E_3 = 0\,\mathrm{kV/mm}$ by mirroring the wing of the positive side—in order to investigate if the prediction quality by the network increases. It is shown in Table 3.6 and on the right sides of Figures 3.22-3.25 that the prediction is closer to the optimal solution with the symmetrised experimental data as input for the ANN. Hence, the ANN is capable of perfectly predicting the simulated material response of the model, but since the experimental data deviates markedly from the simulated material behaviour, the ANN has to extrapolate for a prediction which decreases its overall accuracy with respect to experimental data.

Table 3.6: Predicted two remaining material parameters of the laminate-based model based on LHS and using the optimal set of hyperparameters. Comparison of the predictions based on the original experimental data and on the symmetrised experimental data to the optimal set of the SQP optimisation.

Symbol	Description	NN-prediction	NN-prediction sym.	SQP	Unit
f	objective function value	76.69	69.42	54.77	-
m	viscous-like parameter	1.664	1.615	1.494	-
c	hysteresis shape exponent	9.766	7.323	3.648	-

This application demonstrates the capabilities of the hybrid strategy by employing ANNs. Even if all material parameters can be uniquely identified in the testing phase, indicating that the parameters are independent from each other, the predicted solution using experimental data might clearly deviate. Nevertheless, for the hybrid strategy, the prediction is still an appropriate starting value for a subsequent classic parameter identification.

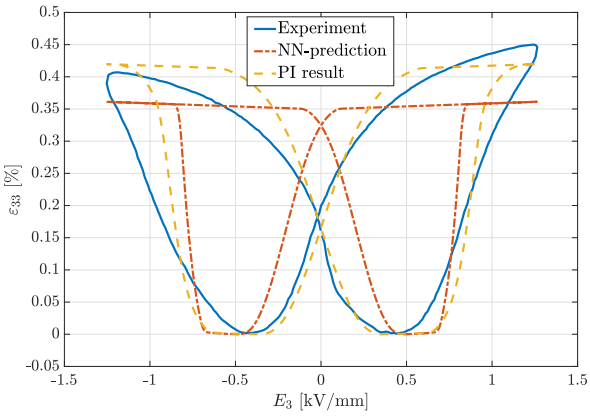

(a) Butterfly curves based on the original experimental data under a constant compressive stress of 2.7 MPa.

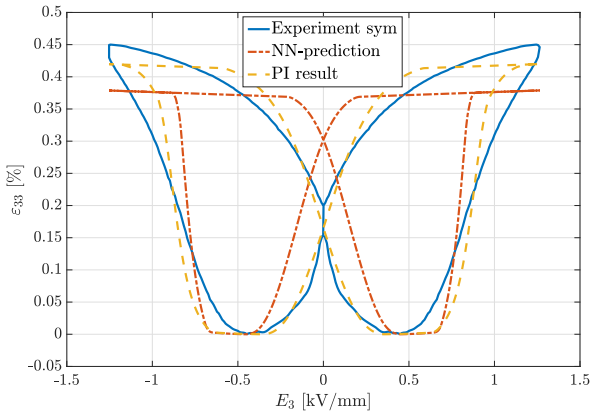

(b) Butterfly curves based on the symmetrised experimental data under a constant compressive stress of 2.7 MPa.

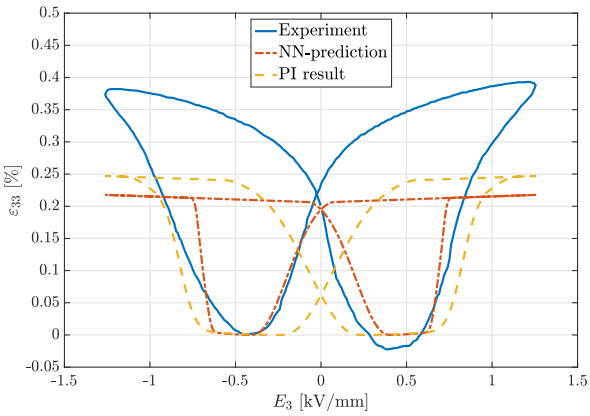

(c) Butterfly curves based on the original experimental data under a constant compressive stress of 1.7 MPa.

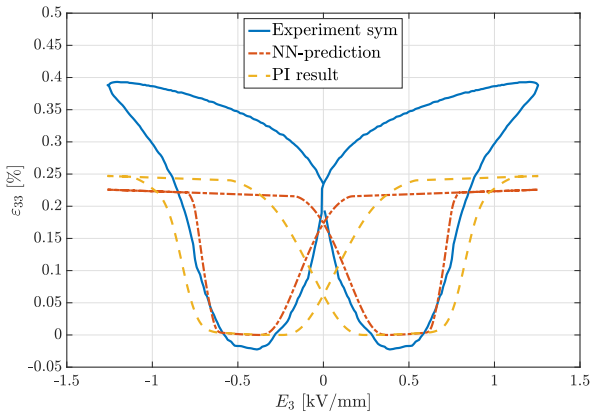

(d) Butterfly curves based on the symmetrised experimental data under a constant compressive stress of 1.7 MPa.

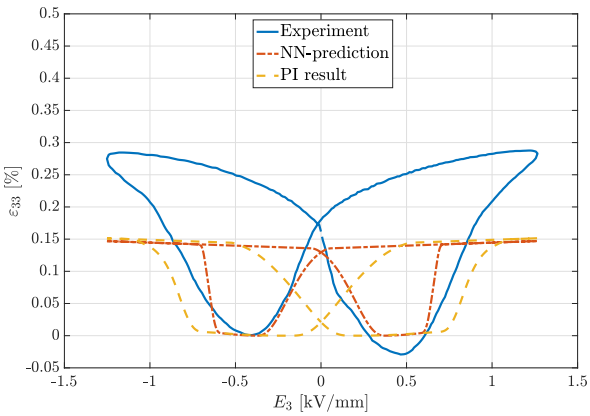

(e) Butterfly curves based on the original experimental data under a constant compressive stress of 1.2 MPa.

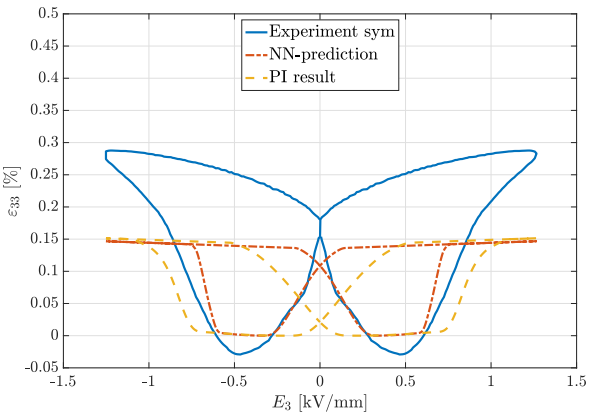

(f) Butterfly curves based on the symmetrised experimental data under a constant compressive stress of 1.2 MPa.

Figure 3.22: Simulated and experimentally measured butterfly curves under various constant compressive stress magnitudes part I—the trained ANN predicts the parameters based on the original experimental data on the left side and on the symmetrised experimental data of the butterfly curves on the right side. Symmetrisation of the butterfly curves is performed due to model properties.

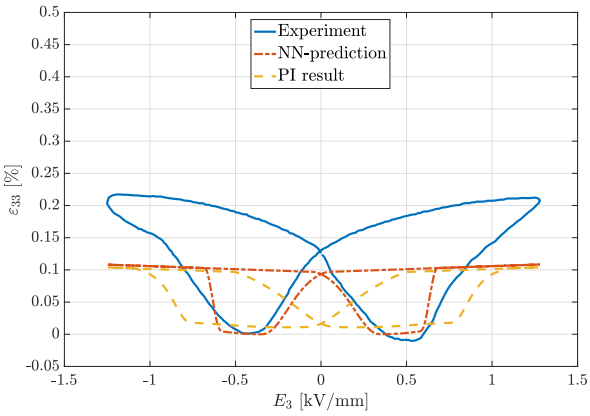

(a) Butterfly curves based on the original experimental data under a constant compressive stress of 0.9 MPa.

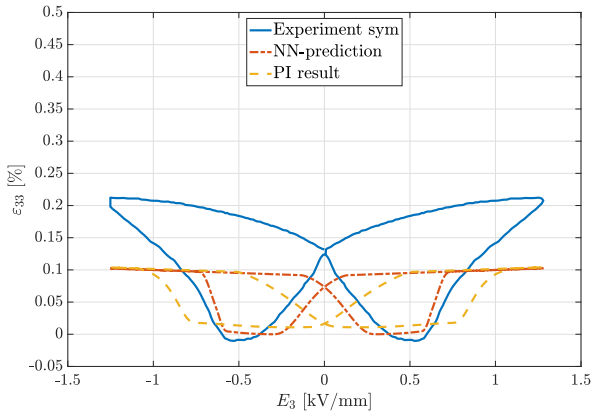

(b) Butterfly curves based on the symmetrised experimental data under a constant compressive stress of 0.9 MPa.

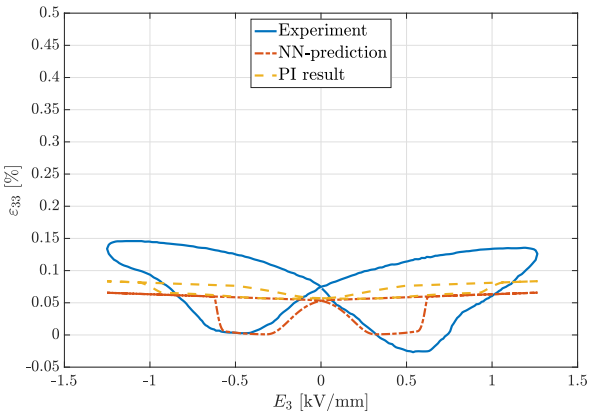

(c) Butterfly curves based on the original experimental data under a constant compressive stress of 0.5 MPa.

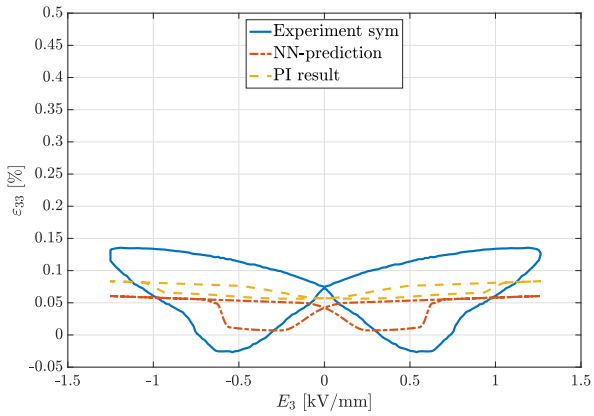

(d) Butterfly curves based on the symmetrised experimental data under a constant compressive stress of 0.5 MPa.

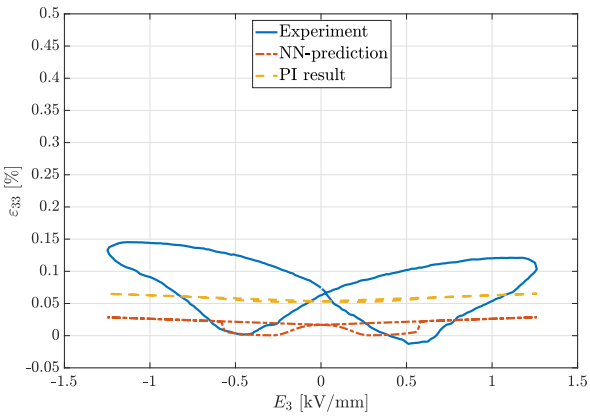

(e) Butterfly curves based on the original experimental data under a constant compressive stress of 0 MPa.

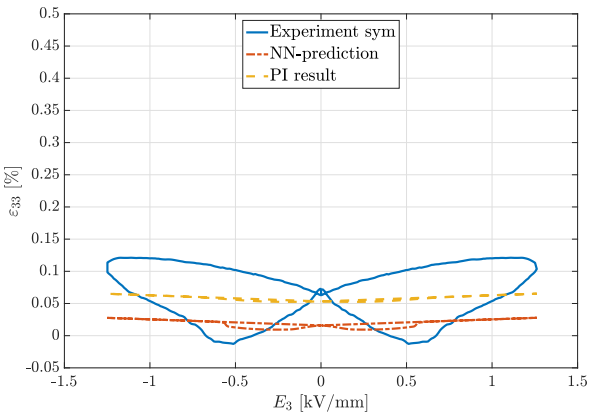

(f) Butterfly curves based on the symmetrised experimental data under a constant compressive stress of 0 MPa.

Figure 3.23: Simulated and experimentally measured butterfly curves under various constant compressive stress magnitudes part II—the trained ANN predicts the parameters based on the original experimental data on the left side and on the symmetrised experimental data of the butterfly curves on the right side. Symmetrisation of the butterfly curves is performed due to model properties.

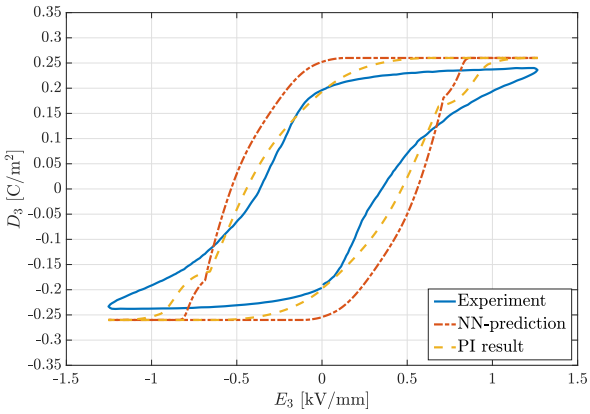

(a) Hysteresis curves based on the original experimental data under a constant compressive stress of 2.7 MPa.

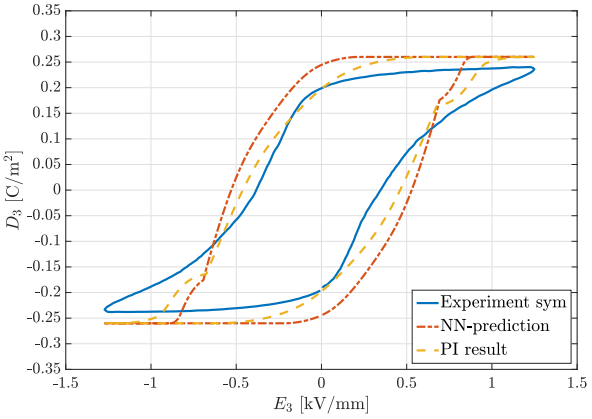

(b) Hysteresis curves based on the symmetrised experimental data under a constant compressive stress of 2.7 MPa.

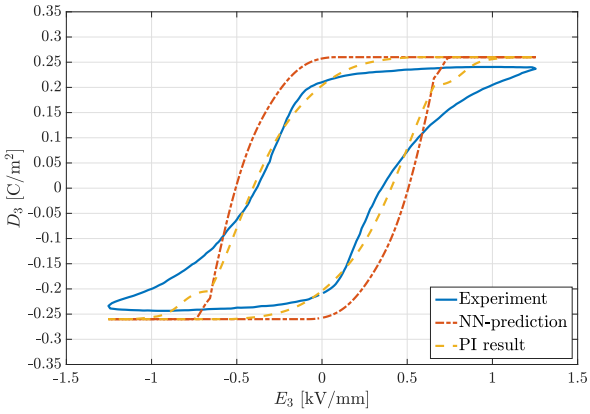

(c) Hysteresis curves based on the original experimental data under a constant compressive stress of 1.7 MPa.

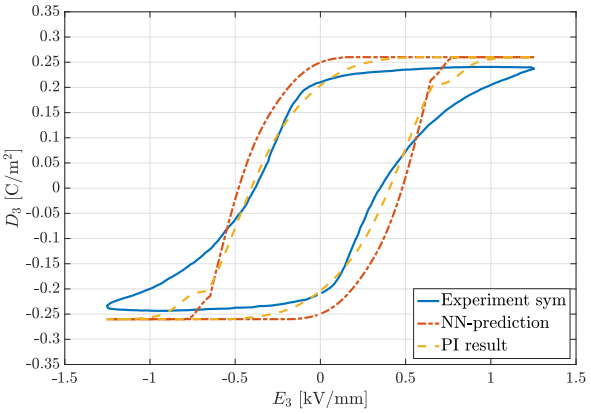

(d) Hysteresis curves based on the symmetrised experimental data under a constant compressive stress of 1.7 MPa.

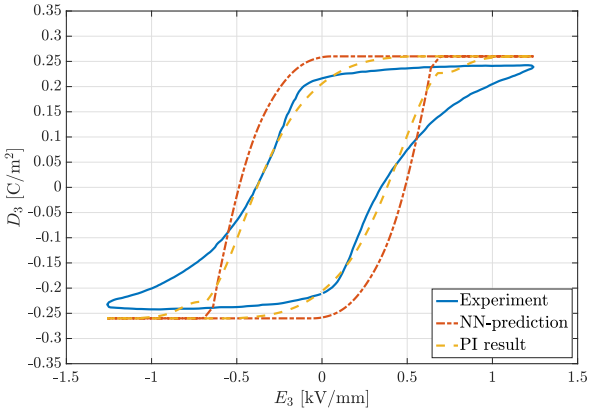

(e) Hysteresis curves based on the original experimental data under a constant compressive stress of 1.2 MPa.

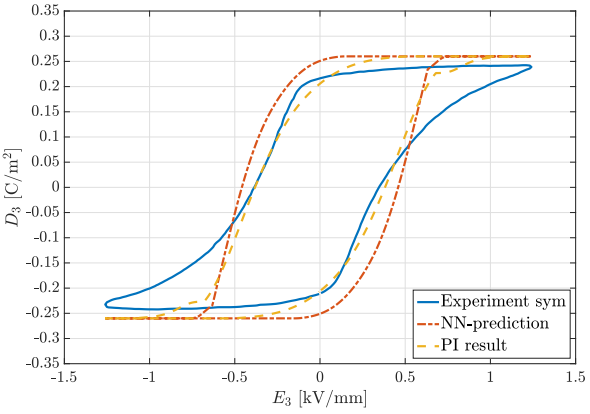

(f) Hysteresis curves based on the symmetrised experimental data under a constant compressive stress of 1.2 MPa.

Figure 3.24: Simulated and experimentally measured hysteresis curves under various constant compressive stress magnitudes part I—the trained ANN predicts the parameters based on the original experimental data on the left side and on the symmetrised experimental data of the butterfly curves on the right side. Symmetrisation of the butterfly curves is performed due to model properties.

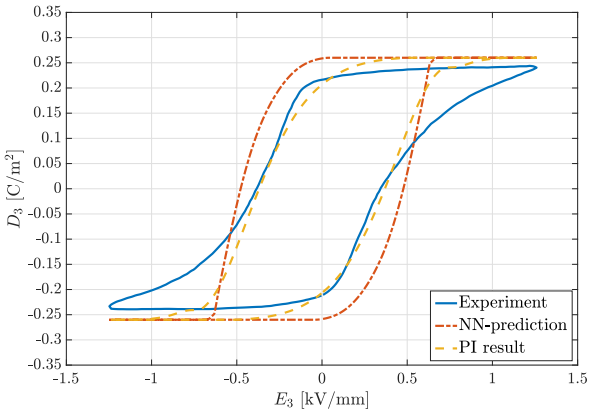

(a) Hysteresis curves based on the original experimental data under a constant compressive stress of 0.9 MPa.

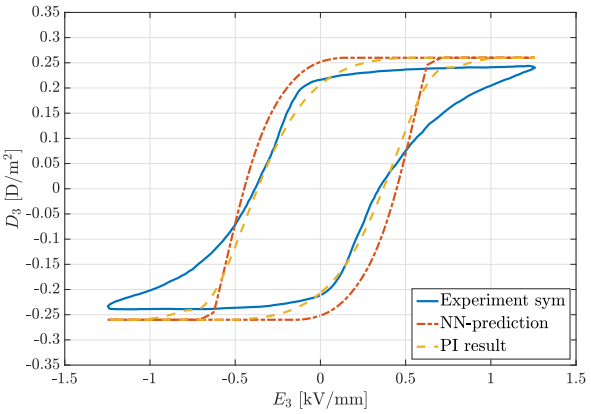

(b) Hysteresis curves based on the symmetrised experimental data under a constant compressive stress of 0.9 MPa.

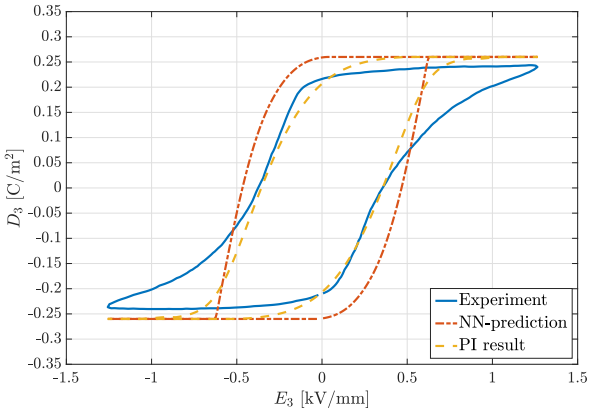

(c) Hysteresis curves based on the original experimental data under a constant compressive stress of 0.5 MPa.

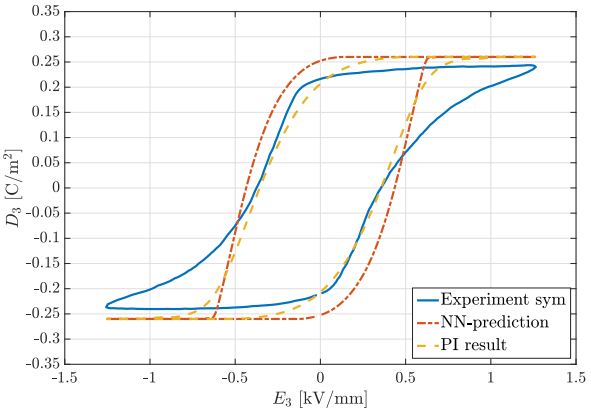

(d) Hysteresis curves based on the symmetrised experimental data under a constant compressive stress of 0.5 MPa.

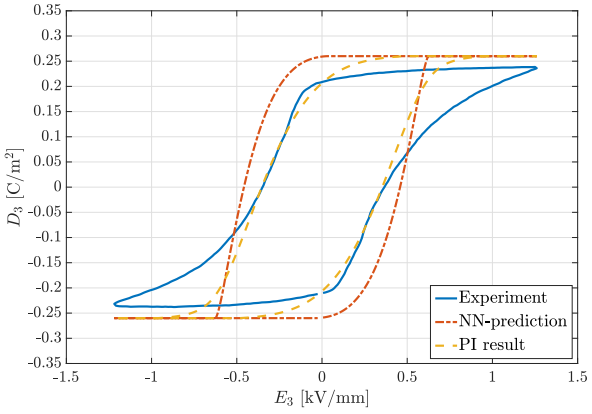

(e) Hysteresis curves based on the original experimental data under a constant compressive stress of 0 MPa.

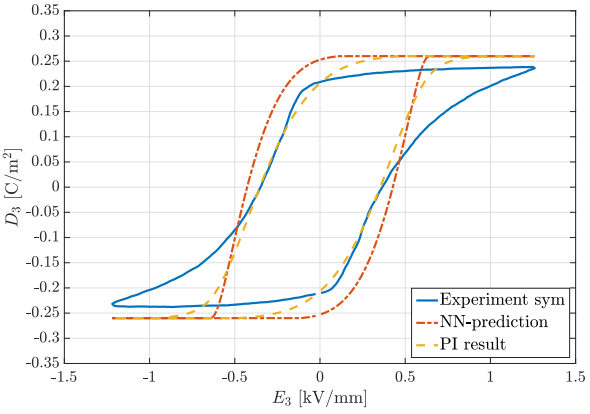

(f) Hysteresis curves based on the symmetrised experimental data under a constant compressive stress of 0 MPa.

Figure 3.25: Simulated and experimentally measured hysteresis curves under various constant compressive stress magnitudes part II—the trained ANN predicts the parameters based on the original experimental data on the left side and on the symmetrised experimental data of the butterfly curves on the right side. Symmetrisation of the butterfly curves is performed due to model properties.

4 Parameter identification based on inhomogeneous states of deformation

Considering several different kinds of material models, at least some of the material parameters can be directly identified based on standard experiments incorporating only homogeneous states of deformation, e.g. the Young's modulus or the yield limit. However, the more complex the material models, the more model parameters exist which cannot be directly identified based on the previously mentioned experiments since these experiments do not provide sufficient information. Hence, especially for non-local material models, experiments with inhomogeneous states of deformation are required. In order to take the different deformation states into account, field data—such as strains or displacements—has to be considered in the objective function of the parameter identification process. Thus, a multi-objective optimisation is necessary where not only the load-displacement data contributes to the objective function but also the field data. A parameter identification framework was already developed in a basic form by Schulte [112]. In this chapter, a complex multi-objective parameter identification process is presented. In this regard, a parameter identification framework was implemented in Schowtjak et al. [104] which is summarised in Section 4.1 and subsequently applied to different materials and corresponding material models in Sections 4.2 and 4.3. However, since the difficulty of generating appropriate starting values for the parameter identification remains, the second step of the hybrid strategy is presented in Section 4.3.5 where the predicted parameter set of the ANN for the DP800 sheet metal is used as a starting set for the multi-objective optimisation of the finite plasticity model coupled to gradient-enhanced damage.

4.1 Parameter identification tool for multi-objective optimisations

In order to be able to consider all kinds of data for the objective function, e.g. strains, displacements or microstructural data, the parameter identification tool *ADAPT—A*

Diversely Applicable Parameter Identification Tool was implemented, cf. [104]. ADAPT provides material parameters for constitutive models for the application to continuum mechanical analyses for finite deformations. The tool is implemented in Python since it is a free programming language including a library with a remarkable amount of different packages. The free, open source code is available on GitHub [26].

4.1.1 Optimisation process

In Figure 4.1, the flowchart of ADAPT is depicted. Subsequent to the selection of an initial guess for the parameter set, the FE-model is simulated. Next, the results are compared to the experimental data while iteratively updating the material parameters until convergence is reached. ADAPT is implemented in a way in order to ensure the efficiency, robustness and flexibility of the underlying optimisation scheme.

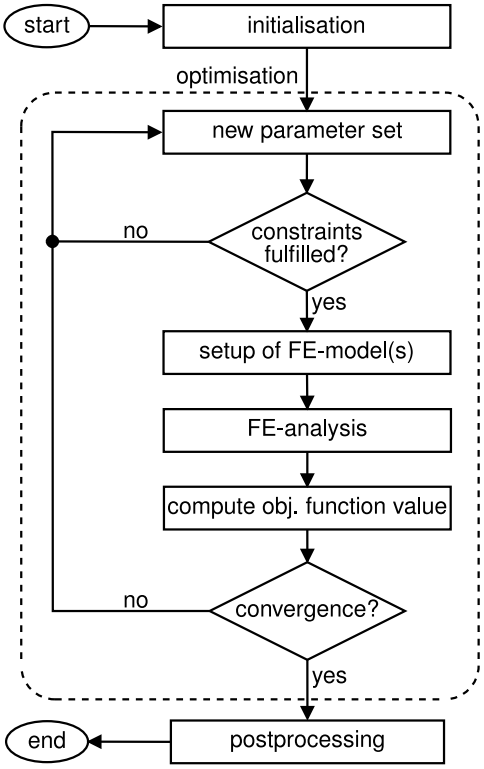

Figure 4.1: The Flowchart shows the parameter identification process as implemented in ADAPT. The iterative optimisation process is controlled by a Python framework. Reprinted from Schowtjak et al., International Journal of Mechanical Sciences 213:106840 (2022), [104], with permission under creative commons licence 4.0.

As in the previous sections, the parameter set is defined as $\boldsymbol{\kappa}$. For the corresponding inverse parameter identification, the following optimisation problem

$$\min(f(\boldsymbol{\kappa})), \forall \boldsymbol{\kappa} \in \mathcal{K}, \text{ with } \mathcal{K} = \{\boldsymbol{\kappa} \,|\, \boldsymbol{h}(\boldsymbol{\kappa}) = \mathbf{0}, \boldsymbol{g}(\boldsymbol{\kappa}) \leq \mathbf{0}\} \tag{4.1}$$

has to be solved, cf. Equation (2.84) and Section 2.4, with $f(\boldsymbol{\kappa})$ representing the scalar objective function which describes the error between experiment and simulation. Contributions $\boldsymbol{h}(\boldsymbol{\kappa}) = \mathbf{0}$ and $\boldsymbol{g}(\boldsymbol{\kappa}) \leq \mathbf{0}$ denote the equality and inequality constraints, respectively. The error between the data from the experiment $\bullet_i^{\text{exp}}$ and the simulation $\bullet_i^{\text{sim}}$ for each of the sample points can be calculated by using the root sum of squares

$$f(\boldsymbol{\kappa}) = \sqrt{\frac{1}{n_{\text{sp}}} \sum_{i=1}^{n_{\text{sp}}} w_i \left[\bullet_i^{\text{sim}}(\boldsymbol{\kappa}) - \bullet_i^{\text{exp}}\right]^2}, \tag{4.2}$$

which is generally used as the objective function in a common formulation. Integer n_{sp} represents the number of sample points in space and time and w_i are weighting coefficients, providing the possibility to introduce different weights to different sample points. In the equation, $\bullet$ can denote any quantity of interest, such as reaction forces or local displacements and strains. In the following, only purely mechanical problems are examined. However, the framework generally also allows for the inclusion of thermal effects, as discussed in, e.g., [95, 97]. Furthermore, electro-mechanically coupled material models can be calibrated as well to the corresponding characteristic experimental data, as it was performed by Dusthakar et al. in [17], cf. the summary in Section 2.5.3. The root sum of squares-function provides the advantage that statistical outliers are particularly penalised due to its quadratic form.

In contrast to strains which only account for displacements arising in deformations, displacements—experimentally measured with DIC—usually contain rigid body motions. The rigid body motions have to be excluded from the experimental data in order to compare the experimentally measured displacements to the simulation results. Relative displacements are an alternative approach which can be considered in the objective function following Rose and Menzel in [97], or the strains can be directly calculated from the DIC-data.

In general, in ADAPT the optimisation algorithms of the *SciPy* package *optimise* are incorporated in order to solve the minimisation problem, see [132]. However, the user is able to implement additional algorithms if necessary due to the open-source publication of the tool. The default optimisation algorithm in ADAPT is the Nelder-Mead-simplex algorithm as a gradient-free method since it turned out to be efficient in solving complex problems with a larger number of model parameters (>5) [84]. The chosen default algorithm provides a robust process since the derivative is not required, but in general many iterations are needed. For many optimisation algorithms, the efficiency highly depends on the chosen initial guess for the parameter set. If a good starting point is selected, the

calibration process can be very efficient. However, if a disadvantageous initial guess was chosen, it can be difficult to efficiently achieve proper results. Stochastic algorithms can be used for these cases since they scan large ranges of the parameter space, cf. Section 2.4. Hence, such algorithms are helpful for specific problems, but in general require a large number of objective function evaluations to obtain an optimal parameter set. Furthermore, the algorithms permit a higher probability of finding the global minimum or at least a local minimum with a lower functional value. As an alternative to the Nelder-Mead-simplex algorithm, the differential evolution algorithm is implemented in ADAPT. Since not all of the possible optimisation algorithms allow the incorporation of constraints for the parameter space, the penalty method is implemented in order to consider the violation of parameter boundaries in the calculation of the objective function. While the incorporation of this method reduces the efficiency of the calibration, it ensures the consideration of important constraints for the model parameters, e.g. the Poisson's ratio.

4.1.2 Postprocessing and interpolation

In addition, the framework of ADAPT contains a postprocessing subroutine in Python which automatically evaluates the output databases (odb-file) for Abaqus by extracting all the relevant data. However, all node and element sets have to be correctly specified in the input-file and config-file, since the user is otherwise required to modify the routine. In general, the experimentally measured data points and the FE node points do not coincide with respect to their locations in space and time. Thus, an interpolation in space and in time is required. The interpolation is divided implementation-wise into integral data, e.g. force-displacement data and field data, e.g. displacement or strain fields. In general, forces are measured at different time steps or at displacements associated with the current loading of the specimen. Regarding the computational efficiency, the data set with the higher resolution is interpolated onto the one containing a lower amount of sample points. In the case of field data, the data is generally measured in the section on the surface of the specimen by using DIC over the time. Besides displacements and strains, field data sets can be basically any kind of data which can be experimentally measured and numerically predicted, e.g. void fractions, texture or hardness. In contrast to the one-dimensional interpolation, Python offers no package containing an interpolation algorithm for irregular—with respect to the spatial distribution—two-dimensional data sets. Therefore, the interpolation framework

$$\bullet = [1 - a - b]\ \bullet_1 + a\ \bullet_2 + b\,\bullet_3\ , \tag{4.3}$$

was implemented, cf., e.g., Scheday[101] and Kleuter [52], with

$$a = \frac{[y_3 - y_1]\,[x - x_1] - [x_3 - x_1]\,[y - y_1]}{[y_3 - y_1]\,[x_2 - x_1] - [x_3 - x_1]\,[y_2 - y_1]} \text{ and} \tag{4.4}$$

$$b = \frac{[y_1 - y_2]\,[x - x_1] + [x_2 - x_1]\,[y - y_1]}{[y_3 - y_1]\,[x_2 - x_1] - [x_3 - x_1]\,[y_2 - y_1]}\,. \tag{4.5}$$

In this scheme, any considered quantity $\bullet$ is interpolated from the three support points $\bullet_i$ with its corresponding coordinates x_i and y_i to the particular one $\bullet$ at location x, y. Usually the scheme is applied to displacement and strain fields. While in the case of strains, the integration point positions are used, the node point coordinates are chosen in the case of displacements. It has to be mentioned that, while the measured strain field is located on the surface of the specimen, the simulated strains are calculated at the integration points which may be located on or close to the surface. If the integration point lies within the finite element, the distance to the surface of the specimen depends on the discretisation of the FE mesh. However, it was demonstrated in a sensitivity study that the simulated strains of the integration points closest to the surface of the sample can be considered if a sufficiently large amount of hexahedral elements is given across the thickness of sheets. A sketch of the interpolation scheme is given in Figure 4.2.

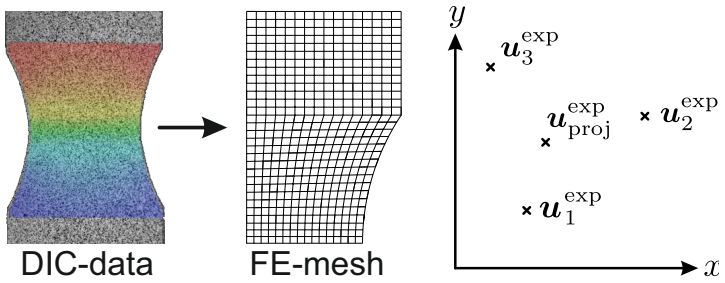

Figure 4.2: Schematic overview of the spatial two-dimensional interpolation. The experimentally measured displacements $\boldsymbol{u}_i^{\mathrm{exp}}$ at the locations x_i, y_i are interpolated onto the FE nodes. Reprinted from Schowtjak et al., International Journal of Mechanical Sciences 213:106840 (2022), [104], with permission under creative commons licence 4.0.

It is important to ensure that the interpolation error is reduced to a minimum. Therefore, the three support points have to be chosen in a way that they span a triangle around the query point. Furthermore, the vertices should have the minimum distance to the query point, as shown in Figure 4.3a. Thus, a nearest neighbour search algorithm was chosen from the Python library to obtain the support points closest to the query point. Furthermore, the ray casting algorithm [124], as shown in Figure 4.3b, was used to ensure that the query point lies within the triangle spanned by the three vertices.

(a) Interpolation sketch **(b)** Ray casting algorithm scheme

Figure 4.3: The corresponding support points are selected based on the comprising of a triangle surrounding the query point $\boldsymbol{x}$ with the least distance of the of this query point to each support point $\boldsymbol{x}_i$ with coordinates x and y, schematically depicted in (a). In (b), the ray casting algorithm is illustrated which is employed to ensure that the query point lies within the triangle spanned by the three support points. The query point lies inside the triangle if a straight line has an odd number of intersections, cf. p_1, or if lying outside if the intersection number is even, see p_2. Reprinted from Schowtjak et al., International Journal of Mechanical Sciences 213:106840 (2022), [104], with permission under creative commons licence 4.0.

Furthermore, if the time spacing in the experiment differs from the simulation time, an additional linear interpolation of the quantities in time is required and implemented following

$$\bullet_i^{\mathrm{exp}} = \frac{t_2 - t_i}{t_2 - t_1} \bullet_1^{\mathrm{exp}} + \frac{t_i - t_1}{t_2 - t_1} \bullet_2^{\mathrm{exp}} \,, \tag{4.6}$$

with t_i representing the step times of the simulation. Since the resolution of the experimental time steps is generally higher than within the simulations, the experimental data is interpolated onto the simulation time steps, where t_1 and t_2 are the experimental time steps before and after t_i, respectively.
As mentioned before, the overall interpolation process is automatically processed in ADAPT. Furthermore, considering the computational cost, the user can select whether the interpolation should be performed only once prior to the optimisation process or within each iteration, where the latter is not required in most application cases.

4.1.3 Multi-objective optimisation

In many optimisation problems more than one objective is usually required for the optimisation process. Thus, multiple objective functions have to be defined and simultaneously optimised. The straight forward solution of the multi-objective optimisation is to reformulate the set of n objective functions

$$\boldsymbol{f}(\boldsymbol{\kappa}) = [f_1(\boldsymbol{\kappa}), f_1(\boldsymbol{\kappa}), ..., f_n(\boldsymbol{\kappa})]^{\mathrm{t}} \tag{4.7}$$

into one single objective function where the normalised sum of all components is considered

$$f(\boldsymbol{\kappa}) = \sum_{i=1}^{n} \frac{f_i(\boldsymbol{\kappa})}{\hat{f}_i} \ , \tag{4.8}$$

with $\hat{f}_i$ denoting a scalar-valued quantity larger than zero which is of the same unit as the associated objective function $f_i(\boldsymbol{\kappa})$. The single objective function values of the first iteration turned out to be a proper choice for the normalisation. Though, as a consequence, the solution depends on the initial parameter set. In general, a multi-objective optimisation problem does not possess a unique solution, since the different objective functions might lead to opposite directions. The design of a lightweight component is a perfect example for this case where a sufficient stiffness has to be achieved while simultaneously reducing the weight of the component as much as possible. In these cases with no unique optimal solution, a Pareto-optimal solution is chosen instead. A Pareto-

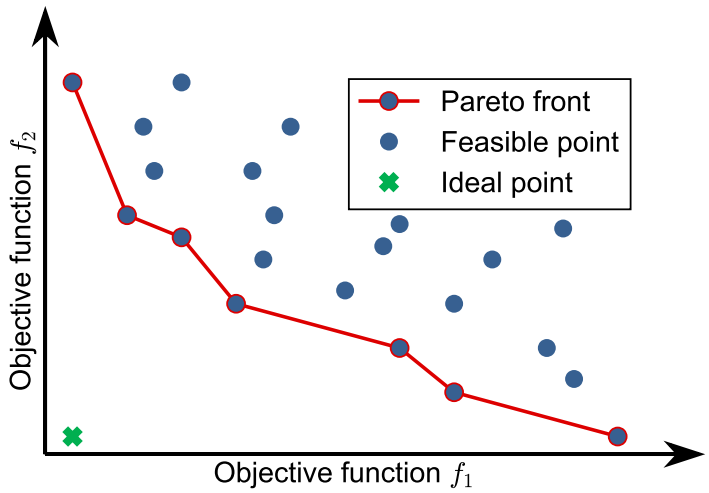

Figure 4.4: Visualisation of the Pareto method when a minimisation problem of two objectives is required. The ideal point depicts the perfect minimum if both objectives could be minimised independently to their minimal objective function value. However, since both objectives cannot be optimised independently, the Pareto front depicts all possible points from which the overall optimum cannot be further improved without increasing the function value of one objective. Reprinted from Schowtjak et al., International Journal of Mechanical Sciences 213:106840 (2022), [104], with permission under creative commons licence 4.0.

optimal solution is found if an improvement cannot be achieved without worsening the other attributes, as shown in Figure 4.4. If the solution of each objective is combined to

a vector, the ideal vector $\boldsymbol{f}^*$ is defined. By using the global criterion method its distance

$$f(\boldsymbol{\kappa}) = \sqrt{\sum_{i=1}^{n} \left[\frac{f_i^* - f_i(\boldsymbol{\kappa})}{f_i^*} \right]^2} \tag{4.9}$$

to the vector function $\boldsymbol{f}(\boldsymbol{\kappa})$ is minimised and thus can be handled as a single-objective minimisation problem. If the correlation of the particular parameters are to be analysed, the impact of each parameter on the objective function can be investigated. Fossum [21] proposed an approach in this regard. Thereby, the derivative $\boldsymbol{q}_i = \mathrm{d}\boldsymbol{f}(\boldsymbol{\kappa})/\mathrm{d}\kappa_i$ has to be evaluated and it has to be investigated whether single parameters κ_i impact the objective function similarly. Hence, unit vectors

$$\boldsymbol{q}_i^* = \frac{\boldsymbol{q}_i}{||\boldsymbol{q}_i||} \quad \text{for} \quad ||\boldsymbol{q}_i|| \neq 0 \tag{4.10}$$

associated to two different material parameters, i.e. κ_i and κ_j with $i \neq j$, are co-linear if $\theta_{ij} = \boldsymbol{q}_i^* \cdot \boldsymbol{q}_j^* = 1$ such that the parameters correlate. In the ideal case, where the underlying model is formulated optimally and the data set is appropriate, the matrix coefficients are $\theta_{ij} = 0$ if $i \neq j$ and $\theta_{ij} = 1$ if $i = j$.

4.1.4 Boundary conditions

Depending on the complexity of the corresponding material model, the computational cost of each iteration is important for the overall computation time. Thus, the reduction of the model using e.g. symmetry properties results in saving computational time. The consideration of an eighth of the sample is often sufficient for the simulations, as in the case of an appropriately symmetric flat test specimen made of isotropic material or of anisotropic material oriented in such manner that the material symmetry planes coincide with the geometric symmetry planes. Moreover, it should be guaranteed that the experimental data reflects symmetry conditions as well. The displacement boundary conditions are directly taken from the measured DIC-data, see Figure 4.5 and [110]. Using the measured displacements for the displacement boundary conditions of the simulations is required if only a section of the specimen is simulated. This is explained in more detail in Section 4.2.

4.1.5 Implementation details

In order to enable the employment of other functionalities, an implementation of a modular manner was chosen for ADAPT. In the provided implementation, the optimisation process can be directly started using Abaqus as the FE-solver. However, considering the modular structure, a different FE-software can be employed if a script for the extraction

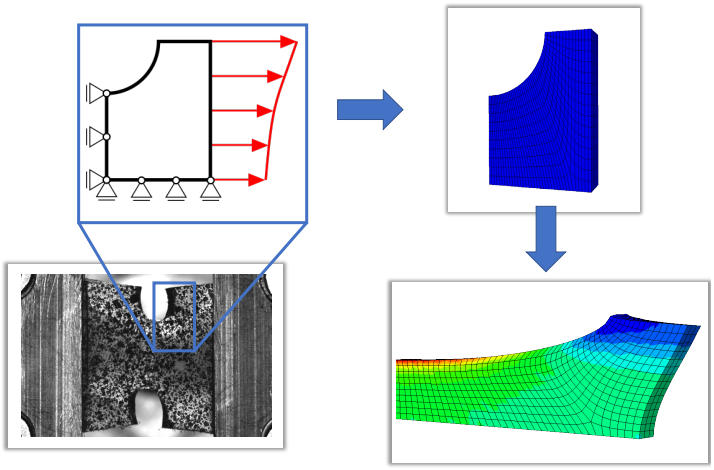

Figure 4.5: The displacement boundary conditions for the simulations of a section of the specimen are obtained from the experimentally measured DIC-data, see [110]. Reprinted from Schowtjak et al., International Journal of Mechanical Sciences 213:106840 (2022), [104], with permission under creative commons licence 4.0.

of relevant output data is implemented. Even though a graphical user interface (GUI) was not generated for ADAPT due to its large amount of modification features, the framework can be easily applied to different material models and boundary value problems if specific node and element sets are defined. In order to check the performance of the overall optimisation process the results can be visualised such that all kinds of difficulties which may occur are identifiable. In order to prevent the loss of any data, e.g. the current solution state, in the case of unforeseen aborts or computer shutdowns, *log*-files containing all important information such as warnings are automatically generated. Furthermore, an *iter*-file containing all data related to the parameter identification process is created to save the optimisation history. In general, the overall parameter identification process using FE-simulations is numerically expensive and especially increases with the complexity of the underlying material model or the boundary value problem. Therefore, ADAPT contains a restart option for the Nelder-Mead-simplex algorithm where the history of the iteration results in the *iter*-file is used. In contrast, in the case of gradient-based optimisation methods, the optimisation can be simply restarted by using the parameter set of the last saved iteration. Furthermore, several different experiments can be considered for the parameter identification process simultaneously in ADAPT. In this case, the numerical efficiency is improved by paralysing the computation of these FE-models.

4.2 Application to self-diagnostic poly(dimethylsiloxane) elastomer

A first application example of a multi-objective optimisation process is given for the viscoelastic material model coupled to gradient-enhanced damage in a finite strain setting, presented in Section 2.2. While the viscoelastic material parameters were already identified in a first step with regard to homogeneous states of deformation in Section 2.5.2, the damage-related parameters are calibrated in this section based on inhomogeneous states of deformation.

4.2.1 Inhomogeneous deformation tests

Apart from the experiments with homogeneous deformation states, an additional experiment with an inhomogeneous deformation state is carried out in order to identify the damage related material parameters. The general experimental setting, e.g. testing machines, has already been presented in Section 2.5.2.1. Considering the regularised gradient-enhanced damage framework, specific information on localisation effects is needed for the identification. Hence, with regard to the possible specimen dimensions, a notched rectangular shape was chosen, see Figure 4.6a. A constant displacement rate of 20.0 µm/s was applied until the sample with an initial length of 10 mm, width of 10 mm, radius of 2 mm and a thickness of 2.2 mm tore apart. In Figures 4.6a-4.6d, prominent states of the experiment are visualised. Moreover, Figure 4.6e shows the corresponding load-displacement-curve.

4.2.2 Parameter identification based on inhomogeneous states of deformation

In the following, the previously identified Yeoh and relaxation parameters, see Section 2.5.2, are used to identify the damage-related material parameters η_d, κ_d, n_iso, and c_d via the tensile test with inhomogeneous deformation states presented in Section 4.2.1. In contrast to the identification of the viscoelastic parameters, the constitutive driver is not sufficient enough to capture the material behaviour of the gradient-enhanced damage model. Thus, a finite element (FE) formulation is required. Therefore, the material model was implemented into a UMAT in Abaqus, as already mentioned in Section 2.2.5.

In addition, a parameter identification tool was implemented in Python, using the Nelder–Mead-Simplex algorithm of the scipy-package. In contrast to the calibration of the Yeoh and relaxation parameters, it did not suffice to solely consider the difference in the Piola stress P_{11} or the (clamping) displacement u_1, depending on the experiment, for the goal function f of the optimisation. Since the gradient terms—capturing the mesh-objectivity of damage—of the regularised damage framework are activated by inhomogeneous deformation states, the difference in the displacement field between the

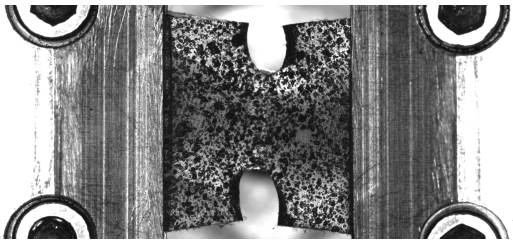

(a) Specimen before loading.

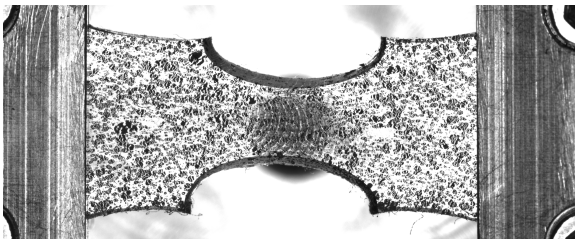

(b) Specimen at $t = 554.64\,\mathrm{s}$.

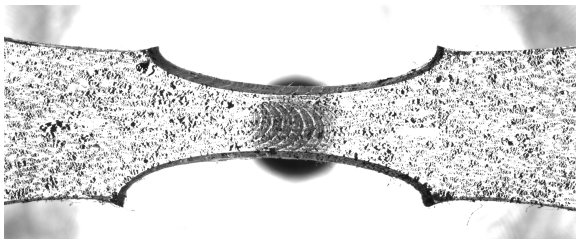

(c) Specimen at $t = 1141.0\,\mathrm{s}$, just before tearing starts.

(d) Specimen at $t = 1407.0\,\mathrm{s}$, after tearing.

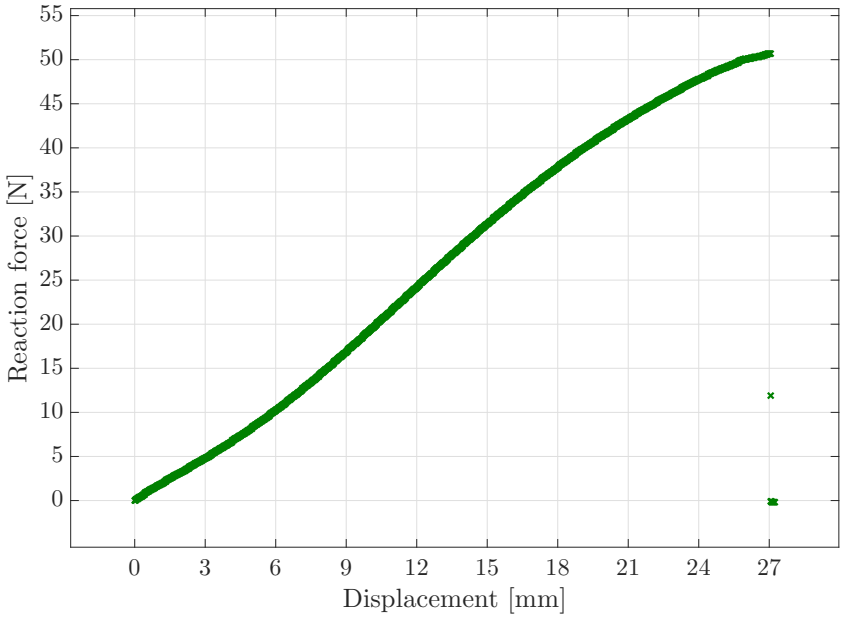

(e) Load-displacement-curve.

Figure 4.6: Experimental results of the tensile test of a notched specimen presenting photos of the sample at characteristic time steps as well as the load-displacement-curve. Reprinted from Schulte et al., Materials 13(14):3156 (2021), [110], with permission under creative commons 4.0.

simulated and experimental material response needs to be added to the goal function apart from the difference in the reaction force

$$f = \sum_t \sum_{i=1}^{n_{\mathrm{np}}} w_u \left\| \boldsymbol{u}_{ti}^{\mathrm{exp}} - \boldsymbol{u}_{ti}^{\mathrm{sim}}(\boldsymbol{\kappa}) \right\|^2 + \sum_t w_F \left| F_t^{\mathrm{exp}} - F_t^{\mathrm{sim}}(\boldsymbol{\kappa}) \right|^2 , \tag{4.11}$$

where n_{np} denotes the number of node points considered, w_u the weighting factor for the displacement contribution, and w_F the weighting factor for the impact of the reaction force. The number of node points was the number of element nodes on the surface of the specimen in the FE simulations. The experimental data was interpolated onto those node points via a 2D-interpolation scheme prior to the parameter identification following Kleuter [52], see Section 4.1.2.

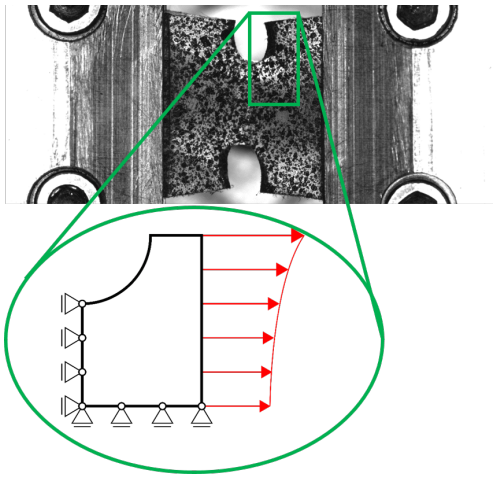

(a) Sketch of the simulated part of the specimen using symmetry properties of the sample.

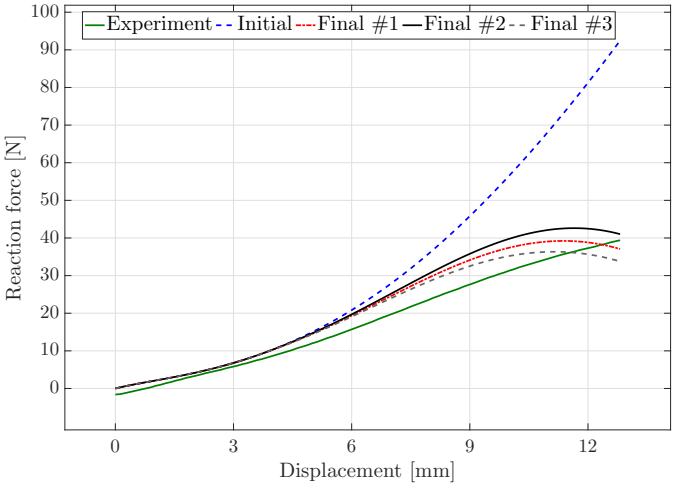

(b) Load-displacement-curves, comparing the experimental to the simulated material response for the initial guess and the final parameter set including two variations. The shown displacement is taken from the bottom node of the right boundary in the symmetry plane.

Figure 4.7: (**a**) Sketch of the chosen segment of the specimen with the applied boundary conditions. (**b**) Comparison of the load-displacement curves of the experiment with the results of the initial parameter set, the optimised Parameter Sets #1 ($n_{\mathrm{iso}} = 1.0$), #2 ($n_{\mathrm{iso}} = 0.9$), and #3 ($n_{\mathrm{iso}} = 1.1$). Reprinted from Schulte et al., Materials 13(14):3156 (2021), [110], with permission under creative commons 4.0.

For the purpose of reducing the computational cost of the FE simulation within each iteration of the parameter identification, the symmetry properties of the sample were used; cf. Figure 4.7a. Furthermore, considering the material properties of the soft polymer, only the segment shown in the figure was used to exclude boundary effects by the clamping jaws. In order to still use the experimental boundary conditions in the simulations, the experimentally measured displacements, taken via the CCD camera system, were applied to the right boundary of the specified segment. As can be seen from the photos of the specimen during the experiment (cf. Figure 4.6) and from the sketch of the segment, the displacements were not uniform over the boundary of the chosen segment of the sample.

The initial guess for the damage-related model parameters was $\eta_{\mathrm{d}} = 0.002$, $\kappa_{\mathrm{d}} = 0.4$, $n_{\mathrm{iso}} = 1.0$, and $c_{\mathrm{d}} = 0.04$ and resulted in no damage initiation in the material; cf. Figure 4.8a. In Figure 4.7b, the comparison of the load-displacement curves is presented. Since the stress-strain path of the homogeneous tensile test already overestimated the experimental curve, the simulated response for the tensile test with inhomogeneous de-

formation states lay above the experimental result as well. Furthermore, considering the large total stretch values present in combination with the identified Yeoh material parameters, the increasing response for the reaction force was triggered by parameters C_2 and C_3 weighting the hyperelastic energy contributions of second and third order.

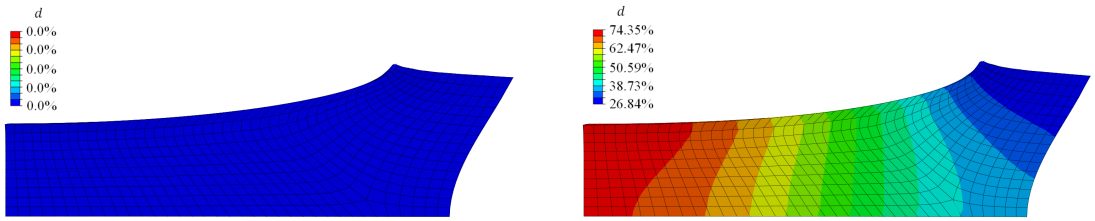

(**a**) Damage values for initial guess. (**b**) Damage values for Final #1.

Figure 4.8: Comparison of the contour plot of the damage value d at the final load step for (**a**) the initial parameter set and (**b**) the optimised Parameter Set #1. Reprinted from Schulte et al., Materials 13(14):3156 (2021), [110], with permission under creative commons 4.0.

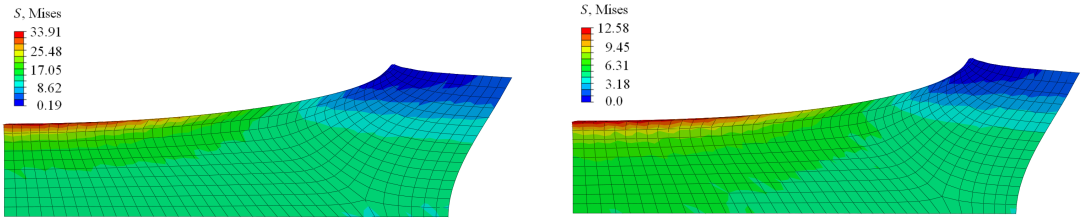

(**a**) von Mises stress for the initial guess. (**b**) von Mises stress for Final #1.

Figure 4.9: Comparison of the contour plot of the von Mises stress at the final load step for (**a**) the initial parameter set and (**b**) the optimised Parameter Set #1. Reprinted from Schulte et al., Materials 13(14):3156 (2021), [110], with permission under creative commons 4.0.

Since parameter n_{iso} strongly influences the simulated deformation behaviour of the specimen in each iteration, n_{iso} was fixed to 1.0 in a first step, thereby neglecting a different damage contribution of the volumetric and isochoric part. The corresponding optimised parameter set, denoted as Final #1, $\eta_{\text{d}} = 0.202531$, $\kappa_{\text{d}} = 0.15185$, and $c_{\text{d}} = 0.52593$, was rounded to five decimal digits. Considering the load-displacement curves, the response of the final set lay closer to the experimental behaviour than the initial guess; see Figure 4.7b. The stress distribution of the initial guess and the final set was comparable; the magnitude of the final set, however, was less than half of the stress of the initial set; cf. Figure 4.9. The von Mises stress distribution within the specimen—with the maximum stress value obtained at the upper surface, corresponding to the region dominated by the initially circular notch—was in line with observations made by, e.g., Kleuter [52].

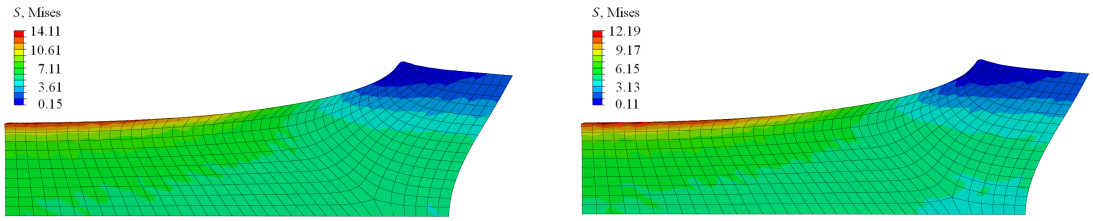

(**a**) von Mises stress for Final #2. (**b**) von Mises stress for Final #3.

Figure 4.10: Comparison of the contour plot of the von Mises stress at the final load step for (**a**) the optimised Parameter Set #2 with $n_{\text{iso}} = 0.9$ and (**b**) the optimised Parameter Set #3 with $n_{\text{iso}} = 1.1$. Reprinted from Schulte et al., Materials 13(14):3156 (2021), [110], with permission under creative commons 4.0.

The contour plot of the damage value d in Figure 4.8 compares the damage value obtained for the initial parameter set with the damage value obtained for the Final #1 set. Initially, no damage was initiated, and with the Final #1 set a damage value of nearly 75% occurred in the symmetry plane of the loading direction.

Figures 4.7b and 4.10 show the influence of the different damage functions for the volumetric and isochoric contributions. The set Final #2 included $n_{\text{iso}} = 0.9$, and Final #3 considered $n_{\text{iso}} = 1.1$. A higher value for n_{iso} flattens the load-displacement curve, while a lower value provides an increased path. Another important impact of the parameter is indicated in Figure 4.10, where apart from the difference in the stress magnitude, the deformation of the sample was already different for slight changes in the parameter with regard to the necking of the sample at the symmetry plane of the loading direction.

The advantage of the regularised damage framework is the mesh objectivity of the simulated material response. To demonstrate this feature, the boundary value problem was calculated with three different meshes for the optimised parameter set. In addition to the mesh containing 1548 elements, used for the results in Figures 4.7–4.10, a coarser mesh with 1092 and a finer mesh with 2613 elements were used in order to analyse the mesh sensitivity of the results. As can be seen in Figure 4.11, only marginal differences in the contour plots of the damage function values and the von Mises stress, as well as the load-displacement curves are visible. Thus, the gradient-enhanced damage model works properly. In contrast, it is noted that the local damage model diverged at different load steps, depending on the mesh discretisation. In the case of the fine mesh, the solution diverged at a displacement of 3.2 mm, for the basis mesh at 3.375 mm and for the coarse mesh at 3.415 mm. The displacement was taken from the bottom node of the right boundary in the symmetry plane.

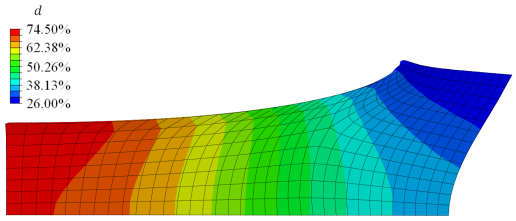

(a) Damage values for a coarser mesh with 1092 elements.

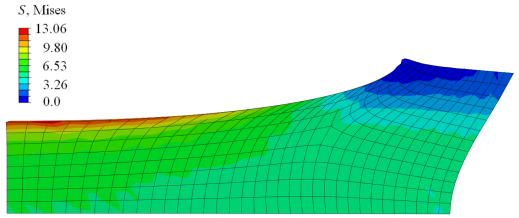

(b) von Mises stress for a coarser mesh with 1092 elements.

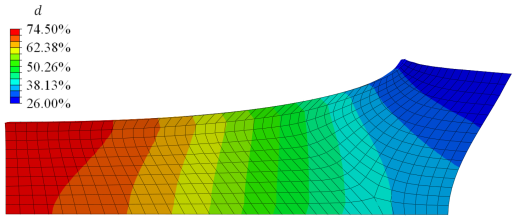

(c) Damage values for the basis mesh with 1548 elements.

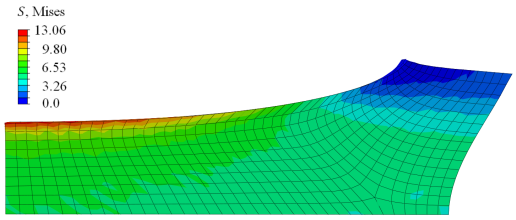

(d) von Mises stress for the basis mesh mesh with 1548 elements.

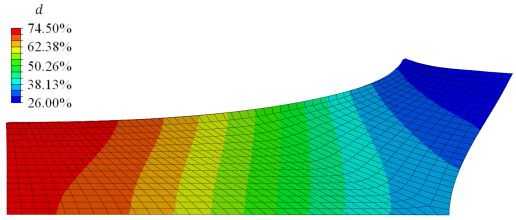

(e) Damage values for a finer mesh with 2613 elements.

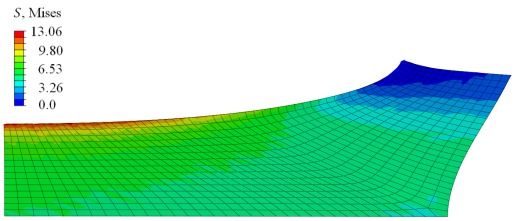

(f) von Mises stress for a finer mesh with 2613 elements.

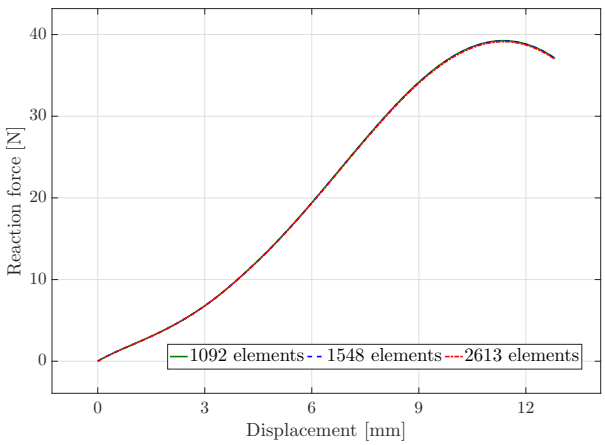

(g) Load-displacement curves for different discretisations. The displacement shown was taken from the bottom node of the right boundary in the symmetry plane.

Figure 4.11: Contour plots of the damage function values and the von Mises stress, as well as load-displacement curves regarding the parameter set Final #1 for different discretisations. Reprinted from Schulte et al., Materials 13(14):3156 (2021), [110], with permission under creative commons 4.0.

4.3 Application to the sheet metal DP800

After an application example of a multi-objective optimisation was given for a polymer, two different material models are calibrated for a DP800-graded steel to demonstrate the application of ADAPT, summarising the work of Schowtjak et al. [104]. In the first case, a simple von Mises plasticity model is calibrated while analysing the impact of different objectives for the error functional, such as forces and strains or displacements. Subsequently, the more complex material model coupling gradient-enhanced damage to finite plasticity, cf. Section 2.1, is used in a parameter identification process. In this case, the model is calibrated based on inhomogeneous states of deformation employing a multi-objective optimisation.

In order to obtain the appropriate local minimum with the lowest objective function value, several different starting sets of the parameters were used for all calibrations, since otherwise no proper minimum is guaranteed. In order to overcome unsuitable local minima, where the Nelder-Mead simplex algorithm may get stuck, an evolutionary algorithm was additionally applied to find the appropriate minimum.

4.3.1 Experiments

Regarding the required experimental data, a short summary of the work of Schowtjak [104] is given, where several different tests were performed at the Institute of Metal Forming and Lightweight Components (IUL), TU Dortmund University, on a Zwick / Roell Z250 tensile testing machine under quasi-static conditions. The length of the specimen is 80 mm and the crosshead velocity was prescribed at 2 mm/min. In order to achieve statistical solid results, the experiments were carried out several times. Nevertheless, the different experimental results depicted no significant deviation. In the following, the experimental data with the load-displacement curve lying closest to the average response has been chosen for the investigations.

An isotropic material behaviour considering elasticity and plasticity was obtained from the analysis of standardised tensile tests within different loading directions with respect to the rolling direction. Following DIN EN ISO 6892-1, the Young's modulus and the Poisson's ratio were identified as $E = 202\,\mathrm{GPa}$ and $\nu = 0.3$, respectively.

The notched specimen, shown in Figure 4.12, was used in the tensile test for the subsequent inverse parameter identification processes. The shape of the specimen was chosen in order to specify the region where necking occurs and to initiate several different states of deformation which can be measured by the DIC-system. Since quasi-static loading conditions were required, the local spatial logarithmic strain rate within loading direction was measured during the experiment and remained under or equal to 0.028/s. During the tensile test, a GOM Aramis DIC-system captured the displacement and (spatial) logarithmic total strain fields. In addition, the elongation of the specimen was measured by the DIC-system by employing a virtual extensometer placed outside the notch—assuming a homogeneous strain field—and had an initial length of 30 mm.

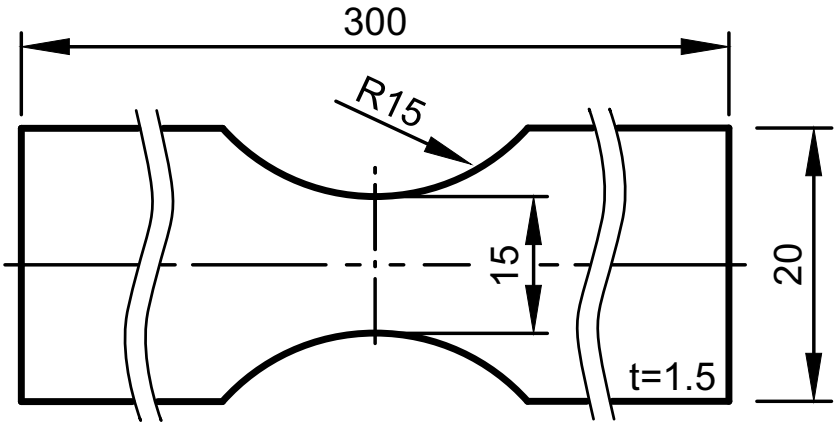

Figure 4.12: Technical drawing of the notched specimen for the DP800-graded steel. Reprinted from Schowtjak et al., International Journal of Mechanical Sciences 213:106840 (2022), [104], with permission under creative commons licence 4.0.

The corresponding measured load-displacement curve is shown in Figure 4.13. The experimental data was captured by the load cell as well as by the DIC-system at equal macroscopic displacement increments, i.e. in total at 60 frames. In Figure 4.14, the evolution of the equivalent strain $\varepsilon_{\mathrm{eq}}$ in loading direction is depicted for the three representative frames marked in Figure 4.13. Assuming incompressibility, the equivalent strain $\varepsilon_{\mathrm{eq}} = \sqrt{\sum_{i=1}^{n}(2/3\ \lambda_i)^2}$ is calculated from the optically measured strain, with λ_i the principal stretches, and $\varepsilon_{\mathrm{eq}}$ is used as measure for the magnitude of deformation. Considering the calibration process of the models, only the data frames prior to the sudden fracture—as a result of the immediate localisation—are taken into account since the fracture behaviour is not covered by the models. The different components of the strain and displacement fields are shown in Figures 4.15 and 4.16, respectively, at the load step right before fracture. Further information regarding the experiments can be found in [104].

4.3.2 FE-model

Since the simulation of the FE-model has to be performed within each iteration of the parameter identification process, the overall efficiency of the calibration can be tremendously reduced if the computational cost of the simulation is reduced. Thus, considering the sample geometry, see Figure 4.12, using the symmetry properties is very convenient. As a consequence, only the top right eighth of the specimen depicted in Figures 4.14, 4.15 and 4.16 is modelled and symmetry boundary conditions are applied as can be seen in Figure 4.17a. However, this is only valid for symmetric material response as observed in the experiments. The displacements of the experiment are applied to the top surface of the specimen. In Abaqus 960 C3D8R and C3D8T elements for Sections

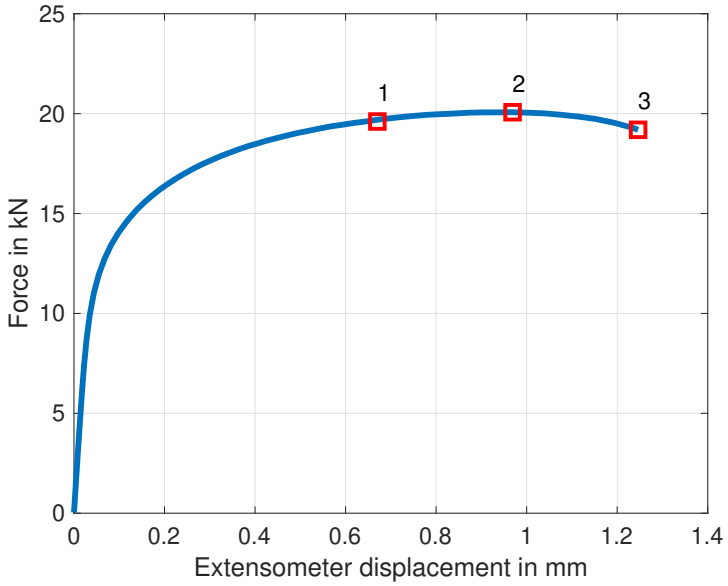

Figure 4.13: Load-displacement curve of the notched specimen, see Figure 4.12, of the tensile test under quasi-static loading speed. The displacement was measured by the DIC-system by employing a virtual extensometer with an initial length of 30 mm in the homogeneous region of the sample. The red marked points show the load steps where the strain fields depicted in Figure 4.14 were measured. Reprinted from Schowtjak et al., International Journal of Mechanical Sciences 213:106840 (2022), [104], with permission under creative commons licence 4.0.

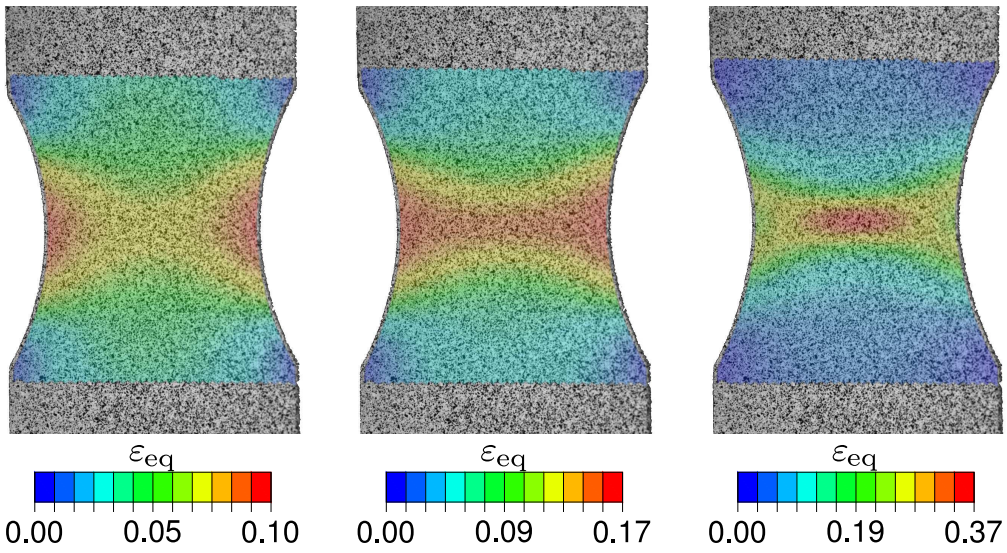

Figure 4.14: Evolution of the equivalent strain ε_{eq} at the three characteristic time steps, shown in Figure 4.13. The left image is associated to point 1 at a loading state before the maximum force is reached, the middle one to point 2 at maximum force and the right image to point 3 right before fracture. Reprinted from Schowtjak et al., International Journal of Mechanical Sciences 213:106840 (2022), [104], with permission under creative commons licence 4.0.

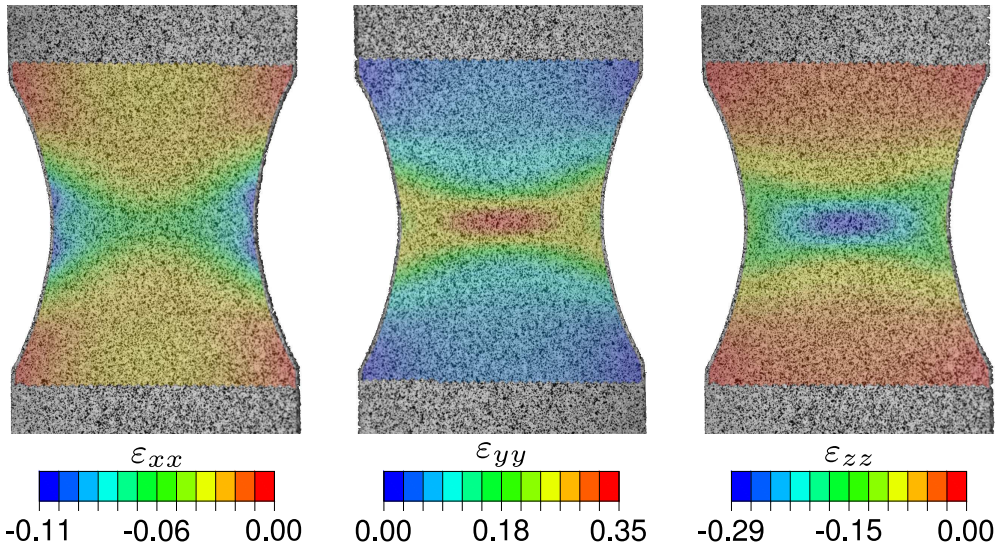

Figure 4.15: DIC-measured logarithmic strain fields in x, y, z-directions within the notch of the specimen at point 3, cf. Figure 4.13, right before fracture. The corresponding coordinate system is visible in Figure 4.17b. Reprinted from Schowtjak et al., International Journal of Mechanical Sciences 213:106840 (2022), [104], with permission under creative commons licence 4.0.

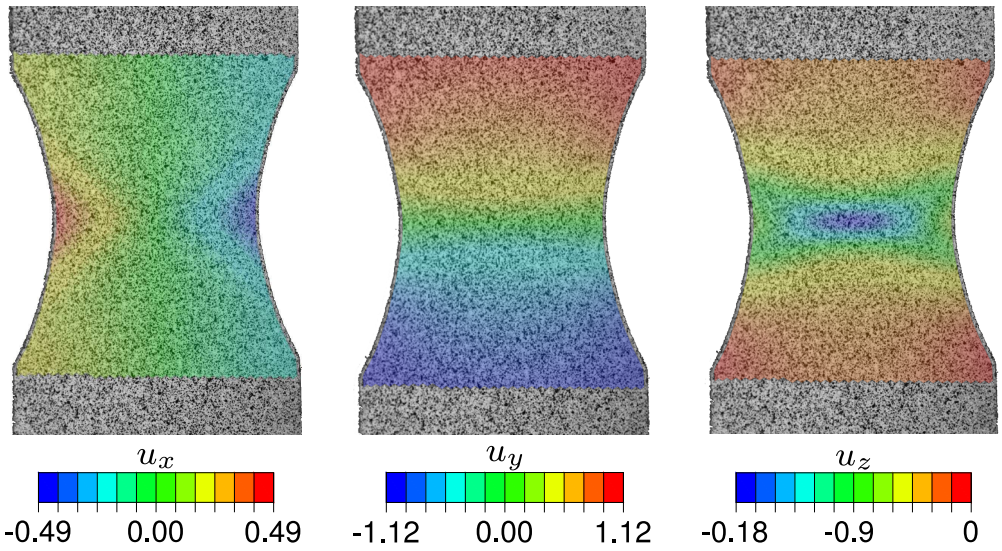

Figure 4.16: DIC-measured displacement fields in x, y, z-directions within the notch of the specimen at point 3, cf. Figure 4.13, right before fracture. The rigid body motions are computationally eliminated using the Aramis software. Alternatively, the procedures described in Sections 4.1.1 and 4.3.5 can be applied. The corresponding coordinate system is visible in Figure 4.17b. Reprinted from Schowtjak et al., International Journal of Mechanical Sciences 213:106840 (2022), [104], with permission under creative commons licence 4.0.

4.3.3 and 4.3.4, respectively, were chosen. The global coordinate system is positioned in the middle of the specimen, see Figure 4.17b.

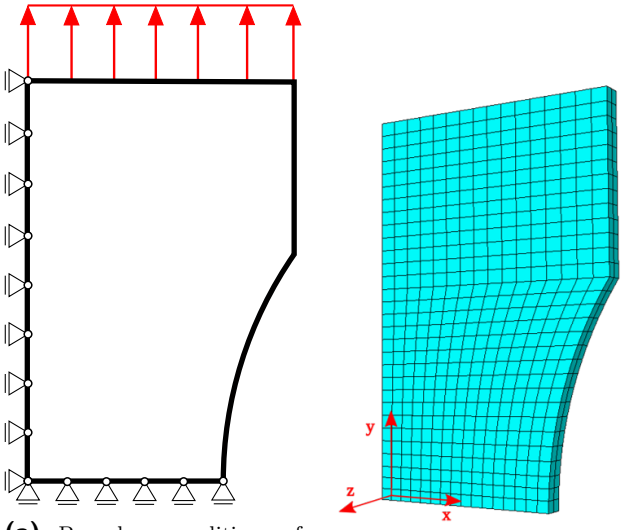

(a) Boundary conditions of the FE-model.

(b) Mesh of the FE model.

Figure 4.17: Finite element model used in the simulations of the parameter identification. Symmetry properties are taken into account in order to reduce the computational cost and only calculate the top right eighth of the specimen. The boundary conditions are shown in (a)—symmetry boundary conditions are applied in z-direction as well—while the mesh with the used global coordinate system is presented in (b). Reprinted from Schowtjak et al., International Journal of Mechanical Sciences 213:106840 (2022), [104], with permission under creative commons licence 4.0.

4.3.3 Parameter identification of a plasticity model

In this section, a summary of the work by Schowtjak in the corresponding section in [104] is given in order to investigate different optimisation strategies of the inverse parameter identification process by employing a simple von Mises plasticity model. The model is directly provided by Abaqus [1], formulated in incremental logarithmic strains and the yield function is given as

$$\Phi = \sigma_{\mathrm{eq}} - \sigma_{\mathrm{y}} = 0 \ , \quad \text{with } \sigma_{\mathrm{y}} = h\left[\alpha_0 + \alpha\right]^{n_{\mathrm{p}}} , \tag{4.12}$$

with σ_{y} as the yield stress following a Swift hardening law and $\sigma_{\mathrm{eq}} = \sqrt{\frac{3}{2}\,\mathrm{dev}(\boldsymbol{\sigma}) : \mathrm{dev}(\boldsymbol{\sigma})}$ as the von Mises equivalent stress. While α is the hardening variable, α_0, h and n_{p} remain as the corresponding material parameters.

In the following, the multi-objective optimisation—following the Pareto-strategy where the forces and strains are considered to obtain the Pareto-optimal solution—is compared to strategies where only the forces, strains or displacements are considered in the objective function. Those are denoted as F-, ε- or u-strategy, respectively. The finally identified optimal material parameters are presented in Table 4.1 and the strain fields of the experiment and the simulations are exemplarily shown for the last time step in Figure 4.18. Furthermore, the corresponding load-displacement curves are compared in

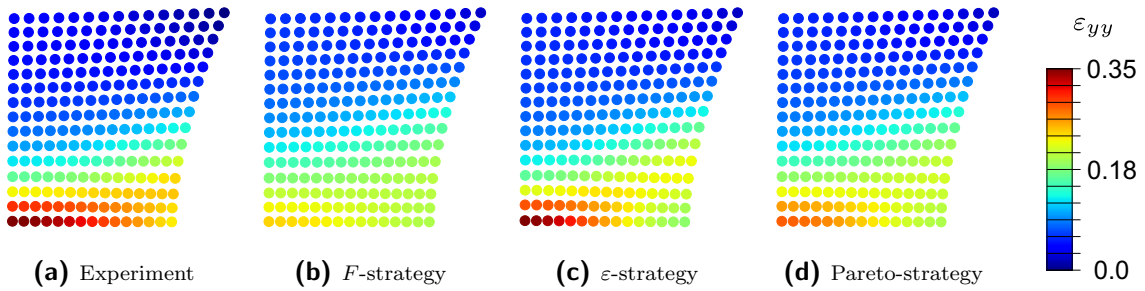

Figure 4.18: Contour plots of the spatial logarithmic strains in loading direction ε_{yy} located within the notch at the final loading step. Comparison of the experimentally measured strains to the simulations based on the optimised parameter sets for all identification strategies in Table 4.1. For comparison purposes, an interpolation of the experimental strain data onto the integration point-coordinates of the FE-model has been performed. Reprinted from Schowtjak et al., International Journal of Mechanical Sciences 213:106840 (2022), [104], with permission under creative commons licence 4.0.

Figures 4.19 and 4.20 and the simulated strains in loading direction are shown for the last time step in Figure 4.21.

Table 4.1: Material parameters of the simple von Mises plasticity model—defining initial yield α_0, hardening coefficient h and hardening exponent n_p identified based on the different mentioned strategies and their corresponding objectives. Reprinted from Schowtjak et al., International Journal of Mechanical Sciences 213:106840 (2022), [104], with permission under creative commons licence 4.0.

Parameter	F-strategy	ε-strategy	Pareto-strategy	u-strategy	Unit
a_0	$1.3 \cdot 10^{-5}$	$6.9 \cdot 10^{-7}$	$6.4 \cdot 10^{-6}$	$8.0 \cdot 10^{-3}$	-
h	1271.4	5128.1	1241.6	7199.9	MPa
n_p	0.15	0.11	0.14	0.12	-

Since the simple von Mises plasticity model is not able to fully capture the experimentally measured material behaviour—i.e. all localisation effects, especially the damage related material softening effect—it is only employed to efficiently investigate various optimisation strategies.

As it can be seen in Table 4.2, the F-strategy shows the lowest deviation with regard to the forces with an error of 908.3 N, which is taken as the global minimum with respect to the forces f_F^*. However, the error regarding the strain fields is the highest of all strategies since the strain fields were not considered in the objective function. Accordingly, the lowest error with respect to the strains is achieved with the ε-strategy as $1.9 \cdot 10^{-5}$ which is assumed as global minimum f_ε^*. Nevertheless, the error regarding the forces is more than 60000 times higher than the global minimum, and the comparison of the load-displacement curves in Figure 4.19 demonstrate that the found solution of this strategy is far away from a realistic mapping. An even worse result is obtained from the u-strategy, see Table 4.2 and Figure 4.19. In contrast, the optimal solution

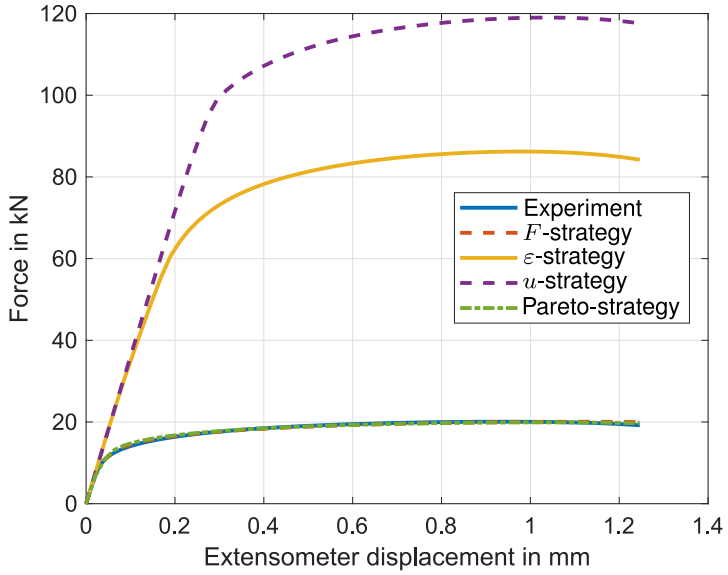

Figure 4.19: Load-displacement-curve for all presented parameter identification strategies. In order to compare both strategies close to the experimental response, a closer section of the figure is shown in 4.20. Reprinted from Schowtjak et al., International Journal of Mechanical Sciences 213:106840 (2022), [104], with permission under creative commons licence 4.0.

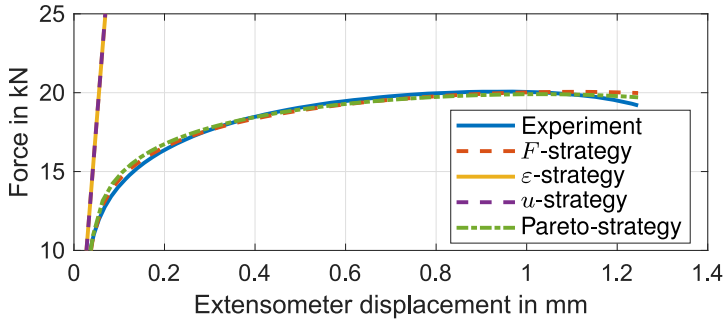

Figure 4.20: Zoom of the load-displacement curves in Figure 4.19 for both calibration strategies close to the experimental response. Reprinted from Schowtjak et al., International Journal of Mechanical Sciences 213:106840 (2022), [104], with permission under creative commons licence 4.0.

considering the Pareto-strategy can be obtained by minimising the following objective function

$$f(\boldsymbol{\kappa}) = \sqrt{\left[\frac{f_F^* - f_F(\boldsymbol{\kappa})}{f_F^*}\right]^2 + \left[\frac{f_\varepsilon^* - f_\varepsilon(\boldsymbol{\kappa})}{f_\varepsilon^*}\right]^2}\,, \tag{4.13}$$

which is normalised by the optima of the corresponding single objective problems. Even though the single function values of the Pareto-optimal solution are 32% and 72% higher than the chosen global minima of the forces and strains, the overall combined error is minimised, cf. Table 4.2. It can be seen in Figures 4.19 and 4.18 that the Pareto

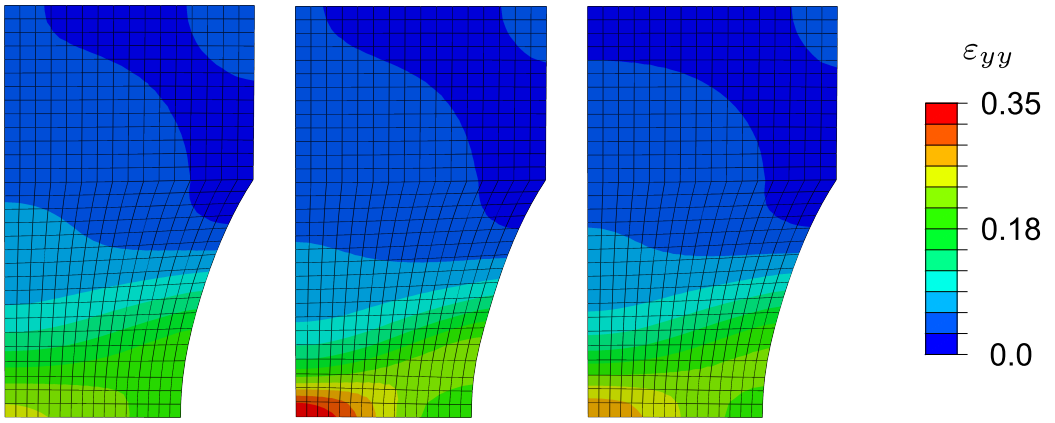

(a) F-strategy **(b)** ε-strategy **(c)** Pareto-strategy

Figure 4.21: Contour plots of the strains in loading direction with regard to the FE-models at the final loading step based on the corresponding optimised parameter sets for three exemplary calibration strategies, cf. Table 4.1. Reprinted from Schowtjak et al., International Journal of Mechanical Sciences 213:106840 (2022), [104], with permission under creative commons licence 4.0.

Table 4.2: Final objective function values of the four different presented calibration strategies, i.e. based solely on either forces F, strains ε or displacements u or on the combined solution regarding the Pareto optimum. The error $f_\bullet$ is calculated following the root sum of squares in Equation (4.2). Reprinted from Schowtjak et al., International Journal of Mechanical Sciences 213:106840 (2022), [104], with permission under creative commons licence 4.0.

Strategy	Objective	f_F in kN	f_ε
F-strategy	F	0.9083	$4.8 \cdot 10^{-5}$
ε-strategy	ε	57503.2425	$1.9 \cdot 10^{-5}$
Pareto-strategy	F and ε	1.2026	$3.2 \cdot 10^{-5}$
u-strategy	u	125005.4490	$2.4 \cdot 10^{-5}$

optimum depicts the closest solution regarding both quantities. Thus, in total, the Pareto-strategy reflects the realistic material behaviour best, followed by the F-strategy which is at least reasonable to some degree, and the other two strategies lead to quite unreasonable results.

4.3.4 Parameter identification of gradient-enhanced material models

As already mentioned in Section 4.3.3, the simple von Mises-based plasticity model was not fully able to capture the softening behaviour of the material since damage was not included in the model. However, in the gradient-enhanced model for coupled damage and plasticity, see Section 2.1, not only damage is taken into account but also many aspects of damage can be captured, such as localisation effects in the context of finite element

applications. Consequently, the model is capable of matching the experimental material response while additionally providing mesh independent simulation results. The fact that the damage regularisation framework used provides mesh-independent results was shown in [86]. The extensions to finite plasticity [119] and finite visco-elasticity [110]—cf. Sections 2.2, 2.5.2 and 4.2—also provide mesh-independent simulation results.

Table 4.3: Material parameters of the initial guess and the optimised parameter set, calibrated with regard to the load-displacement curve. For further details on the model formulation see 2.1. The parameters indicated with "fix" were not identified within the parameter identification procedure since these were pre-defined in previous experiments, e.g. in the case of E and ν, see Section 4.3.1, or these have been pre-defined manually. For example, the value for β_{d} is set sufficiently high to ensure the coupling between the non-local and local damage variables. Reprinted from Schowtjak et al., International Journal of Mechanical Sciences 213:106840 (2022), [104], with permission under creative commons licence 4.0.

Symbol	Description	Initial guess	Final set	Unit
E	Young's modulus	202.0	fix	GPa
ν	Poisson's ratio	0.3	fix	–
α_0	defining initial yield stress	$1.4 \cdot 10^{-5}$	$2.6027 \cdot 10^{-5}$	–
h	hardening coefficient	1700.0	1386.9	MPa
n_{p}	hardening exponent	0.25	0.1676	–
$q_{\max}$	max. damage threshold	1.0	0.8062	MPa
n_{d}	damage exponent	2/3	fix	–
η	damage rate factor	0.7	0.4751	–
ξ_{vol}	volumetric damage factor	1.0	fix	–
ξ_{iso}	isochoric damage factor	0.4	0.5816	–
ξ_q	threshold factor	1.0	0.5477	–
ξ_m	effective stress factor	0.3	0.4296	–
η_α	coupling factor	0.0	fix	–
c_{d}	regularisation parameter	20.0	fix	N
β_{d}	penalty parameter	10.0	fix	MPa
$q_{\min}$	initial damage threshold	0.5	0.6025	MPa

In a first step, the model parameters were only calibrated with regard to the load-displacement curve. The identification process was conducted with different starting sets for the material parameters. The best fit for the parameters is presented in Table 4.3 with the corresponding starting values, and the comparison of the experimental and simulated load-displacement curve is shown in Figure 4.22. The simulated distribution of the damage value is depicted in Figure 4.23a. It can be seen that the damage initiation and further evolution in terms of the damage variable d takes place in the necking region of the notched specimen which is quite reasonable since the regime of highest tensile load corresponds to the damage initiation regime. Nevertheless, Figure 4.23 perfectly

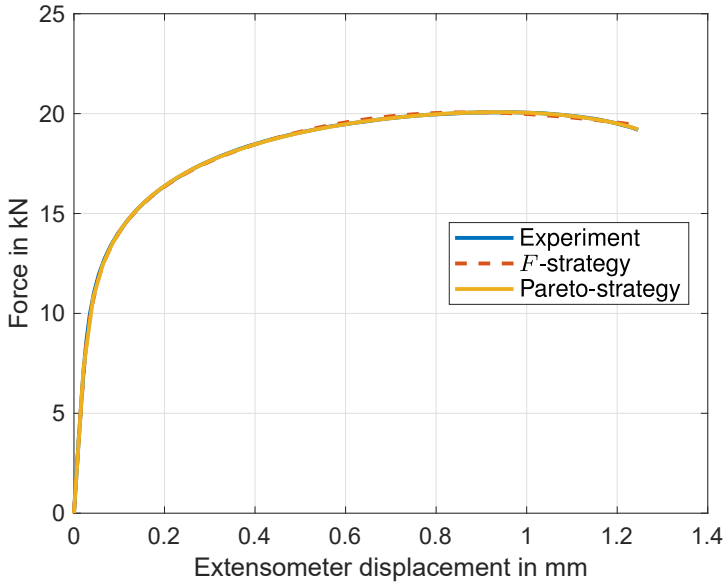

Figure 4.22: Comparison of the load-displacement curves of the simulations of the final parameter sets with different calibration strategies with the experimental response. Reprinted from Schowtjak et al., International Journal of Mechanical Sciences 213:106840 (2022), [104], with permission under creative commons licence 4.0.

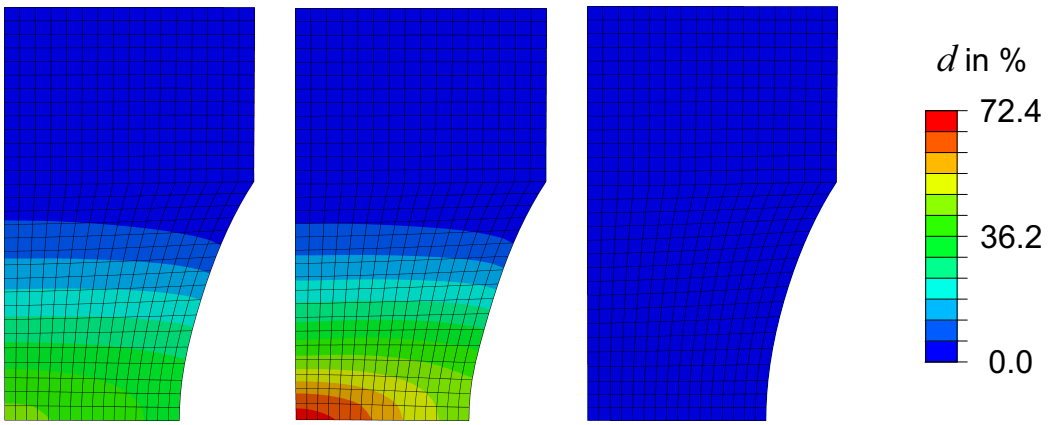

(a) Parameter set 1 **(b)** Parameter set 2 **(c)** Parameter set 3

Figure 4.23: Contour plots of the damage variable d at the final load step for three different parameter sets obtained via optimisations with different initial guesses. Parameter set 1 (a) represents the best solution according to the force-response. These plots are associated with the load-displacement curves in Figure 4.24. Reprinted from Schowtjak et al., International Journal of Mechanical Sciences 213:106840 (2022), [104], with permission under creative commons licence 4.0.

demonstrates the difficulties during the parameter identification process. First, the importance of using many different starting sets for the model parameters in order to find an appropriate minimum since, considering the amount of parameters, the appearance of local minima substantially increases. Alternatively, an evolutionary algorithm should

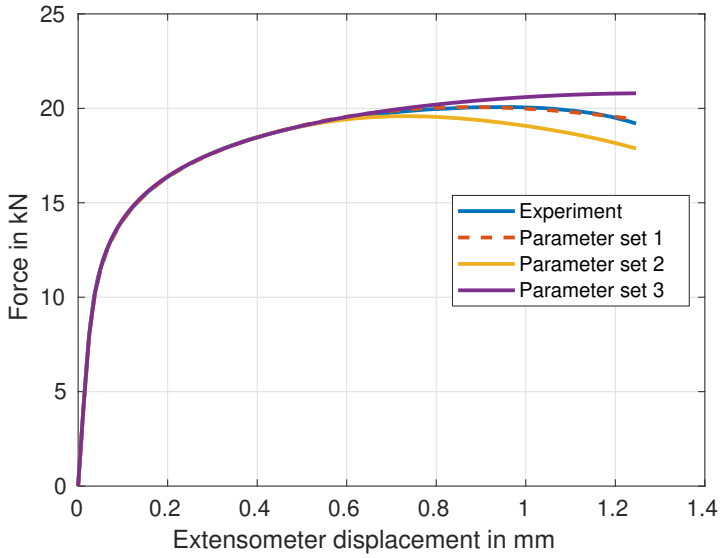

Figure 4.24: Load-displacement curves for three different parameter sets obtained via optimisations with different initial guesses. These graphs are associated with the damage contour plots shown in Figure 4.23. Reprinted from Schowtjak et al., International Journal of Mechanical Sciences 213:106840 (2022), [104], with permission under creative commons licence 4.0.

be used. Secondly, the specified load path of the experiment, in other words the data available, is not sufficient in order to uniquely identify the damage related material parameters, since, e.g., unloading steps are not considered. For example, the slope of the unloading curve indicates the amount of damage induced in the material as related to the reduction of the Young's modulus, while the remaining strain is associated with the amount of plastic strain stored in the material. Thus, the degradation effect can be captured, see [119]. The results show that some starting sets can lead to local minima where the simulated damage distribution does not predict the experimental material behaviour sufficiently and where the damage amplitude in terms of the damage variable d may show a significant difference.

Table 4.4: Result of the optimisation process of the combined solution associated with the Pareto optimum for the calibration of the gradient-enhanced damage model calibrated with regard to the forces and the displacement field. The error $f_\bullet$ is given in the form of the root sum of squares, see Equation (4.2). Reprinted from Schowtjak et al., International Journal of Mechanical Sciences 213:106840 (2022), [104], with permission under creative commons licence 4.0.

Step	Objective	f_F in N	f_u in mm
Initial	F and u	36922.53	$1.294 \cdot 10^{-3}$
Final	F and u	13.69	$3.478 \cdot 10^{-4}$

Thus, precise planning of the experimental setup prior to the parameter identification is absolutely necessary. Depending on the capabilities of the material model, the

experimental requirements need to be determined, e.g. considering different deformation modes in terms of proportional and non-proportional loading paths, unloading sequences, multi-cyclic responses and step tests. In addition, modelling errors have to be identified in order to avoid or at least control them.

Table 4.5: Material parameters of the initial guess and the optimised parameter set, calibrated with regard to the load-displacement curve and the displacement field, while Table 4.3 showed the calibration results only based on the load-displacement data. Reprinted from Schowtjak et al., International Journal of Mechanical Sciences 213:106840 (2022), [104], with permission under creative commons licence 4.0.

Symbol	Description	Initial guess	Final set	Unit
E	Young's modulus	202.0	fix	GPa
ν	Poisson's ratio	0.3	fix	–
α_0	defining initial yield stress	$1.4 \cdot 10^{-5}$	$1.3765 \cdot 10^{-5}$	–
h	hardening coefficient	1700.0	1404.4	MPa
n_p	hardening exponent	0.25	0.1703	–
q_max	max. damage threshold	1.0	1.611	MPa
n_d	damage exponent	2/3	fix	–
η	damage rate factor	0.7	0.9457	–
ξ_vol	volumetric damage factor	1.0	fix	–
ξ_iso	isochoric damage factor	0.4	0.3752	–
ξ_q	threshold factor	1.0	1.089	–
ξ_m	effective stress factor	0.3	0.1123	–
η_α	coupling factor	0.0	fix	–
c_d	regularisation parameter	20.0	21.3755	N
β_d	penalty parameter	10.0	fix	MPa
q_min	initial damage threshold	0.5	0.5527	MPa

As mentioned in the previous section, by restricting the calibration process to load-displacement data, especially field quantities—e.g. strains or displacements—are not necessarily matched accurately. Therefore, the displacement field on the surface of the specimen can be included into a multi-objective optimisation problem. Hence, specific parameters such as the regularisation parameter, that control localising effects can be identified more precisely. Furthermore, several types of deformation states—considering experiments with inhomogeneous deformation states—are incorporated in the objective function.

In order to improve the parameter identification results based on these experiments, the experimentally measured displacement field is taken into account and compared to the simulated response analogously to equation (4.13), though alternatively the displacements are considered instead of the strains this time. The initial guess remains the same as for the previous calibration restricted to load-displacement curve data. Nevertheless,

this time, the regularisation parameter c_d as well as the initial damage threshold q_min, cf. Equation (2.5), are additionally calibrated, since the DIC-data enables their identification. The Pareto-strategy is chosen since it was already shown in Section 4.3.3 to be the most efficient one. The Pareto-optimum was chosen based on an equal weighting of both the objective function contributions. The initial and the final objective function values are shown in Table 4.4. The corresponding final parameter set is given in Table 4.5 and the comparison of the simulated and experimental material response is presented with respect to the load-displacement curve in Figure 4.22 and to the displacements in Figure 4.25. While the load-displacement curve and the displacement field in y-direction are matched nearly perfectly, the displacement field in x-direction still shows slight differences. For a moment it may appear confusing as to why the parameter identification based on the Pareto-strategy results in a better agreement of the load-displacement curve in contrast to the calibration based only on load-displacement curve data. However, with the Pareto-strategy, two more parameters were calibrated and especially the initial damage threshold q_min influences the load-displacement behaviour of the material. As a consequence, q_min can be already calibrated based on load-displacement data.

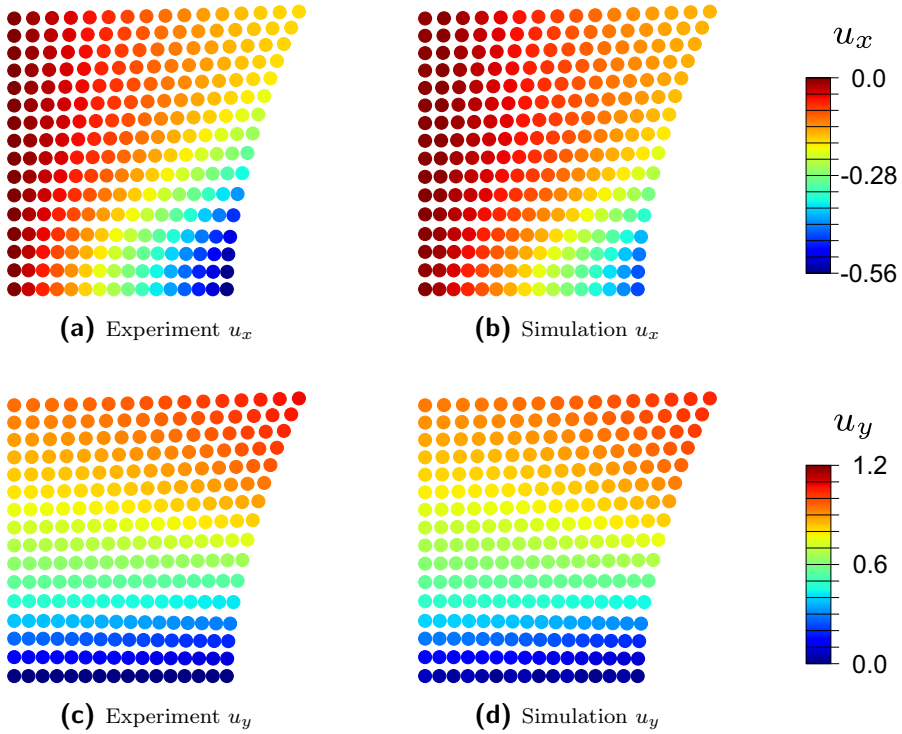

(a) Experiment u_x **(b)** Simulation u_x

(c) Experiment u_y **(d)** Simulation u_y

Figure 4.25: Contour plots of the displacements at the final load step with the optimised parameter set, see Table 4.5 for (a) the experimental displacements u_x, (b) the simulated displacements u_x, (c) the experimental displacements u_y and (d) the simulated displacements u_y. The measured displacement data has been interpolated onto the FE nodes. Reprinted from Schowtjak et al., International Journal of Mechanical Sciences 213:106840 (2022), [104], with permission under creative commons licence 4.0.

After all, it was shown that the more complex gradient-enhanced damage model captures the material behaviour of the DP800 way better than the simple model does. By incorporating the displacement field into the objective function of the calibration process, the material parameters are better fitted, although still no fully representative set of parameters is obtained since the experiment lacks unloading steps.

4.3.5 Starting value generated via machine-learning assisted parameter identification

In the previous section, all material parameters of the gradient-enhanced damage model coupled to finite plasticity presented in Section 2.1 were identified by using classic parameter identification strategies. Therefore, the elastic parameters were pre-identified in standard experiments and subsequently the plasticity- and damage-related material parameters were calibrated. The overall identification process was quite time-consuming considering that the parameter identification process was performed with different characteristic initial guesses and different strategies in order to find an appropriate solution. In order to improve the efficiency of the overall identification process—especially regarding the difficulty in finding appropriate starting values for the calibration if the user is not deeply familiar with the underlying material model—the advantage of the hybrid strategy is analysed in the following. The hybrid approach was presented in Chapter 3 and applied to the mentioned finite plasticity model coupled to non-local damage.

Since the generation of qualitative starting values for the material parameters by incorporating an ANN was based on homogeneous deformation states, some of the damage-related material parameters could not be identified. However, in view of real-life applications of coupled damage and plasticity formulations, the non-local regularisation-related model parameters ensuring mesh independent results need to be calibrated as well, see e.g. [119, 120]. Thus, a multi-objective parameter identification is carried out with respect to inhomogeneous states of deformation. Therefore, not only the experimentally measured load-displacement curve is considered but also the displacement field on the corresponding surface measured via DIC. This enables a more accurate calibration of the constitutive model to the material behaviour, since different deformation states and modes are taken into account and as already mentioned in the previous sections. Moreover, the mentioned regularisation-related parameters, such as the regularisation parameter c_{d}, can additionally be identified. The overall identification process is comparable to the previous section, in the following however, the starting values were obtained from the ANN and not guessed by the user. Furthermore, to increase the complexity of the problem and showing the capability of this approach, no subsets of the material parameters were pre-identified. In addition, unloading steps are considered in the underlying experimental data.

To give an example of a subsequent calibration considering inhomogeneous states of deformation, sheet metal DP800 is considered in the following. The experimental data was generated by Sprave and Menzel, see [119]. The sketch of the specimen is depicted

in Figure 4.27a, whereby the geometry of the specimen has a total length of 52 mm, a maximum width of 10 mm, a minimum width of 3.85 mm and a radius of 39.4 mm. The thickness of the specimen is 1.5 mm. The experiments were conducted with a micro-tensile machine from Kammrath & Weiß with a load cell of 10 kN in combination with the DIC-software Veddac 7. During the experiment, only a section of the domain with a length in longitudinal direction of 10 mm in the centre of the specimen is taken into account. Hence, the FE simulations are restricted to that section of the specimen, visible in Figure 4.27a, where the experimentally measured data is directly used for the applied Dirichlet boundary conditions. The section is discretised with 4000 8-noded brick elements which were enhanced by the F-bar method. The nodes deal with three displacement degrees of freedom and one non-local damage degree of freedom and both fields are linearly interpolated. Further details can be taken from [119].

Table 4.6: Final material parameters of the DP800 after the multi-objective optimisation with respect to the load-displacement curve and DIC-measured displacement data by a classic parameter identification. The predicted parameter set $\boldsymbol{\kappa}^{\text{pred}}$ of the ANN and set $\boldsymbol{\kappa}^{\text{opt}}_{\text{hom}}$ after the subsequent Nelder-Mead simplex optimisation are used as starting points for this calibration based on inhomogeneous states of deformation. For the illustration of the evolution of the objective function value, the initial objective function value with the predicted parameter set $f_{\text{DIC}}(\boldsymbol{\kappa}^{\text{pred}})$ is set to 100 %. Thus, the initial objective function value with $\boldsymbol{\kappa}^{\text{opt}}_{\text{hom}}$ is $f_{\text{DIC}}(\boldsymbol{\kappa}^{\text{opt}}_{\text{hom}}) = 111.91\,\%$. Reprinted from Schulte et al., European Journal of Mechanics - A/Solids 98:104854 (2023), [113], with permission under creative commons licence 4.0.

Symbol	Description	$\boldsymbol{\kappa}^{\text{pred}}_{\text{DIC}}$	$\boldsymbol{\kappa}^{\text{opt}}_{\text{DIC}}$	Unit
f_{DIC}	objective function value	61.67	62.72	%
f^{F}_{DIC}	error in force	24.51	24.02	%
E	Young's modulus	171.455	173.188	GPa
ν	Poisson's ratio	0.151	0.304	–
σ_{y_0}	initial yield stress	399.299	130.3	MPa
h	hardening parameter	1030.137	1250.045	MPa
n_{p}	hardening exponent	0.278	0.183	–
q_{var}	variable damage threshold	1.35	3.636	MPa
n_{d}	damage exponent	fixed at 0.667		–
η	damage rate factor	2.203	2.609	–
ξ_{vol}	volumetric damage factor	fixed at 1.0		–
ξ_{iso}	isochoric damage factor	0.184	1.617	–
ξ_q	threshold factor	1.409	10.332	–
ξ_m	effective stress factor	3.393	0.001	–
η_α	coupling factor	0.246	2.715	–
c_{d}	regularisation parameter	266.111	30.591	N
β_{d}	penalty parameter	fixed at 500.0		MPa
q_{min}	initial damage threshold	256.837	29.748	MPa

In the following, the DIC-based parameter identification procedure is carried out with two different starting points. The first starting point is parameter set $\boldsymbol{\kappa}^{\text{pred}}$ as predicted by the ANN and the second point is optimal parameter set $\boldsymbol{\kappa}^{\text{opt}}_{\text{hom}}$ including the subsequent Nelder-Mead simplex optimisation step. Even though the simulations with both parameter sets were able to match the homogeneous stress-strain behaviour quite accurately and the deviation between the curves was only marginal, some of the identified material parameters showed considerable differences, e.g. the Young's modulus, see Table 3.3. In this section, the influence of the different starting points shall be analysed.

Even though the network was in this case trained with a tensile load path only, the shear deformation was qualitatively predicted. Moreover, the final calibration performed in this section considers full-field data including different deformation modes in order to obtain a set of material parameters suitable for the prediction of the material response in the context of more general loading paths.

As shown in Table 4.6, the final objective function value of both identifications is nearly on the same level, although the deviation of the initial function values featured a difference of $\Delta f_{\text{DIC}} = 11.91\,\%$. Hence, two local minima were found due to the significantly differing starting values and final parameter sets. The objective function value was calculated following Sprave and Menzel [119], i.e.

$$f_{\text{DIC}} = w_F\, f^F_{\text{DIC}} + w_{\Delta u}\, f^{\Delta u}_{\text{DIC}} \quad \text{with} \tag{4.14}$$

$$f^F_{\text{DIC}} = \sum_t w_t \left[F^{\text{exp}} - F^{\text{sim}}\right]^2_t \tag{4.15}$$

$$f^{\Delta u}_{\text{DIC}} = \sum_t w_t / n_{\text{np}} \sum_i^{n_{\text{np}}} \|\Delta \boldsymbol{u}^{\text{exp}}_i - \Delta \boldsymbol{u}^{\text{sim}}_i\|^2_t\,, \tag{4.16}$$

where $w_\bullet$ denote the weighting factors. In order to eliminate rigid body motions, the difference of the displacement of two neighbouring measurement points is divided by their distance. Thus, a simple strain-like quantity $\Delta \boldsymbol{u}$ is obtained, see [97, 119]. To ensure a comparable contribution of both terms—the force- and displacement-related terms—to the objective function, both weighting factors are chosen such that the objective function has the unit of stress squared. Thus, $w_F = [4/A_0]^2$ and $w_{\Delta u} = 0.7\,E^2$, where factor 4 relates to the symmetry of the specimen and where 0.7 was determined empirically as a good balance factor, see [119]. The first starting point leads to a minimum were the error in displacement is lower compared to the result with the second starting point, though the error in force is slightly higher. Comparing each of the parameters, some of them lie close to each other, e.g. the Young's modulus, even though this parameter was very different in the initial points. Nevertheless, several other parameters, e.g. the Poisson's ratio, the initial yield stress or the initial damage threshold, show larger deviations.

In Figure 4.26, both simulated load-displacement curves are compared to the experimentally measured one, both showing a quite accurate fit. Only two regions feature larger deviations. Especially the force decrease at the end of the experiment due to

material softening and damage evolution is not matched very accurately. With the second parameter set $\boldsymbol{\kappa}_{\mathrm{DIC}}^{\mathrm{opt}}$, in the last steps, however, damage increases markedly and the response approaches the values obtained in the experiment.

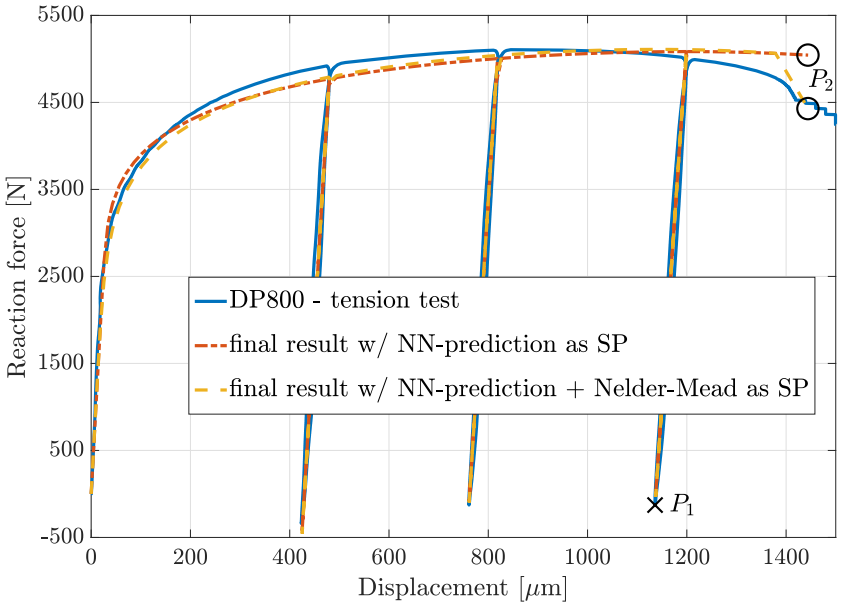

Figure 4.26: Load-displacement curve of the tension test of the DP800 considering inhomogeneous states of deformation compared to the simulated curves with the final optimal parameter sets depending on the starting point (SP), i.e. directly from the NN-prediction or after the subsequent Nelder-Mead simplex calibration. Reprinted from Schulte et al., European Journal of Mechanics - A/Solids 98:104854 (2023), [113], with permission under creative commons licence 4.0.

The contour plots of the squared absolute error of the relative displacements depict nearly the same deviations compared to the DIC-measured displacements, see Figure 4.27. This demonstrates that both solutions provide a comparable minimum for the error in displacements and that the highest deviations cannot be captured by the model itself due to, e.g., inhomogeneities in the specimen.

Examining the material parameters in Table 4.6 and the load-displacement curve in Figure 4.26 of the first identified parameter set, it is indicated that no damage evolution occurs. The contour plot of the isochoric damage function value after the final load step demonstrates that damage does not evolve for the first set. In contrast, for the second set, damage increases vastly in the final load steps in the necking region.

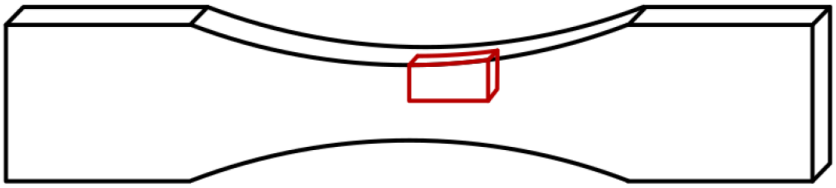

(a) Sketch of the tensile specimen taken from Sprave and Menzel [119] marking the plotted section of the specimen.

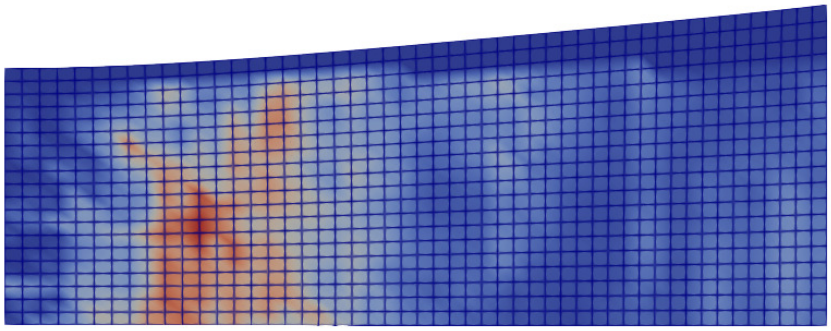

(b) Simulation with the optimal parameter set $\boldsymbol{\kappa}_{\mathrm{DIC}}^{\mathrm{pred}}$.

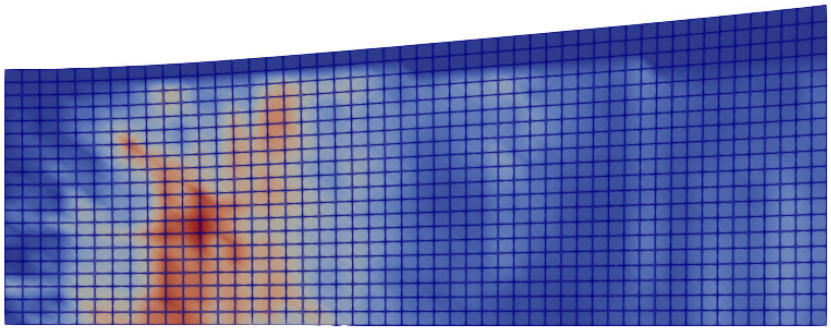

(c) Simulation with the optimal parameter set $\boldsymbol{\kappa}_{\mathrm{DIC}}^{\mathrm{opt}}$.

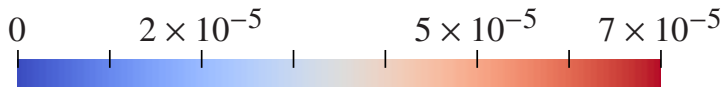

Figure 4.27: Contour plots of the squared absolute error of the relative displacements $f_{\mathrm{DIC}}^{\Delta u}$, following the calculation presented in Sprave and Menzel [119], at each node at time $t = 3520\,\mathrm{s}$, at the beginning of the last loading step, point P_1 in Figure 4.26, for both optimal parameter sets. Reprinted from Schulte et al., European Journal of Mechanics - A/Solids 98:104854 (2023), [113], with permission under creative commons licence 4.0.

These results demonstrate that the ANN already provides an adequate starting point for a subsequent multi-objective parameter identification since the difference in the results is due to the fact that, for this complex material model and the experimental data

used, many local minima exist which feature a comparable material behaviour. As a consequence, this makes it not only difficult for the ANN to identify the features of the model but also for the general parameter identification to find an appropriate minimum, especially if the user is not familiar with the material model and not able to identify a good starting point.

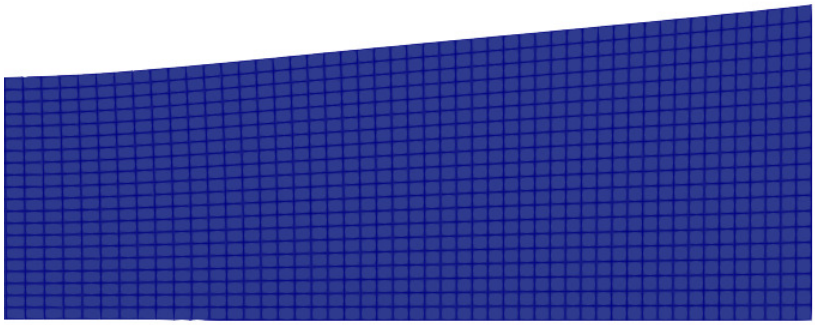

(a) Simulation with the optimal parameter set $\boldsymbol{\kappa}_{\mathrm{DIC}}^{\mathrm{pred}}$.

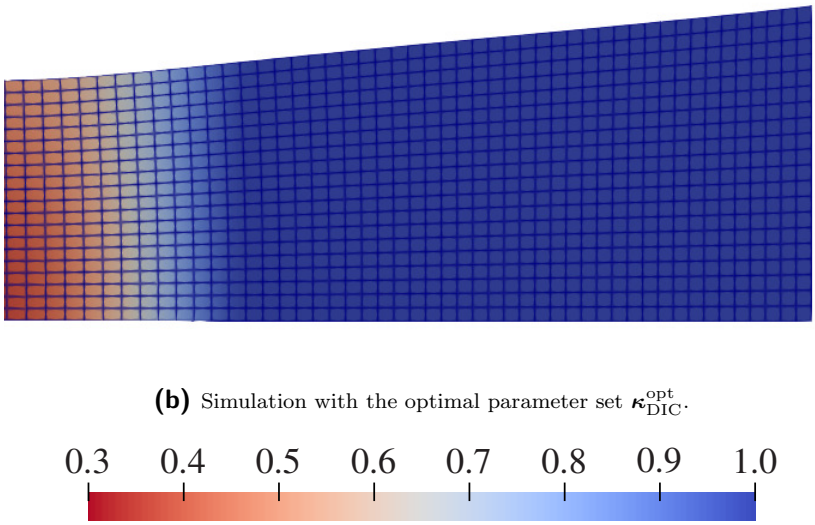

(b) Simulation with the optimal parameter set $\boldsymbol{\kappa}_{\mathrm{DIC}}^{\mathrm{opt}}$.

Figure 4.28: Contour plots of the isochoric damage function value $f_{\mathrm{iso}}(d_\phi) = \exp(-\eta\,\xi_{\mathrm{iso}}\,d_\phi)$ after the final load step at $t = 3730\,\mathrm{s}$, point P_2 in Figure 4.26, for both optimal parameter sets. Reprinted from Schulte et al., European Journal of Mechanics - A/Solids 98:104854 (2023), [113], with permission under creative commons licence 4.0.

Nevertheless, in future applications subsets of material parameters should be identified based on subsets of the experimental data, as discussed in [77, 142]. To give an example, parameters related to the purely elastic material response shall be identified based on

data related to the elastic regime only, i.e. the regime where inelastic effects are not activated, cf. Section 4.3.

5 Concluding remarks

This work dealt with the difficulty of identifying a proper set of material parameters in order to be able to accurately predict a specific material behaviour. The effort and difficulty to calibrate model parameters for the chosen material increases with the complexity of a material model and the number of its material parameters, especially if some of the parameters do not possess an obvious physical interpretation. Thus, the definition of an appropriate starting point for a classic parameter identification algorithm is challenging, and the obtained optimum is often sensitive with respect to the starting point. Therefore, three quite different and complex material models were chosen as application examples. They differ not only with regard to the mechanisms which are simulated, but also regarding the groups of materials.

For this purpose, in **Chapter 2**, a finite plasticity model coupled to gradient-enhanced damage, developed by Sprave and Menzel [119], was described in Section 2.1 and was later applied to metals which are used in metal forming processes. In addition, the underlying damage framework, introduced by Ostwald et al. [86], was adapted to a finite strain viscoelasticity model in Section 2.2 which was later on calibrated for polymers. Furthermore, a laminate-based model for single- and polycrystalline ferroelectric materials, developed by Dusthakar et al. [17], was described and investigated regarding the numerical treatment of the Karush-Kuhn-Tucker conditions in Section 2.3 and the remaining two characteristic model parameters were identified later on.

Subsequently, the most challenging case in parameter identification is depicted regarding the first mentioned material model, where none of the parameters were preidentified via specific experiments and thus all of the parameters—except for the nonlocal contributions—had to be identified at once based on homogeneous deformation states. Therefore, a Nelder-Mead simplex algorithm was applied in combination with three different starting values for the parameter sets for the sheet metal DP800 and the case-hardened steel 16MnCrS5. With this calibration strategy, different local minima were found which fit the experimental material behaviour properly, but the corresponding identified material parameters clearly varied. This demonstrates that the combination of the different material mechanisms enables multiple parameter combinations to depict a nearly equal material behaviour, if only a rather simple tensile test is considered

and too many material parameters are simultaneously identified. Thus, as many material parameters as possible should be identified separately with respect to characteristic experiments, e.g. the Young's modulus and the Poisson's ratio with regard to a tension test in the elastic region.

As a consequence, a different strategy was applied for the next material model. In order to identify the set of over 12 material parameters for the gradient-enhanced damage model in rate-dependent materials under finite strains, an efficient scheme for the process was carried out. At first, the basic constitutive model parameters, namely elastic parameters, were calibrated with respect to experiments displaying homogeneous states of deformation. Considering the deformation states, the computational cost of the identification was further reduced by using constitutive drivers for the simulations of all three required types of experiments within each iteration of the calibration process. In the next step, the already identified parameters were fixed during the identification of the damage-related material parameters.
For the purpose of developing a general framework for the calibration of rate-dependent materials coupled to damage, the constitutive viscoelasticity model by Simo and Hughes [117] was coupled to the gradient-enhanced damage formulation. Thus, the advantages of both models were combined, enabling different types of hyperelastic energy formulations—considering the energy-independent viscoelastic derivations by Simo and Hughes [117]—as well as mesh-independent results with respect to the damage evolution due to the damage regularisation framework by Ostwald et al. [86].
In order to investigate whether the framework works even for very large deformations, a self-diagnostic elastomer incorporating the mechanophore units within the polymeric microstructure was chosen as an application. With regard to the material behaviour of the soft polymer, the hyperelastic model by Yeoh and Fleming [139] was applied to the viscoelastic damage model.
The results of the parameter identification in Section 2.5.2.2 showed that the general framework of the implemented material model, as well as the parameter identification works properly. Even though the chosen self-diagnostic elastomer was only a first attempt at applying the framework, the experimental results already basically matched, cf. Figures 2.27.
Nevertheless, further improvements could be achieved for example by using different weighting factors for the contributions of the three different experiments with homogeneous deformation states to the goal function of the optimisation in order to improve the calibration of the parameters with respect to the tensile test. However, after all, the largest improvement could be achieved by a refinement of the experiments. The material properties led to difficulties in the sample manufacturing—such as uniformly cutting the shape—and in the clamping of the specimen, since the clamping jaws already generated deformations in the soft polymer. An improvement would be if the samples were directly moulded or if clamping were conducted with a very accurate torque spanner. Furthermore, experimental data based on different strain rates could be included in the identification framework.

In the case of the third example, the laminate-based model for ferroelectric materials was implemented incorporating many material parameters which are characteristic for the class of ferroelectrics, e.g. the piezoelectric or the spontaneous strain coefficients, cf. [17] or the summary in Section 2.3. Thus, regarding the calibration to $BaTiO_3$, Dusthakar et al. were able to take many parameters directly from the literature, see [17] or from the summary of the identification process in Section 2.5.3, and only two remaining model parameters had to be calibrated. However, considering that twelve characteristic curves had to be considered for the optimisation process, Dusthakar et al. separately applied a generic algorithm for the optimisation process of each of the different stress levels in a first step Thus, they could select appropriate starting values for each of the remaining model parameters for a subsequent optimisation considering all experimental data simultaneously. Here, a SQP-based algorithm was chosen.

After all, it required luck to guess an appropriate initial guess or time and effort to identify proper starting values for a parameter identification process. Thus, **Chapter 3** provided a combination of two approaches—artificial neural networks and classic parameter identification—in order to overcome the severe difficulty in connection with the application of complex material models to a specific material behaviour. By using an ANN for the generation of a valid initial guess for a subsequent classic parameter identification, as described in Chapter 3, the calibration process becomes more efficient. Furthermore, if the trained ANN is provided along the corresponding constitutive material model to the user, he is not required to be familiar with the model itself.

It was shown that it can therefore be advantageous to use an ANN ahead of a classic PI. Nevertheless, it has to be ensured that a sufficient amount of training data is generated. Moreover, the prediction accuracy of the ANN is only as good as the material model is able to capture the various features of the material behaviour. For the applications considered in this work, the results show that the Latin Hypercube Sampling method in combination with a hyperparameter optimisation yielded the best network performance. The ANN was able to provide a very good prediction of the experimental material behaviour which could be further improved to a nearly perfect fit with the following classic PI. If different types of loading paths were included in the training process an overall better prediction of the different experiments could be obtained. The results demonstrate that the ANN is capable of directly providing a quite accurate solution, i.e. starting point, for a subsequent multi-objective parameter identification even without the intermediate step of a subsequent optimisation based on homogeneous deformation states. Nevertheless, in future work, the prediction accuracy of the framework for complex material models can be further improved when subsets of material parameters are calibrated with regard to specific loading path sequences.

Further research can be conducted in the ANN-architecture of the demonstrated system. Autoencoders, which are an established type of ANN with the ability to learn encodings and therefore extract features of given data, are a possible candidate. This approach could reduce the ANN's size and therefore increase the efficiency while main-

taining capabilities.
Nevertheless, since the user still has to choose a proper material model for the corresponding material, one could provide another neural network prior to this hybrid identification approach or to every other classic parameter identification. This additional network would be trained in order to classify the experimentally measured material behaviour, e.g. rubber or steel, and thereby provide an appropriate material model available to the user.
Since the chosen material model is restricted to isotropic plasticity, the model is currently extended to cover anisotropic effects to simulate the material behaviour more precisely. In contrast to a classic parameter identification, the results of the ANN can show immediately if the underlying dataset, e.g. regarding the loading paths, is chosen properly in order to identify each of the parameters, thus providing sensitivity-like information. However, if a parameter turns out to have no influence on the material response, a model reduction should be performed, which also increases the efficiency of the model.

In addition, in order to explore the benefit of the hybrid strategy, it was applied to a different material model, i.e. the laminate-based model for ferroelectric materials, cf. Section 2.3. Since it was previously ascertained that it is very important to identify as many material parameters as possible in corresponding specific experiments, most of the parameters were taken from Table 2.6 following Dusthakar et al. [17] except for the two remaining model parameters which remained to be identified. In [17], it was quite time consuming to find proper starting values for the parameters. Thus, the hybrid approach can still be advantageous even though most of the parameters are already fixed to a specific material.

The results in Section 3.2 demonstrate that the trained ANN is able to perfectly predict the simulated material response of the model and that the parameters are independent from each other. However, it was shown that, if the experimentally measured material response deviating massively from a possible simulated response, the ANN has to extrapolate which decreases the prediction quality. Nevertheless, this prediction is still sufficient for a subsequent classic calibration procedure.

However, experimental data with solely homogeneous deformation states is not always sufficient for an accurate prediction, especially in terms of gradient-enhanced contributions, e.g. with regard to damage evolution. Thus, field data in combination with a multi-objective optimisation are required. The parameter identification tool ADAPT, summarised in **Chapter 4**, provides this feature and is available on GitHub [26] as open source code. In this work, the tool is applied to the two mentioned damage frameworks, see Sections 2.1 and 2.3.1, in order to identify the material parameters of the self-diagnostic PDMS elastomer and the sheet metal DP800. The two step strategy was employed for the polymer, where the elastic parameters were pre-identified, and for the DP800 different strategies of the multi-objective optimisation as well as two various complex material models were compared to each other.

In the case of the polymer, the results of the parameter identification based on the inhomogeneous deformation states demonstrated once again that the framework of the underlying model, as well as the calibration worked properly. Furthermore, since the simulations for the experiments with inhomogeneous deformation states were conducted before the sample started to tear in the necking region, the damage distribution with the optimised parameter set—showing damage evolution of nearly 75% in the symmetry plane of the loading direction, i.e., the necking region—reflected such a material behaviour.
In addition, in a future step, the load path for the inhomogeneous experiments could be changed to cyclic loading, improving the damage characterisation, though increasing the computational cost within each iteration of the parameter identification procedure. Nevertheless, further experiments including unloading should be included in the calibration process to enhance the accuracy. Until now, only damage activated prior rupture has been taken into account. As a long-term goal, the current framework should be combined with a rupture model to improve the overall prediction of the material behaviour. After all, the general parameter identification framework provides an efficient scheme for the calibration of gradient-enhanced damage in rate-dependent material models under finite strains. In the future, an interesting extension of the parameter identification framework is the incorporation of the self-diagnostic properties of the elastomer in terms of additional field data that is considered within the objective function.

In conclusion, it is generally beneficial to employ additional data for the overall calibration process, especially if the weighting between different contributions is done properly, e.g. by using a Pareto-scheme to find the optimal solution with respect to all contributions. Furthermore, the more material mechanisms a model can capture, the more accurate the prediction of the realistic material behaviour becomes. However, simultaneously, all the more experimental data is required—e.g. unloading sequences or field data—for an accurate parameter identification. Nevertheless, this results in higher computational costs within each iteration, which becomes even more expensive if the calibration process has to be performed with several different starting values. Thus, the hybrid strategy provides an efficient alternative and the results in Section 4.3.5 demonstrated that the ANN is capable of providing a quite accurate solution, i.e. starting point, for a subsequent multi-objective parameter identification.

A Numerical time integrations and algorithmic pseudo-code of the finite-strain viscoelasticity

In this appendix, the numerical update procedure of the convolution integrals introduced in Section 2.2.2 is shown in more details. Subsequently, the pseudo-codes of the strain- and stress-driven constitutive drivers are presented which are employed for the parameter identification regarding the viscoelastic material parameters.

A.1 Numerical time-integration of the local constitutive relations

In order to transform the convolution integral expression obtained in Section 2.2.2 to a standard recurrence formula, we adopt the following internal algorithmic variables,

$$\boldsymbol{H}^{(i)}(t) \coloneqq \int_{-\infty}^{t} \exp[-(t-s)/\tau_i]\, \frac{\mathrm{d}}{\mathrm{d}s}\big(f_{\mathrm{d}}^{n_{\mathrm{iso}}}(\kappa)\mathrm{DEV}\left(2\,\partial_{\bar{\boldsymbol{C}}}\psi_{\mathrm{ich}}(\bar{\boldsymbol{C}}(s))\right)\big)\,\mathrm{d}s\,, \tag{A.1}$$

where $\boldsymbol{H}^{(i)}(t), i = 1, 2, \ldots, N$, i.e. we have one stress-type tensor-valued internal variable $\boldsymbol{H}^{(i)}$ for each Maxwell element considered in the generalised relaxation model, cf. Simo and Hughes [117].

Using the semigroup property $\exp([t+\Delta t]/a) = \exp(\Delta t/a)\exp(t/a)$ and the property of additivity of the integral over the interval of integration we obtain the recurrence relation

$$\begin{aligned}\boldsymbol{H}^{(i)}(t_{n+1}) &= \exp[-\Delta t_n/\tau_i]\,\boldsymbol{H}^{(i)}(t_n) \\ &\quad + \int_{t_n}^{t_{n+1}} \exp[-(t_{n+1}-s)/\tau_i]\,\frac{\mathrm{d}}{\mathrm{d}s}\big(f_{\mathrm{d}}^{n_{\mathrm{iso}}}(\kappa)\mathrm{DEV}\left(2\,\partial_{\bar{\boldsymbol{C}}}\psi_{\mathrm{ich}}(\bar{\boldsymbol{C}}(s))\right)\big)\,\mathrm{d}s\,.\end{aligned} \tag{A.2}$$

Finally, integral (A.2) is approximated using the midpoint rule, so that

$$\boldsymbol{H}_{n+1}^{(i)} = \exp(-\Delta t/\tau_i)\,\boldsymbol{H}_{n}^{(i)} + f_{\mathrm{d}}^{n_{\mathrm{iso}}}(\kappa)\exp(-\Delta t/2\,\tau_i)\big(\tilde{\boldsymbol{S}}_{\mathrm{hyp}}^{n+1} - \tilde{\boldsymbol{S}}_{\mathrm{hyp}}^{n}\big)\,, \tag{A.3}$$

using the abbreviations

$$\tilde{\boldsymbol{S}}_{\mathrm{hyp}}^{n+1} \coloneqq \mathrm{DEV}_{n+1}(2\,\partial_{\bar{\boldsymbol{C}}}\psi_{\mathrm{ich}}(\bar{\boldsymbol{C}}_{n+1})) \quad \text{and} \quad \tilde{\boldsymbol{S}}_{\mathrm{hyp}}^{n} \coloneqq \mathrm{DEV}_{n}(2\,\partial_{\bar{\boldsymbol{C}}}\psi_{\mathrm{ich}}(\bar{\boldsymbol{C}}_{n}))\,, \tag{A.4}$$

where DEV_n and DEV_{n+1} are computed with respect to $\boldsymbol{C}_n$ and $\boldsymbol{C}_{n+1}$, respectively, consistent with

$$\mathrm{DEV}_{n+1}(\bullet) = [\bullet] - \frac{1}{3}\,[[\bullet] : \boldsymbol{C}_{n+1}]\,\boldsymbol{C}_{n+1}^{-1}\,. \tag{A.5}$$

The algorithmic approximation of the Piola-Kirchhoff stress tensor at time t_{n+1} then takes the form

$$\begin{aligned}\boldsymbol{S}_{n+1} &= J_{n+1}\,f_{\mathrm{d}}(\kappa_{n+1})\,\partial_J\psi_{\mathrm{vol}}(J_{n+1})\,\boldsymbol{C}_{n+1}^{-1} \\ &\quad + \gamma_\infty\,f_{\mathrm{d}}^{n_{\mathrm{iso}}}(\kappa_{n+1})\,\tilde{\boldsymbol{S}}_{\mathrm{hyp}}^{n+1} + \sum_{i=1}^{N}\gamma_i\;J_{n+1}^{-\frac{2}{3}}\;\mathrm{DEV}_{n+1}(\boldsymbol{H}_{n+1}^{(i)})\end{aligned} \tag{A.6}$$

with $\tilde{\boldsymbol{S}}_{\mathrm{hyp}}^{n+1}$ representing relation (A.4) evaluated at the current time t_{n+1} and with κ_{n+1} as the (updated) internal variable representing the evolution of damage within the material. For details on the straightforward time-integration of κ via a standard Euler backward scheme, the reader may refer to, e.g., [86, 133]. The spatial counterpart of (A.6), i.e. the current approximation of the Kirchhoff stress tensor is then computed by using a standard push-forward operation in terms of

$$\boldsymbol{\tau}_{n+1} = \boldsymbol{F}_{n+1}\cdot\boldsymbol{S}_{n+1}\cdot\boldsymbol{F}_{n+1}^{\mathrm{t}}\,. \tag{A.7}$$

By employing the fact that $\boldsymbol{F}\cdot\boldsymbol{C}_{n+1}^{-1}\boldsymbol{F}_{n+1}^{\mathrm{t}} = \boldsymbol{I}$ and the relation

$$\mathrm{dev}\Big[\bar{\boldsymbol{F}}_{n+1}\boldsymbol{H}_{n+1}^{(i)}\bar{\boldsymbol{F}}_{n+1}^{\mathrm{t}}\Big] = J_{n+1}^{-\frac{2}{3}}\;\mathrm{DEV}_{n+1}[2\partial_{\bar{\boldsymbol{C}}}\bar{W}^{\circ}(\bar{\boldsymbol{C}}_{n+1})]\,, \tag{A.8}$$

the Kirchhoff stress tensor is finally computed

$$\begin{aligned}\boldsymbol{\tau}_{n+1} &= J_{n+1}U^{\circ\prime}(\Theta_{n+1})\boldsymbol{I} + \gamma_\infty\mathrm{dev}\Big[2\bar{\boldsymbol{F}}_{n+1}\cdot\partial_{\bar{\boldsymbol{C}}}\bar{W}^{\circ}(\bar{\boldsymbol{C}}_{n+1})\cdot\bar{\boldsymbol{F}}_{n+1}^{\mathrm{t}}\Big] \\ &\quad + \sum_{i=1}^{N}\gamma_i\mathrm{dev}\Big[\bar{\boldsymbol{F}}_{n+1}\cdot\boldsymbol{H}_{n+1}^{(i)}\cdot\bar{\boldsymbol{F}}_{n+1}^{\mathrm{t}}\Big],\end{aligned} \tag{A.9}$$

which is the spatial counterpart of (A.6).

In order to evaluate the update formulas (A.3) the kinematic variables $\boldsymbol{C}_{n+1}$ and $\bar{\boldsymbol{C}}_{n+1}$ are needed which are easily computed within the context of a strain-driven type of algorithm as follows.
Let $\mathcal{S}_n = \boldsymbol{\varphi}_n(\mathcal{B})$ be the current placement of the body at time t_n, defined by the configuration $\boldsymbol{\varphi}_n : \mathcal{B} \to \mathbb{R}^3$, which is assumed to be given. Let Δt_n be the time step size, and assume that an incremental displacement field, denoted by

$$\Delta \boldsymbol{u} : \mathcal{B} \to \mathbb{R}^3, \tag{A.10}$$

is given. Then we compute the updated placement field $\mathcal{S}_{n+1} = \boldsymbol{\varphi}_{n+1}(\mathcal{B})$ simply by setting

$$\boldsymbol{\varphi}_{n+1}(\boldsymbol{X}) = \boldsymbol{\varphi}_n(\boldsymbol{X}) + \Delta \boldsymbol{u}(\boldsymbol{X}), \tag{A.11}$$

which defines the confiuration $\boldsymbol{\varphi}_{n+1} : \mathcal{B} \to \mathbb{R}^3$ at time $t_{n+1} \coloneqq t_n + \Delta t_n$. Then the deformation gradient and Jacobian determinant are computed as

$$\boldsymbol{F}_{n+1} = \nabla_{\boldsymbol{X}} \boldsymbol{\varphi}_{n+1}(\boldsymbol{X}) \quad \text{and} \quad J = \det(\boldsymbol{F}_{n+1})\,. \tag{A.12}$$

The right Cauchy-Green tensor and the volume-preserving part of the right Cauchy-Green tensor follows as

$$\boldsymbol{C}_{n+1} = \boldsymbol{F}_{n+1}^{\mathrm{t}} \cdot \boldsymbol{F}_{n+1} \quad \text{and} \quad \bar{\boldsymbol{C}}_{n+1} = J^{-\frac{2}{3}}\, \boldsymbol{C}_{n+1}. \tag{A.13}$$

A.2 Algorithmic pseudo-code

This section shows the pseudo-codes of the algorithms employed in Section 2.5.2.2 for the identification of the viscoelastic material parameters. The strain-driven constitutive driver is shown in Algorithm 1 and the stress-driven constitutive driver in Algorithm 2.

initialize internal variables $\tilde{\boldsymbol{S}}^{n}_{\mathrm{hyp}},\ \boldsymbol{H}^{(i)}_{n}, \forall\ i = 1, \ldots, N.$

get material parameters $C_1,\ C_2,\ C_3,\ \gamma_1,\ \tau_1, \ldots,\ \gamma_i,\ \tau_i.$

initialize $\boldsymbol{P}_{n+1}$.

for every time step t_n **do**

  given: the stretch λ_{11}.

  while $\|\widehat{\boldsymbol{P}}_{n+1}\| < tol$ **do**

    compute ${}^{(k)}\boldsymbol{F}_{n+1}$, ${}^{(k)}J_{n+1}$, ${}^{(k)}\boldsymbol{C}_{n+1}$, ${}^{(k)}\widehat{\boldsymbol{F}}_{n+1}$, ${}^{(k)}\widehat{\boldsymbol{C}}_{n+1}$.

    compute initial elastic stress Kirchhoff tensor $\boldsymbol{\tau}^{\mathrm{hyp}}_{n+1}$.

    compute algorithmic internal variables $\tilde{\boldsymbol{S}}^{n+1}_{\mathrm{hyp}}$, $\boldsymbol{H}^{(i)}_{n+1}$.

    compute ${}^{(k)}\boldsymbol{S}_{n+1}$ according to (A.6).

    compute Piola stress tensor ${}^{(k)}\boldsymbol{P}_{n+1}$.

    compute tangent operator ${}^{(k)}\mathbf{A}_{n+1}$.

    partition stress tensor and the deformation gradient:

    ${}^{(k)}\boldsymbol{P}_{n+1} = {}^{(k)}P_{11}\,\boldsymbol{e}_{11} \otimes \boldsymbol{e}_{11} + {}^{(k)}\widehat{\boldsymbol{P}}_{n+1}$

    ${}^{(k)}\boldsymbol{F}_{n+1} = {}^{(k)}F_{11}\,\boldsymbol{e}_{11} \otimes \boldsymbol{e}_{11} + {}^{(k)}\widehat{\boldsymbol{F}}_{n+1}.$

    partition the tangent operator:

    ${}^{(k)}\widehat{\mathbf{A}}_{n+1} = \dfrac{{}^{(k)}\mathrm{d}\widehat{\boldsymbol{P}}_{n+1}}{{}^{(k)}\mathrm{d}\widehat{\boldsymbol{F}}_{n+1}}.$

    update the transverse deformation gradient:

    ${}^{(k+1)}\widehat{\boldsymbol{F}}_{n+1} \leftarrow {}^{(k)}\widehat{\boldsymbol{F}}_{n+1} - {}^{(k)}\widehat{\mathbf{A}}_{n+1} : {}^{(k)}\widehat{\boldsymbol{P}}_{n+1}.$

  end while

  update internal variables $\{\tilde{\boldsymbol{S}}^{n+1}_{\mathrm{hyp}},\ \boldsymbol{H}^{(i)}_{n+1}\} \leftarrow \{\tilde{\boldsymbol{S}}^{n}_{\mathrm{hyp}},\ \boldsymbol{H}^{(i)}_{n}\}$.

end for

Algorithm 1: Strain-driven constitutive driver (relaxation)—uni-axial stress state.

initialize internal variables $\tilde{\boldsymbol{S}}^{n}_{\text{hyp}},\ \boldsymbol{H}^{(i)}_{n}, \forall\ i = 1, \ldots, N.$

get material parameters $C_1,\ C_2,\ C_3,\ \gamma_1,\ \tau_1, \ldots,\ \gamma_i,\ \tau_i.$

initialize $\boldsymbol{F}_{n+1}$.

for every time step t_n **do**

    given: Piola stress tensor $\boldsymbol{P}^{\text{exp}}$.

    while $\|\boldsymbol{P} - \boldsymbol{P}^{\text{exp}}\| < tol$ **do**

        compute ${}^{(k)}\boldsymbol{F}_{n+1}$, ${}^{(k)}J_{n+1}$, ${}^{(k)}\boldsymbol{C}_{n+1}$, ${}^{(k)}\widehat{\boldsymbol{F}}_{n+1}$, ${}^{(k)}\widehat{\boldsymbol{C}}_{n+1}$.

        compute initial elastic Kirchhoff stress tensor $\boldsymbol{\tau}^{\text{hyp}}_{n+1}$.

        compute algorithmic internal variables $\tilde{\boldsymbol{S}}^{n+1}_{\text{hyp}}, \boldsymbol{H}^{(i)}_{n+1}$.

        compute ${}^{(k)}\boldsymbol{S}_{n+1}$ according to (A.6).

        compute Piola stress tensor ${}^{(k)}\boldsymbol{P}_{n+1}$.

        compute tangent operator ${}^{(k)}\mathbf{A}_{n+1}$.

        compute ${}^{(k)}\Delta\boldsymbol{P}_{n+1} = {}^{(k)}\boldsymbol{P}_{n+1} - {}^{(k)}\boldsymbol{P}^{\text{exp}}_{n+1}$.

        update the deformation gradient

        ${}^{(k+1)}\boldsymbol{F}_{n+1} \leftarrow {}^{(k)}\boldsymbol{F}_{n+1} - {}^{(k)}\mathbf{A}_{n+1} : {}^{(k)}\Delta\boldsymbol{P}_{n+1}$

    end while

    update internal variables $\{\tilde{\boldsymbol{S}}^{n+1}_{\text{hyp}},\ \boldsymbol{H}^{(i)}_{n+1}\} \leftarrow \{\tilde{\boldsymbol{S}}^{n}_{\text{hyp}},\ \boldsymbol{H}^{(i)}_{n}\}$

end for

Algorithm 2: Stress-driven constitutive driver (creep)—uni-axial stress state.

B Derivation of the smoothed Fischer-Burmeister nonlinear complementarity problem function

The roots of the original NCP function need to be solved in an approximative manner for the smoothed Fischer-Burmeister NCP approach. Thus, the perturbation parameter δ controls the accuracy and the equality constraint to be solved. The corresponding derivation of the smoothed Fischer-Burmeister function provided that $r \geq 0$ and $\Gamma \geq 0$ reads as follows

$$r\,\Gamma = \delta^2 \tag{B.1}$$

$$2\,r\,\Gamma = 2\,\delta^2 \tag{B.2}$$

$$r^2 + \Gamma^2 + 2\,r\,\Gamma = r^2 + \Gamma^2 + 2\,\delta^2 \tag{B.3}$$

$$[r + \Gamma]^2 = r^2 + \Gamma^2 + 2\,\delta^2 \tag{B.4}$$

$$r + \Gamma = \sqrt{r^2 + \Gamma^2 + 2\,\delta^2} \tag{B.5}$$

$$0 = \sqrt{r^2 + \Gamma^2 + 2\,\delta^2} - [r + \Gamma] \tag{B.6}$$

Bibliography

[1] Dassault Systémes Simulia. Abaqus 2016 Documentation (2016). Abaqus theory manual, 4.2.1 Plasticity models: general discussion.

[2] W. Alt. *Nichtlineare Optimierung: Eine Einfürung in Theorie, Verfahren und Anwendungen*. Vieweg+Teubner Verlag, Wiesbaden, Germany, 2nd edition edition, 2011.

[3] S. Avril, M. Bonnet, A.-S. Bretelle, M. Grédiac, F. Hild, P. Ienny, F. Latourte, D. Lemosse, S. Pagano, E. Pagnacco, and F. Pierron. Overview of identification methods of mechanical parameters based on full-field measurements. *Experimental Mechanics*, 48:381–402, 2008. doi:10.1007/s11340-008-9148-y.

[4] T. Bartel and K. Hackl. A micromechanical model for martensitic phase-transformations in shape-memory alloys based on energy-relaxation. *Zeitschrift für Angewandte Mathematik und Mechanik*, 89(10):792–809, 2009. doi:10.1002/zamm.200900244.

[5] T. Bartel, A. Menzel, and B. Svendsen. Thermodynamic and relaxation-based modeling of the interaction between martensitic phase transformations and plasticity. *Journal of the Mechanics and Physics of Solids*, 59(5):1004–1019, 2011. doi:10.1016/j.jmps.2011.02.006.

[6] T. Bartel, R. Schulte, A. Menzel, B. Kiefer, and B. Svendsen. Investigations on enhanced Fischer-Burmeister NCP functions: application to a rate-dependent model for ferroelectrics. *Archive of Applied Mechanics*, 89:995–1010, 2019. doi:10.1007/s00419-018-1466-7.

[7] A. Benaarbia, A. Chrysochoos, and G. Robert. Influence of relative humidity and loading frequency on the PA6.6 cyclic thermomechanical behavior: Part I. mechanical and thermal aspects. *Polymer Testing*, 40:290–298, 2014. doi:10.1016/j.polymertesting.2014.09.019.

[8] J. Bergström and M. Boyce. Constitutive modeling of the large strain time-dependent behavior of elastomers. *Journal of the Mechanics and Physics of Solids*, 46(5):931–954, 1998. ISSN 0022-5096. doi:10.1016/S0022-5096(97)00075-6.

[9] K. Bhattacharya. Comparison of the geometrically nonlinear and linear theories of martensitic transformation. *Continuum Mechanics and Thermodynamics*, 5(3): 205–242, 1993. doi:10.1007/BF01126525.

[10] J. Bonet and R. D. Wood. *Nonlinear continuum mechanics for finite element analysis*. Cambridge Univ. Press, New York, second edition edition, 2008. doi:10.1017/CBO9780511755446.

[11] R. Brighenti and F. Artoni. Mechanical modelling of self-diagnostic polymers. *Procedia Structural Integrity*, 13:819 – 824, 2018. ISSN 2452-3216. doi:10.1016/j.prostr.2018.12.157. ECF22 - Loading and Environmental effects on Structural Integrity.

[12] B. Chen, X. Chen, and C. Kanzow. A penalized Fischer-Burmeister NCP-function. *Math. Program.*, 88:211–216, 2000. doi:10.1007/PL00011375.

[13] J.-S. Chen. On some NCP-functions based on the generalized Fischer-Burmeister function. *Asia-Pacific Journal of Operational Research*, 24:401–420, 2007. doi:10.1142/S0217595907001292.

[14] J.-S. Chen and S. Pan. A family of NCP functions and a descent method for the nonlinear complementarity problem. *Asia-Pacific Journal of Operational Research*, 24:401–420, 2007. doi:10.1007/s10589-007-9086-0.

[15] B. Dimitrijevic and K. Hackl. A method for gradient enhancement of continuum damage models. *Technische Mechanik*, 28(1):43–52, 2008.

[16] D. K. Dusthakar, A. Menzel, and B. Svendsen. Comparison of phenomenological and laminate-based models for rate-dependent switching in ferroelectric continua. *GAMM-Mitteilungen*, 38(1):147–170, 2015. doi:10.1002/gamm.201510008.

[17] D. K. Dusthakar, A. Menzel, and B. Svendsen. Laminate-based modelling of single and polycrystalline ferroelectric materials - application to tetragonal barium titanate. *Mechanics of Materials*, 117:235–254, 2018. doi:10.1016/j.mechmat.2017.10.005.

[18] S. Engelke and C. Kanzow. Predictor-corrector smoothing methods for linear programs with a more flexible update of the smoothing parameter. *Computational Otimization and Apllication*, 23:299–320, 2002. doi:10.1023/A:1020598927544.

[19] A. Fischer. A special Newton-type optimization method. *Optimization*, 24(3-4): 269–284, 1992. doi:10.1080/02331939208843795.

[20] S. Forest. Micromorphic approach for gradient elasticity, viscoplasticity, and damage. *Journal of Engineering Mechanics*, 135(3):117–131, 2009. doi:10.1061/(ASCE)0733-9399(2009)135:3(117).

[21] A. F. Fossum. Parameter estimation for an internal variable model using nonlinear optimization and analytical/numerical response sensitivities. *Journal of Engineering Materials and Technology*, 119(4):337–345, 1997. doi:10.1115/1.2812267.

[22] A. Früh, F. Artoni, R. Brighenti, and E. Dalcanale. Strain field self-diagnostic poly(dimethylsiloxane) elastomers. *Chemistry of Materials*, 29(17):7450–7457, 2017. doi:10.1021/acs.chemmater.7b02438.

[23] T. Furukawa and G. Yagawa. Inelastic constitutive parameter identification using an evolutionary algorithm with continuous individuals. *International Journal for Numerical Methods in Engineering*, 40(6):1071–1090, 1997. doi:10.1002/(SICI)1097-0207(19970330)40:6<1071::AID-NME99>3.0.CO;2-8.

[24] C. Geiger and C. Kanzow. *Numerische Verfahren zur Lösung unrestringierter Optimierungsaufgaben*. Springer-Verlag, Berlin Heidelberg, 1999. doi:10.1007/978-3-642-58582-1.

[25] J.-C. Gelin and O. Ghouati. An inverse solution procedure for material parameters identification in large plastic deformations. *Communications in Numerical Methods in Engineering*, 12(3):161–173, 1996. doi:10.1002/(SICI)1099-0887(199603)12:3<161::AID-CNM961>3.0.CO;2-E.

[26] GitHub. URL `https://github.com/aschowtjak/ADAPT`.

[27] M. Grédiac and F. Pierron. Applying the virtual fields method to the identification of elasto-plastic constitutive parameters. *International Journal of Plasticity*, 22 (4):602–627, 2006. ISSN 0749-6419. doi:10.1016/j.ijplas.2005.04.007.

[28] Z. Guo, R. Bai, Z. Lei, H. Jiang, D. Liu, J. Zou, and C. Yan. CPINet: Parameter identification of path-dependent constitutive model with automatic denoising based on CNN-LSTM. *European Journal of Mechanics - A/Solids*, 90:104327, 2021. ISSN 0997-7538. doi:10.1016/j.euromechsol.2021.104327.

[29] A. L. Gurson. Continuum Theory of Ductile Rupture by Void Nucleation and Growth: Part I - Yield Criteria and Flow Rules for Porous Ductile Media. *Journal of Engineering Materials and Technology*, 99(1):2–15, 01 1977. ISSN 0094-4289. doi:10.1115/1.3443401.

[30] D. J. Hartl, B. Kiefer, R. Schulte, and A. Menzel. Computationally-efficient modeling of inelastic single crystal responses via anisotropic yield surfaces: Applications to shape memory alloys. *International Journal of Solids and Structures*, 136-137: 38–59, 2018. doi:10.1016/j.ijsolstr.2017.12.002.

[31] S. Hartmann. Parameter estimation of hyperelasticity relations of generalized polynomial-type with constraint conditions. *International Journal of Solids and Structures*, 38:7999–8018, 2000. doi:10.1016/S0020-7683(01)00018-X.

[32] S. Hartmann and R. Gilbert. Identifiability of material parameters in solid mechanics. *Archive of Applied Mechanics*, 88:3–26, 2018. doi:10.1007/s00419-017-1259-4.

[33] S. Hartmann, J. Gibmeier, and B. Scholtes. Experiments and material parameter identification using finite elements. uniaxial tests and validation using instrumented indentation tests. *Experimental Mechanics*, 46:5–18, 2006. doi:10.1007/s11340-006-5857-2.

[34] S. Hartmann and R. R. Gilbert. Material parameter identification using finite elements with time-adaptive higher-order time integration and experimental full-field strain information. *Computational Mechanics*, 68:633–650, 2021.

doi:10.1007/s00466-021-01998-3.

[35] O. Hering. *Schädigung in der Kaltmassifumformung: Entwicklung, Auswirkung und Kontrolle*. Dissertation Thesis, Technische Universität Dortmund, 2020. doi:10.17877/DE290R-21691.

[36] J. E. Huber. Micromechanical modelling of ferroelectrics. *Current Opinion in Solid State and Materials Science*, 9(3):100–106, 2005. doi:10.1016/j.cossms.2006.05.001.

[37] J. Huber. *Electromechanical Models of Ferroelectric Materials*, pages 179–226. Eds.: J. Schröder and D.C. Lupascu, first edition, 2018. doi:10.1007/978-3-319-68883-1. Ferroic Functional Materials.

[38] N. Huber and C. Tsakmakis. A neural network tool for identifying the material parameters of a finite deformation viscoplasticity model with static recovery. *Computer Methods in Applied Mechanics and Engineering*, 191:353–384, 2001. doi:10.1016/S0045-7825(01)00278-X.

[39] S. C. Hwang, C. S. Lynch, and R. M. McMeeking. Ferroelectric/ferroelastic interactions and a polarization switching model. *Acta Metallurgica et Materialia*, 43 (5):2073–2084, 1995. doi:10.1016/0956-7151(94)00379-V.

[40] B. Jaffe, W. R. Cook, and H. Jaffe. *Piezoelectric Ceramics*. Academic Press, 1971. doi:10.1016/B978-0-12-379550-2.X5001-7.

[41] L. Kachanov. Time of the rupture process under creep conditions. *Izvestija Akademii Nauk Sojuza Sovetskich Socialisticeskich Respubliki*, 8:26–31, 1958. doi:10.1023/A:1018671022008.

[42] L. Kachanov. *Introduction to continuum damage mechanics*. Martinus Jijhoff Publishers, Leiden, 1986. doi:10.1007/978-94-017-1957-5.

[43] J. Kajberg and G. Lindkvist. Characterisation of materials subjected to large strains by inverse modelling based on in-plane displacement fields. *International Journal of Solids and Structures*, 41(13):3439–3459, 2004. ISSN 0020-7683. doi:10.1016/j.ijsolstr.2004.02.021.

[44] M. Kaliske and H. Rothert. Formulation and implementation of three-dimensional viscoelasticity at small and finite strains. *Computational Mechanics*, 19:228–239, 1997. doi:10.1007/s004660050171.

[45] V. Kalpakides and A. Arvanitakis. A level set approach to domain wall kinetics and domain patterning in elastic ferroelectrics. *Computational Methods in Applied Mechanics and Engineering*, 199:2865–2875, 2010. doi:10.1016/j.cma.2010.05.009.

[46] M. Kamlah. Ferroelectric and ferroelastic piezoceramics – modeling of electromechanical hysteresis phenomena. *Continuum Mechanics and Thermodynamics*, 13 (4):219–268, 2001. doi:10.1007/s001610100052.

[47] C. Kanzow. Some noninterior continuation methods for linear complementarity problems. *SIAM Journal on Matrix Analysis and Applications*, 17(4):851–868,

1996. doi:10.1137/S0895479894273134.

[48] P. Kattan and G. Voyiadjis. A coupled theory of damage mechanics and finite strain elasto-plasticity - I. damage and elastic deformations. *International Journal of Engineering Science*, 28(5):421–435, 1990. doi:10.1016/0020-7225(90)90007-6.

[49] K. T. Kavanagh and R. W. Clough. Finite element applications in the characterization of elastic solids. *International Journal of Solids and Structures*, 7(1):11–23, 1971. ISSN 0020-7683. doi:10.1016/0020-7683(71)90015-1.

[50] B. Kiefer, T. Bartel, and A. Menzel. Implementation of numerical integration schemes for the simulation of magnetic sma constitutive response. *Smart Materials and Structures*, 21(9):094007, 2012. doi:10.1088/0964-1726/21/9/094007.

[51] B. Kiefer, T. Waffenschmidt, L. Sprave, and A. Menzel. A gradient-enhanced damage model coupled to plasticity—multi-surface formulation and algorithmic concepts. *International Journal of Damage Mechanics*, 27(2):253–295, 2018. doi:10.1177/1056789516676306.

[52] B. Kleuter. *Generalized Parameter Identification for Finite Viscoelasticity.* Dissertation thesis, TU Kaiserslautern, 2007.

[53] B. Kleuter, A. Menzel, and P. Steinmann. Generalized parameter identification for finite viscoelasticity. *Computer Methods in Applied Mechanics and Engineering*, 196:3315–3334, 07 2007. doi:10.1016/j.cma.2007.03.010.

[54] F. Kolpak, H. Traphöner, O. Hering, and A. E. Tekkaya. Large strain flow curves of sheet metals by sheet extrusion. *CIRP Annals*, 70(1):247–250, 2021. ISSN 0007-8506. doi:10.1016/j.cirp.2021.03.023.

[55] D. Krajcinovic. *Damage mechanics, vol 41.* Elsevier, New York, 1996.

[56] D. Krajcinovic and J.-L. Lemaitre. *Continuum damage mechanics-theory and applications.* CISM Courses and Lectures No. 295, Springer, Wien, 1987. doi:10.1007/978-3-7091-2806-0.

[57] Z. Ktari, C. Leitão, P. A. Prates, and A. Khalfallah. Mechanical design of ring tensile specimen via surrogate modelling for inverse material parameter identification. *Mechanics of Materials*, 153:103673, 2021. ISSN 0167-6636. doi:10.1016/j.mechmat.2020.103673.

[58] F. Kublik and E. Steck. *Comparison of Two Constitutive Models with One- and Multiaxial Experiments*, pages 37–46. Finite Inelastic Deformations – Theory and Applications. International Union of Theoretical and Applied Mechanics. Eds.: D. Besdo, E. Stein. Springer, Berlin, Heidelberg, 1992. doi:10.1007/978-3-642-84833-9_4.

[59] K. Langenfeld, A. Schowtjak, R. Schulte, O. Hering, K. Möhring, T. Clausmeyer, R. Ostwald, F. Walther, A. Tekkaya, and J. Mosler. Influence of anisotropic damage evolution on cold forging. *Prod. Eng. Res. Devel.*, 14:115–121, 2020.

doi:10.1007/s11740-019-00942-y.

[60] D. Lasry and T. Belytschko. Localization limiters in transient problems. *International Journal of Solids and Structures*, 24(6):581–597, 1988. ISSN 0020-7683. doi:10.1016/0020-7683(88)90059-5.

[61] F. Leckie and E. Onat. *Tensorial nature of damage measuring internal variables*, pages 140–155. Eds.: J. Hult and J. Lemaitre, 1981. doi:10.1007/978-3-642-81582-9_20.

[62] J. Lemaitre. A continuous damage mechanics model for ductile fracture. *Journal of Engineering Materials and Technology*, 107(1):83–89, 1985. doi:10.1115/1.3225775.

[63] J. Lemaitre. *A Course on Damage Mechanics*. Springer, Berlin Heidelberg, 1996. doi:10.1007/978-3-642-18255-6.

[64] J. Lemaitre and J.-L. Caboche. *Mechanics of solid materials*. Cambridge University Press, Cambridge, 1990. doi:10.1017/CBO9781139167970.

[65] J.-Y. Li and D. Liu. On ferroelectric crystals with engineered domain configurations. *Journal of the Mechanics and Physics of Solids*, 52(8):1719–1742, 2004. doi:10.1016/j.jmps.2004.02.011.

[66] J.-Y. Li, C.-H. Lei, L.-J. Li, Y.-C. Shu, and Y.-Y. Liu. Unconventional phase field simulations of transforming materials with evolving microstructures. *Acta Mechanica Sinica*, 28(4):915–927, 2012. doi:10.1007/s10409-012-0129-0.

[67] Y. W. Li and F. X. Li. The effect of domain patterns on 180° domain switching in $BaTiO_3$ crystals during antiparallel electric field loading. *Applied Physics Letters*, 104(4):042908–042911, 2014. doi:10.1063/1.4863672.

[68] M. Lines and A. Glass. *Principles and Applications of Ferroelectrics and Related Materials*. Oxford University Press, 2001. doi:10.1093/acprof:oso/9780198507789.001.0001.

[69] N. Liu and A. E. Jeffers. Feature-preserving rational Bézier triangles for isogeometric analysis of higher-order gradient damage models. *Computer Methods in Applied Mechanics and Engineering*, 357:112585, 2019. ISSN 0045-7825. doi:10.1016/j.cma.2019.112585.

[70] D. Luenberger and Y. Ye. *Linear and Nonlinear Programming*. Springer Cham, Switzerland, 4th edition edition, 2016. doi:10.1007/978-3-319-18842-3.

[71] C. S. Lynch. On the development of multiaxial phenomenological constitutive laws for ferroelectric ceramics. *Journal of Intelligent Material Systems and Structures*, 9(7):555–563, 1998. doi:10.1177/1045389X9800900707.

[72] R. Mahnken. *Identification of Material Parameters for Constitutive Equations*, chapter 19, pages 637–655. Eds.: E. Stein, R. de Borst, T.J.R. Hughes. John Wiley and Sons, second edition, 2004. doi:10.1002/0470091355.ecm043. Encyclopedia of Computational Mechanics.

[73] R. Mahnken and E. Stein. A unified approach for parameter identification of inelastic material models in the frame of the finite element method. *Computer Methods in Applied Mechanics and Engineering*, 136:225–258, 1996. doi:10.1016/0045-7825(96)00991-7.

[74] R. Mahnken. *Theoretische und numerische Aspekte zur Parameteridentifikation und Modellierung bei metallischen Werkstoffen*. Forschungs- und Seminarbereichte aus dem Bereich der Mechanik der Universität Hannover, Habilitation Thesis, 1998.

[75] R. Mahnken and E. Kuhl. Parameter identification of gradient enhanced damage models with the finite element method. *European Journal of Mechanics - A/Solids*, 18(5):819–835, 1999. ISSN 0997-7538. doi:10.1016/S0997-7538(99)00127-8.

[76] R. Mahnken and E. Stein. Parameter identification for finite deformation elasto-plasticity in principal directions. *Computer Methods in Applied Mechanics and Engineering*, 147:17–39, 1997. doi:10.1016/S0045-7825(97)00008-X.

[77] A. Marek, F. M. Davis, and F. Pierron. Sensitivity-based virtual fields for the non-linear virtual fields method. *Computational Mechanics*, 60:409 – 431, 2017. doi:10.1007/s00466-017-1411-6.

[78] J. Mergheim, G. Possart, and P. Steinmann. Modelling and computation of curing and damage of thermosets. *Computational Materials Science*, 53(1):359–367, 2012. ISSN 0927-0256. doi:10.1016/j.commatsci.2011.09.013.

[79] C. Miehe and D. Kiefer, B.and Rosato. An incremental variational formulation of dissipative magnetostriction at the macroscopic continuum level. *International Journal of Solids and Structures*, 48(13):1846–1866, 2011. doi:10.1016/j.ijsolstr.2011.02.011.

[80] C. Miehe and D. Rosato. A rate-dependent incremental variational formulation of ferroelectricity. *International Journal of Engineering Science*, 49(6):466–496, 2011. doi:10.1016/j.ijengsci.2010.11.003.

[81] C. Miehe, D. Rosato, and B. Kiefer. Variational principles in dissipative electro-magneto-mechanics: A framework for the macro-modeling of functional materials. *International Journal for Numerical Methods in Engineering*, 86(10):1225–1276, 2011. doi:10.1002/nme.3127.

[82] C. Miehe, D. Zäh, and D. Rosato. Variational-based modeling of micro-electro-elasticity with electric field-driven and stress-driven domain evolutions. *International Journal for Numerical Methods in Engineering*, 91(2):115–141, 2012. doi:10.1002/nme.4254.

[83] C. Miehe. A multi-field incremental variational framework for gradient-extended standard dissipative solids. *Journal of the Mechanics and Physics of Solids*, 59(4): 898–923, 2011. ISSN 0022-5096. doi:10.1016/j.jmps.2010.11.001.

[84] J. A. Nelder and R. Mead. A simplex method for function minimization. *The Computer Journal*, 13:308–313, 1965. doi:10.1093/comjnl/7.4.308.

[85] J. Nocedal and S. Wright. *Numerical Optimization*. Springer, New York, USA, 2nd edition edition, 2006. doi:10.1007/978-0-387-40065-5.

[86] R. Ostwald, E. Kuhl, and A. Menzel. On the implementation of finite deformation gradient-enhanced damage models. *Computational Mechanics*, 64:847–877, 2019. doi:10.1007/s00466-019-01684-5.

[87] F. Pedregosa, G. Varoquaux, A. Gramfort, V. Michel, B. Thirion, O. Grisel, M. Blondel, P. Prettenhofer, R. Weiss, V. Dubourg, J. Vanderplas, A. Passos, D. Cournapeau, M. Brucher, M. Perrot, and E. Duchesnay. Scikit-learn: Machine learning in Python. *Journal of Machine Learning Research*, 12:2825–2830, 2011. doi:10.48550/arXiv.1201.0490.

[88] C. Polindara, T. Waffenschmidt, and A. Menzel. Simulation of balloon angioplasty in residually stressed blood vessels - application of a gradient-enhanced fibre damage model. *Journal of Biomechanics*, 49(12):2341–2348, 2016. doi:10.1016/j.jbiomech.2016.01.037.

[89] C. Polindara, T. Waffenschmidt, and A. Menzel. A computational framework for modelling damage-induced softening in fibre-reinforced materials - application to balloon angioplasty. *International Journal of Solids and Structures*, 118-119: 235–256, 2017. doi:10.1016/j.ijsolstr.2017.02.010.

[90] C. Polizzotto, G. Borino, and P. Fuschi. A thermodynamically consistent formulation of nonlocal and gradient plasticity. *Mechanics Research Communications*, 25(1):75–82, 1998. doi:10.1016/S0093-6413(98)00009-3.

[91] A. Quarteroni, R. Sacco, and F. Saleri. *Numerical Mathematics, Texts in Applied Mathematics*, volume 37. Springer, Berlin/Heidelberg, Germany, 2nd edition edition, 2007. doi:10.1007/b98885.

[92] S. Reese and S. Govindjee. A theory of finite viscoelasticity and numerical aspects. *International Journal of Solids and Structures*, 35(26):3455–3482, 1998. doi:10.1016/S0020-7683(97)00217-5.

[93] A. Rieger. *Zur Parameteridentifikation komplexer Materialmodelle auf der Basis realer und virtueller Testdaten*. Dissertation thesis, University of Stuttgart, 2005.

[94] R. Rivlin. Chapter 10 - large elastic deformations. In F. Eirich, editor, *Rheology: Theory and Applications*, volume 1, pages 351–385. Academic Press, 1956. doi:10.1016/B978-0-12-395694-1.50016-6.

[95] L. Rose and A. Menzel. Identification of thermal material parameters for thermo-mechanically coupled material models. *Meccanica*, 56(2):393–416, 2021. doi:10.1007/s11012-020-01267-2.

[96] L. Rose. *Optimierungsbasierte Parameteridentifikation mittels optischer Feldmessungen*. Dissertation thesis, Institute of Mechanics, TU Dortmund University, Fakultät Maschinenbau, 2022.

[97] L. Rose and A. Menzel. Optimisation based material parameter identification using full field displacement and temperature measurements. *Mechanics of Materials*, 145:103292, 2020. doi:10.1016/j.mechmat.2019.103292. Erratum - 151 (2020), 103630.

[98] M. Rossi and F. Pierron. Identification of plastic constitutive parameters at large deformations from three dimensional displacement fields. *Computational Mechanics*, 49:53–71, 2012. doi:10.1007/s00466-011-0627-0.

[99] M. Rossi, A. Lattanzi, L. Morichelli, J. M. P. Martins, S. Thuillier, A. Andrade-Campos, and S. Coppieters. Testing methodologies for the calibration of advanced plasticity models for sheet metals: A review. *Strain*, page e12426, 2022. doi:10.1111/str.12426.

[100] G. Scheday and C. Miehe. An unified computational framework for parameter identification of material models in finite inelasticity. *Proc. Appl. Math. Mech.*, 1:189–190, 2002. doi:10.1002/1617-7061(200203)1:1<3C189::AID-PAMM189>3E3.0.CO;2-K.

[101] G. Scheday. *Theorie und Numerik der Parameteridentifikation von Materialmodellen der finiten Elastizität und Inelastizität auf Grundlage optischer Feldmeßmethoden*. Dissertation thesis, Institut für Mechanik, Lehrstuhl I, Universität Stuttgart, Fakultät Bauingenieur- und Vermessungswesen, 2003.

[102] M. Schmidt-Baldassari. Numerical concepts for rate-independent single crystal plasticity. *Computer Methods in Applied Mechanics and Engineering*, 192(11): 1261–1280, 2003. doi:10.1016/S0045-7825(02)00563-7.

[103] A. Schowtjak, S. Wang, O. Hering, T. Clausmeyer, J. Lohmar, R. Schulte, R. Ostwald, G. Hirt, and A. E. Tekkaya. Prediction and analysis of damage evolution during caliber rolling and subsequent cold forward extrusion. *Prod. Eng. Res. Devel.*, 14:33–41, 2020. doi:10.1007/s11740-019-00935-x.

[104] A. Schowtjak, R. Schulte, T. Clausmeyer, R. Ostwald, A. E. Tekkaya, and A. Menzel. ADAPT – A Diversely Applicable Parameter Identification Tool: Overview and full-field application examples. *International Journal of Mechanical Sciences*, 213:106840, 2022. doi:10.1016/j.ijmecsci.2021.106840.

[105] D. Schrade, R. Mueller, B.-X. Xu, and D. Gross. Domain evolution in ferroelectric materials: A continuum phase field model and finite element implementation. *Computer Methods in Applied Mechanics and Engineering*, 196(41):4365–4374, 2007. doi:10.1016/j.cma.2007.05.010.

[106] J. Schröder and M.-A. Keip. Two-scale homogenization of electromechanically coupled boundary value problems. *Computational Mechanics*, 50:229–244, 2012.

doi:10.1007/s00466-012-0715-9.

[107] J. Schröder and H. Romanowski. A thermodynamically consistent mesoscopic model for transversely isotropic ferroelectric ceramics in a coordinate-invariant setting. *Archive of Applied Mechanics*, 74(11-12):863–877, 2005. doi:10.1007/s00419-005-0412-7.

[108] R. Schulte, T. Bartel, A. Menzel, B. Kiefer, and B. Svendsen. Investigations on different Fischer-Burmeister functions applied to the modelling of ferroelectrics. *Proc. Appl. Math. Mech.*, 18(e201800331), 2018. doi:10.1002/pamm.201800331.

[109] R. Schulte, A. Menzel, and B. Svendsen. A laminate-based material model applied to ferroelectrics. *Proceedings of the 3rd Seminar on The Mechanics of Multifunctional Materials*, 18:105–108, 2018.

[110] R. Schulte, O. Ostwald, and A. Menzel. Gradient-enhanced modelling of damage for rate-dependent material behaviour—a parameter identification framework. *Materials*, 13(14):3156, 2020. doi:10.3390/ma13143156.

[111] R. Schulte, R. Ostwald, and A. Menzel. A computational framework for gradient-enhanced damage – implementation and applications. *Proc. Appl. Math. Mech.*, 20(e202000215), 2021. doi:10.1002/pamm.202000215.

[112] R. Schulte. *Parameter identification framework for inhomogeneous states of deformation using Abaqus: Application to inelastic and gradient-enhanced material models*. Master thesis, Institute of Mechanics, TU Dortmund University, Fakultät Maschinenbau, 2016.

[113] R. Schulte, C. Karca, R. Ostwald, and A. Menzel. Machine learning-assisted parameter identification for constitutive models based on concatenated loading path sequences. *European Journal of Mechanics - A/Solids*, 98:104854, 2023. ISSN 0997-7538. doi:10.1016/j.euromechsol.2022.104854.

[114] J. Shieh, J.-H. Yeh, Y.-C. Shu, and J.-H. Yen. Operation of multiple 90° switching systems in barium titanate single crystals under electromechanical loading. *Applied Physics Letter*, 91:062901, 2007. doi:10.1063/1.2766658.

[115] Y.-C. Shu and K. Bhattacharya. Domain patterns and macroscopic behaviour of ferroelectric materials. *Philosophical Magazine Part B*, 81(12):2021–2054, 2001. doi:10.1080/13642810108208556.

[116] J. C. Simo. On a fully three-dimensional finite-strain viscoelastic damage model: formulation and computational aspects. *Computer Methods in Applied Mechanics and Engineering*, 60:153–173, 1987. doi:10.1016/0045-7825(87)90107-1.

[117] J. Simo and T. Hughes. *Computational Inelasticity*. Interdisciplinary Applied Mathematics. Springer, New York, 1998. doi:10.1007/b98904.

[118] R. C. Smith. *Smart Material Systems - Model Development*. Society for Industrial and Applied Mathematics, Philadelphia, 2005. doi:10.1137/1.9780898717471.

[119] L. Sprave and A. Menzel. A large strain gradient-enhanced ductile damage model: finite element formulation, experiment and parameter identification. *Acta Mechanica*, 231:5159–5192, 2020. doi:10.1007/s00707-020-02786-5.

[120] L. Sprave, A. Schowtjak, R. Meya, T. Clausmeyer, A. Tekkaya, and A. Menzel. On mesh dependencies in finite-element-based damage prediction: application to sheet metal bending. *Prod. Eng. Res. Devel.*, 14:123–134, 2020. doi:10.1007/s11740-019-00937-9.

[121] D. Sun and L. Qi. On NCP-functions. *Computational Optimization and Applications*, 13:201–220, 1999. doi:10.1023/A:1008669226453.

[122] D. Sun and R. S. Womersley. A new unconstrained differentiable merit function for box constrained variational inequality problems and a damped Gauss-Newton method. *SIAM J. Optim.*, 9(2):388–413, 1999. doi:10.1137/S1052623496314173.

[123] R. Sundaram. *A First Course on Optimization Theory*. Cambridge University Press, Camebridge, UK, 1996. doi:10.1017/CBO9780511804526.

[124] I. E. Sutherland, R. F. Sproull, and R. A. Schumacker. A characterization of ten hidden-surface algorithms. *ACM Comput. Surv.*, 6(1):1–55, 1974. ISSN 0360-0300. doi:10.1145/356625.356626.

[125] A. Tagantsev, L. Cross, and J. Fousek. *Domains in Ferroic Crystals and Thin Films*. Springer New York, NY, New York, USA, 1st edition edition, 2010. doi:10.1007/978-1-4419-1417-0.

[126] A. E. Tekkaya, N. Ben Khalifa, O. Hering, R. Meya, S. Myslicki, and F. Walther. Forming-induced damage and its effects on product properties. *CIRP Annals*, 66 (1):281–284, 2017. doi:10.1016/j.cirp.2017.04.113.

[127] A. Tekkaya, J. Allwood, P. Bariani, S. Bruschi, J. Cao, S. Gramlich, P. Groche, G. Hirt, T. Ishikawa, C. Löbbe, J. Lueg-Althoff, M. Merklein, W. Misiolek, M. Pietrzyk, R. Shivpuri, and J. Yanagimoto. Metal forming beyond shaping: Predicting and setting product properties. *CIRP Annals*, 64(2):629–653, 2015. doi:10.1016/j.cirp.2015.05.001.

[128] H. Traphöner, T. Clausmeyer, and A. E. Tekkaya. Methods for measuring large shear strains in in-plane torsion tests. *Journal of Materials Processing Technology*, 287:116516, 2021. doi:10.1016/j.jmatprotec.2019.116516.

[129] N. Tsou and J. Huber. Compatible domain structures and the poling of single crystal ferroelectrics. *Mechanics of Materials*, 42(7):740–753, 2010. doi:10.1016/j.mechmat.2010.04.004.

[130] N. Tsou, J. Huber, and A. Cocks. Evolution of compatible laminate domain structures in ferroelectric single crystals. *Acta Materialia*, 61(2):670–682, 2013. doi:10.1016/j.actamat.2012.10.015.

[131] V. Tvergaard and A. Needleman. Analysis of the cup-cone fracture in a round tensile bar. *Acta Metallurgica*, 32(1):157–169, 1984. doi:10.1016/0001-6160(84)90213-X.

[132] P. Virtanen, R. Gommers, T. E. Oliphant, M. Haberland, T. Reddy, D. Cournapeau, E. Burovski, P. Peterson, W. Weckesser, J. Bright, S. J. van der Walt, M. Brett, J. Wilson, K. J. Millman, N. Mayorov, A. R. J. Nelson, E. Jones, R. Kern, E. Larson, C. J. Carey, İ. Polat, Y. Feng, E. W. Moore, J. VanderPlas, D. Laxalde, J. Perktold, R. Cimrman, I. Henriksen, E. A. Quintero, C. R. Harris, A. M. Archibald, A. H. Ribeiro, F. Pedregosa, P. van Mulbregt, and SciPy 1.0 Contributors. SciPy 1.0: Fundamental Algorithms for Scientific Computing in Python. *Nature Methods*, 17:261–272, 2020. doi:10.1038/s41592-019-0686-2.

[133] T. Waffenschmidt, C. Polindara, A. Menzel, and S. Blanco. A gradient-enhanced large-deformation continuum damage model for fibre-reinforced materials. *Computer Methods in Applied Mechanics and Engineering*, 268:801–842, 2014. doi:10.1016/j.cma.2013.10.013.

[134] T. Waffenschmidt, C. Polindara, and A. Menzel. *A Gradient-Enhanced Continuum Damage Model for Residually Stressed Fibre-Reinforced Materials at Finite Strains*, pages 19–40. Eds. T. Lenarz, P. Wriggers. Springer International Publishing, Cham, 2015. doi:10.1007/978-3-319-10981-7_2. Biomedical Technology.

[135] D. Yao, Y. Duan, M. Li, and Y. Guan. Hybrid identification method of coupled viscoplastic-damage constitutive parameters based on BP neural network and genetic algorithm. *Engineering Fracture Mechanics*, 257:108027, 2021. doi:10.1016/j.engfracmech.2021.108027.

[136] J.-H. Yen, Y.-C. Shu, J. Shieh, and J.-H. Yeh. A study of electromechanical switching in ferroelectric single crystals. *Journal of the Mechanics and Physics of Solids*, 56(6):2117–2135, 2008. doi:10.1016/j.jmps.2008.02.004.

[137] O. H. Yeoh. Characterization of elastic properties of carbon-black-filled rubber vulcanizates. *Rubber Chemistry and Technology*, 63(5):792–805, 1990. doi:10.5254/1.3538289.

[138] O. H. Yeoh. Some forms of the strain energy function for rubber. *Rubber Chemistry and Technology*, 66(5):754–771, 1993. doi:10.5254/1.3538343.

[139] O. H. Yeoh and P. D. Fleming. A new attempt to reconcile the statistical and phenomenological theories of rubber elasticity. *Journal of Polymer Science Part B: Polymer Physics*, 35:1919 – 1931, 09 1997. doi:10.1002/(SICI)1099-0488(19970915)35:12<1919::AID-POLB7>3.0.CO;2-K.

[140] M. Zgonik, P. Bernasconi, M. Duelli, R. Schlesser, P. Günter, M. Garrett, D. Rytz, Y. Zhu, and X. Wu. Dielectric, elastic, piezoelectric, electro-optic, and elasto-optic tensors of batio3 crystals. *Phys Rev B Condens Matter*, 50(9):5941–5949, 1994. doi:10.1103/physrevb.50.5941.

[141] B. Zhang, B. Endelt, L. Lang, and K. B. Nielsen. Identification of constitutive parameters for thin-walled aluminium tubes using a hybrid strategy. *Materials Today Communications*, 28:102670, 2021. doi:10.1016/j.mtcomm.2021.102670.

[142] Y. Zhang, A. Van Bael, A. Andrade-Campos, and S. Coppieters. Parameter identifiability analysis: Mitigating the non-uniqueness issue in the inverse identification of an anisotropic yield function. *International Journal of Solids and Structures*, 243:111543, 2022. doi:10.1016/j.ijsolstr.2022.111543.

Publication series of the Institute of Mechanics

published to date:

2010/01 Palnau, V.: Implementierung eines netzfreien Diskretisierungsverfahrens und seine Anwendung auf die Scherbandanalyse.
ISBN 978-3-921823-51-4

2010/02 Klusemann, B.: Application of homogenization methods and crystal plasticity to the modeling of heterogeneous materials of technological interest.
ISBN 978-3-921823-53-8

2011/01 Hortig, C.: Local and non-local thermomechanical modeling and finite-element simulation of high-speed cutting.
ISBN 978-3-921823-54-5

2011/02 Parvizian, F.: Modeling of microstructure evolution in aluminum alloys during hot extrusion.
ISBN 978-3-921823-56-9

2011/03 Noman, M.: Characterization and model identification for the simulation of the forming behavior of ferritic steels.
ISBN: 978-3-921823-55-2

2011/04 Kayser, T.: Characterization of microstructure in aluminum alloys based on electron backscatter diffraction.
ISBN: 978-3-921823-57-6

2011/05 Bargmann, S.: Computational modeling of material behavior on different scales based on continuum mechanics.
ISBN: 978-3-921823-58-3

2013/01 Waffenschmidt, T.: Modelling and simulation of adaptation and degradation in anisotropic biological tissues.
ISBN: 978-3-921823-61-3

2015/01 Ostwald, R.: Modelling and simulation of phase-transformations in elastoplastic polycrystals.
ISBN: 978-3-921823-66-8

2016/01 Subramanian, M.: Phenomenological modelling and simulation of ferroelectric ceramics.
ISBN: 978-3-921823-74-3

2016/02 Clausmeyer, T.: Evolution of plastic anisotropy in metals.
ISBN: 978-3-921823-76-7

2017/01 Holtermann, R.: Computational multiscale modelling of grinding processes.
ISBN: 978-3-921823-86-6

2017/02 Bartels, A.: Modelling of evolving microstructures at different scales.
ISBN: 978-3-921823-93-4

2017/03 Dusthakar Kumar Rao, D. K.: Computational modelling of single and polycrystalline ferroelectric materials.
ISBN 978-3-921823-94-1

2019/01 Buckmann, K.: Microstructure evolution in functional magnetic materials.
ISBN 978-3-947323-09-8

2019/02 Kaiser, T.: Computational modelling of non-simple and anisotropic materials.
ISBN 978-3-947323-14-2

2019/03 Heitbreder, T.: Modelling of material interfaces at different length scales.
ISBN 978-3-947323-18-0

2020/01 Berthelsen, R.: Computational homogenisation of thermomechanical problems.
ISBN 978-3-947323-19-7

2020/02 Sievers, C.: Describing the macroscopic behavior of surfaces based on atomistic models.
ISBN 978-3-947323-24-1

2022/01 Rose, L.: Optimisation based parameter identification using optical field measurements.
ISBN 978-3-947323-31-9

2023/01 Langenfeld, K.: Continuum modeling of brittle and ductile damage: theory and computational frameworks.
ISBN 978-3-947323-41-8

2023/02 Schulte, R.: Parameter identification approaches with application to different classes of materials.
ISBN 978-3-947323-45-6